Optimized AFM approaches for force-indentation measurements associated with cell elasticity

Inauguraldissertation
zur
Erlangung des akademischen Grades eines
Doktors der Naturwissenschaften (Dr. rer. nat.)
der
Mathematisch-Naturwissenschaftlichen Fakultät der
Ernst-Moritz-Arndt-Universität Greifswald

vorgelegt von
Michael Glaubitz
geboren am 18. Juli 1984
in Riesa

Greifswald, im August 2014

Dekan:	Prof. Dr. rer. nat. Klaus Fesser
1. Gutachter:	Prof. Dr. rer. nat. Christiane A. Helm
2. Gutachter:	Prof. Dr. rer. nat. Hans-Jürgen Butt
Tag der Einreichung:	22.08.2014
Tag der Promotion:	07.11.2014

This work is dedicated
to my dear wife
Ines.

Contents

Abbreviations and Symbols

Abbreviations

AF	actin filaments (F-actin)
AFM	atomic force microscopy
APLNR/APJ	endothelial apelin receptor
APLNR-KD HUVEC	endothelial cell with knocked down APLNR
CFB	cardiac fibroblast
CLSM	confocal laser scanning microscopy
CP	colloidal probe
CSK	cytoskeleton
CD	cytochalasin D
DCM	dilated cardiomyopathy
EBR-PMMA	electron beam resist PMMA
ESS	endothelial shear stress
EC	endothelial cell
ECM	extracellular matrix
FC	flow cytometry
FDC	force-distance curve
FDM	force-distance measurement
FIC	force-indentation curve
FMLP	Formyl-Methionyl-Leucyl-Phenylalanine
FVM	force-volume measurement
GAT	granulocyte aglutination test
GIFT	granulocyte immunofluorescence test
HUVEC	human umbilical vein endothelial cell

HNA	human neutrophil alloantigen
IF	intermediate filament
LMS	least mean squares
LV	left heart ventricle
MT	microtubule
MWUT	Mann-Whitney U test
PBS	phosphate-buffered saline
PEG	polyethylene glycol
PMMA	poly(methyl methacrylate)
PMN	polymorphonuclear neutrophils
PolyHEMA	poly(2-hydroxyethyl methacrylate)
RCA-1	procedure for removing organic residues from surfaces
ROCM	recent onset cardiomyopathy
RV	right heart ventricle
SEM	scanning electron microscopy
TRALI	transfusion related acute lung injury
UV	ultra violet (light)
WT HUVEC	wild type endothelial cell with working APLNR

Symbols - Latin

a	contact radius between AFM probe/indenter and sample
d_c	cantilever deflection
E_1	Young's modulus of the AFM probe/indenter
E_2	Young's modulus of the cell/sample
E_3	Young's modulus of the substrate
E_s	Young's modulus of the cell determined with the simple Hertz model
E_{dc}	Young's modulus of the cell determined with the double contact model

E_{sdc}	Young's modulus of the cell determined with the simplified double contact model
ΔE	error in the estimation of Young's modulus E_2 [%]
$\mathbb{F}$	free energy
F	force
F_c	cantilever force
F_g	gravity force
F_{lim}	maximum cantilever force (setpoint)
F_s	substrate force
g	acceleration due to gravity (9.80665 m/s^2)
$\boldsymbol{G}$	Green's tensor of the equilibrium
$\mathbb{G}$	free enthalpy
h	cell/sample thickness
J_c	moment of inertia of the cantilever
k_c	cantilever spring constant
k_b	Boltzmann constant (1.3806488 $\cdot 10^{-23}$ J/K)
K_c	bending stiffness of the cantilever
l_c	length of the cantilever
l_p	persistence length
p	statistic significance level
P	pressure
R_1	radius of the AFM probe/indenter
R_2	radius of the cell/sample
R_3	radius of the substrate
S	entropy
t	experiment time
T	temperature
T_r	room temperature ($\approx 24°$C)
$\boldsymbol{u}$	strain tensor
$\mathbb{U}$	internal energy

$\boldsymbol{v}$	displacement vector
V	volume
W	work
z	3D-scanner position
z_0	3D-scanner position at the contact point

Symbols - Greek

$\epsilon^{(0)}$	LMS error over the whole force-distance curve
$\epsilon^{(1)}$	LMS error over the non-contact area of the force-distance curve
$\epsilon^{(2)}$	LMS error over the contact area of the force-distance curve
φ	angle between cantilever beam and substrate
γ	surface energy
η	indentation depth of the AFM probe/indenter
$\lambda^{(1)}$	Lamé's first parameter
$\lambda^{(2)}$	Lamé's second parameter
ν_1	Poisson's ratio of the AFM probe/indenter
ν_2	Poisson's ratio of the cell/sample
ν_3	Poisson's ratio of the substrate
$\boldsymbol{\sigma}$	stress tensor

Other Symbols

$\langle \mathsf{data} \rangle$	a median or mean value of the data
$\langle \mathsf{data} \rangle^{mix}$	an averaged value of the data according to a *linear mixed-effects model*

Chapter 1

Introduction

The cell in the focus of science - from macro- to nano-scales

Until the 17th century, physicians understood the human body as the sum of macroscopic body parts, organs and tissues. Diseases were described by macroscopic observations such as the color of the skin or the size of an organ. First, in the second half of the 17th century, the English physicist Robert Hooke was looking on slices of cork bark [1], using a simple compound light microscope. He found repetitive microstructures, and described them with the words: "*... those pores were neer as thin in proportion to their pores, as those thin films of Wax in a Honey-comb ...*" and as "*... pores, or cells, ... not very deep ...*". As with the used microscope he was able to resolve only the cell wall, he used the word "*cells*" to describe the structure of the investigated plant specimen. What Hooke found, today is still called cell, but is known as the basic element of life having a complex structured interior. Afterward, in 1838/39, Jacob Matthias Schleiden and Theodor Schwann continued focusing on the microscopic scale like Hooke did. They recognized that all living beings consist of cells. Thereafter, in 1858, Rudolf Virchow discovered that "*Omnis cellula e cellula*" ("*Every cell originates from another existing cell like it.*"). In 1865, the Augustinian monk Gregor Johann Mendel published his investigations concerning plant hybridization [2] and showed that the inheritance of macroscopic properties to the subsequent plant generation follows fixed rules. Subsequently, in 1902, Walter Sutton and Theodor Boveri bridged from the microscopic scale to the nanoscopic scale by founding the chromosome theory

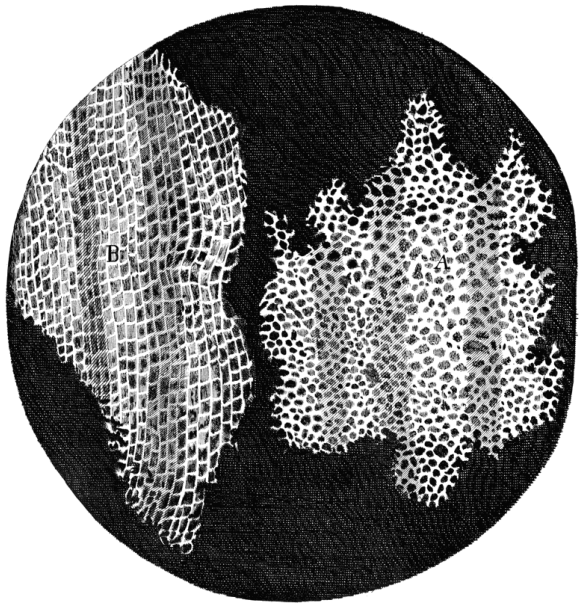

Figure 1.1: *Cells in a cork bark. Adapted from Hooke et al. [1].*

of inheritance [3, 4]. This theory first described chromosomes as carriers of nanoscopic genes. Finally, in 1953, the whole nanoscopic double helical structure of the Deoxyribonucleic Acid (DNA) building up the chromosomes was published by Watson and Crick [5]. Their closing remark on the structure of the DNA was: "*It has not escaped our notice that the specific pairing we have postulated immediately suggests a possible copying mechanism for the genetic material.*" Finally, in 1998, improving DNA-decoding technologies for the first time enabled the decoding of the complete genome of a metazoan[1] organism (*Caenorhabditis elegans*, a roundworm) [6] and in 2003 the human genome[2] was sequenced completely.

This means, with increasing time and enhancing technological capabilities, science has described the human body from the macroscopic scale of body parts, organs and tissues over the microscopic scale of cells to the nanoscopic scale of molecules and macromolecules, such as the DNA. Nowadays, it is proven, that all biological processes like cell division, protein synthesis or metabolism are carried out using information from the DNA. Therefore, macroscopic observations as described by Mendel can be understood as a consequence of nanoscopic mechanisms.

[1] "metazoan" = "multicellular"

[2] the decoding was done within the "*Human Genome Project*"

Cell elasticity - an important microscopic marker for the state of cells

Although, the decoding of the human genome was an important step in human biology, due to the fact that most of the processes in human cells are regulated by a multitude of genes, the correlation between macroscopic or microscopic processes observed in the human body with the causing nanoscopic genes of the DNA (or proteins) remains challenging. Nevertheless, this type of correlation

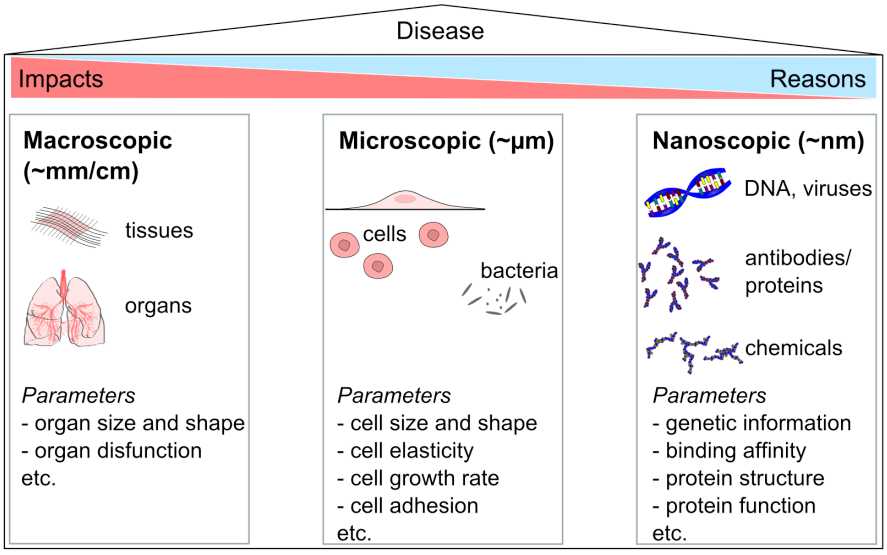

Figure 1.2: *Schematic showing the three length scales needed to be investigated to fully understand a disease. right: on the nano scale mostly the reasons for a disease can be found. This reasons can be given by genetic disorders, antibody binding and chemicals. middle: on the microscopic scale cells are influenced by nanoscopic reasons, which leads them to change their parameters. The change of this parameters itself can be the reason for macroscopic observed diseases. left: tissues or whole organs consist of cells and their secretions and are highly determined by microscopic and nanoscopic conditions.*

is needed, being particularly obvious in human diseases. To fully understand a disease it is necessary to know both: its nanoscopic reasons just as its impacts on microscopic cells forming macroscopic organs and tissues (see Figure 1.2). Only **the sum of observations on the different scales and the correlation of these observations can create a full description of a disease**. Therefore, even if modern technologies allow to identify nanoscopic (e.g. genetic) reasons for a disease it is still needed to understand their impact on single cells, cells in a tissue or whole organs. For example, diseases have

been shown to alter cell parameters, such as cell growth rate (e.g. in hyperplasia [7]) or cell size (e.g. in hypertrophy [8] or atrophy [9]). Such changed cell parameters can be used as marker for the state of the cell.

One additional parameter has been shown to be a very **important marker for the cell state [10] too: the cell elasticity**. First experiments concerning the elasticity of cells have already been carried out in 1967 [11]. Since this time, the elasticity of cells has been extensively studied and found to be relevant in numerous severe human diseases like cancer [12, 13] or the sickle cell disease [14]. Additionally, influences like cell differentiation and cell aging [15, 16], mechanical stimuli (e.g. shear stress) [17, 15, 18], drugs and chemicals [19], the substrate stiffness [20] or a pathogenesis (attack of viruses and parasites, etc.) [21] can change the elasticity of cells. The observed differences in cell elasticity (Young's modulus E_2)[3] can be very pronounced and have been reported up to a factor of three [22], involving the possibility to diagnose diseases. For example in the case of cancer, experiments have shown the possibility to detect cancer cells in tissue by cell elasticity measurements [23].

Literature shows a broad variety of techniques used to measure the mechanical properties of cells, such as: Micropipette Aspiration Technique (MAT; [24, 25]), Magnetic Twisting Cytometry (MTC; [26]), Attached and Embedded Magnetic Particles [27, 28], Optical Tweezer (OTZ; [29, 30]), Scanning Acoustic Microscopy (SAM; [31]), Laser-Tracking Microrheology (LTM; [32]) and Atomic Force Microscopy (AFM; [33]).

All elasticity measurements in this thesis are carried out using AFM, which has become an important tool for probing mechanical properties of cells. One reason for this is its capability to gain information about the local elasticity and the surface morphology of cells in parallel [21], what is used extensively in this thesis. Moreover, the AFM allows to achieve a high spacial resolution of the cells local elastic modulus and to apply a large range of forces. The latter allows even to determine the local elasticity of relatively stiff cells[4]. Moreover,

[3] Note: the Young's modulus of cells is always denoted by E_2, as in Chapter 6 additionally the Young's moduli of the AFM probe/indenter and of the cell substrate are denoted by E_1 and E_3.

[4] Cells showing Young's moduli in the range of 10 kPa or even higher.

by the use of microscopic Colloidal Probes (CPs), the AFM can cause pronounced (300 nm - 400 nm) and defined cell deformations, allowing to extract spatial averaged values of Young's modulus. These measurements describe the mean cell elasticity of small cell volumes in contrast to other techniques e.g. MAT sensing mainly the cell surface mechanics.

Thesis aims and Outline

This thesis was made in the ZIK HIKE (Center for Innovation Competence - Humoral Immune Reactions in Cardiovascular Diseases) in Greifswald, which is an interdisciplinary institute investigating the mechanisms of auto immune diseases with interdisciplinary approaches. Therefore, this thesis is an interdisciplinary one and aims for **the adaptation and improvement of established AFM approaches for nanoindentation experiments on living cells. A special focus is laid on the development of a fast reliable data analysis, which includes the development of an appropriate contact model for measurements on spherical cells. A second aim of this thesis is the application of these improved/developed AFM approaches to medical/biological investigations. For this purpose, the microscopic cell elasticity is interpreted with respect to nanoscopic and macroscopic biological observations.** Accounting for this, this thesis is divided into **two parts: a physical/technical one and a medical/biological one**. Despite the strict separation of these two parts, the answer of the medical/biological questions addressed in this thesis was only possible due to results described in the physical/technical part.

Physical/technical part

The physical/technical part consists of the two Chapters 5 and 6 concerning the development of an automated AFM Force-Distance Curve (FDC) data analysis and a novel contact model describing FDCs measured on soft spherical cells or cell-like particles.

Development of a fully automated AFM force-distance curve analysis (Chapter 5)

The AFM allows to sense small forces below 10 pN [34, 35] acting between the AFM probe (mounted on a flexible AFM cantilever) and the cell. By pressing the AFM probe against the cell, AFM cantilever and cell get deformed, which is called **nanoindentation experiment**. The appearing forces can be measured by the AFM. The result is a Force-distance Curve (FDC), showing the coherence of AFM cantilever movement and interaction force. FDCs contain information about the mechanical properties (e.g. Young's modulus E_2) of the investigated cell. Mostly, these FDCs are analyzed semi-automatically, which means that the user has to determine manually a certain point of the curve (contact point z_0)[36] indicating the first contact between probe and cell. Nowadays, algorithms to automate this process are mostly not included in commercial software and still under discussion in the literature [34]. Because in this thesis living cells were investigated, numerous FDCs were recorded in order to achieve reliable statistics despite of large biological variances. For example, large FDC data sets were obtained by force-volume measurements carried out on cells, in order to correlate topological details (e.g. cell thickness) with the local elastic modulus of these cells. In sum for the following studies more than $2.27 \cdot 10^5$ FDCs were analyzed.

Therefore, a fast, reliable and fully automated data analysis algorithm, that extracts the local elastic modulus E_2 of cells and the contact point z_0 from FDCs was implemented. The algorithm is robust against systematic errors (e.g. drifts in FDCs), judges automatically each FDC by strict rules and allows to rule out significantly disturbed measurements.

Development of an appropriate contact model for AFM nanoindentation experiments on spherical cells (Chapter 6)

Mammalian cells show a large variety of Young's modulus E_2 on cell level [37] and between different cell species [21]. Also, cell shape and size can scatter intensively [38, 39]. AFM nanoindentation experiments presented in the literature mostly concern flat adhered cells on a rigid substrate using conical, spherical or pyramidal AFM probe geometries. For this case, various contact theories have been developed [40, 41, 42, 43], describing the relation

between indentation depth η of the AFM probe and interaction force F_c between AFM probe and cell. Still a challenging problem is the investigation of weakly adhered spherical cells, as they tend to roll or slide under the load of the AFM probe [44]. For this purpose, **a new protocol for the production of wedged cantilevers was developed**. These cantilevers prevent the cell moving during a nanoindentation experiment [45]. The new protocol overcomes rough cantilever surfaces appearing, in case established protocols (presented in the literature) are used.

Furthermore, for spherical cells, the fitting of FDCs to established contact models, leads to significant errors in the estimation of the cell Young's modulus E_2. This is because these models do not take into account cell deformations appearing on the bottom side of the cell during a nanoindentation experiment (and in advance). Therefore, **an appropriate contact model applicable to soft spherical cells and cell-like particles was developed.** The derivation of the model is described in Chapter 6. The model is a general one, and describes the force-indentation relation for all possible combinations of indenter radius and substrate radius. Additionally, the model was used to study the influence of cell-substrate interactions on the FDCs and to estimate the error appearing in the determination of Young's modulus E_2, if the simple Hertz model is used for the analysis.

Medical/biological part

The medical/biological part of this thesis is given in the Chapters 7, 8 and 9 concerning changes in cell elasticity with respect to diseases and mechanically stress (shear stress). Here a focus is set on the creation of new insights by **bridging between nanometer-, micrometer- and centimeter-scales** as described above. In the context of the heart muscle disease Recent Onset Cardiomyopathy (ROCM), Chapter 7 investigates the correlation of the elasticity of **microscopic human Cardiac Fibroblasts (CFBs)** with the size of the **macroscopic heart ventricles**. In contrast Chapter 8 describes the relevance of **nanoscopic specific antibodies** on the elasticity of **microscopic human blood-derived neutrophil granulocytes** in the context of the Transfusion Related Acute Lung Injury (TRALI). Findings are then interpreted with respect to the **macroscopic human lung**. Furthermore, Chapter

9 investigates the influence of the **nanoscopic Apelin Receptor (APLNR)** on the mechanotransduction of **microscopic endothelial cells**.

Cell elasticity in the context of Recent Onset Cardiomyopathy (Chapter 7)

Recent Onset Cardiomyopathy (ROCM) is a relevant cause of heart failure and the most frequent cause for human heart transplantations. In a large number of cases ROCM becomes apparent by enlarged heart ventricles and a decreased pumping rate of the heart muscle, which is also called Dilated Cardiomyopathy (DCM). Until now the (micro-/nanoscopic) reasons for this macroscopic changes are not clarified. For this reason, Chapter 7 studies the elasticity of Cardiac Fibroblasts (CFBs) obtained by clinical biopsies from patients with ROCM. According the aim of this thesis to bridge between scales, **the study correlates the cell elasticity (Young's modulus E_2) of the microscopic fibroblasts from either the Left (LV) or the Right (RV) heart Ventricle with clinical data concerning the size of these macroscopic heart ventricles**.

Cell elasticity in the context of Transfusion Related Acute Lung Injury (Chapter 8)

As described above, cells have been shown to adapt and change their elasticity in dependency of a multitude of nanoscopic factors, such as the presence of drugs and chemicals in their environment. In the (mammalian) body, cells like red blood cells or neutrophil granulocytes (neutrophils), are in an aqueous environment containing several types of antibodies. Currently, there are no investigations on the influence of antibodies on the elasticity of cells. Nevertheless, there is a bunch of diseases known to be caused by specifically binding antibodies. In order to investigate, if specifically binding antibodies can influence the mechanics of cells, living human neutrophils were studied in the context of Transfusion Related Acute Lung Injury (TRALI).

TRALI is a server adverse effect of blood transfusion, and caused by antibodies specifically binding to the Human Neutrophil Antigen 3a (HNA-3a) on the surface of neutrophils. Different aspects of TRALI, such as neutrophil aggregation and the production of Reactive Oxigen Species (ROS) due to HNA-3a activa-

tion, have already been studied. The elasticity of neutrophils in the context of TRALI is of scientific importance, as stiffer neutrophils may get stuck in the narrow capillaries of the human lung and may thereby contribute to the emergence of TRALI. Hence, **human neutrophil elasticity was investigated in dependency of the presence of specifically binding HNA-3a antibodies**. Additionally, different inhibitors which were shown to influence aspects of TRALI (e.g. neutrophil aggregation) were tested to have an influence on antibody mediated changes in cell elasticity. Moreover, in the context of TRALI, the elasticity of microscopic neutrophils influenced by the nanoscopic antibodies is interpreted with respect to the macroscopic human lung.

The role of the Apelin Receptor (APLNR) for the mechanotransduction in endothelial cells (Chapter 9)

Numerous publications show that cell elasticity is mainly coined by the cytoskeleton. Hence, for changing cell elasticity, a conversion of the cytoskeleton has to take place. In the case of endothelial cells, a cell stiffening in the presence of shear forces is reported, but the exact mechanotransduction pathway of this process is still unknown. Human Umbilical Vein Endothelial Cells (HUVECs) use several mechanisms to transduce intravascular mechanical forces into biochemical signals. The activation of G-Protein-Coupled Receptors (GPCRs) is one way to generate such signals initiating a process of cytoskeleton rearrangement. In order to clarify the relevance of the G-protein-coupled Apelin Receptor (APLNR) in the endothelial mechanotransduction, **the relation between the function of the nanoscopic shear stress regulated GPCR APLNR and the elasticity of the microscopic endothelium was examined**. The investigation was carried out by the use of a flow-chamber-model. The elastic modulus E_2 of HUVECs was determined by the application of the new FDC analysis algorithm (Chapter 5) to two different contact models. The first one is the simple Hertz model, the second one is a thin layer model published by Dimitriadis et al.

Chapter 2

Theory of Elasticity

In this thesis Young's modulus E, which is an important parameter in the linear elastic theory, was used as measure for the local cell elasticity. The determination of E was carried out using linear contact theories derived by Heinrich Hertz et al. [40] and Dimitriadis et al. [41]. Therefore, the following chapter outlines briefly the derivation of the most important parameters and equations of the linear elastic theory for homogeneous elastic materials, needed to understand the mechanics of cells (Chapter 3) and AFM cantilevers (Chapter 4.1). The thread follows mainly the work of Landau and Lifschitz [46] who summarized and re-derived main results of the linear elastic theory (e.g. the results of Hooke et al. [1] and Hertz et al. [40]). The derivation of common contact models from the equations of the linear elastic theory is shown in a modern fashion, *via* the determination of Green's functions for point loads.

For the description, the following mathematical syntax is used: Cartesian coordinates are symbolized by $x_1 = x, x_2 = y, x_3 = z$. Vectors, such as the position vector $\boldsymbol{r} = [x_i]$ or tensors, for example $\boldsymbol{\sigma} = [\sigma_{ij}]$, are noted bold. Their components are indexed by the latin letters i, j, k or l with the co-domains $1, 2, 3$. Further, the "Einstein notation" is used [47], meaning that for an index appearing twice in a term, a summation over the full range of the index has to be carried out, e.g. $x_i x_i = x_1^2 + x_2^2 + x_3^2$. Moreover, derivatives $\frac{\partial}{\partial x_i}$ with respect to the Cartesian coordinates x_i are denoted as ∂_i. Combining these two conventions, for instance $-\sum_{j=1}^{3} \frac{\partial\left(\sigma_{ij}+\sum_{k=1}^{3}\sigma_{kj}\frac{\partial u_i}{\partial x_k}\right)}{\partial x_j}$ is written as $-\partial_j(\sigma_{ij}+\sigma_{kj}\partial_k u_i)$ [48].

2.1 Basic equations of the linear elastic theory

In an non-deformed rigid body in thermodynamic equilibrium, in average each atom of the body has the same kinetic energy and is situated on its equilibrium position[1], as attractive and repulsive forces acting on it, sum up to zero. An important assumption of the linear elastic theory is that the interactions between the atoms and molecules of the body are short ranged. Therefore, subvolumes of the body can exchange interactions only *via* their surfaces [46]. Hence, in an non-deformed body, the integral of all forces acting on a subvolume $\mathrm{d}V$ of the body vanishes:

$$\int \boldsymbol{F}\mathrm{d}V = 0, \tag{2.1}$$

which is called **mechanical equilibrium**. Additional outer forces, acting on the body surface, change this equilibrium and lead to small changes of the equilibrium positions of the atoms within the body with respect to each other. Therefore, every rigid body deforms under the influence of outer forces. In general, such a deformation influences not only the shape of the body but also its volume. Geometrically, the body can be described by the **position vectors** $\boldsymbol{r} = [x_1, x_2, x_3]$ of all its points[2]. During the deformation process, the position of these points is changed to $\boldsymbol{r'} = [x'_1, x'_2, x'_3]$. The displacement of the points is given by $\boldsymbol{v}$:

$$v_i = x'_i - x_i, \tag{2.2}$$

which is known as **displacement vector**. The distance of two neighbored points in a non-deformed body is given by $\mathrm{d}l = \sqrt{\mathrm{d}x_i \mathrm{d}x_i} = \sqrt{\mathrm{d}x_i^2}$ and after its deformation by $\mathrm{d}l' = \sqrt{\mathrm{d}x_i'^2}$. Using the substitution $\mathrm{d}v_i = \partial_k v_i \mathrm{d}x_k$, the expression

$$\mathrm{d}l'^2 = \mathrm{d}l^2 + 2\partial_k v_i \mathrm{d}x_i \mathrm{d}x_k + \partial_k v_i \partial_l v_i \mathrm{d}x_k \mathrm{d}x_l \tag{2.3}$$

[1] More precisely, each atom moves with the kinetic energy of $1/2 k_B T$ per degree of freedom around its equilibrium position.

[2] With "*points*" here the corners of infinitesimal subvolume elements are meant, which can be, for example, single atoms.

can be obtained. Because the indexes i, k and l in Eq. 2.3 are independent of each other, they can be interchanged. This results in

$$\mathrm{d}l'^2 = \mathrm{d}l^2 + 2u_{ik}\mathrm{d}x_i\mathrm{d}x_k. \tag{2.4}$$

Herein $\boldsymbol{u}$ is a symmetric ($u_{ik} = u_{ki}$) tensor [46]

$$u_{ik} = 1/2\left(\partial_k v_i + \partial_i v_k + \partial_i v_l \partial_k v_l\right), \tag{2.5}$$

which is referred to as the **strain tensor** of second order. For small deformations, the contribution of the second order parts in u_{ik} is small and, therefore, the strain tensor can be reduced to

$$u_{ik} = 1/2\left(\partial_k v_i + \partial_i v_k\right). \tag{2.6}$$

Figure 2.1 schematizes the components of $\boldsymbol{u}$. The non-diagonal elements of

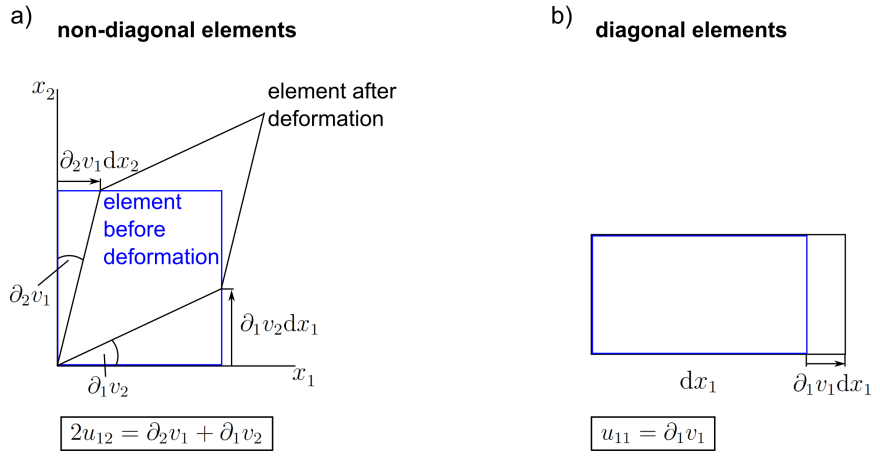

Figure 2.1: *Schematics on the components of strain tensor* $\boldsymbol{u}$ *(projected in two dimensions) [49].* ***a)*** *The non-diagonal elements of* $\boldsymbol{u}$ *correspond to shear movements.* ***b)*** *The diagonal elements of* $\boldsymbol{u}$ *describe dilations or compressions, respectively.*

$\boldsymbol{u}$ are related to shear movements (Figure 2.1a), while the diagonal elements describe dilations or compressions, respectively (Figure 2.1b). The assumption of small strains holds in the most cases, because even during the bending of a long rod, where the ends of the rod can undergo a displacement in the scale of meters, the displacement of individual molecules or atoms with respect to each other remains small [46].

During the deformation process, the body is out of its mechanical equilibrium state and its inner molecular forces tend to bring it back into its former shape. In this situation, Eq. 2.1 has to be replaced by

$$\int F_i \mathrm{d}V = \int \partial_k \sigma_{ik} \mathrm{d}V = \oint \sigma_{ik} \mathrm{d}f_k, \tag{2.7}$$

with $\mathrm{d}\boldsymbol{f}$ describing the surface normal on the volume element [46]. Thus, the sum of forces acting on a certain volume element $\mathrm{d}V$ does not cancel out while the deformation is created. Moreover, the right side of Eq. 2.7 shows, that using the divergence theorem[3] this sum of inner forces can be transformed into a surface integral over a second order tensor $\boldsymbol{\sigma}$, called **stress tensor**. Figure 2.2 shows the meaning of the stress tensor for a small subvolume of the body. The first index i in σ_{ik} defines the direction of the surface normal of the surface which is stressed. The second index k relates to the direction of the stress component.

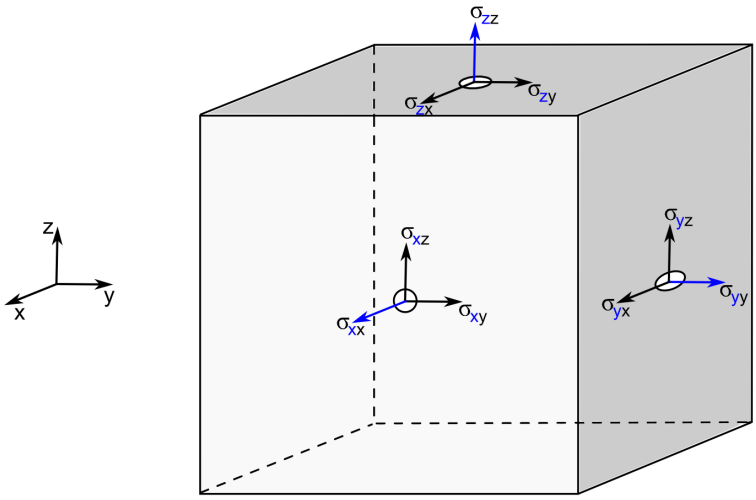

Figure 2.2: *Schematic of stress components acting on a volume element. The first index i in the stress tensor σ_{ik} defines the direction of the surface normal (blue arrows) of the stressed surface. The second index k determines the direction of the stress component [50].*

[3] also known as Gauss's theorem

2.1.1 Thermodynamic potentials in the linear elastic theory

An infinitesimal displacement δv_i of a small subvolume $\mathrm{d}V$ needs to overcome the internal tensions acting on the volume. Therefore, the work $\delta W = F_i \delta v_i = \partial_k \sigma_{ik} \delta v_i$ is needed. The work W needed to deform the whole body is given by the integral over all δW [46]:

$$W = \int \delta W \mathrm{d}V = \int F_i \delta v_i \mathrm{d}V = \int \partial_k \sigma_{ik} \delta u_i \mathrm{d}V = -\int \sigma_{ik} \delta u_{ik} \mathrm{d}V. \tag{2.8}$$

The right hand side of this equation can be verified by the use of the symmetry of $\boldsymbol{\sigma}$. It shows, that the work δW needed to deform the body can be expressed by the change of the strain tensor $\boldsymbol{u}$. Combining Eq. 2.8 with the general thermodynamic equation for the internal energy $\mathbb{U}$ results in:

$$\mathrm{d}\mathbb{U} = T\mathrm{d}S - P\mathrm{d}V = T\mathrm{d}S + \sigma_{ik}\mathrm{d}u_{ik}, \tag{2.9}$$

wherein T describes the temperature, S the entropy and P the pressure. By applying Legendre transformations to Eq. 2.9 [51], additionally the expressions

$$\mathrm{d}\mathbb{F} = -S\mathrm{d}T + \sigma_{ik}\mathrm{d}u_{ik} \tag{2.10}$$

and

$$\mathrm{d}\mathbb{G} = \mathbb{F} - \sigma_{ik}u_{ik} \tag{2.11}$$

for the free energy $\mathbb{F}$ and the free enthalpy $\mathbb{G}$ can be found. This leads directly to the important equations

$$\sigma_{ik} = \left(\frac{\partial \mathbb{U}}{\partial u_{ik}}\right)_S = \left(\frac{\partial \mathbb{F}}{\partial u_{ik}}\right)_T \tag{2.12}$$

and

$$u_{ik} = -\left(\frac{\partial \mathbb{G}}{\partial \sigma_{ik}}\right)_T. \tag{2.13}$$

2.1.2 Lamé parameters and Hooke's law

For the use of the thermodynamic Eqs. 2.12 and 2.13 it is useful to derive an expression relating the free energy $\mathbb{F}$ to the strain tensor $\boldsymbol{u}$. Such an equation can be obtained by expressing $\mathbb{F}$ in powers of u_{ik} which is given by:

$$\mathbb{F} = \mathbb{F}_0 + \frac{\lambda^{(1)}}{2} u_{ii}^2 + \lambda^{(2)} u_{ik}^2 \tag{2.14}$$

wherein $\lambda^{(1)}$ and $\lambda^{(2)}$ are called first and second Lamé parameter [46]. Please note, within the linear elastic theory $\lambda^{(2)}$ can be identified with the shear modulus G, which can be alternatively defined as

$$\lambda^{(2)} = G = \sigma_{ik}/u_{ik} \text{ for } i \neq k \tag{2.15}$$

("*shear stress*"/"*shear strain*") using the non-diagonal elements of $\boldsymbol{\sigma}$ and $\boldsymbol{u}$. Landau and Lifschitz showed [46], that using the identity

$$u_{ik} = (u_{ik} - \delta_{ik} u_{ll}/3) + \delta_{ik} u_{ll}/3, \tag{2.16}$$

wherein δ_{ik} is the Kronecker delta[4], the free energy $\mathbb{F}$ (Eq. 2.14) can be approximated by

$$\mathbb{F} = \lambda^{(2)} (u_{ik} - \delta_{ik} u_{ll}/3)^2 + K u_{ll}^2/2. \tag{2.17}$$

Please note, at this point K is just a material parameter, which is useful for the description of the free energy $\mathbb{F}$. The (physical) meaning of this parameter is identified in the following (Eq. 2.21) and K will be found to be the bulk modulus of the material. In general, the free energy $\mathbb{F}$ has its minimum in the thermodynamic equilibrium. In order to have a positive $\mathbb{F}$ for all possible $\boldsymbol{u}$, the parameters K and $\lambda^{(2)}$ must be positive [52, 46]:

$$K > 0 \text{ and } \lambda^{(2)} > 0 \tag{2.18}$$

Now calculating the total differential $\mathrm{d}\mathbb{F}$ and considering the general thermodynamic Eq. 2.12 leads to:

$$\sigma_{ik} = K u_{ll} \delta_{ik} + 2\lambda^{(2)} (u_{ik} - 1/3 \delta_{ik} u_{ll}) . \tag{2.19}$$

[4]Kronecker delta: $\delta_{ik} = 0$ for $i \neq k$; $\delta_{ik} = 1$ for $i = k$

Equation 2.19 allows to extract the stress tensor $\boldsymbol{\sigma}$ from the strain tensor $\boldsymbol{u}$. *Vice versa*, the expression determining the strain tensor $\boldsymbol{u}$ from the stress tensor $\boldsymbol{\sigma}$ is given by:

$$u_{ik} = \delta_{ik}\sigma_{ll}/(9K) + (\sigma_{ik} - 1/3\delta_{ik}\sigma_{ll})/(2\lambda^{(2)}). \tag{2.20}$$

In the special case of a hydrostatic compression no shear forces but only the pressure p appears on the surface of the body. Then, the stress tensor is given by $\sigma_{ik} = -p\delta_{ik}$, which means that only the diagonal elements of $\boldsymbol{\sigma}$ differ from zero [46]. Using Eq. 2.20 in this case the sum of the diagonal elements (trace) of $\boldsymbol{u}$ is given by: $tr(\boldsymbol{u}) = (\sum_i u_{ii}) = u_{ii} = -p/K$, which describes the relative volume change of the body. Hence, in the absence of shear forces, the volume change is determined only by the parameter K and not by the second Lamé parameter $\lambda^{(2)}$. Because the relative volume change $tr(\boldsymbol{u}) = u_{ii}$ and the pressure p are small, the ratio u_{ii}/p can be written in the differential form: $1/V\,(\partial V/\partial p)_T$. Moreover, using $u_{ii} = -p/K$ the equation

$$\frac{1}{K} = \frac{u_{ii}}{p} = -\frac{1}{V}\left(\frac{\partial V}{\partial p}\right) \tag{2.21}$$

can be found. This equation shows what is known today as **Hooke's law** and what Robert Hooke described as "*ut tensio, sic vis*" ("*as the extension, so the force*"), namely the deformation is proportional to the acting forces [46]. Additionally, Eq. 2.21 explains the material parameter K as being the resistance of the body to infinitesimal uniform compressions. Hence, $\boldsymbol{K}$ **is the bulk modulus of the material**.

In the following, the ratio between the negative longitudinal strain and the transverse strain **in the case of uniaxial stress** (here along the z-axes) is defined as

$$\nu = -u_{xx}/u_{zz} \text{ with } \nu = (3K - 2\lambda^{(2)})/(6K + 2\lambda^{(2)}), \tag{2.22}$$

and called the **Poisson's ratio** $\boldsymbol{\nu}$. Note, in the general case of a non-isotropic material, ν depends on the direction of the applied load. Typically the co-domain of the Poisson's ratio is given by $0 < \nu \leq 0.5$. Nevertheless, some materials with $\nu < 0$ (auxetics) are known too [53]. **The Poisson's ratio of**

a cell $\nu_{cell} = \nu_2$ is an important parameter in this thesis, as it was used to analyze the FDCs by means of linear contact models (Eqs. 2.43, 2.47). Due to the high water content of cells, their Poisson's ratio was assumed to be $\nu_2 = 0.5$ in all calculations.

Additionally, for the case of uniaxial stress (here in z-direction) the **Young's modulus** or elastic modulus E is defined by

$$E = \sigma_{zz}/u_{zz} = 2\lambda^{(2)}(1+\nu). \tag{2.23}$$

Please note, Young's modulus E has the dimension ("*tensile stress*"/"*strain*" [Pa = N/m^2]) and describes the resistance of a body to elongations/compressions along an axis, if two opposing forces act on this axis. Hence, E is a simplified version of the bulk modulus K. *Vice versa*, K is the three-dimensional extension of E. **The elastic modulus $E_{cell} = E_2$ of cells is the main measurement parameter in this thesis.** With the help of ν and E the Eqs. 2.19 and 2.20 can be written as

$$\sigma_{ik} = \frac{E}{1+\nu}\left(u_{ik} + \frac{\nu}{1-2\nu}u_{ll}\delta_{ik}\right) \tag{2.24}$$

and

$$u_{ik} = \frac{1}{E}\left[(1+\nu)\sigma_{ik} - \nu\sigma_{ll}\delta_{ik}\right]. \tag{2.25}$$

The last commonly used elastic parameter is the P-wave modulus M which is similar to E defined as the ratio "*tensile stress*"/"*strain*" for uniaxial stress

$$M = \sigma_{zz}/u_{zz} \text{ for } u_{ik} = 0 \text{ if } i,k \neq z. \tag{2.26}$$

Please take notice that in contrast to Young's modulus E, M is restricted to cases where no non-axial strains appear. An example for this is the uniaxial compression of a soft sampling cylinder (e.g. a soft sponge) which is surrounded by a rigid cylinder. In this situation no increase of the sample cylinder diameter can appear during the compression, as this is prevented by the surrounding rigid cylinder.

In sum, **there are six material parameters used in the linear elastic**

theory: bulk modulus K, elastic modulus E, first Lamè parameter $\lambda^{(1)}$, Poisson's ratio ν, shear modulus G (equal to the second Lamè parameter $\lambda^{(2)}$) and P-wave modulus M. Nevertheless, as these parameters are not independent of each other, **in the case of a homogeneous elastic material only two of these material parameters are needed in order to fully describe the elastic behavior of the material [54]. In this thesis, Young's modulus E and the Poisson's ratio ν were used in order to describe the elastic properties of cells.**

2.1.3 Equilibrium conditions for isotropic rigid bodies

In a body in its mechanically equilibrium[5], the forces of the inner tensions have to cancel out in each volume element, otherwise the volume element would start moving and, thus, the shape of the body would change. Therefore, in this case one has

$$\partial_k \sigma_{ik} = 0. \tag{2.27}$$

The same holds for a body under the influence of gravity (volume forces) as well, but then the inner tensions have to compensate the gravity on each volume element:

$$\partial_k \sigma_{ik} + \rho g_i = 0. \tag{2.28}$$

Here $\boldsymbol{g}$ denotes the acceleration due to gravity, while ρ denotes the mass density of the body [46]. The substitution of σ_{ik} in this equation by Eq. 2.24 and the use of Eq. 2.6 for the strain tensor leads directly to

$$\Delta \boldsymbol{v} + \frac{1}{1-2\nu} \text{ grad } \text{ div } \boldsymbol{v} = -\rho \boldsymbol{g} \frac{2(1+\nu)}{E}. \tag{2.29}$$

In the simple case of no appearing gravity all deformations are initiated by outer forces, acting *via* the body surface. Then

$$\Delta \boldsymbol{v} + \frac{1}{1-2\nu} \text{ grad } \text{ div } \boldsymbol{v} = 0 \tag{2.30}$$

[5] which is also given for a body which is constantly deformed by constant outer forces

describes the equilibrium condition. Please note, for both equations (Eqs. 2.29 and 2.30), the influence of outer forces has to be considered solely *via* boundary conditions [46].

2.1.4 Equilibrium of a semi-infinite elastic media limited by a plane

An important case for biomechanical studies is described by an elastic half-space limited by a plane, which is deformed by outer forces. This is due to the fact, that a large percentage of cells shows a flat nearly plane-like surface when adhering to common cell culture materials as, for example, glass. In general, the behavior of the elastic half-space is described by the equilibrium condition Eq. 2.29. Landau and Lifschitz showed that, if deformation and forces disappear with infinite distance, this equation can be integrated. The solution of this equation is a superposition of a vector $\boldsymbol{f}$ and a scalar ϕ:

$$\boldsymbol{v} = \boldsymbol{f} + \text{grad } \phi \tag{2.31}$$

Landau and Lifschitz showed that the problem can be reduced to the determination of four potential functions which can be seen in detail in [46]. A simplified solution $\boldsymbol{v}$ of the general problem (Eq. 2.30) can be obtained, if only a point force/point load $\boldsymbol{F}\delta(x)\delta(y)$ (acting perpendicular to the surface) is considered. Here $\delta(x)$ and $\delta(y)$ are Dirac delta functions. Figure 2.3 schematizes such a point force and the deformation of the elastic half-space. In case

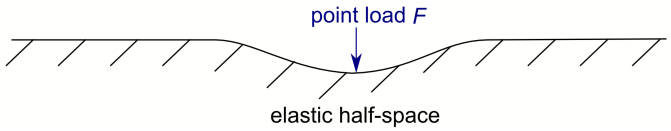

Figure 2.3: *Schematics of the deformation of a semi-infinite elastic half-space due to a point force F acting on its surface.*

a solution

$$v_i = G_{ik}(x, y, z) \cdot F_k \tag{2.32}$$

describing the deformation caused by the point force can be found, afterward, the deformation caused by (continuously distributed) forces $\boldsymbol{F}(x, y)$ can be

calculated by solving the integral

$$v_i = \iint G_{ik}(x - x', y - y', z) F_k(x', y') \mathrm{d}x' \mathrm{d}y'. \tag{2.33}$$

The tensor $\boldsymbol{G}$ is called Green's tensor of the equilibrium of a half-space. After a comprehensive calculation, the three components of the displacement vector can be determined as:

$$\begin{aligned} v_x = \frac{1+\nu}{2\pi E} \Bigg\{ & \left[\frac{xz}{r^3} - \frac{(1-2\nu)x}{r(r+z)} \right] F_z + \frac{2(1-\nu)r + z}{r(r+z)} F_x \\ & + \frac{\left[2r(\nu r + z) + z^2\right] x}{r^3 (r+z)^2} (x F_x + y F_y) \Bigg\}, \end{aligned} \tag{2.34}$$

$$\begin{aligned} v_y = \frac{1+\nu}{2\pi E} \Bigg\{ & \left[\frac{yz}{r^3} - \frac{(1-2\nu)y}{r(r+z)} \right] F_z + \frac{2(1-\nu)r + z}{r(r+z)} F_y \\ & + \frac{\left[2r(\nu r + z) + z^2\right] y}{r^3 (r+z)^2} (x F_x + y F_y) \Bigg\}, \end{aligned} \tag{2.35}$$

and

$$\begin{aligned} v_z = \frac{1+\nu}{2\pi E} \Bigg\{ & \left[\frac{2(1-\nu)}{r} + \frac{z^2}{r^3} \right] F_z \\ & + \left[\frac{1-2\nu}{r(r+z)} + \frac{z}{r^3} \right] (x F_x + y F_y) \Bigg\}. \end{aligned} \tag{2.36}$$

A detailed calculation for these components is presented by Landau and Lifschitz [46].

2.2 Contact models in the literature

2.2.1 Hertz model

Already in 1826, Heinrich Hertz derived a model (in the following called *Hertz model* or *simple Hertz model*) which describes the force-displacement relation appearing, if two elastic spheres, with the radii R_1 and R_2, are pressed together. Below, the derivation of this model is outlined in a way published by Landau and Lifschitz. The derivation bases on the Green's tensor derived in Eq. 2.36. The surfaces of the spheres near the pitch point are described as quadratic forms $z = \varsigma_{ik} \chi_i \chi_k$ respectively $z' = \varsigma'_{ik} \chi_i \chi_k$ in two different coordinate systems.

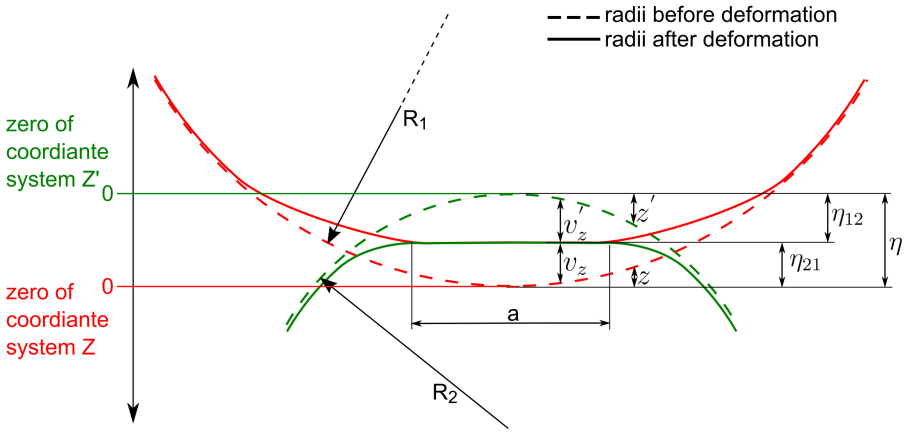

Figure 2.4: *The deformations appearing, if two elastic spherical half-spaces are pressed together (cf. [46]). By the pressing, their initial shape (blue dashed lines) changes and flattens in and around the area of contact, which has the radius a. For the derivation of the force-displacement relation (simple Hertz model) the upper and bottom half-space is described in different coordinate systems (Z and Z′) with opposing z-directions. The overall displacement is denoted by η, while the (maximum) individual displacements appearing on the upper or bottom half-space, respectively are denoted by η_{12} or η_{21}. The variables v_z, v_z' describe the local displacement of the surfaces.*

Herein, ς_{ik} and ς_{ik}' are tensors of second order, describing the curvature of the spheres. According to Figure 2.4, the relations

$$(z + v_z) + (z' + v_z') = \eta \Leftrightarrow (\varsigma_{ik} + \varsigma_{ik}')\chi_i\chi_k + v_z + v_z' = \eta \tag{2.37}$$

describe the displacement η of both half-spaces. The variables v_z and v_z' describe the local displacement of the surfaces. The x- and y-direction of the two coordinate systems are chosen in a way bringing the sum $\varsigma_{ik} + \varsigma_{ik}'$ (which is also a tensor of second order) into diagonal form. Then, the principal values of this sum are called A and B [46]. This allows to rearrange Eq. 2.37 to

$$Ax_1^2 + By_1^2 + v_z + v_z' = \eta. \tag{2.38}$$

In order to solve Eq. 2.38, first the displacement v_z in Eq. 2.36 is compared with Eq. 2.33 concerning the displacement caused by a point force. This is possible, because the surfaces of the spheres in the contact region can be approximated by a plane, as the absolute displacement η of the spheres is small. Therefore, in the case contemplated here, concerning only normal forces

F_z acting between the spheres, the Green's tensor is given by

$$\boldsymbol{G}(r) = \frac{1+\nu}{2\pi E}\left[\frac{2(1-\nu)}{r} + \frac{z^2}{r^3}\right], \tag{2.39}$$

with r being the amount of the position vector. For the surfaces of the elastic half-space in the contact area ($z \approx z' \approx 0$), this leads to

$$\boldsymbol{G_1}(r) = \frac{1+\nu_2^2}{\pi E_2} r^{-1} \text{ and } \boldsymbol{G_2(r)} = \frac{1+\nu_2^2}{\pi E_2} r^{-1}, \tag{2.40}$$

respectively. Therefore, the ratio between the two displacements v_z and v_z' is given by

$$\frac{v_z}{v_z'} = \frac{(1-\nu_1^2)E_2}{(1-\nu_2^2)E_1}, \tag{2.41}$$

and is constant [46]. The substitution of Eq. 2.40 into Eq. 2.33 leads to an expression for v_i, which can be inserted into Eq. 2.38. This finally leads to the following integral equation:

$$\frac{1}{\pi}\left(\frac{1-\nu_1^2}{E_1} + \frac{1-\nu_2^2}{E_2}\right)\iint \frac{P_z(x_2, y_2)}{r}\mathrm{d}x_2\mathrm{d}y_2 = q - Ax_1^2 - By_1^2 \tag{2.42}$$

The items q, A and B of this equation were determined by Landau and Lifschitz [46]. By subsequently setting $A = B = 1/2(R_1^{-1} + R_2^{-1})$ for the description of spherical objects in contact, they re-derived the simple Hertz model with the force-displacement relation

$$\begin{aligned} &\eta(F) = \left(\frac{3F}{4E_{12}} \cdot \frac{1}{\sqrt{R_{12}}}\right)^{2/3} \\ &\text{with } \frac{1}{R_{12}} = \frac{1}{R_1} + \frac{1}{R_2} \text{ and } \frac{1}{E_{12}} = \frac{1-\nu_1^2}{E_1} + \frac{1-\nu_2^2}{E_2}. \end{aligned} \tag{2.43}$$

The radius a of the contact area between both half-spaces (in this thesis cell and colloidal probe) can be calculated by

$$a = \left(\frac{3FR_{12}}{4E_{12}}\right)^{1/3}. \tag{2.44}$$

The maximum pressure between the spheres is given by

$$p_{max} = \frac{3F}{2\pi a^2} = \left(\frac{6FE_{12}^2}{\pi^3 R_{12}^2}\right)^{1/3}. \tag{2.45}$$

Equation 2.43 is one of the main equations in this thesis, as it was used to calculate the local Young's modulus E_2 of cells. Additionally, using the Force-Distance Curve (FDC) fitting algorithm described in Chapter 5, this equation was used to determine the contact point z_0 of FDCs, which was needed for the analysis of the local cell thickness h.

Please note, the simple Hertz model assumes the sample thickness h to be approximately infinite, therefore, it is an **infinite thickness model**. Additionally, the adhesion between the two half-spaces is assumed to be negligible and the displacement η to be small compared to the involved radii R_1 and R_2. Thus, the appearing strains $\boldsymbol{v}$ are proportional to the acting forces (according to Hooke's law). Despite of the simplicity of this model, for cell mechanics studies it is still one of the most frequently used models in literature. This is because most of the experiments concerning living cells are carried out in a salty aqueous environment (e.g. in Phosphate Buffered Saline (PBS)), reducing adhesive interactions between cell and (colloidal) probe.

2.2.2 Johnson-Kendall-Roberts model

In some cases significant adhesion forces between indenter/probe and sample appear. Due to this adhesion, a different force-indentation relation appears between indenter and sample than predicted by the simple Hertz model. The adhesion can be described by 2γ, which is the surface energy of both surfaces per unit area. In 1971, Johnson, Kendall and Roberts were solving this contact problem by assuming the adhesive forces to act only within the contact area of indenter and sample [55]. Their solution, the relation

$$\eta(F) = \left[\frac{3(F + 6\gamma\pi R_{12} + \sqrt{12\gamma\pi R_{12}F + (6\gamma\pi R_{12})^2})}{4E_{12}R_{12}^{1/2}}\right]^{2/3} \tag{2.46}$$
$$\text{with } \frac{1}{R_{12}} = \frac{1}{R_1} + \frac{1}{R_2} \text{ and } \frac{1}{E_{12}} = \frac{1-\nu_1^2}{E_1} + \frac{1-\nu_2^2}{E_2}$$

gives the relation between the force F (actively pressing the half-spaces together) and the displacement η. Equally to the simple Hertz model R_1 and R_2 describe the radii of indenter and sample, while E_1, E_2, ν_1 and ν_2 describe their elastic moduli and Poisson's ratios. Equation 2.46 is called Johnson-Kendall-Roberts (JKR) model in the following and converges for infinitesimal values of γ into the simple Hertz model (Eq. 2.43). Please note, the JKR model assumes infinite thickness h of the sample, therefore, it is an **infinite thickness model**.

2.2.3 Thin layer models

Infinite thickness models do not hold for sample thicknesses h in the order of the displacement η. Under such conditions, the elastic modulus E_2 is mostly overestimated by these models [56], what is called **"substrate effect"**. Nanoindentation experiments on thin polymer samples showed, that a rigid substrate significantly influences the sensed elastic modulus E of thin samples [57] (if an infinite thickness model is used for the data analysis). The influence of this effect differs between adhered and non-adhered samples [58]. To avoid such overestimations, Dimitriadis et al. derived a model describing the force-indentation relation for thin adhered and non-adhered samples [41]. It assumes $E_1 >> E_2$ and describes the force-indentation relation as

$$\begin{aligned}\eta(F) = &\left(\frac{3F(1-\nu_2^2)}{4E_2}\frac{1}{\sqrt{R_1}}\right)^{2/3}\left[1-\frac{2\alpha_0}{\pi}\chi+\frac{4\alpha_0^2}{\pi^2}\chi^2\right.\\ &\left.-\frac{8}{\pi^3}\left(\alpha_0^3+\frac{4\pi^2}{15}\beta_0\right)\chi^3+\frac{16\alpha_0}{\pi^4}\left(\alpha_0^3+\frac{3\pi^2}{5}\beta_0\right)\chi^4\right]^{-2/3}\\ &\text{with } \chi=\sqrt{R_1\eta_{12}}/h,\end{aligned} \tag{2.47}$$

wherein the parameters α_0 and β_0 are functions of the binding conditions between cell and substrate [59, 60]. Using *the method of images*, the parameters α_0 and β_0 have been calculated as

$$\alpha_0 = -0.347\frac{3-2\nu}{1-\nu} \text{ and } \beta_0 = 0.056\frac{5-2\nu}{1-\nu} \tag{2.48}$$

in the case of a non-adhered sample. For the case of an adhered sample, the substrate effect is even stronger and α_0 and β_0 are given by

$$\alpha_0 = -\frac{1.2876 - 1.4678\nu + 1.3442\nu^2}{1-\nu}$$
$$\text{and} \tag{2.49}$$
$$\beta_0 = \frac{0.6387 - 1.0277\nu + 1.5164\nu^2}{1-\nu}.$$

This was shown using a integral transformation method to derive the *Green's function for a finite thickness sample bonded to the substrate* similar to the Green's function derived in Eq. 2.36. Equation 2.47 is, besides the simple Hertz model (Eq. 2.43), one of the main equations in this thesis. In Chapter 9 it is used to extract the elastic modulus of thin ($h < 1$ μm) and thick parts of shear stressed cells. Similar to the simple Hertz model this equation allows to extract the contact point z_0 from FDCs by the fitting procedure described in Chapter 6.

For large sample thicknesses h, the square bracket on the right hand side of Eq. 2.47 vanishes, and the model converges to the simple Hertz model. The use of Eq. 2.47 is limited to sample thicknesses $h/R_1 \geq 0.1$. For even smaller ratios of h/R_1 the equations of Chadwick et al. are recommended to use [59]. Chadwick et al. derived the force-indentation relation

$$F = \frac{2\pi E_2 R^2 \eta^3}{3h^3} \tag{2.50}$$

for the case of a bonded sample, and for a non-bonded sample they calculated

$$F = \frac{2\pi E_2 R \eta^2}{3h^3}. \tag{2.51}$$

Thus, for very thin samples, the scaling of the force-indentation law significantly differs between bonded ($F \propto \eta^3$) and non-bonded samples ($F \propto \eta^2$). Nevertheless, even in the model of Dimitriadis et al. the scaling of the force-indentation law differs from the one of the simple Hertz model, as the factor $\chi = \sqrt{R_1 \eta_{12}}/h$ in Eq. 2.47 depends on the indentation depth.

Chapter 3

Theory of cell mechanics

After the discussion of the elastic theory of homogeneous materials in Chapter 2, now the mechanics of highly inhomogeneous cells are in the focus. First, the basic concepts of life related to the mechanics of cells are discussed (Chapter 3.1). Thereafter, in the Chapters 3.2 and 3.3, the discussion will focus on the mechanical properties of the main components of cells. The complex functional interaction of these components is discussed and the applicability of contact models for elastic homogeneous materials to inhomogeneous cells is motivated. Finally, the interplay of cells in tissues and organs is outlined in Chapter 3.4.

3.1 Basic mechanical concepts of life

Typical animal cells show sizes between 2 μm - 30 μm. Nevertheless, some cells, for example neurons[1], can have lengths up to 1 m, while their diameter is in the range of micrometer. In contrast, platelet cells have a diameter of only 2 μm - 3 μm. Despite of this enormous variety in cell size and shape, there are basic components and concepts given among all types of animal cells, allowing the cell to fulfill necessary requirements of life. Two important requirements related to the mechanics of cells are the **isolation against the extracellular environment** and **mechanical strength**. In the following, the cell components contributing the most to the cell's mechanical strength, are briefly described. Figure 3.1 schematizes a typical cell with its most important components: the cell membrane, the cytosol (containing all the cell organelles, the cytoplasm and the Cytoskeleton (CSK)) and the nucleus.

[1] The enormous length is created by axons, a type of protoplasmic protrusion.

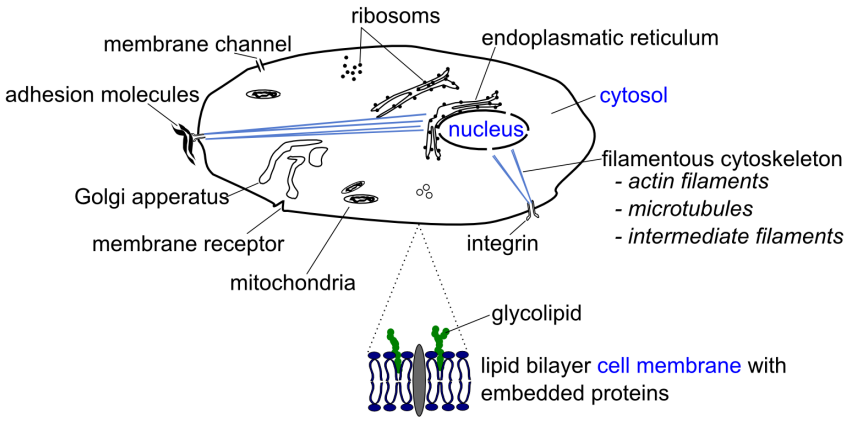

Figure 3.1: *Schematic of a typical animal cell with its main components: lipid bilayer cell membrane, nucleus and the cytosol containing the organelles and the cytoskeleton. The cytoskeleton is important for the integrity of the cell structure and consists of actin filaments, microtubules and intermediate filaments [61].*

3.2 Cell components related to cell mechanics

3.2.1 Cell membrane

The first of the requirements of life mentioned above, the isolation against the environment ensures a closed reaction space for biochemical processes. To create such a reaction space, the cell is equipped with a semipermeable lipid bilayer cell membrane [62]. This 3 nm - 7.5 nm [63, 64] thin membrane allows the cell to vary its internal chemical conditions (e.g. pH value) independently from the extracellular surrounding, which is e.g. necessary for a defined synthesis of proteins. In procariotic and eucariotic cells the principle of isolation against the environment is also given inside the cell, as the cell is divided into different compartments/organelles. This enables the cell to carry out different metabolistic reactions independently of each other, in parallel and under defined conditions. Next to the purpose of isolation, the cell membrane was shown to be a site for chemical reactions not likely to occur in an aqueous environment. Furthermore, the cell membrane carries membrane embedded receptor proteins, allowing the cell to sense and react to chemical, electrical or mechanical signals from its extracellular environment [65]. These proteins can either lay or swim in or on the cell membrane according to the "*fluid mosaic model*" of Singer et al. [66]. By their activation (e.g. by the binding of extracellular signaling molecules), they induce complex chemical signaling cascades, steering defined chemical processes inside the cell, which is called

signal transduction [67, 68, 69]. Such a signal transduction can also induce mechanical adaptation processes of the cell, e.g. a rearrangement of the cytoskeleton.

3.2.2 Cytoplasm

Cytoplasm is the umbrella term for the cell components inside the cell membrane excluding the nucleus. It includes the cytosol, the cytoskeleton and organelles, such as the endoplasmatic riticulum[2] or the Golgi apparatus[3]. The mechanically relevant components (cytosol and cytoskeleton) are discussed in the following:

Cytosol

The cytosol is the fluid part of the cytoplasm. It consists of approximately 70% of water as well as dissolved ions and proteins [70]. Because of the high concentration of large molecules the cytosol behaves more like a gel than like water [71]. Due to this gel-like behavior, the cytosol contributes significantly to the viscoelastic properties of cells. Additionally, the high water content of the cytoplasm leads to the incompressibility of most of the cells and, therefore, to a Poisson's ratio of ($\nu_{cell} \approx 0.5$). Nevertheless, some cells were reported to show smaller values of Poisson's ratio ($\nu_{cell} = 0.36$) [72].

Cytoskeleton

To maintain chemical reaction spaces of the cell even under the influence of mechanical stress, the cell needs the second capability pointed out at the beginning of this chapter: mechanical strength. The mechanical strength of cells is mainly created by the cytoskeleton, a dynamic multi-component 3D-network of protein structures, called filaments. The three main filaments of the cytoskeleton are: Actin Filaments (AFs), Microtubules (MTs) and Intermediate Filaments (IFs) which are cross-linked by a multitude of cross-linking

[2]The endoplasmatic riticulum is a series of folded sheets, continuous with the membrane of the nucleus. The large surface (due to the folding) is used to synthesize proteins using ribosomes.

[3]In the membrane bounded Golgi apparatus, protein sorting takes place. Proteins and other molecules are packed into vesicles (diameter = 0.2 μm - 0.5 μm) and transported to certain regions of the cell.

proteins, such as espin, fascin, scruin, filamin and α-actinin [73, 74, 75]. Additionally, these filaments consist of different materials, making the cytoskeleton to a biocomposite structure [76]. Cells are able to vary this structure actively by synthesizing and degrading filaments [77]. This capacity is used for the directed transport and the fixation of cell components, e.g. of organelles or vesicles. Some cells are also able to change their shape actively (which includes the ability of directed cell movement) or even their mechanical strength (Young's modulus E) *via* rearrangements of their cytoskeleton. In the cell, these components are concentrated in different regions fulfilling specific tasks. Table 3.1 gives an overview of important material parameters of the different filaments. In the following, the three main components (microtubules, intermediate filaments and microfilaments) are discussed in greater detail:

	Diameter $2r\,[nm]$	Persistence length $l_p\,[\mu m]$	Bending stiffness $K_B\,[Nm^2]$	Young's modulus $E\,[Pa]$
Microtubule	25	6000	$2.1 - 2.6 \cdot 10^{-23}$	$1.9 \cdot 10^9$
Interm. filament	10	≈ 1	$4 \cdot 10^{-27}$	$1 \cdot 10^9$
Actin filament	6 - 8	15 - 17.7	$7 - 7.3 \cdot 10^{-26}$	$1.3 - 2.5 \cdot 10^9$

Table 3.1: *Material properties of cytoskeletal filaments [74, 78]. The Young's modulus E of all three filaments is in the range of GPa. A significant difference is given in the persistence length l_p. For microtubules the persistence length is distinctly larger than the filament length l_f and, therefore, they can be described as stiff rods. Whereas, for actin filaments and intermediate filaments $l_p \cong l_f$ was shown, therefore, they can be described with the theories for semiflexible polymers [63]. This means, the thermal movement of the filaments counteracts deformations (strains) of the network by outer forces.*

- **Microtubules (MTs)** are hollow cylinders of tubulin created by the centrosome. They show a diameter of ≈ 25 nm, a length in the range of micrometer [79, 80] and a persistence length distinctly larger than the filament length l_f. Thus, they can be described as stiff rods and are able to resist compression. Further, microtubules were shown to promote a stiffening of F-actin networks for high strains [76] which is known as **non-linear elasticity**[4]. Therefore, they help to prevent the cell from extreme deformations. Additionally, MTs hold and move[5] organelles in

[4] In contrast to simple polymer gels, many biological materials increase their elastic modulus when they are strained. This is called non-linear elasticity and prevents large deformations which could harm the integrity of a tissue [81].

[5] The movements are carried out using the motor proteins dynein and kinesin.

the cytoplasm. Next to the stiffening for high strains, MTs contribute to the local compressibility of the cell, as it was shown, that the Poisson's ratio ν of pure F-actin networks is higher than ν in F-actin-microtubules composite networks [82].

- **Intermediate Filaments (IFs)** are important in terms of mechanical stability of a cell [83]. In all metazoan cells, they form networks which can be described with the theories for semiflexible polymers. Important cross-linkers for this filaments are divalent ions [84]. There are six different types of these filaments known at the moment. In contrast to microtubules IF, networks have been shown to "*withstand large stresses and strains without losing elasticity.*" [85, 86].

- **Microfilaments (MFs)** (or Actin Filaments (AFs)) have a thickness of 7 nm and consist of F-actin. The monomers of actin are called G-actin, as they show a globular shape. AFs can be degraded to G-actin monomers using chemicals, such as Cytochalasin D (CD). Because the persistence length f_p of AFs is in the range of the filament length l_f, microfilaments behave like semiflexible polymers. Therefore, actin networks (intertwined with the help of myosine motor proteins and other cross-linking proteins) behave like semiflexible polymer networks [63]. These networks serve as stabilizing scaffold of the cell and keep the outer cell shape. Additionally, they hold some peripheral membrane proteins on a fixed site [87]. Most cells show an actin cortex, a dense actin network underneath the cell membrane, which supports the membrane. Additionally, in the most animal cells, there are stress fibers, running through the cytoplasm. Stress fibers are bundles of 10 - 30 actin filaments fixed on the focal adhesion points of the cell. They contribute to the mechanical stability and migration of cells [88].

  In general, the effective Young's modulus E of F-actin networks depends on the F-actin content of the network and the number of cross-linkings between the F-actin fibers. Moreover, Gardel et al. showed that there are two regimes of elasticity in F-actin networks. For a low density of F-actin fibers or a low cross-linking density the network withstands deformations mainly by the enthalpy. This means, a deformation of the network causes mostly a bending of its

F-actin filaments. Hence, the bending modulus K_B of the single filaments determines the rigidity of the network. For a dense F-actin network or for a high rate of cross-links the behavior of the stressed network is dominated by the entropy [89] (see Figure 3.2). Therefore, the thermal movements of the filaments are working against a stretching of the network, similar to the oscillations of a guitar string which create additional tensile forces to the string fixation points. Equation 3.1 describes this entropic effect:

$$E =\propto \frac{K_B^2}{k_B T \xi^2 l_c^3}. \tag{3.1}$$

Here, $K_B = I \cdot E_{bundle}$ denotes the bending modulus of an F-actin bundle, which is defined as the product of its Young's modulus E_{bundle} and the second moment of area I of the bundle cross-section. Furthermore, T describes the temperature, k_B the Boltzmann constant, ξ the average distance between the filaments, l_c the average distance between cross-links. Obviously, decreased values in ξ or l_c lead to an increase in cell rigidity (Young's modulus E).

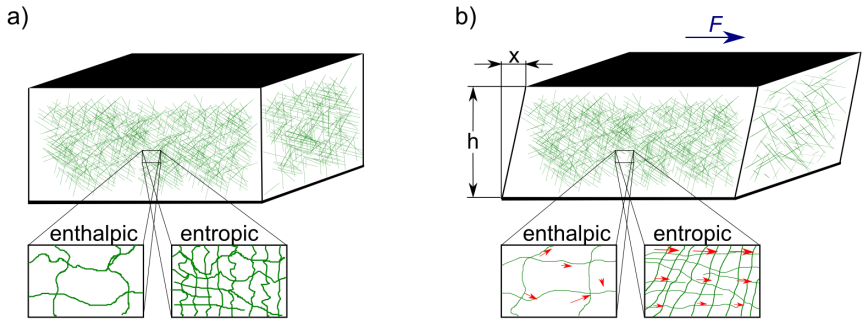

Figure 3.2: *Schematics on strains appearing in an F-actin network (Reprint from [89]).* ***a)*** *Two unstressed networks with either low (left) or high (right) density of F-actin filaments and cross-links.* ***b)*** *The same networks under shear stress. The red arrows indicate the appearing strains. In the case of low F-actin filament or cross-link density the filaments are mainly bended (enthalpy driven process). Therefore, the strain distribution in the network is highly inhomogeneous. For a high filament or cross-link density the network properties are determined not by bending but by the stretching of filaments vibrating due to their thermal energy (entropy driven process).*

3.2.3 Nucleus

The nucleus contains nearly all the DNA of the cell and is wrapped in a double layer of membranes having pores to allow the passage of molecules. The size of the cell nucleus mostly varies between diameters of 3 μm and 10 μm, and is correlated with the cell size [90]. Besides this, the nucleus size is reported to be an important factor for the protection of the genes from chemical mutagens [91]. Moreover, in some cases the nucleus itself is reported to act as mechanosensor of the cell [92]. For some cells, e.g. human neutrophils. the nucleus can be of granular shape and fill up to 50% of the cell volume. The mechanics of nuclei is reported to be viscoelastic [93]. The majority of publications finds that the elastic modulus E of the nucleus is 2 - 4 times higher than the one of the cytoplasm of a cell [94]. Therefore, in the case of flat adhered cells, (e.g. fibroblasts on a glass surface) with a nucleus covered only by a thin (< 1 μm) layer of cytosol, the elasticity of this cell region can be highly influenced by the material properties of the nucleus, which has to be considered in investigations concerning the elasticity of the cell.

3.3 Elastic behavior of cells

Cells are complex structured dynamic composite objects. Nevertheless, due to the fact that their cytoskeleton (present in the most of the cell volume) shows elastic and their cytosol and nucleus show viscoelastic behavior, the whole cell behaves viscoelastic [95, 93, 71, 96, 97, 98]. Nevertheless, since cross-linking proteins couple most of the cell components, this **viscoelastic behavior of the whole cell is more complex than a mere superposition of the mechanical properties of the individual cell components** [99]. Literature shows that (due to this cross-linking), **despite of the inhomogeneity of the cell interior, linear elastic contact models (such as the simple Hertz model), assuming the cell to be of homogeneous elastic material, can be applied to extract local mechanical parameters (e.g. Young's modulus E_2)** of the cell [100, 101]. In the last years, a growing number of studies, concerning the measurement of elastic properties of cells has been carried out using Atomic Force Microscopy (AFM) nanoindentation experiments. Nevertheless, the determination of reliable elastic parameters remains challenging, as the cell shape, thickness and activation status are

important factors for these measurements [41, 17, 102]. Also the shape and the size of the used indenters have been proved to influence the extracted parameters significantly [41, 43].

3.4 Tissues and Organs

In addition to the complex mechanical properties of single cells which were discussed up to here, for the most clinically relevant studies it has to be taken into consideration, that single cells are part of larger cell associations. In fact, this means that the cell and its environmental cells have to be contemplated, which is a scale up to the macroscopic scale like described in Chapter 1.

Within an animal body approximately between 100 and 200 cell types are present. Cells together with their secretions (e.g. extra cellular matrix secreted by fibroblasts) form a tissue [75]. Some tissues together can form an organ. As tissues and organs sum up the microscopic volumes of the cells forming them, they show sizes in the centimeter scale. Furthermore, not only the volume of the cells is summed up in organs, locomotion parameters like the contraction force of single muscle cells are multiplied by parallel cell disposal. By contrast, parameters like the contraction length and the contraction speed of single muscle cells are summed up by cascading them. This allows organs and tissues to carry out fast macroscopic movements (in the range of meters/second) and to create relatively large forces (in the range of Newton), as it is needed in the human heart muscle. *Vice versa*, since the organ is the sum of its cells, if an organ such as the heart shows macroscopic changes in its parameters (e.g. elasticity, contraction force or contraction speed), there must be microscopic/nanoscopic reasons in at least one of its cell types.

Chapter 4

Experimental setup

4.1 Atomic Force Microscope (AFM) - Principle

The Atomic Force Microscope (AFM) is a scanning probe microscope and mainly consists of four parts: first an AFM controller, second a piezo driven 3D-scanner, third a probe mounted on a flexible AFM cantilever, and fourth a (cantilever-)deflection detection system (mostly based on a laser beam reflected by the cantilever tip). Please note, for larger movements of the cantilever in z-direction most AFMs are equipped with AFM stepper motors, additionally to the 3D-scanner. In AFM nanoindentation measurements the AFM cantilever is approached to the cell using the 3D-scanner. The JPK NanoWizard 3 (JPK, Berlin, Germany) 3D-scanner here used provides 15 μm piezo-driven stroke in z-direction and 100 μm piezo-driven scanning range in x- and y-direction. The principle structure of an AFM along with a sample (cell) and the substrate (e.g. glass or mica) is schematized in Figure 4.1.

A contact between cell and AFM probe leads to interaction forces which deflect the flexible AFM cantilever. This deflection is sensed *via* an infrared laser (980 nm) reflected from the cantilever tip to a Position-Sensitive Detector (PSD). Mostly this is a four-segmented photodiode. Each of the four diode segments independently measures the intensity of the incident laser light. A deflection of the cantilever causes a movement of the incident laser spot on the PSD which results in changes of the four measured laser intensities, while the sum of the measured intensities remains constant. Knowing the geometry of the AFM system and the Inverse Optical Lever Sensitivity (InvOLS, [m/V])

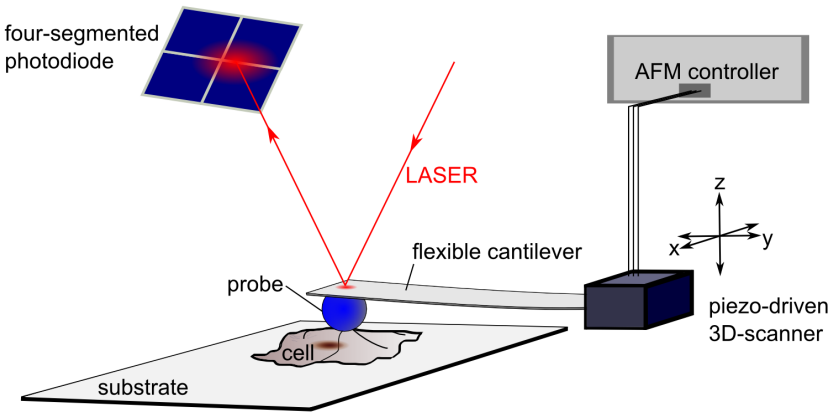

Figure 4.1: *The principle structure of an AFM system. The AFM consists of a fast AFM controller, a piezo-driven 3D-scanner, a probe mounted on a flexible cantilever a (laser based) deflection detection system. Forces acting on the probe lead to deflections of the cantilever, which causes a measurable movement of the laser spot on the photodetector.*

of the AFM cantilever, the cantilever deflection d_c can be calculated by the differences in laser intensity (Signal Intensity Difference (SIDR)) measured between the diode segments. More accurately, the AFM measures the inclination $\mathrm{d}d_c/dx$, not the deflection d_c of the cantilever.

The InvOLS gives the cantilever deflection needed for a SIDR of one volt and was determined by the measurement of Force-Distance Curves (FDCs) on clean rigid substrates (freshly cleaved mica). By pressing the cantilever against a rigid substrate, the deflection d_c of the cantilever is equal to the change in the position z of the 3D-scanner, as no indentation appears. Furthermore, as for small deflections an AFM cantilever obeys Hooke's law (see Chapter 2.1.2), the resulting deflection d_c is linear proportional to the interaction force F_c acting on the cantilever, as described in Eq. 4.1:

$$k_c \cdot d_c = F_c \tag{4.1}$$

In this equation, k_c denotes the cantilever spring constant. Nevertheless, for a non-rigid sample, not only the cantilever deforms/deflects under the influence of the interaction forces, but also the sample. Hence, the probe is pressed into the sample, causing an indentation η which is related to k_c and d_c by

$$d_c + \eta = z - z_0 \text{ with } z \leq z_0. \tag{4.2}$$

Here, z is the z-position of the AFM 3D-scanner. The cantilever position leading to a first slight contact between probe and sample, but neither to a deflection of the cantilever nor to a sample deformation, is called contact point z_0. The whole measurement process is steered by the AFM controller, examining (quasi-continuously) the cantilever position (more accurate the 3D-piezo position) and the measured cantilever deflection.

4.2 AFM Probes

4.2.1 Colloidal probe preparation

All Force-Distance Curves (FDCs) in this thesis have been measured using Colloidal Probes (CPs) made by glueing silica microspheres (radius $R_1 = 2.5$ μm; Bangs Laboratories, Fishers, IN, USA) with high accuracy on the front of tipless CSC12 AFM-cantilevers (Mikromasch, Tallinn, Estonia). Figure 4.2 shows such a colloidal probe from two different perspectives. Techniques to glue microspheres to tipless cantilevers are commonly performed in air. In this context approaches, that employ thin filaments to place the microsphere on the cantilever, are often accompanied by a discontinuous movement/jump of the microsphere from the filament to the cantilever. This problem is caused by capillary forces (arising between microsphere and cantilever) and often makes it difficult to achieve a central microsphere position on the cantilever front. To increase the positional accuracy, other approaches (in air) try to catch and lift up a microsphere (laying on a glass slide) directly with a glue-covered cantilever. However, these procedures become unfeasible, if there are strong adhesion forces between substrate and microsphere.

For this purpose, a new procedure was developed, which eliminates both effects as most of the steps are performed in aqueous solution. Using this procedure, it is possible to position the microsphere with an accuracy of approximately 500 nm on the cantilever beam. The following steps were carried out (in the sequence indicated) to create the CPs: First, for 15 min two glass slides were cleaned in a RCA 1-solution ($6 : 1 : 1$ solution of Ultra Pure Water (UPW; arium pro VF, Sartorius AG, Goettingen, Germany) : H_2O_2 (Sigma-Aldrich, St. Louis, MO, USA) : NH_4OH (VWR, Radnor, PA, USA)) [103, 104], which avoids sphere contamination. In a second step a thin filament was used to

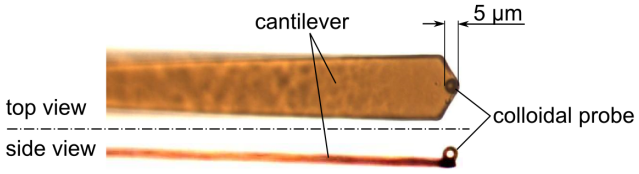

Figure 4.2: *Bright field image of a typical colloidal probe on a CSC12 AFM-cantilever created by the described procedure. The silica AFM probe has a diameter of 5 µm.*

put a line of the UV-curable and hydrophobic adhesives NOA68 or NOA68T (Edmund Optics GmbH, Karlsruhe, Germany) on a clean glass slide, perpendicular to the orientation/long axis of the cantilever beam. Afterward, using the piezo-driven AFM 3D-scanner, the front of the cantilever was immersed ($\approx$ 1 μm) into the adhesive. After 1 sec of indentation, the cantilever was retracted. A small drop of glue remained on the bottom side of the front of the cantilever. Thereafter, 1 mL of a solution of UPW and microspheres (0.006 wt.%) was pipetted on a second clean glass slide.

Due to the RCA 1-cleaning, the solution spread over the whole glass slide, so that most of the microspheres inside the solution became separated. Due to their aqueous environment, microspheres laid on the glass but did not adhere. After pipetting a drop of UPW ($\approx$ 10 μL) on the cantilever, which helps to protect the cantilever from being destroyed by surface tensions during the immersion process, the AFM stepper motors were used for driving the cantilever into the solution. A single microsphere was approached with the cantilever front using low approach velocities (1 μm/sec)[1]. When the glue-covered end of the cantilever beam was over the microsphere, the z-piezo was used to press the microsphere into the adhesive with a force of 5 nN for 5 sec. Mostly, at this point of the procedure, small adjustments of the position of the microsphere with respect to the cantilever tip were achievable *via* cantilever-movement with the help of the AFM 3D-scanner. After this, the microsphere weakly adhered to the cantilever front and the cantilever was retracted from the surface. It was important now, not to pull the cantilever out of the water, because its surface tension could either detach the microsphere from the cantilever or relocate it on the cantilever. A portable UV lamp (254 nm; UVGL-25, VWR,

[1]Using high tip-velocities, due to the induced flow the microsphere could move away from its former position.

Darmstadt, Germany) was used to cure the adhesive in solution. Despite of the UV absorption in water, enough radiation reached the cantilever, so that the glue started curing. Usually, this took 7 min at a distance of $\approx$ 10 cm between lamp and cantilever. Afterward, the cantilever was pulled out of the water and the curing process was completed in air.

For the measurements carried out on human blood derived neutrophil granulocytes **CPs were additionally coated with PEG** (polyethylene glycol, 2-[Methoxy(polyethyleneoxy)propyl]trimethoxysilane 90% 6-9, ABCR GmbH & Co. KG, Karlsruhe, Germany) to reduce adhesive forces between CP and neutrophils and to prevent the neutrophils from getting activated by the contact with the silica AFM probe. For this purpose the CPs were plasma cleaned for 30 sec in an oxigen plasma (500 sccm, 600 W, 1 mbar; PVA TePla AG, Kirchheim, Germany). Thereafter, the CPs were incubated in a solution of PEG (20 μL), toluene (2 mL; Cat. No. 244511, Sigma-Aldrich, St. Louis, MO, USA) and triethylamine (20 μL; Cat. No. 90335, Sigma-Aldrich, St. Louis, MO, USA) for three hours. After this time the CPs were rinsed with pure toluene and UPW, in this sequence.

4.2.2 Wedged cantilever preparation

A crucial problem for nanoindentation experiments on spherical cell-like objects is the weak adhesion between cell and substrate. If the indenter/probe does not press precisely on the apex of the cell, forces tangential to the cell surface appear and the cell tends either to slide or to roll under the load of the cantilever. Then, the resulting FDCs are disturbed and a precise estimation of cell Young's modulus E_2 is not possible. It was shown, that wedged cantilevers can overcome this problem, as they inhibit the appearance of lateral forces [45].

Wedged cantilevers presented in the literature have been created by the curing of UV-curable adhesives on the cantilever front. For this purpose the glue-covered cantilever front was pressed against a surface (in order to bring the glue into an wedge-like shape) and cured afterward. This procedure resulted in wedged but rough cantilever fronts [45]. For the experiments presented in Chapter 6 wedged cantilevers with high quality and low roughness were needed (see Figure 4.3). In order to **glue a Poly(methyl methacrylate)**

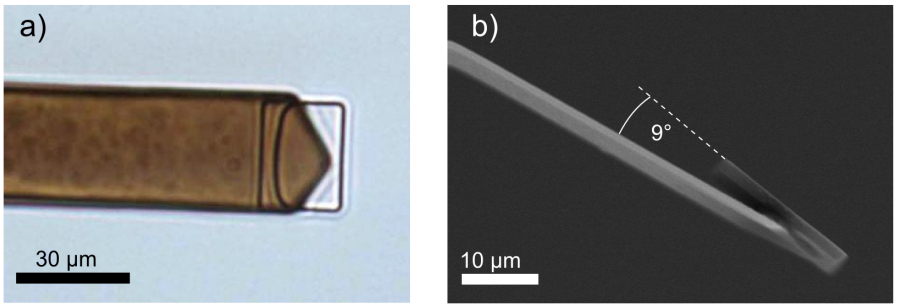

Figure 4.3: ***a)*** *Bright field image of a wedged cantilever. A transparent Poly(methyl methacrylate) (PMMA) rectangle was glued to the front of a tipless CSC12 cantilever. The transparency of the PMMA was useful to position the Polyethylene Glycol (PEG) microbeads correctly under the center of the microrectangle (see Chapter 6.7).* ***b)*** *Scanning Electron Microscopy (SEM) image from the side of the cantilever. The cantilever front compensates the angle φ between cantilever beam and substrate. Using wedged cantilevers for nanoindentation experiments, the investigated sample is compressed between two parallel planes.*

(PMMA) microrectangle to the front of a tipless cantilever, first, (using the AFM 3D-scanner) the cantilever front was immersed in UV-curable adhesive (NOA68; Norland Adhesives, Cranbury, NJ, USA) and then softly pressed against a PMMA microrectangle laying on a glass cover slip[2]. The cantilever was kept in this position for 30 min, while UV light (254 nm; UVGL-25, VWR, Darmstadt, Germany) was used to cure the glue. After 30 min of UV irradiation, the cantilever was gently covered with 50 μL of UPW (to reduce possibly appearing adhesion forces between microrectangle and substrate) and retracted afterward. This resulted in wedged cantilevers precisely compensating the angle[3] $\varphi \approx 9°$ between the cantilever and the substrate for the used JPK NanoWizard 3. Note, the transparency of the PMMA rectangles is very useful in order to position cells and microparticles centrally under the wedge, as it was done for the experiments presented in Chapter 6.7.

Microrectangle preparation

Microrectangles (30 μm x 25 μm) were made of PMMA and were obtained using Electron Beam Lithography (EBL; see Figure 4.4). For this purpose, silica chips (1 cm x 1 cm) were cleaned with RCA-1 cleaning solution (6 : 1

[2]The glass slide caring the PMMA squares was mounted in the AFM in a way that the longer edge of the aimed PMMA square was laying perpendicularly to the cantilever beam.

[3]Please note, as the NanoWizard 3 has three independent stepper motors, the angle φ is adjustable and can be varied.

: 1 solution of UPW (arium pro VF; Sartorius AG, Goettingen, Germany) : H_2O_2 (Sigma-Aldrich, St. Louis, MO, USA) : NH_4OH (VWR, Radnor, PA, USA)) [103, 104]. Afterward, a layer of gold (20 nm thick) was sputter coated (Q150R S, Quorum Technologies, United Kingdom) on the clean chip. Then, 20 μL of 4% PMMA (AR-P 679.02(950K); ALLRESIST GmbH, Strausberg, Germany) in ethyl lactate (Sigma-Aldrich, St. Louis, MO, USA) were spin coated on the gold layer (DELTA6 RC TT, Süss Micro Tec, Garching, Germany) at 2000 rpm for 120 sec. EBL was carried out using the ELPHY Quantum EBL system (Rait GmbH, Dortmund, Germany) in a Zeiss Supra 40 VP Scanning Electron Microscope. An electron beam dosage of 200 μC/cm^2 and an acceleration voltage of 20 kV were used to create rectangles. After

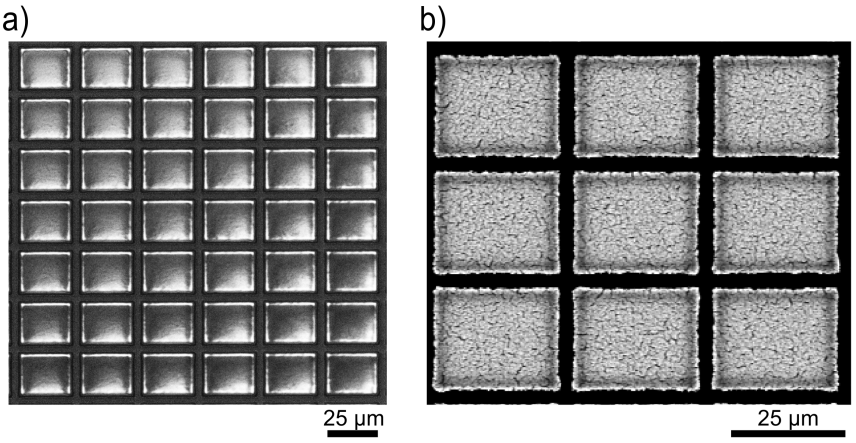

Figure 4.4: *Scanning Electron Microscopy (SEM) image of Poly(methyl methacrylate) (PMMA) microrectangles on a silica chip.* ***a)*** *Imaging at 5 kV accelerating voltage shows the surface of the PMMA microrectangles.* ***b)*** *Imaging at 20 kV (high power electron beam) leads to an increased penetration depth of the electrons and resolves the underlaying sputter coated gold structure.*

the lithography process, the chip was processed for 5 min with developer (AR 600-55, Allresist, Strausberg, Germany) and rinsed with isopropanol (Sigma-Aldrich, Taufkirchen, Germany) for 1 min. To separate the PMMA rectangles from the substrate the silica chip was incubated with gold etchant (consisting of: 4 g potassium iodide (KI; Sigma-Aldrich, St. Louis, MO, USA), 1 g iodine (I_2; Sigma Aldrich, St. Louis, MO, USA) and 40 mL UPW (arium pro VF; Sartorius AG, Goettingen, Germany)) for 10 min. After resolving the gold according to Eq. 4.3

$$2Au + I_2 \rightarrow 2AuI, \tag{4.3}$$

the small rectangles and a PMMA frame structure (outside of the EBL area) still adhered to the chip (see Figure 4.4). The frame structure was removed using a tweezer, the PMMA rectangles were washed off of the silica chip using UPW. After washing the microrectangles off of the chip, the washing solution ($\approx$ 1 mL) was still containing iodide. Therefore, the solution was diluted with 10 mL UPW. After sedimentation of the microrectangles, 90% of the supernating solution were removed. By repeating this procedure twice, the solution was cleaned from iodide iteratively and the microrectangles were cleaned for use.

4.2.3 AFM probe calibration

Thermal noise methods

In this thesis exclusively rectangular AFM cantilevers were used. Such a cantilever approximately is described by a bar of homogeneous material and length l_c, broad b_c and thickness h_c (see Figure 4.5). The spring constant k_c of such a homogeneous bar fixed at one side is given by

$$k_c = \frac{3 \cdot E_c \cdot I_c}{l_c^3}, \tag{4.4}$$

wherein E_c denotes the elastic modulus of the cantilever material and I_c describes the second moment of area of the cantilever beam. Nevertheless, the

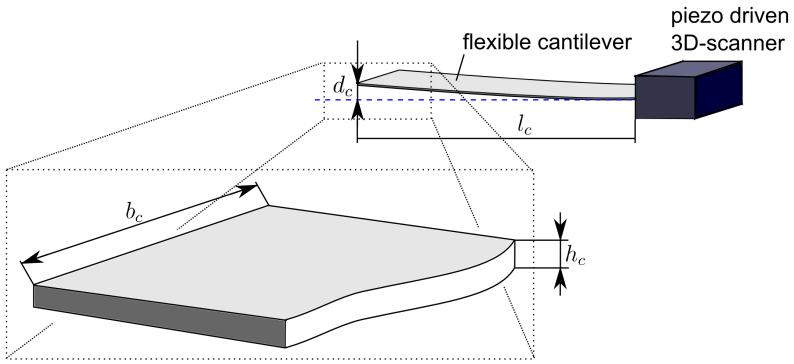

Figure 4.5: *Schematic of a rectangular cantilever with length l_c, broad b_c, thickness h_c and a deflection d_c.*

direct determination of k_c using $I_c = h_c^3 b_c/12$ (for rectangular cantilevers) is not reliable, as Young's modulus E_c and the thickness h_c of the cantilever beam

are mostly not known accurately. AFM cantilevers are oscillators showing different specific modes. These modes can be excited by thermal energy. Using Eq. 4.4 and **assuming that there is only the fundamental oscillation present in the cantilever**, the cantilever can be assumed to behave like an harmonic oscillator. Cleveland et al. [105] showed that this can be used to determine the cantilever spring constant by dynamic measurements. If the first mode resonance frequency $\omega_{1,vac}$ of a cantilever can be determined, the equation

$$k_c = \frac{b_c (l_c \omega_{1,vac})^3}{4} \left(\rho_c^3 / E_c\right)^{1/2} \tag{4.5}$$

gives an approximation of the cantilever spring constant k_c. Please note, in this equation the thickness h_c of the cantilever is not needed to be known.

Nevertheless, in general the kinetic properties of the cantilever are described by the Euler-Lagrange differential equation:

$$F(x,t) = E_c \cdot I_c \frac{\partial^4 z(x,t)}{\partial x^4} + \mu_c \cdot \frac{\partial^2 z(x,t)}{\partial t^2}, \tag{4.6}$$

with F describing the force acting on the cantilever, t describing the time, x describing a spacial coordinate and μ_c being the mass per cantilever unit length. Moreover, in the here assumed case of a homogeneous cantilever, the product $I_c \cdot E_c$ gives its **bending stiffness**. Solving Eq. 4.6, for a cantilever in vacuum the deflection $d_c(x,t)$ is described by

$$d_c(x,t) = \sum_n C_n \cdot \sin(\omega_{n,vac} t + \zeta_n) \cdot \Theta_n, \tag{4.7}$$

wherein C_n and ζ_n are constant parameters and Θ_n is a function of x [106]. The resonance frequency of the n-th mode is given by:

$$\alpha_n^4 = \frac{12 \rho \omega_{n,vac}^2 l_c^4}{E_c h_c^2} \text{ with } \cos\alpha_n \cosh\alpha_n = -1. \tag{4.8}$$

Hence, the resonances are defined by sharp peaks $\omega_{n,vac}$ in the frequency spectrum, and the movement of the cantilever is the superposition of harmonic oscillations.

Nonetheless, most of the AFM measurements are not carried out in vacuum. As shown by Sader et al. cantilevers in air (and even more in aqueous solution) show Reynolds numbers in the scale of one. Hence, dissipative (viscous) effects are not negligible and can be described by a complex hydrodynamic function $\Gamma = \Gamma_r + i\Gamma_{im}$ (here i is the imaginary unit). These viscous effects of the medium surrounding the cantilever lead to decreased resonance frequencies, decreased vibration amplitudes and a broadening of the resonance peaks. In 1998, Sader et al. showed the following proportionality for the frequency response of the n-th mode with the resonance frequency $\omega_{n,amb}$:

$$D_n(\omega) \propto \omega_{n,amb}^2 \cdot \left[(\omega^2 - \omega_{n,amb}^2)^2 + \frac{\omega^2 \omega_{n,amb}^2}{Q_n^2} \right]^{-1/2}. \tag{4.9}$$

Please note, here and in the following the subscribed "amb" indicates parameters of the fluid/gas surrounding the AFM cantilever. Equation 4.9 shows that the amplitude $D_n(\omega)$ of the n-th mode of the deflection is dependent on a quality factor Q_n, which is defined by

$$Q_n = \left[\frac{4\mu}{\pi \rho_{amb} b_c^2} + \Gamma_r(\omega_{n,amb}) \right] / \Gamma_{im}(\omega_{i,amb}). \tag{4.10}$$

Herein Γ_r denotes the real part of the hydrodynamic function Γ. Moreover, the frequency shifts of the resonant frequencies are defined by

$$\omega_{n,amb} = \omega_{n,vac} \left[1 + \frac{\pi \rho_{amb} b_c^2}{4\mu} \Gamma_r(\omega_{n,amb}) \right], \tag{4.11}$$

using the real part Γ_r of the hydrodynamic function. An analytical description for Γ was derived for cantilevers with circular cross-section [107]:

$$\begin{aligned} \Gamma_{circ} &= 1 + \frac{aiK_1(-i\sqrt{iRe})}{\sqrt{iRe} \cdot K_0(-i\sqrt{iRe})} \\ &\text{with the appropriate Reynolds number} \\ Re &= \frac{\rho_{amb} \omega b_c}{4\eta_{amb}}. \end{aligned} \tag{4.12}$$

In 1999, Sader et al. derived a complex correction Ω in order to correct for rectangular cantilever cross-sections: $\Gamma_{rect} = \Omega \cdot \Gamma_{circ}$. Using this new Γ_{rect} the cantilever spring constant for thin rectangular cantilevers (with $b_c >> h_c$) can

be described as

$$k_c = 0.1906 \cdot \rho_{amb} b_c^2 l_c Q_{amb} \Gamma_{im}(\omega_{amb}) \omega_{amb}^2. \tag{4.13}$$

In this equation, ρ_{amb} is the mass density of the ambient medium, Q_i the cantilever quality factor (in the medium) and Γ_{im} the imaginary part of the hydrodynamic function Γ related to the cantilever and its surrounding medium. For a detailed description of the correction Ω please refer to Sader et al. [108].

In this thesis AFM cantilevers were either calibrated using the thermal noise procedure implemented in the JPK software (JPK NanoWizard Control V4, JPK, Berlin, Germany) or homemade scripts implemented by Block et al. [109]. The procedure of JPK bases on the Eqs. 4.9 and 4.16. It was applied for the calibration of AFM cantilevers used for the measurements on human cardiac fibroblasts (see Chapter 7). The parameters Q_n and $\omega_{n,amb}$ were obtained by fits of the thermal noise spectra to Eq. 4.9 in a semi-automated fashion.

The scripts of Block use three different methods: The first one is a method based on the Eq. 4.5 of Cleveland et al. [105]. For this purpose, $\omega_{n,amb}$ is converted into $\omega_{n,vac}$ using the equation

$$\omega_{n,amb} = \omega_{n,vac} \left(1 + \frac{\pi \rho_{amb} b_c}{4 \rho_c h_c} \right) \tag{4.14}$$

of Sader et al. [110]. The second method implemented by Block uses Eq. 4.13 [110, 108]. Here, the quality factor Q_n of the n-th mode and the resonant frequencies $\omega_{n,amb}$ are obtained by fits of the thermal noise spectra to Eq. 4.9. Third, a method described by Butt and Jaschke [106] is implemented in the scripts of Block et al. Butt and Jaschke showed that the potential energy of a vibration mode is given by

$$W_n = \frac{k_c q_n^2(t) \alpha_n^4}{2} \frac{(\sin \alpha_n + \sinh \alpha_n)^2}{3}. \tag{4.15}$$

Moreover, the Parseval's theorem states that the integral over the power spectral density equals the square of the signal magnitude. Thus, the integral over the power spectral density is equal to the Root Mean Square (RMS) deflection

$\langle d_c^2 \rangle$ of the AFM cantilever. This leads to the following equation:

$$\langle d_c^2 \rangle = \frac{12 k_B T}{k_c} \sum_n \frac{1}{\alpha_n^4} = \frac{k_B T}{k_c} \tag{4.16}$$

The script of Block first fits the power spectral density to Eq. 4.9 for the determination of: the amplitude $D_{n,0}$ of the n-th mode, $\omega_{n,amb}$ and Q_i [109]. Then, the Lorentzian curve described by Eq. 4.9 is integrated with respect to ω and $\langle d_c^2 \rangle$ is calculated by the sum of $\chi_n^2 A_n$. Herein A_n is the area under the peak of the n-th mode in the power spectral density plot of the thermal noise. Further, χ_n^2 is a correction factor accounting for the fact, that the AFM measures the inclination $\mathrm{d}d_c/dx$, not the deflection d_c of the cantilever. The three methods have been applied and their results have been compared in order to determine the cantilever spring constants reliably. Only for proper fits of the power spectral density to Eq. 4.9 and if at least two methods led to a similar value of k_c (outliers were ignored) the cantilever was used.

Relative AFM probe calibration (spring-on-spring method)

In some cases thermal noise methods are not appropriate in order to determine the spring constant of a cantilever, for example, for wedged cantilevers with comparatively large wedges. The added mass of the microrectangle and the used glue can be significantly higher than for a colloidal probe, which can decrease the resonance frequency of the cantilever artificially. For this reason, the spring constant (k_c=0.007 N/m) of the wedged cantilever was determined by measuring FDCs with the wedged cantilever on an (inverted) calibrated colloidal probe (k_c=0.029 N/m). Subsequently, the unknown spring constant was calculated by the following equation [111]:

$$k_c = k_{ref} \left(\frac{s_{rig} - s_{ref}}{s_{ref} \cdot \cos \varphi} \right) \approx k_{ref} \left(\frac{s_{rig}}{s_{ref}} - 1 \right) \tag{4.17}$$

Here φ describes the angle between cantilever beam and substrate, while s_{ref} and s_{rig} are the slopes of the contact areas of FDCs, measured either on the reference cantilever or on a rigid substrate. To reduce the influence of adhesion between both cantilevers, in this thesis the procedure was carried out in UPW. This indirect procedure is schematized in Figure 4.6.

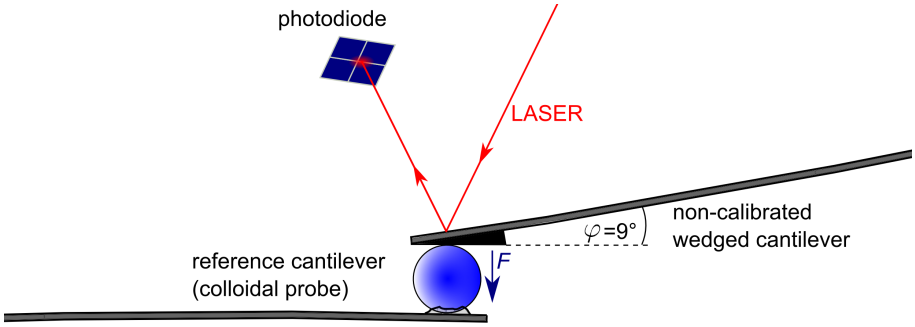

Figure 4.6: *Schematic showing a spring-on-spring calibration process using a calibrated second cantilever (colloidal probe). A FDC is recorded by pressing the wedged cantilever against the front of a CP with a known spring constant. This causes a deflection of both: CP and wedged cantilever. Using Eq. 4.17, the slope of the contact area of the FDC can be used to calculate the spring constant of the wedged cantilever.*

4.3 Details on sample preparation and measurements

4.3.1 Measurements on Polyethylene Glycol (PEG) microbeads

PEG microbead preparation

Polyethylene Glycol (PEG) microbeads were synthesized by precipitation polymerization, as shown by Pussak et al. [112, 113]. Briefly, 0.5 wt.% PEG diacrylamide (number average molecular mass M_n=20 kDa, 50 mg) were dispersed in 1 M sodium sulfate solution (10 mL) with Irgacure 2959 (BASF, Ludwigshafen, Germany) as a UV photoinitiator at a concentration of 0.01 wt.% (1 mg) [114]. Vigorous shaking of the solution resulted in PEG diacrylamide microdroplets that were photo-polymerized for 90 sec using a Heraeus HiLite Power curing unit (Heraeus Kulzer, Wehrheim, Germany). Afterward, the resulting solution (containing the microspheres) was centrifuged at 5000 rpm for 10 min and washed with UPW to remove salts. Using a microscale (GH-252, A&D, Tokyo, Japan), the mass density ρ_{PEG} = 1036 kg/m^3 of the used PEG was determined by measuring the mass of a tube filled with either PEG, or PEG and UPW, or only UPW. Figure 4.7 shows PEG microbeads in UPW. Please note, the PEG microbeads were created by Dr. Daniel Pussak (Max Planck Institute of Colloids and Interfaces, Potsdam, Germany).

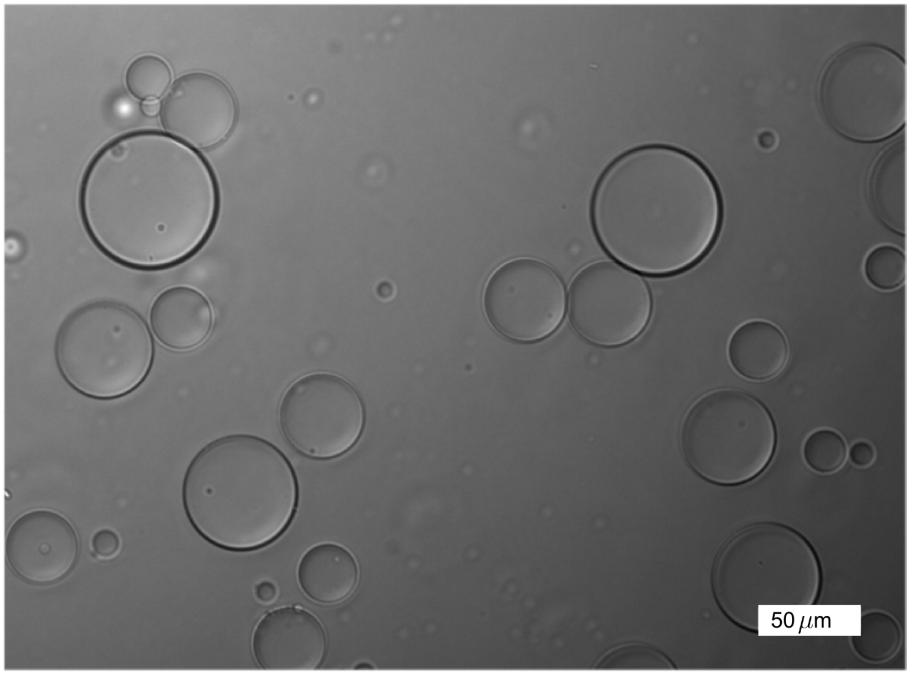

Figure 4.7: *PEG microbeads in ultra pure water (UPW) as they were obtained by the described protocol.*

AFM force-distance measurements

In order to characterize the elastic properties of PEG microbeads and to prove the predictions of the *mixed double contact model* presented in Chapter 6, single FDCs were measured on PEG microbeads on a glass substrate. As the measurements were carried out in UPW (arium pro VF, Sartorius AG, Goettingen, Germany), a low approach velocity of 0.75 μm/sec was used, in order to decrease hydrodynamic effects. Moreover, the measurements have been carried out with a wedged cantilever (see Chapter 4.2.2). The FDC fits according to the simple Hertz model and the *mixed double contact model* were calculated using the exact same contact point z_0 to increase comparability.

4.3.2 Measurements on human Cardiac Fibroblasts (CFBs)

Culture and treatment of human CFBs

After the second passage of the CFBs, they were seeded on clean glass slides in 6-well plates (BD Falcon, Franklin Lakes, NJ, USA), where they spread and adhered. 24 hours later, the AFM measurements were carried out. For more

details on cell culture and passages see Appendix A.1.3.

AFM force-distance measurements

The investigated CFBs showed a large variety in cell morphology. Hence, the application of an infinite thickness model was preferable. The reason for this is that to determine the local cell thickness h, additional Force-Distance Measurements (FDMs) on the substrate next to the cell are needed. This is time consuming and would have reduced the amount of biological replicates (cells of one patient and heart ventricle) measurable per hour. The application of FVMs was also not preferable for this purpose, as some of the cells showed length up to 100 μm, which is the maximum lateral movement of the cantilever in the used AFM. Nevertheless, in the same population also cells with diameters of only 20 μm were found. Therefore, the area covered by the FVM would have been needed to be adjusted manually for each individual cell. This would be time consuming too, and reducing the number of cells measurable per hour. To overcome these limitations, single FDCs were measured on the CFBs. Therefore, to characterize a larger number of CFBs per experiment, their elastic properties were estimated from the measurement of solely three FDCs taken at two different positions on the cell (six FDCs/cell). This made it possible to investigate at least twelve CFBs per hour and heart ventricle, for each patient.

FDCs were measured in a distance of 5 μm - 10 μm from the nucleus, as the cell thickness in this region was found to be between 1.5 μm and 5.0 μm but never below 1.5 μm; therefore, the influence of substrate effects in this cell region is reduced. Using bright field microscopy, this distance was easy to estimate as it is a multiple of the diameter of the CP. The force setpoint was set to 2.5 nN in order to prevent cell damage. The approach velocity was set to 5 μm/sec in order to minimize hydrodynamic effects. All measurements were carried out in culture medium (79% iscove basalmedium, 10% fetal calf serum, 10% human serum, 1% Penicillin-Streptomycin) at 37°C in a JPK BioCell (JPK, Berlin, Germany).

Please note, for the 15 FVMs wich were measured in order to characterize the lateral distribution of cell Young's modulus E_2 in CFBs the same parameters

have been used. Disturbed measurements were excluded from the statistics by using only FDCs showing small Least Mean Squares (LMS) errors ($\epsilon_{lim}^{(0)} < 25$ pN, $\epsilon_{lim}^{(1)} < 22$ pN, $\epsilon_{lim}^{(2)} < 45$ pN) with respect to the determined fit function (see Chapter 5.5.4).

4.3.3 Measurements on human neutrophil granulocytes

HNA-3 antibody containing plasmas and control plasmas

HNA-3a antibody containing plasmas (P1, P2 and P3) were obtained from alloimmunized blood donors (identified by serological screening) and characterized by Flow Cytometry (FC), Granulocyte Agglutination Test (GAT), Granulocyte Immunofluorescence Test (GIFT) and Lymphocyte Immunofluorescence Test (LIFT) using a panel of genotyped granulocytes and lymphocytes, as described previously[115]. Control plasma (P0) was pooled from ten healthy non-transfused male blood donors of blood group AB. Granulocyte reactive antibodies in these plasmas were excluded serologically.

Glass coating procedure

Glass slides (diameter = 24 mm, Thermo Scientific, Braunschweig, Germany) were cleaned with acetone (99.8% in H_2O, Merk, Darmstadt, Germany), ultrasound (10 min at 50°C; Elamsonic S 30H, Elma) in UPW (arium pro VF, Sartorius AG, Göttingen, Germany), RCA 1-solution (6 : 1 : 1 solution of ultra pure water (UPW; arium pro VF, Sartorius AG, Göttingen, Germany) : H_2O_2 (Sigma-Aldrich, St. Louis, MO, USA) : NH_4OH (VWR, Radnor, PA, USA)) and UPW, in this sequence. Finally 200 μL of a Poly-HEMA (Poly-2-hydroxyethyl methacrylate; Sigma-Aldrich, St. Louis, MO, USA) solution (0.025 mg/mL in ethanol) were pipetted on the dried glass slides and evaporated using a spin coater (120 rpm; DELTA6 RC TT, Süss Micro Tec, Garching, Germany). Small spots (diamter $\approx$ 500 nm - 1000 nm) of Poly-HEMA hydrogel remained on the glass slide, forming a coating with homogeneous spot density over the whole glass slide (excluding the absulute edge regions of the glass). The used Poly-HEMA concentration was found to be optimal, as neutrophils only slightly adhered on this substrate and remained almost naive and spherical enabling valid AFM measurements. Figure 4.8 shows a typical Poly-HEMA coating as it results from this precedure.

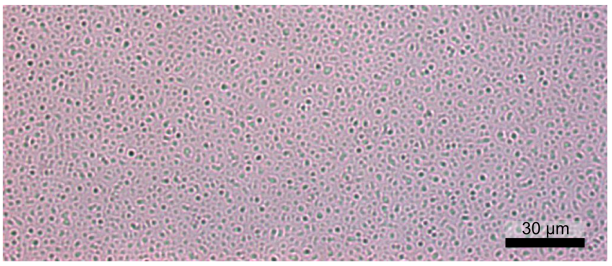

Figure 4.8: *Poly-HEMA coating of a clean gass slide. The Poly-HEMA spots show a homogeneous lateral density on the slide.*

Culture and treatment of neutrophils

For each experiment $5 \cdot 10^5$ neutrophils were settled on Poly-HEMA coated glass slides in 6 well culture plates (BD Falcon, Franklin Lakes, NJ, USA) containing 3 mL VLE-RPMI (RPMI 1640 Liquid Medium, Biochrome, Cat. No. F 1215) for 30 min at 37°C. In inhibitor experiments, 10 min prior to the end of cell settlement, either trypsin-like serine protease inhibitor (TLCK; 100 μM; Sigma-Aldrich, Taufkirchen, Germany), chymotrypsin-like serine protease inhibitor (TPCK; 50 μM; Sigma-Aldrich, Taufkirchen, Germany), NADPH[4] oxidase inhibitor (VAS; 100 μM; VAS2870, Sigma-Aldrich, Taufkirchen, Germany), Diphenyleneiodonium chloride (DPI; 100 μM; Sigma-Aldrich, Taufkirchen, Germany) or Cytochalasin D (CD; 1 μM; Calbiochem, Darmstadt, Germany) were added. After settlement, 500 μL of either P0, P1, P2, P3 or a solution of P0 and FMLP (10 μM; Formyl-Methionyl-Leucyl-Phenylalanine; Sigma-Aldrich, Taufkirchen, Germany) were added and neutrophils were incubated for additional 30 min. Afterward, the glass slides were rinsed three times with 3 mL VLE-RPMI supplemented with either TLCK (100 μM), TPCK (10 μM), VAS2870(25 μM), DPI (25 μM) or CD (1 μM). Then, cells were transferred to a JPK BioCell (JPK, Berlin, Germany) and covered again with VLE-RPMI supplemented with the respective inhibitor (concentration as used for washing).

AFM force-distance measurements

For each donor and treatment (e.g. treatment with FMLP, VAS etc.), 10 - 15 neutrophils were probed by FVMs (7 μm x 7 μm, 12 x 12 FDCs) within the measurement time of one hour. The measurements were carried out in

[4]NADPH: nicotinamide adenine dinucleotide phosphate

a JPK BioCell (JPK, Berlin, Germany) using a JPK NanoWizard 3 (JPK, Berlin, Germany). The approach velocity was set to 10 μm/sec in order to decrease the measurement time of the FVMs. Nevertheless, no significant hydrodynamic effects were observed in test measurements on the glass substrate (data not shown). All measurements were carried out at room temperature $T_r = 24°C$. This was needed in order to decelerate cellular processes such as cytoskeleton rearrangement after the incubation. The used cantilevers showed spring constants between 0.009 N/m and 0.031 N/m which were determined using the methods of Butt, Sader and Cleveland as implemented by Block et al. [105, 106, 110, 109] (see Chapter 4.2.3). Disturbed measurements were excluded from the statistics by using only FDCs showing small Least Mean Squares (LMS) errors ($\epsilon_{lim}^{(0)} < 30$ pN, $\epsilon_{lim}^{(1)} < 25$ pN, $\epsilon_{lim}^{(2)} < 90$ pN) with respect to the determined fit function (see Chapter 5.5.4).

4.3.4 Measurements on Human Umbilical Vein Endothelial Cells (HUVECs)

Please note, HUVEC culture, flow chamber experiments, transduction and transfection (as described in the following) were carried out by Malte Pennewitz and Dipl.-Chemist Anne Strohbach (University Medicine of the Ernst-Moritz-Arndt-University, Greifswald, Germany). Moreover, after training and under the guidance of the author, Malte Pennewitz carried out the AFM measurements on HUVECs.

Culture and treatment of HUVECs

Using collagenase type II (Biochrom, Berlin, Germany), umbilical cords were digested. Then, HUVECs were isolated and cultivated as described previously by Jaffe et al. [116]. The cells were cultured in endothelial cell growth medium (MCDB 131; Pan Biotech, Aidenbach, Germany) supplemented with 10% Fetal Bovine Serum (FBS; Life Technologie, Carlsbad, CA, USA) at 37°C and with 5% CO_2 in a humidified incubator. The investigation conforms to the principles outlined in the Declaration of Helsinki for the use of human tissues (World Medical Association, 2013).

Flow chamber experiments

For the experiments, cells were seeded at passage three at a density of $1 \cdot 10^5$ cells on glass cover slips (diameter = 24 mm; VWR, Radnor, PA, USA) and cultured until reaching confluence. Two different setups were used for Endothelial Shear Stress (ESS) experiments. For ESS-exposure, cover slips were placed in a parallel-plate Flow Chamber System (FCS; Provitro, Berlin, Germany) perfused with 10% MCDB 131 at 37°C and 5% CO_2. Subsequently, cells were either kept under static conditions or subjected to physiological laminar shear stress using a tubing pump (IPC 4; Ismatec, Wertheim, Germany).

For immunohistochemical staining and live cell imaging, HUVECs were seeded at a density of $3 \cdot 10^5$ cells/mL in tissue culture treated μ-Slides (μ-Slide 0.8 Luer; Ibidi, Martinsried, Germany). Prior to flow experiments, cells were starved on endothelial cell growth medium (MCDB 131) supplemented with 0.5% Fetal Bovine Serum (FBS; Invitrogen, Carlsbad, CA, USA) overnight. The μ-Slides were perfused using a suitable air pressure pump system (Ibidi, Martinsried, Germany). Air bubbles were removed by perfusion of the system 10 min before experiments. The shear stress exposure was ramped in both experimental setups in intervals of 10 min (37 mN/m^2, 74 mN/m^2, 112 mN/m^2 up to 150 mN/m^2) until the final shear level of 150 mN/m^2 was reached and kept for three hours. Control cells not exposed to shear stress were kept under identical conditions.

Transduction for immunocytochemical staining

Two adenoviral vectors were used for immunocytochemical staining of the Cytoskeleton (CSK) and the APLNR receptor. Cells plated in μ-Slides were transduced with rAVCMV-LifeAct-TagRFP (Ibidi, Matrinsried, Germany) for F-actin staining, as previously described [117]. Furthermore, an Ad5-CMV-APLNR-tGFP vector (Siron Biotech, Martinsried, Germany) was used to detect APLNR. HUVECs were incubated with a mixture of virus particles and endothelial cell growth medium (MCDB 131; Pan Biotech, Aidenbach, Germany; + 10% FBS) for 24 hours in a humidified incubator using a Multiplicity of Infection (MOI)[5] of 70. Thereafter, Hank's Buffered Salt Solution (HBSS; Life Technologies, Carlsbad, CA, USA) was used to rinse the cells, and

[5]MOI: the number of virus particles per cells (infection target)

endothelial cell growth medium was added to the flow channel.

Transfection for APLNR-Knock Down (KD)

For AFM experiments, HUVECs were seeded on glass cover slips (diameter = 24 mm; VWR, Radnor, PA, USA) in 6-well plates. There they grew until 50% of confluency in 2 mL of endothelial cell growth medium (MCDB 131; Pan Biotech, Aidenbach, Germany; + 10% FBS)/well. Thereafter, the cells were transfected with APLNR specific small interfering RNA (siRNA) in serum-reduced[6] Opti-MEM I Medium (Life Technologie, Carlsbad, CA, USA). For this purpose 30 pM RNA interference[7] (RNAi) duplex were diluted in 250 μL Opti-MEM I, and 5 μL of Lipofectamine RNAiMAX (Invitrogen, Carlsbad, CA, USA) were diluted in 250 μL Opti-MEM I. Next, the diluted RNAi duplex was combined with the diluted Lipofectamine RNAiMAX and incubated for 15 min at room temperature, resulting in the **formation of siRNA duplex-Lipofectamine RNAiMAX complexes**. This solution was added to the endothelial cell growth medium in each well, which resulted in a final siRNA-concentration of 10 nM. Control HUVECs were incubated with Lipofectamine RNAiMAX complexes. During six hours of incubation in a CO_2 incubator, the cells were mixed gently at 37°C. Afterward, the transfection mixture was replaced by endothelial cell growth medium (MCDB 131; Pan Biotech, Aidenbach, Germany; + 10% FBS), and the cells were incubated for another 42 hours before flow experiments.

For flow experiments in μ-Slides, the HUVECs were seeded inside the flow channel of μ-Slides (0.8 Luer) as described above. The cells were cultured until sub-confluency ($\approx 80\% - 90\%$), and then transfected with APLNR specific siRNA in serum-reduced Opti-MEM I Medium. Therefore, 12.6 pM RNAi duplex were diluted in 50 μL Opti-MEM I, and 2 μL of Lipofectamine RNAiMAX were also diluted in 50 μL Opti-MEM I. After combining both solutions and incubating them for 15 min at room temperature 150 μL endothelial cell growth medium (MCDB 131, Pan Biotech, Aidenbach, Germany) were added. Then the solution was used to replace the endothelial cell growth medium inside the μ-Slide (I Luer). The resulting siRNA concentration was 50 nM. The cells were then incubated for 6 hours at 37°C in a humified CO_2 incubator. Con-

[6] serum-reduced: without FBS, as this would hinder the transfection
[7] RNA interference: the inhibition of gene expression *via* RNA

trol cells were incubated with Lipofectamine RNAiMAX complexes. Finally, the HUVECs were incubated for 42 hours in endothelial cell growth medium (MCDB 131, Pan Biotech, Aidenbach, Germany; + 10% FBS) before flow experiments.

Immunohistochemical staining

After flow experiments in the μ-Slides, the cells were rinsed with HBSS to flush away the rest of media. Then, the HUVECs were fixed immediately with HistoFix (Roth, Karlsruhe, Germany) for 12 min and washed twice with Phosphate Buffered Saline (PBS; PAA, Fairfield, CT, USA) containing 1% of Bovine Serum Albumin (BSA; Roth, Karlsruhe, Germany). Afterward, the HUVECs were permeabilized with 0.2% of Triton-X-100 (Roth, Karlsruhe, Germany) in PBS for 10 min and then washed and blocked for at least 30 min with 1% of BSA containing PBS. Further, samples were incubated with primary antibodies solubilized in blocking solution over night at 4°C. Anti-APLNR (R&D, Minneapolis, MN, USA) was used in this case. After washing three times with blocking solution, the cells were incubated with Anti-mouse IgG-NL 557 (R&D, Minneapolis, MN, USA) secondary antibodies for one hour at room temperature. Then the HUVECs were washed for three times with cold blocking solution, their nuclei were stained with DAPI (1:10000; Roth, Karlsruhe, Germany) and reservoirs were covered, after the flow channel was filled with PBS.

Live cell imaging and Confocal Laser Scanning Microscopy (CLSM)

For live cell imaging, HUVECs were seeded in μ-Slides (I Luer) and cultured until confluency. Then the cells were transduced with rAVCMV-LifeAct-TagRFP and Ad5-CMV-APLNR-tGFP (MOI 70) as already described above. After rinsing and replacing the transduction-media by endothelial cell growth medium containing 2 drops/mL NucBlue (Invitrogen, Carlsbad, CA, USA) for nucleus staining, slides were placed inside a stage top incubator (Spectra Services, Ontario, NY, USA) at 37°C. Then, the HUVECs were examined using a 63x water immersion objective of a Leica SP5 confocal microscope (Leica Microsystems, Wetzlar, Germany). A 405 nm laser line was used for 4',6-diamidino-2-phenylindole (DAPI)[8], a 488 nm line for Green Fluorescent

[8]DAPI: mainly binds to adenine and thymine in the DNA

Protein (GFP) and a 559 nm line for Red Fluorescent Protein (RFP). The cells were observed for three hours while performing z-stacks (stack-height: 500 nm) in defined time intervals of 15 min (resolution: 512 x 512 pixels). Please note, HUVEC live cell imaging and CLSM were carried out by Dr. Raghavendra Palankar (ZIK HIKE, Greifswald, Germany).

For flow generation, the ibidi pump system was used (as described above). During the experiment, the fluidic unit with mounted perfusion sets was placed inside a μ-Galaxy Cell Culture Incubator (Eppendorf, Hamburg, Germany) next to the microscope. The tubing was connected to the μ-Slide through a rear port of the incubator. The onset of flow was ramped in 10 min steps while imaging (37 mN/m^2, 74 mN/m^2, 112 mN/m^2 up to 150 mN/m^2).

For investigations of APLNR-KD HUVECs, cells were plated in μ-Slides (I Luer), grown till 50% of confluency and transfected with APLNR specific siRNA as described above. Then the transfection media was exchanged and the cells were transduced with rAVCMV-LifeAct-TagRFP (as described above) for the investigation of their F-actin-structure. After 24 hours incubation with the virus, the transduction media was replaced with endothelial cell growth medium and live cell imaging under perfusion was carried out as described above.

To investigate the mean signal intensity of certain structures labeled with fluorescence dyes, the optical data was exported and used for a maximum intensity projection in ImageJ. In live cell imaging data sets, a constant Region Of Interest (ROI) was defined, covering the perinuclear area and a part of the cell periphery to monitor the signal intensity over time. The values of ten representative cells were calculated in each experiment by three independent setups. In previously fixed cells, a freehand tool was used to select the cell boundary and cover the entire cell area with an appropriate ROI to calculate the mean signal intensity of virus-transduced GFP-signal and antibody stained signal. To analyze the volume and number of vinculin spots, ImageJ with the Particle Analyzer Plugin "*Object Counter 3D*" and Imaris were used for the investigation of 3D-projections of the CSK.

AFM force-distance measurements

FVMs (100 μm x 100 μm, 20 x 20 FDCs) were carried out at 37°C in endothelial cell growth medium (MCDB; Pan Biotech, Aidenbach, Germany) in a JPK BioCell (JPK, Berlin, Germany) using a JPK NanoWizard 3 (JPK, Berlin, Germany). The cantilever spring constants k_c (0.023 - 0.028 N/m) were determined using the methods of Butt, Sader and Cleveland as implemented by Block et al. [105, 106, 110, 109] (see Chapter 4.2.3). FVMs were analyzed by converting the AFM FDCs of the FVMs into force-indentation curves using Eq. 4.1 and Eq. 4.2. Subsequently, these curves were fitted to the simple Hertz model (Eq. 2.43) or the thin layer model Eq. (2.47) of Dimitriadis et al. For this purpose, the local cell thickness h was determined by comparing the contact points z_0 of FDCs measured on the rigid glass substrate and on the HUVECs. For the statistics concerning the cell elasticity on the thickest cell regions respectively, five FDCs (the FDC on the cell apex and its four closest neighbored FDCs) for each cell have been taken into account. Disturbed measurements were excluded from the statistics by using only FDCs showing small least mean squares (LMS) errors
($\epsilon_{lim}^{(0)} < 30$ pN, $\epsilon_{lim}^{(1)} < 25$ pN, $\epsilon_{lim}^{(2)} < 90$ pN) with respect to the determined fit function (see also Chapter 5.5.4).

4.4 Figures and numerical calculations

Barplots have been created using GraphPad Prism 5 (GraphPad Software, La Jolla, CA, USA). All other plots were made by homemade MATLAB scripts (The MathWorks, Natick, MA, USA). MATLAB was also used for all numerical calculations and for the implementation of the fitting algorithm presented in Chapter 5. All other figures were created using the free software Inkscape 0.48. Photos were taken either by the digital camera (FireWire 400 Color Industrial Camera, The Imaging Source Europe GmbH, Bremen, Germany), coupled to the AFM system, or by the Zeiss Supra 40 VP Scanning Electron Microscope (Zeiss, Oberkochen, Germany).

Chapter 5

Automated analysis of AFM Force-Distance Curves (FDCs)

5.1 Motivation and background

Commercial AFM software mostly facilitates only a semi-automatic analysis of Force-Distance Curves (FDCs). This means, the user manually has to define the 3D-scanner position z_0 (contact point) indicating the first contact between cell and AFM probe in a FDC. This involves the danger of errors in the determination of z_0 which is a critical parameter for the determination of cell thickness and the sample elastic modulus E_2 [36].

Furthermore, a manual determination of z_0 might involve high time consumptions. For example, in this thesis approximately $2.27 \cdot 10^5$ FDCs were analyzed/fitted with either the simple Hertz model (Eq. 2.43) or the thin layer model of Dimitriadis et al. [41] (Eq. 2.47). This high number of measurements was either needed to obtain reliable statistics (despite of high cell-to-cell/on-cell variations of Young's modulus E_2) or to identify cell apex positions *via* the analysis of contact points in Force-Volume Measurements (FVMs). Estimating a proper manual determination of z_0 to take 5 sec per FDC (in average), more than 315 hours of work would have been needed for this analysis.

Therefore, to analyze such large data sets reliably, it is necessary to automate the data analysis. Although an appropriate algorithm for a fully automated analysis of FDCs is under discussion in literature [34], the exact determination

of z_0 remains still challenging. The reason for this is that a FDC can be influenced by numerous systematic and non-systematic errors as for instance: baseline drift, baseline offset or non-linearities in the baseline. Additionally, for measurements in aqueous environment, as they are needed for experiments concerning the elasticity of living cells, disturbances caused by dust and cell fragments moving through the laser beam appear. To solve this problem, in this thesis robust homemade MATLAB scripts have been written, doing the complete data analysis routinely. The scripts report on the Least Mean Squares (LMS) error of the fit-function, the contact point of a FDC and the sample Young's modulus E_2.

5.2 Information in AFM FDCs

A single nanoindentation experiment is divided into two consecutive parts. In the first part, the distance between AFM cantilever and sample is decreased until the AFM probe first touches and finally presses onto the sample with increasing force. This force is limited by a maximum value F_{max}, called force setpoint. The Force-Distance Curve (FDC) resulting from this movement is called **approach curve**. The 3D-scanner position z, given in the moment of initial contact between probe and sample, is called contact point z_0. In the absence of long-range interactions, no significant force appears between probe and sample at the contact point. For this reason, the cantilever is almost not deflected at z_0. The part of the FDC after this point is called **contact area**, whereas the part before (baseline) is called **non-contact area** [36]. The contact area represents 3D-scanner positions related to significant mechanical interactions between AFM probe and sample, involving the deformation of sample and AFM cantilever. This part of a FDC contains information about the mechanical properties of the sample.

After the force setpoint F_{max} is reached, the cantilever movement is stopped and the second part of the nanoindentation experiment begins. Now, the distance between cantilever and sample is increased (probe and sample are separated) until the cantilever reaches the starting point again. The FDC resulting from this movement is called **retraction curve**. Figure 5.1a shows that in the absence of adhesive or repulsive forces and for a perfectly elastic sample, approach curve and retraction curve are overlapping and, therefore,

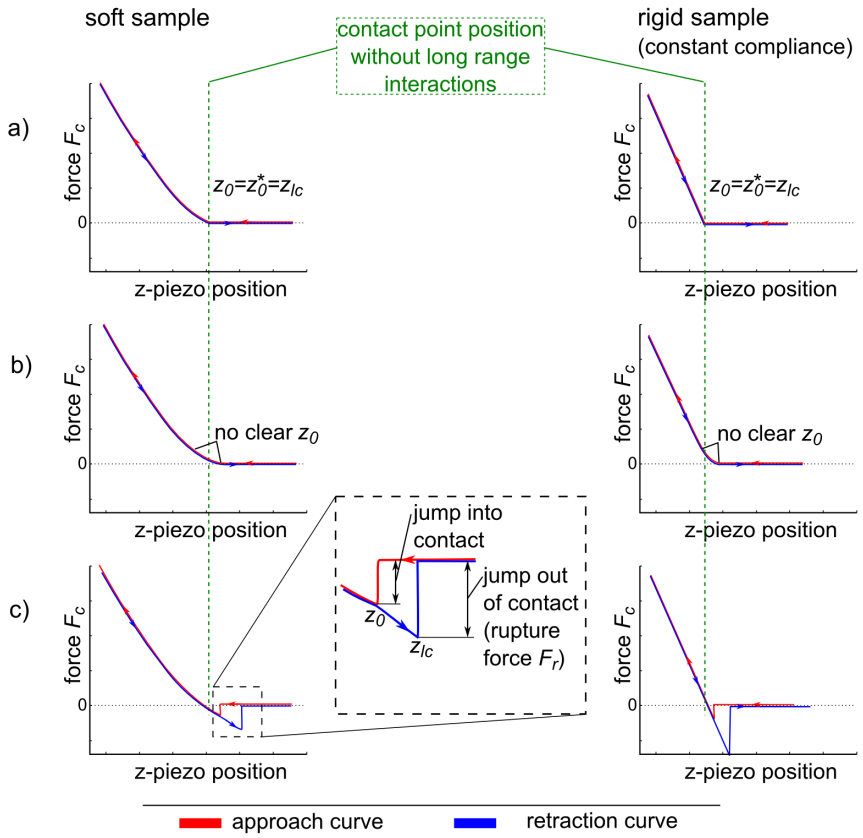

Figure 5.1: *Schematics of different shapes of Force-Distance Curves (FDCs) measured on either soft samples (left column) or hard samples (right column).* ***a)*** *On FDCs measured in the absence of repulsive or adhesive forces $z_0 = z_{lc}$ (the index "lc" indicates the* ***last contact position of the cantilever****)* ***b)*** *FDCs measured in the presence of repulsive probe-sample interactions do not show a clear contact point z_0.* ***c)*** *FDCs influenced by adhesive probe-sample interactions show a "jump into contact" and a "jump out of contact", therefore, $z_0 \neq z_{lc}$.*

the 3D-scanner position z_{lc} indicating the **last contact** between probe and sample is identical with z_0.

For the following discussion, we additionally denote the contact point appearing in a FDC without long-range interactions between probe and sample as z_0^*. In real experiments the absence of such interactions is not always given. Therefore, when the cantilever approaches the sample, adhesive (e.g. electrostatic) or repulsive (e.g. electrostatic or hydrodynamic) forces appear between sample and probe. In general, these interactions lead to a significant deflection of the cantilever for 3D-scanner positions $z \geq z_0^*$. In the case of repulsive forces (Figure 5.1b), the cantilever is bended away from the sample (positive forces

are sensed) before it comes to a mechanical contact between both. The contact point z_0 in this case is not clearly identifiable. In the case of attractive forces (Figure 5.1c) at a certain position $z_0 > z_0^*$, the attractive forces will overcome the bending forces of the cantilever. At this position, the cantilever will "*jump into contact*" with the sample before z_0^* is reached by the 3D-scanner (negative forces are sensed).

The shape of the contact area of a FDC depends strongly on the ratio of the sample elastic modulus E_2 and the spring constant k_c of the cantilever. For example, the probe of a comparatively soft cantilever will only insignificantly indent into a rigid sample (e.g. glass). Therefore, for $z \leq z_0$ the approach of the cantilever leads directly to a cantilever deflection, resulting in a sharp kink of the FDC at z_0 and a linear behavior (constant compliance; see right side of Figure 5.1a/c) of the FDC contact area. For a sample approximately matching the stiffness of the cantilever, both the cantilever and the sample will be deformed for $z \leq z_0$. This leads to a continuous transition between contact and non-contact area (left side in Figure 5.1a/c). **In the following, as long as not announced differently, all FDCs show approach curves. Because the measurements in this thesis have been carried out in (salty) buffer solution, there was no significant adhesive or repulsive interaction observed between sample and AFM probe in the approach curves. Nevertheless, some retraction curves showed rupture events, which might be caused by active adhering of the cells to the silica probe.**

5.3 FDC data pre-processing

In general, a measured FDC is a discrete function

$$F_c(z_i) \text{ with } i = 1, 2, .., m \tag{5.1}$$

giving the relation between cantilever force F_c and 3D-scanner position z. Here m is the index of the last data point of the FDC (measurement at the force setpoint F_{max}), which is approximately between $1 \cdot 10^3$ and $3 \cdot 10^3$. The exact

value of m depends (next to the sampling rate[1] and the approach velocity) on the length of the baseline, therefore, on the local sample thickness and on the elastic modulus E_2 of the sample. Before a FDC can be analyzed and its contact point z_0 and a value for E_2 can be extracted, it has to be pre-processed, to remove systematic errors. Figure 5.2 shows four steps of data pre-processing that were implemented in a homemade MATLAB algorithm. In Figure 5.2a, a typical FDC is shown. Obviously, the right side of the baseline is not linear. The inertia[2] of the cantilever, a hydrodynamic drag for measurements in liquid media or non-linearities in the z-piezo movements for long distances might be the reason for that.

Additionally, the baseline of the FDC is tilted and shows an offset with respect to the z-axes. Therefore, in a first step (Figure 5.2b) the baseline (length) is reduced by 3 μm. The number of data points in the FDC is thereby reduced and given by n rather than by m. Because the contact point z_0 and consequently the exact baseline length is still unknown, in a second step, only the first 1.5 μm of the remaining baseline are linearly fitted by a line $y(z)$. Subsequently, the force $F_c(z_i)$ in each data point of the (raw) FDC is reduced by $y(z_i)$:

$$F_c(z_i) = F_c^{raw}(z_i) - y(z_i) \text{ with } i = 1, 2, ..., n \tag{5.2}$$

This procedure removes the tilt and the offset of the baseline in first order quality (Figure 5.2c). Nevertheless, as this correction takes only the first 1.5 μm of the baseline into account, its accuracy is not sufficient. This is because even small baseline non-linearities in this region can influence the positioning of the whole corrected FDC. Therefore, a second baseline correction is needed taking the whole baseline into account. For this purpose, the contact point $z_0^{(1)}$ of the FDC is estimated in first order (as indicated by the superscripted "(1)") using a series of Mann-Whitney U Tests[3] (MWUTs). As schematized

[1] The value of 50 data points iteratively was determined to be an applicable one for the used sampling rate of 5000 data points/sec and an approach velocity of 5 μm/sec. Therefore, the broad of each interval is approximately 50 nm.

[2] If high approach velocities are used, at the beginning of the cantilever movement high accelerations appear, leading to a cantilever bending.

[3] also known as: Wilcoxon rank-sum test; please note, a simple student's t-test should not be applied instead, since usually the data of the contact area are not normally distributed.

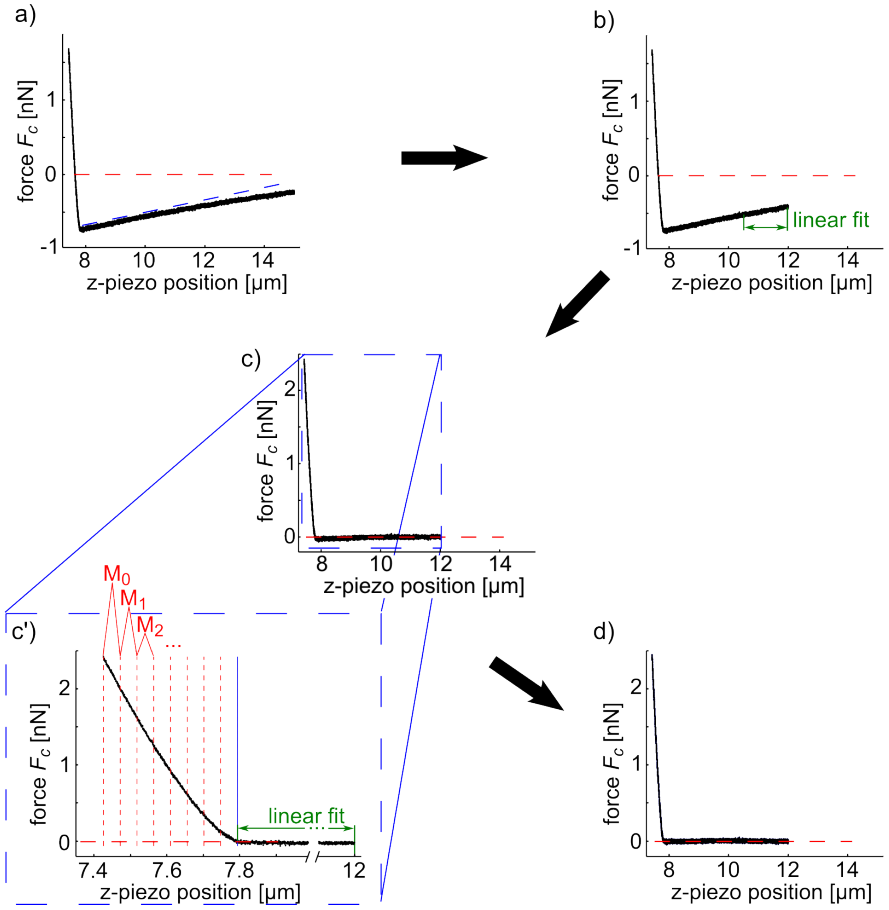

Figure 5.2: *Pre-processing of FDCs (approach curve).* ***a)*** *Typical raw data with bended and tilted baseline with respect to the z-axis (axes corresponding to the z-piezo position);* ***b)*** *the first 3 µm of the baseline is cut. The indicated interval (green) shows the part of the baseline which is linearly fitted afterward to correct for baseline drift and offset. ;* ***c)*** *FDC after first baseline correction;* ***c')*** *The contact point $z_0^{(1)}$ is identified (in a first approximation) using MWUTs for intervals $M_0, M_1, ...$ of 50 data points. Again, the indicated interval (green; 1.5 µm) shows the part of the baseline which is linearly fitted to correct a second time for baseline drift and offset;* ***d)*** *After the second baseline correction, the baseline of the FDC is optimally aligned with respect to the z-axes.*

in Figure 5.2c', the FDC is divided into half-open intervals

$$M_j = [F_c(z_{n-j\cdot 50}), F_c(z_{n-(j+1)\cdot 50})[\text{ with } j = 0, 1, 2... \tag{5.3}$$

of 50 data points, for this purpose. The first interval M_0 begins with the last point $z_n = z(F_{max})$ of the contact area and contains the last 50 data points of the FDC. Subsequently, for each pair $Q_j = (M_j, M_{j+1})$ of neighbored intervals a MWUT is carried out. The first interval pair Q_{crit} that fulfills the three

requirements

$$\begin{aligned} &\text{I} && \langle M_j \rangle > \langle M_{j+1} \rangle \\ &\text{II} && p_j < 0.05 \\ &\text{III} && F_c(z_{n-(j+1)\cdot 50}) < 4 \cdot \sigma^{(F_c)} \end{aligned} \tag{5.4}$$

is assumed to contain the exact contact point z_0. In these equations $\langle M_j \rangle$ is the median of the 50 data points in the j'th interval. The p-value of the applied MWUT is described by p_j. The standard deviation of F_c on the baseline is described by $\sigma^{(F_c)}$. Especially for measurements in liquid media, the first and the third requirement are necessary, as in some cases small cell fragments or dust particles are moving through the laser beam. This can lead to disturbances in the contact part of the FDC. These disturbances can cause a non-monotone behavior of the contact part and, therefore, result in $p_j < 0.05$, in significant distance to the true contact point z_0. After identifying Q_{crit} the value of $z_0^{(1)}$ is set to:

$$z_0^{(1)} = max(z_i) \in M_{j+1} \text{ with } j = j(Q_{crit}), \tag{5.5}$$

which is identical with the right edge data point in the Q_{crit} interval[4]. After the determination of $z_0^{(1)}$, a second linear baseline correction according to Eq. 5.2 is carried out including all data points of the baseline, inclusive $z_0^{(1)}$. After this step the baseline shows an optimal alignment with the z-axis (Figure 5.2d).

5.4 Extraction of the sample Young's modulus and the contact point from FDCs

In order to extract E_2 from a FDC $F_c(z_i)$ the first order contact point $z_0^{(1)}$ is used from the pre-processing. It can be assumed that the real contact point z_0 is within a small interval ($\pm$ 200 nm $\Leftrightarrow$ s = 200) around $z_0^{(1)}$:

$$I_- = z_{i_0-s} < z_0 < z_{i_0+s} = I_+. \tag{5.6}$$

[4]The selection of $z_0^{(1)}$ as the right edge of the Q_{crit} interval is a conservative assumption and prevents a significant influence of data points which belong to the contact area, on the second baseline correction.

Here, the index i_0 denotes the data point index corresponding to $z_0^{(1)}$, while s is an integer number, defining the interval size around $z_0^{(1)}$. The $2s+1$ possible 3D-scanner positions in this interval can be summarized in a discrete vector $\boldsymbol{z}^{(I)}$ with the elements $z_k^{(I)}$ (k = 1,2,...$2s$+1). **Please note, $\boldsymbol{i}$ is a global index running over all $\boldsymbol{n}$ elements of the FDC. In contrast $\boldsymbol{k}$ is a local index, used only for the elements within the interval $[\boldsymbol{I_-}, \boldsymbol{I_+}]$.** In order to identify z_0, for each element $z_k^{(I)}$ a Least Mean Squares (LMS) fit over the whole FDC (including the non-contact area) has to be carried out. The fit is calculated with respect to a certain contact model. In this thesis the simple Hertz model (Eq. 2.43) and the thin layer model of Dimitriadis et al. (Eq. 2.47) were used for that purpose.

As the used contact models do not take into account adhesive and attractive interactions, they predict forces only, if there is mechanical contact between AFM probe and cell. Therefore, the prediction of these models for the non-contact area is represented by a line $F_{model}(z) = 0$. Due to the data pre-processing, the FDC baseline is aligned with the z-axis. For this reason, assuming $z_k^{(I)}$ to be the contact point, the residuum $\epsilon_k^{(1)}$ between FDC (in the non-contact area) and **fit function $\boldsymbol{F_{model}(z) = 0}$** is simply given by the mean value of the absolute values of $F_c(z_i)$:

$$\epsilon_k^{(1)} = \frac{1}{i_k - 1} \sum_{i=1}^{i_k - 1} |F_c(z_i)| \tag{5.7}$$

Here and in the following equations, i_k denotes the (global) data point index of z_i corresponding to the (temporally) assumed contact point $z_k^{(I)}$. After determining the residuum of the non-contact area with respect to the contact model, hereafter the residuum in the contact area is derived. For this purpose each z_i is correlated with an indentation depth η_i ($i = 1, 2, ..., n$). The values η_i can be summarized in the vector $\boldsymbol{\eta}$ and are defined by the force-distance curve $F_c(z_i)$ and the Eqs. 4.1 and 4.2. For $i \geq i_k$ the elements of the vector $\boldsymbol{\eta}$ are given by

$$\eta_i = \eta_i(z_i) = z_i - z_k^{(I)} - d_c = z_i - z_k^{(I)} - F_c(z_i)/k_c, \tag{5.8}$$

whereas for $i < i_k$ (non-contact area) the elements are equal to zero. By the use of $\boldsymbol{\eta}$, the FDC contact area can be described in dependency of the indentation

depth:

$$F_c(z_i) \rightarrow F_c(\eta_i) \text{ for } i \geq i_k. \tag{5.9}$$

Please note, in the following chapters the function $F_c(\eta)$ is called Force-Indentation Curve (FIC). In the literature it is also called Force-displacement Curve.

For each nanoindentation experiment the elastic modulus E_2 of the sample can be assumed to be within a certain interval $[E_{min}, E_{max}]$. In the following, the accuracy ΔE describes the desired maximum error of the determination of E_2. This error strongly influences the required computational costs, as possible values of E_2 are described in a discrete vector $\boldsymbol{E}^*$ (quantization):

$$E_l^* = E_{min} + l \cdot \Delta E; \qquad l = 0, 1, ..., l_{end} \text{ with } l_{end} = (E_{max} - E_{min})/\Delta E \tag{5.10}$$

Subsequently, **assuming a certain $\boldsymbol{E_l^*}$ to be the Young's modulus of the sample and $\boldsymbol{z_k^{(I)}}$ to be the contact point**, the residuum between FDC and **fit function $\boldsymbol{F_{model}(\eta_i, E_l^*)}$** in the contact area is given by:

$$\epsilon_{k,l}^{(2)} = \frac{1}{i_{limit} - i_k + 1} \sum_{i=i_k}^{i_{lim}} |F_c(\eta_i) - F_{model}(\eta_i, E_l^*)| \tag{5.11}$$

Please note, that the residuum is calculated until a certain indentation depth η_{lim}. This indentation depth is an important parameter, because some contact models, such as the simple Hertz model, are only applicable for an indentation depth much smaller than the involved radii (cell radius R_2 and/or indenter radius R_1). Until this step, neither z_0 nor E_2 are determined, as for Eq. 5.11 these values were set to constant values (represented by $z_k^{(I)}$ and E_l^*). Moreover, the residuum of the FDC baseline (non-contact area) is not included in this equation.

In order to find E_2 (still for a fixed value of z_0), Eq. 5.11 has to be solved for all E_l^* and additionally the residuum of the FDC baseline has to be taken into account. Hence, for a certain fixed $z_k^{(I)}$ assumed to be the contact point, the best fit $F_{model}(\eta_i, E_l^*)$ with respect to the whole FDC of the cell shows the

least mean squares (LMS) residuum

$$\begin{aligned}\epsilon_k^{(0)} &= min\left(\frac{(i_k-1)\cdot\epsilon_k^{(1)}+(i_{lim}-i_k+1)\cdot\epsilon_{k,l}^{(2)}}{i_{lim}}\right)\\ &= min\left(\frac{\sum_{i=1}^{i_k-1}|F_c(z_i)|+\sum_{i=i_k}^{i_{lim}}|F_c(\eta_i)-F_{model}(\eta_i,E_l^*)|}{i_{lim}}\right)\\ &\text{with } l=0,...,l_{end}.\end{aligned} \tag{5.12}$$

Until this step, the contact point z_0 was assumed to be known, and was set to a constant value $z_k^{(I)} \in [I_-\ ,\ I_+]$. The parameter value l fulfilling Eq. 5.12 defines the sample Young's modulus E_2 assuming that $z_k^{(I)}$ is the contact point. In the last step, this assumption is skipped and both parameters l and k (describing the contact point z_0 and the sample Young's modulus E_2) are varied independently. Therefore, Eq. 5.12 has to be applied to all $2s+1$ temporary contact points $z_k^{(I)}$. Then, the optimal fit with respect to Young's modulus E_2 and the contact point z_0 (over the whole FDC) will show the LMS residuum $\epsilon^{(0)}$:

$$\epsilon^{(0)} = min\left(\epsilon_k^{(0)}\right) \quad \text{with } k=1,2,...,2s+1. \tag{5.13}$$

Please note, $\boldsymbol{\epsilon^{(0)}}$ describes the LMS value of the best fit with respect to $\boldsymbol{E_2}$ and $\boldsymbol{z_0}$ over the complete FDC. The values of $\boldsymbol{E_2}$ and $\boldsymbol{z_0}$ are precisely determined by the parameters $\boldsymbol{k}$ and $\boldsymbol{l}$ defining this LMS residuum between the fit $\boldsymbol{F_{model}(k,l)}$ and the FDC. In the following, $\boldsymbol{\epsilon^{(1)}=\epsilon_k^{(1)}}$ (LMS residuum of the baseline) and $\boldsymbol{\epsilon^{(2)}=\epsilon_{k,l}^{(2)}}$ (LMS residuum of the contact area) will be used additionally as denotations for the appearing residuals in the case of such an optimal fit $\boldsymbol{F_{model}(k,l,\eta_{lim})}$.

In order to solve Eq. 5.13 and to identify the optimal parameters l and k, the Eqs. 5.7 and 5.11 have to be solved iteratively with varied parameter values. Especially the number $N_{iter}^{(2)}$ of the iterative calculations of Eq. 5.11, required to solve Eq. 5.13, is large, as $N_{iter}^{(2)} \propto 2s$, $N_{iter}^{(2)} \propto (E_{max}-E_{min})$ and $N_{iter}^{(2)} \propto 1/\Delta E$. This indicates, that high computational costs arise, if the interval, used for the search of z_0, is large, the scanned range of Young's modulus E_2 is large or small errors ΔE are needed. For example, if $s = 200$ (the 200

data points to the right and the left-hand side of $z_0^{(1)}$ are tested for being z_0), the cell elasticity is expected to be in the range between 200 Pa and 50 kPa (a typical range for biological samples) and the allowed error $\Delta E = 1$ Pa, more than $19.9 \cdot 10^6$ iterations of Eq. 5.11 have to be calculated in order to solve Eq. 5.13.

5.5 Optimization of the fitting procedure

Due to the high computational costs of the pure algorithm presented in Chapter 5.4, it is necessary to develop optimization mechanisms, as otherwise the algorithm is practically not applicable to large data sets, similar to those that have been analyzed in this thesis.

5.5.1 Early stopping the variation of Young's modulus

The high number of iterative calculations of Eq. 5.11 can be reduced by early stopping the variation of l. In the moment when the contact area of the fitted curve F_{model} is steeper than the contact area of the force-indentation curve $F_c(\eta_i)$, it is not needed to further vary (increase) l. For this purpose, for each fit, the number N_{steep} of data points in the contact area fulfilling the condition

$$F_c(\eta_i) - F_{model}(\eta_i, E_l^*) < 0 \text{ with } i = i_k, i_k + 1, ..., l_{lim} \tag{5.14}$$

is counted. If the counted number N_{steep} is higher than $0.7 \cdot (i_{lim} - i_k + 1)$ the variation of l is stopped. The factor 0.7 in this expression was empirically determined. It defines, that more than 70% of the FDC data points (in the contact area) have to show forces F_i lower than the fit, in order to stop the variation of E_2.

5.5.2 Iterative search for the contact point

To carry out the variation of E_l^* for each 3D-scanner position, $z_k^{(I)}$ (in the interval $[I_- \ , \ I_+]$ (Eq. 5.6)) leads to high computational costs. Therefore, not every $z_k^{(I)}$ is used for that purpose. In a first step only every γ_1'th $z_k^{(I)} \in [I_- \ , \ I_+]$ is used for that variation process. Out of these $z_k^{(I)}$ the $z_k^{\min'}$ correlating with a minimum value of $\epsilon^{(0)}(k, E_l)$ is determined. This $z_k^{\min'}$ then is used as the

center of a new variation interval

$$I_{-}^{'} = z_{k-2\gamma_1}^{\min^{'}} < z_0^{(2)} < z_{k+2\gamma_1}^{\min^{'}} = I_{+}^{'} \tag{5.15}$$

instead of Eq.5.6. In this new variation interval, every γ_2'th $z_k^{(I)} \in [I_{-}^{'}\ ,\ I_{+}^{'}]$ is used for the variation of E_l^*. Again, a $z_i^{\min^{''}}$ correlating with a minimum value of $\epsilon^{(0)}(k, E_l)$ is determined and

$$I_{-}^{''} = z_{k-2\gamma_2}^{\min^{''}} < z_0^{(2)} < z_{k+2\gamma_2}^{\min^{''}} = I_{+}^{''} \tag{5.16}$$

defines the limits for the next variation process. This sequence can be repeated arbitrarily often until γ_n reaches 1 and z_0 is identified precisely (in the limits of the sampling rate). In this thesis, $\gamma_1 = 15, \gamma_2 = 10, \gamma_3 = 3, \gamma_4 = 1$ were used.

5.5.3 Iterative search for Young's modulus

The execution of the full variation of E_l^* in steps of ΔE (Eq. 5.10) for each z_k also leads to high computational costs. Therefore, an equivalent approach as shown in Chapter 5.5.2 is used for the variation of E_l^*. For this purpose, in a first approach E_l^* is varied in the interval $[E_{min}\ ,\ E_{max}]$ using steps of $\Delta E_1^{(1)}$. The parameter l minimizing $\epsilon^{(0)}(k, E_l)$ is gained from this procedure, resulting in a first approximation $E_2^{'}$ of the sample elastic modulus. This approximation then is used as the center of a new variation interval

$$E_{min}^{'} = E_2^{'} - 2 \cdot \Delta E^{(1)} < E_2 < E_2^{'} + 2 \cdot \Delta E^{(1)} = E_{max}^{'}, \tag{5.17}$$

which is used for the next variation of E_l^* with steps of $\Delta E^{(2)}$. This second variation process again results in a better approximation of E_2 which is denoted by $E_2^{''}$. Afterward, a next variation of E_l^* is carried out in the interval

$$E_{min}^{''} = E_2^{''} - 2 \cdot \Delta E^{(2)} < E_2 < E_2^{''} + 2 \cdot \Delta E^{(2)} = E_{max}^{''}, \tag{5.18}$$

using the step width $\Delta E^{(3)}$. Similar to Chapter 5.5.2, this sequence can be repeated arbitrarily often until E_2 is defined with the aimed precision ΔE. In this thesis $\Delta E^{(1)} = 250$ Pa, $\Delta E^{(2)} = 50$ Pa, $\Delta E^{(3)} = 10$ Pa, $\Delta E^{(4)} = 1$ Pa were used, aiming for a maximum error of $\Delta E = 1$ Pa.

5.5.4 FDC fitting errors

The error $\epsilon^{(0)}$ is important for the quality of the fit. If the investigated part of the cell is not an approximately homogeneous elastic medium, the measured FDC will deviate significantly from the predictions made by the used linear contact models. In this case $\epsilon^{(0)}$ will be increased. To avoid erroneous values of E_2 in the statistics, a limit value $\epsilon^{(0)}_{lim}$ defining an acceptable LMS fit was defined.

Nevertheless, in some cases a long baseline with small $\epsilon^{(1)}$ can lead to $\epsilon^{(0)} < \epsilon^{(0)}_{lim}$ even if the value of $\epsilon^{(2)}$ is unacceptably high (bad fit in the contact area). Therefore, two additional limits were defined: $\epsilon^{(1)}_{lim}$ for the non-contact area and $\epsilon^{(2)}_{lim}$ for the contact area. FDCs have only been used for the statistics, in case $\epsilon^{(0)} < \epsilon^{(0)}_{lim}$ and $\epsilon^{(1)} < \epsilon^{(1)}_{lim}$ and $\epsilon^{(2)} < \epsilon^{(2)}_{lim}$ were fulfilled. Table 5.1 shows the parameters that have been chosen for the investigation of certain cell types. In general, to fulfill the condition of the implemented contact models to use

cell type	model	$\epsilon^{(0)}_{lim}$ [pN]	$\epsilon^{(1)}_{lim}$ [pN]	$\epsilon^{(2)}_{lim}$ [pN]	η_{lim} [nm]
CFB	simple Hertz	25	22	45	300
PMN	simple Hertz	30	25	90	400
HUVEC	simple Hertz	30	25	90	300
HUVEC	thin layer model	30	25	90	300

Table 5.1: *The parameters $\epsilon^{(0)}_{lim}$ [pN], $\epsilon^{(1)}_{lim}$ [pN], $\epsilon^{(2)}_{lim}$ [pN] and η_{lim} [nm] used for the data analysis in this thesis. The used parameters are correlated with the investigated cell type (CFB: Cardiac Fibroblast; PMN: Polymorphonuclear Neutrophil; HUVEC: Human Umbilical Vein Endothelial Cell). In the column captioned by model, it is shown which contact model was used for the FDC analysis, either simple Hertz model (Eq. 2.43) or thin layer model according to Dimitriadis (Eq. 2.47).*

only small indentation depths η, the maximum fitted indentation depth η_{lim} was set to 300 nm. One exception was made in the case of Polymorphonuclear Neutrophils (PMNs), which showed a spherical shape and occasionally pronounced surface roughnesses (membrane protrusions). Here η_{lim} was set to 400 nm, in order to achieve a sufficient signal-to-noise ratio and to decrease the influence of membrane protrusions on the measurements.

5.5.5 The case of two apparent Least Mean Squares (LMS) minima with respect to the contact point position

There are some cases (in the following denoted as *"abnormal shaped curves"*) in which FDCs show two parts in their contact area: at the very beginning the slope of the curve is extremely low (part 1), whereas after some hundreds nm (part 2) the curve shows the typical course described by the simple Hertz model ($F_c \propto \eta^{3/2}$). As exemplarily shown in Figure 5.3, for this type of FDCs the position z_0 determined by the LMS fitting routine depends on the maximum indentation depth η_{lim}. Using a small indentation depth ($\eta \approx 300$ nm), two minimum LMS error positions (left and right minimum) appear in $\epsilon_k^{(0)}$, if k is varied ($k = 1, 2, ..., 2s+1$) with respect to the contact point position. Mostly in this cases, the absolute minimum position (z_0) was found at the right edge of the "*part 1*"-interval (right minimum). For FDC fits with larger indentation depth ($\eta > 500$ nm), only one LMS error minimum position appears in $\epsilon_k^{(0)}$, if k is varied. The position is similar to the left minimum in $\epsilon_k^{(0)}$, appearing for the fits with small indentation depth.

One reason for the occurrence of this type of FDCs might be given in rough cell surfaces. Such surfaces may lead to a first slight contact between probe and parts of the cell membrane (protrusions, loose cell fragments etc.) before the probe is significantly indenting the cell body. In the case of a manual FDC analysis, the user identifies such curves by eye. After this identification, a decision whether the curve is used for the statistics or not, has to be taken. If the FDC should be used, the user has to make one additional decision, as he has to decide which part of the contact area is used for the fit. Such a manual procedure is not reliable, as it includes the possibility of (human) errors. In this thesis, the aim was to treat all FDCs in the same way, in order to reduce human influences on the data analysis. Therefore, for the automatic analysis of force-distance curves showing the described "*abnormal*" behavior, the decision was made, to always fit these curves to the steeper part of the contact area (left minimum). Nevertheless, the resulting fit curves F_{model} on "*abnormal shaped curves*" had to fulfill the same strict conditions (Chapter 5.5.4) regarding the errors $\epsilon^{(0)}$, $\epsilon^{(1)}$, $\epsilon^{(2)}$ as "*normal shaped curves*", otherwise they were not included in the statistics.

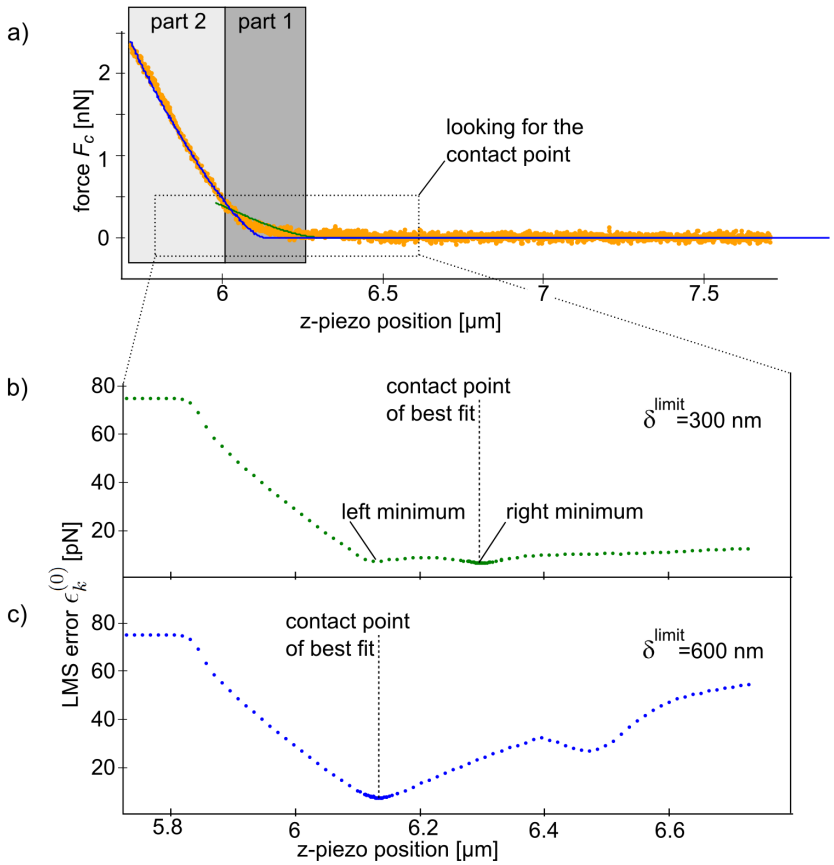

Figure 5.3: ***a)*** *An "abnormal shaped" FDC is shown. There are two parts of the contact area, a flat one (part 1) and a steeper one (part 2). In dependence of the maximum allowed indentation depth η_{lim}, different positions of z_0 are identified. Subfigures* ***b)*** *and* ***c)*** *show the minimum LMS residuum calculated by Eq.5.12 for different z_k assumed to be the contact point z_0. For small values of η_{lim} (green dotted line in graph* ***b****), there are two possible minimum LMS residuum positions z_0 for larger η_{lim}, only one clearly identifiable z_0 appears (blue dotted line in graph* ***c****). In the implemented automated analysis of the FDCs, always the left minimum (which is approximately identical with the position of z_0 for larger values of η^{limit}) is used for the fit.*

5.6 Overview - Workflow of the data analysis

Figure 5.4 gives an overview of the workflow of the whole FDC analysis algorithm. The workflow is divided into two main-parts: Data pre-processing and FDC-analysis. In the data pre-processing the FDCs are corrected for systematic errors of the measurement, such as drift and offset of the FDC baseline. The correction is carried out *via* two linear fits to the FDC baseline. After excluding the first 3 μm from the baseline, the first linear fit uses only the first 1.5 μm of the (shortened) baseline. After the determination of a first order

contact point $z_0^{(1)}$, the second linear fit uses the whole baseline.

In the consecutive FDC-analysis the FDC is fitted by a two parameter LMS fit. The fit varies the sample Young's modulus E_2 and the contact point z_0. There are three accelerating mechanisms implemented, in order to decrease the appearing computational costs (optimization) of the algorithm. The first one stops the variation of E_2, in case the contact area of the fit function F_{model} is steeper than the contact area of the FDC. The second and the third accelerating mechanism reduce computational costs by decreasing the number of values E_2 and z_0 which are tested to describe the optimal fit. In the case of "*abnormal shaped curves*" always the steeper part of the curve is used for the fit. In general, only fits with low LMS residuals/errors $\epsilon^{(0)}$, $\epsilon^{(1)}$, $\epsilon^{(2)}$ are used for the statistics.

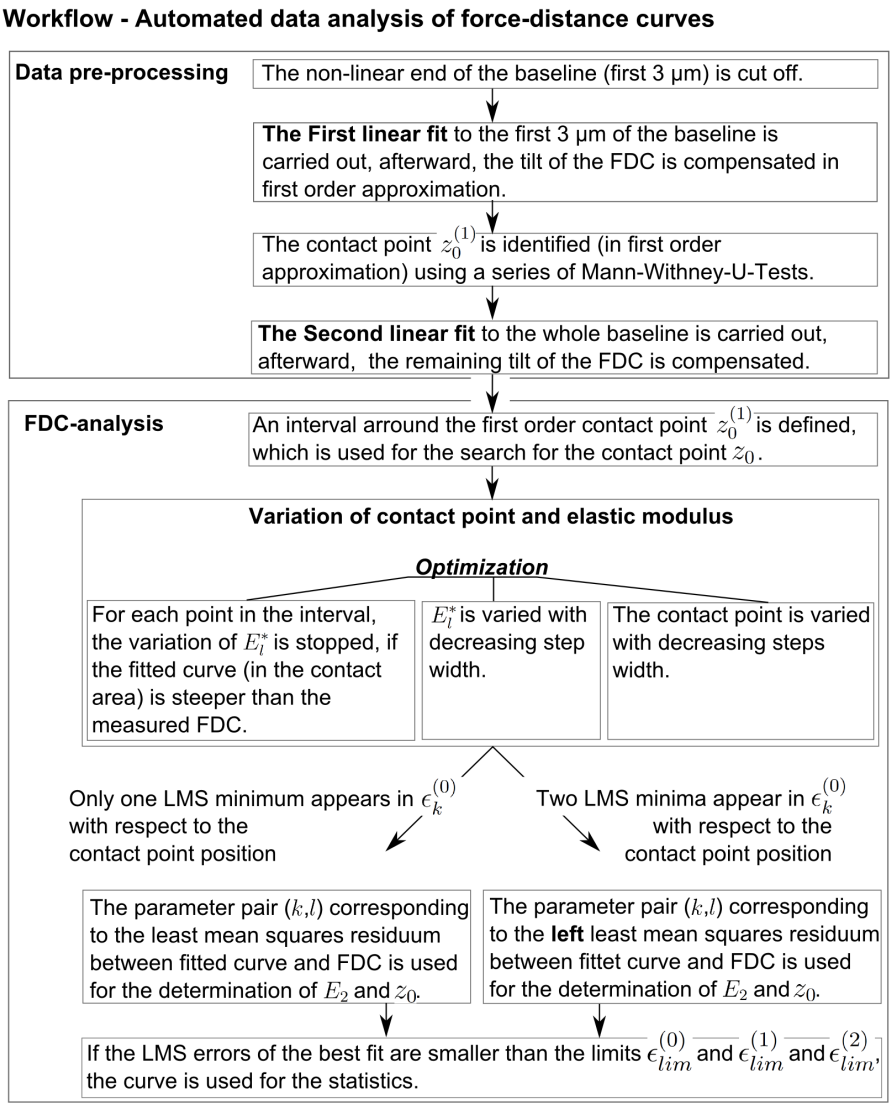

Figure 5.4: *The workflow of the implemented FDC analysis. First, in a data pre-processing, the FDC is corrected for baseline drifts and a baseline offset. A first approximation* $z_0^{(1)}$ *of the contact point is part of this pre-processing. This approximation is used in the following FDC-analysis, as center point of a variation interval used for the search for the real contact point* z_0*. In the FDC-analysis, contact point and elastic modulus are varied until the LMS errors of the fit function are minimal. The variation process uses three optimization procedures concerning the range and the step width of tested elastic moduli as well as the step with of tested contact points. In case two LMS minimum positions appear in the analysis (with respect to the contact point position), always the left one is used as contact point. At the end of the procedure, only FDCs fulfilling quality standards (least mean square residuals between fit and measured data), determined by the parameters* $\epsilon_{lim}^{(0)}$ *[pN],* $\epsilon_{lim}^{(1)}$ *[pN],* $\epsilon_{lim}^{(2)}$ *[pN] (Table 5.1), are used for the statistics.*

Chapter 6

Derivation of a novel *mixed double contact model* for spherical cells and cell-like particles

6.1 Motivation and background

Atomic Force Microscopy (AFM) has become an important tool for probing the mechanical properties of cells and microparticles [21, 118, 119]. For certain cell types, AFM measurements have revealed changes in the cell elasticity as a consequence or as a major reason for diseases [22, 13, 17]. Moreover, the influence of drugs and chemicals on the cell elasticity has been extensively studied [19, 120]. Most studies have been carried out on the elasticity of comparatively flat adhered cells, such as fibroblasts on glass substrates. For some cell types, their shape, activation status and elasticity have been reported to be correlated [121, 122]. Cells, such as non-activated human neutrophils show a spherical shape *in vivo*, but tend to activate and spread, in case they come in contact with certain materials (e.g. glass or silicon nitride). Substrate coatings (e.g. Polyethylene Glycol (PEG)) or hydrogels (e.g. Poly(2-hydroxyethyl methacrylate) (PolyHEMA)) are able to prevent cells from adhering to substrates [123, 124]. Some substrates have been shown to slow down cell activation by cell-substrate interactions. This allows to keep the cells *ex vivo* in a spherical shape [121, 123, 125]. It is important (especially for clinical studies) to analyze the elasticity of such cells *ex vivo* in their native-like spherical shape. This increases the alienability of findings to the *in vivo* situation.

For spherical cell-like microparticles, AFM nanoindentation experiments allow to determine the elastic properties of particles [126, 127]. This yields insight into particle behavior under normal and shear stress. Moreover, the knowledge of particle elastic properties is needed to understand adhesiveness, colloidal stability and other important material parameters [128]. The study of these parameters is obligatory for the improvement of applied particles, such as particles for drug delivery [129, 130, 128].

The results of the following investigation are applicable to soft spherical cells as well as to soft spherical microparticles. **For this reason, in the following the sample is called cell or cell-like particle, emphasizing this double applicability.**

During a nanoindentation experiment on a spherical cell-like particle, mainly two regions of the particle get deformed: *i)* its top region, which is deformed by the AFM probe/indenter and, *ii)* its bottom region, which is compressed by the substrate. Cells can be highly compliant (50 Pa - 500 Pa). Also microparticles based on polymer gels or microcapsules can show compliances in that range. In the case of such soft objects, interactions with the substrate can deform the cell bottom side [55]. For example, adhesion forces and even the particle weight force can lead to significant pre-deformations of the cell bottom side. This is because adhesion and in some cases gravity forces might be in the same scale like the cantilever force needed to indent into a soft cell-like particle. Nevertheless, in studies concerning the elasticity of spherical cells, it is mostly assumed that the compression appears only in the top region of the cell [44]. For this reason, single-contact models, such as the simple Hertz model (Eq. 2.43), are used for the analysis of the Force-Distance Curves (FDCs) [40]. This can lead to significant errors in the determination of the cell Young's modulus E_2 [102]. Consequently, for an accurate determination of E_2, an appropriate model concerning cell top and bottom deformation has to be applied.

This problem is further increased due to the use of large AFM probes, in order to improve the signal to noise ratio of the AFM measurement. The use of large AFM probes/indenters involves increased deformations of the cell bottom side. Moreover, in some cases large AFM probes are also used to reduce

a sliding/rolling of spherical non-adhered cells which might appear under the load of the AFM cantilever [44]. Such a movement leads to additional errors in the determination of Young's modulus E_2 from the resulting FDCs. Well-like substrates with vertical walls have been shown to be useful in order to prevent such a cell movement during the measurement [44]. Nevertheless, because the cell size scatters, it is difficult to have the perfect well/deepening size for each individual cell. Therefore, it is difficult to apply this approach to a whole cell population, like it is needed in clinical studies. Despite of the substrate geometry, it was shown that the sliding of the cells can also be suppressed by a wedged cantilever [45] having a tip geometry which equalizes the angle φ between cantilever and substrate. This setup prevents the appearance of lateral forces. Therefore, during the indentation experiment, the cell is compressed between two parallel planes [131].

However, as mentioned above, large AFM probes/indenters, such as Colloidal Probes (CPs) or wedged cantilevers involve significant deformations on the bottom side of the cell, that have not been considered sufficiently. The *mixed double contact model*, derived here, overcomes this problem by also taking into account the deformation of the cell bottom side. Hereafter, the new *mixed double contact model* is derived and a theoretical analysis of the compressions appearing in a spherical cell during a nanoindentation experiment is presented.

Regardless of the biological context of this work, as the developed contact theory is a general one, it can be applied to any macro- and microscopic homogeneous elastic spherical particle.

6.2 Derivation of the novel *mixed double contact model*

For the following calculations, Young's modulus E_1 of the AFM probe/indenter and Young's modulus E_3 of the substrate are assumed to be much larger than the typical Young's modulus E_2 of cells:

$$E_1, E_3 >> E_2, \tag{6.1}$$

what is given for the most experimental setups[1]. Further, E_2^* is defined as $E_2/(1-\nu_2^2)$, with ν_2 being the Poisson's ratio of the cell. Hence, in the simple Hertz model (Eq. 2.43) E_{12} can be expressed by E_2^* and the model converges to:

$$\eta_{12}(F_c) = \left(\frac{3F_c}{4E_2^*} \cdot \frac{1}{\sqrt{R_{12}}}\right)^{2/3}. \tag{6.2}$$

Here F_c denotes the cantilever force, as in the following the simple Hertz model is used to describe the deformations appearing in the top region of the cell-like particle. Furthermore, the Johnson-Kendall-Roberts (JKR) model (Eq. 2.46) is used to describe the contact between cell bottom side and substrate. Considering Eq. 6.1 also for the JKR model, the model converges to:

$$\eta_{32}(F_{JKR}) = \left[\frac{3\left(F + 6\gamma\pi R_{32} + \sqrt{12\gamma\pi R_{32}F + (6\gamma\pi_{32})^2}\right)}{4E_2^* R_{32}^{1/2}}\right]^{2/3} \tag{6.3}$$
$$\text{with } \frac{1}{R_{32}} = \frac{1}{R_3} + \frac{1}{R_2}$$

Similar to the simple Hertz model, the JKR model describes the force-displacement relation between two elastic homogeneous spheres (here: cell and substrate) with the radii R_2 and R_3. The JKR model additionally takes into account attractive forces between these spheres, represented by 2γ which is the surface energy of both spheres per unit area. Equivalently to the simple Hertz model, E_2 and E_3 describe the elastic modulus of the cell and the substrate, whereas ν_2 and ν_3 denote their Poisson's ratios.

Because of Newton's law: "*action equals to reaction*", for slow (quasi-stationary) indentation processes, the indentation η_{12} between AFM probe/indenter and the top of the cell can only appear, if the cantilever force F_c, the gravity force F_g of the cell and the adhesive force F_γ between cell and substrate is balanced by other forces (equal in magnitude, opposite in direction). Generally, these correspond to the normal force F_s from the substrate and the buoyant force F_b of the liquid medium, which might surround the cell. This force equilibrium

[1] Typically indenter and substrate materials are silicon nitride (280 - 290 GPa) or silica with Young's moduli in the range of GPa [132], whereas cells show Young's moduli between approximately 50 Pa [44] and 100 - 300 kPa [21, 133].

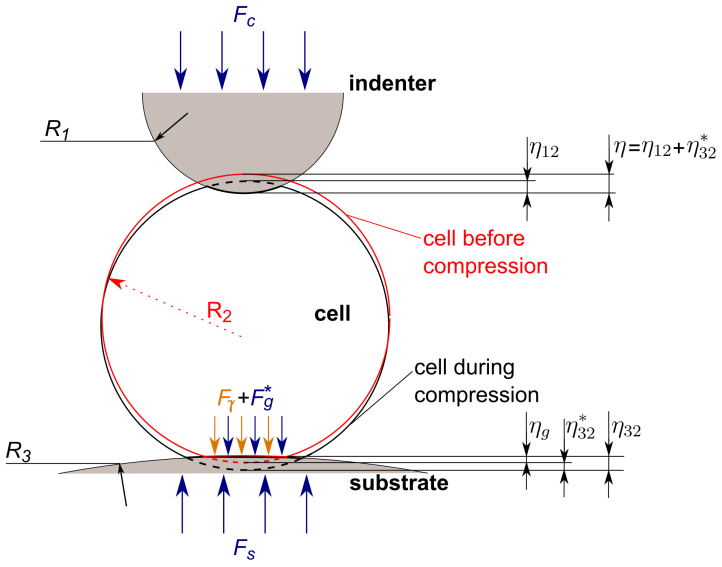

Figure 6.1: *Schematics of a nanoindentation experiment and the appearing forces for the case of spherical cells. The AFM probe/indenter with the radius R_1 presses from above with the force F_c on the highest point (apex) of the spherical cell, while an inverse force F_s raises from the substrate, pushing it into the cell bottom region. F_s is larger than F_c, since the cell weight force F^*_g and the adhesive force F_γ has to be balanced additionally. The cell radius is given by R_2 and the substrate radius is R_3. During the indentation process, the apex of the cell moves by the sum η of top and bottom indentation, which are caused by F_c. The deformation due to F^*_g and F_γ takes place before the measurement and is not sensed by the AFM.*

is described by

$$\begin{aligned} &F_c + F^*_g + F_\gamma + F_s = 0 \text{ with} \\ &F^*_g = (F_g - F_b) = \frac{-4(\rho_{cell} - \rho_{amb})\pi}{3} R_2^3 g = \frac{-4\Delta\rho\pi}{3} R_2^3 g. \end{aligned} \tag{6.4}$$

A schematic on this is shown in Figure 6.4. Here ρ_{cell} and ρ_{amb} denote the mass density of the cell and the ambient media, whereas g describes the acceleration due to gravity. The resulting weight force of the cell considering the buoyancy F_b is described by F^*_g. Therefore, during the compression of the upper part of the cell, also a compression of its bottom part takes place. For a small indentation depth, it can be assumed that the upper cell deformation is independent from the bottom cell deformation, in the sense, that the strain fields created by both compressions do not overlap. Therefore, **the measurement is more a two contact problem** than a single contact problem. As a consequence, in case the spherical indenter is pressed into the upper half of the cell, an indentation described by Eq. 6.2 appears. Additionally, on the

bottom side of the cell, the substrate with the radius R_3 compresses the cell, leading to an indentation

$$\begin{aligned}\eta_{32} &= \eta_c(F_c, F_\gamma) + \eta_{g\gamma}(F_g^*, F_\gamma) \\ &= \left[\frac{3\left(F_c + F_g + 6\gamma\pi R_{32} + \sqrt{12\gamma\pi R_{32}\left(F_c + F_g^*\right) + \left(6\gamma\pi R_{32}\right)^2}\right)}{4E_2^* R_{32}^{1/2}}\right]^{2/3}.\end{aligned} \tag{6.5}$$

The bottom indentation η_{32} is the sum of two compressions, the compression due to the weight force and adhesive force $\eta_{g\gamma}(F_g^*, F_\gamma)$ and the compression due to the cantilever force $\eta_c(F_c, F_\gamma)$, which might also be influenced by adhesion. The compression $\eta_{g\gamma}(F_g^*, F_\gamma)$ takes place before the measurement. Therefore, this compression cannot be sensed by the AFM. Due to this fact, the correct force indentation law for the bottom side of the cell is given by

$$\begin{aligned}\eta_{32}^* &= \eta_{32} - \eta_{g\gamma}(F_g^*, F_\gamma) \\ &= \left[\frac{3\left(F_c + F_g^* + 6\gamma\pi R_{32} + \sqrt{12\gamma\pi R_{32}\left(F_c + F_g^*\right) + \left(6\gamma\pi R_{32}\right)^2}\right)}{4E_2^* R_{32}^{1/2}}\right]^{2/3} \\ &- \left[\frac{3\left(F_g^* + 6\gamma\pi R_{32} + \sqrt{12\gamma\pi R_{32}F_g^* + \left(6\gamma\pi R_{32}\right)^2}\right)}{4E_2^* R_{32}^{1/2}}\right]^{2/3}.\end{aligned} \tag{6.6}$$

For a certain cantilever force F_c the absolute movement η of the cell apex is the sum of top indentation η_{12} and bottom indentation η_{32}^* (see Figure 6.2).

Thus, the force indentation law sensed by the AFM cantilever is given by

$$\begin{aligned}\eta &= \eta_{12} + \eta_{32}^{*} \\ &= \left(\frac{3F_c}{4E_2^*} \cdot \frac{1}{\sqrt{R_{12}}}\right)^{2/3} \\ &+ \left[\frac{3\left(F_c + F_g^* + 6\gamma\pi R_{32} + \sqrt{12\gamma\pi R_{32}\left(F_c + F_g^*\right) + \left(6\gamma\pi R_{32}\right)^2}\right)}{4E_2^* R_{32}^{1/2}}\right]^{2/3} \\ &- \left[\frac{3\left(F_g^* + 6\gamma\pi R_{32} + \sqrt{12\gamma\pi R_{32}F_g^* + \left(6\gamma\pi R_{32}\right)^2}\right)}{4E_2^* R_{32}^{1/2}}\right]^{2/3} .\end{aligned} \tag{6.7}$$

This implicit equation is called *mixed double contact model* in the following and gives the most general and accurate description presented so far. Please note, Eq. 6.7 is not invertible to $F_c(\eta)$ as, for example, the simple Hertz model. This requires that the user fits the force-indentation curves to $\eta(F_c)$. Nevertheless, the *mixed double contact model* could be simplified for some experimental conditions. For example, in the absence of gravity forces, this equation reduces to

$$\begin{aligned}\eta &= \eta_{12} + \eta_{32}^{*} \\ &= \left(\frac{3F_c}{4E_2^*} \cdot \frac{1}{\sqrt{R_{12}}}\right)^{2/3} \\ &+ \left[\frac{3\left(F_c + 6\gamma\pi R_{32} + \sqrt{12\gamma\pi R_{32}F_c + \left(6\gamma\pi R_{32}\right)^2}\right)}{4E_2^* R_{32}^{1/2}}\right]^{2/3} \\ &- \left[\frac{9\gamma\pi}{E_2^*}\right]^{2/3} \cdot R_{32}^{1/3}\end{aligned} \tag{6.8}$$

which is referred to as *simplified mixed double contact model* in the following. Furthermore, if no adhesive forces appear between cell bottom side and

substrate, the *mixed double contact model* converges into Eq. 6.9:

$$\begin{aligned}\eta &= \eta_{12} + \eta_{32}^{*} \\ &= \left(\frac{3F_c}{4E_2^*}\cdot\frac{1}{\sqrt{R_{12}}}\right)^{2/3} \\ &+ \left(\frac{3}{4E_2^*}\cdot\frac{1}{\sqrt{R_{32}}}\right)^{2/3}\cdot\left[(F_c+F_g^*)^{2/3} - F_g^{*2/3}\right].\end{aligned} \tag{6.9}$$

This equation is called *double contact model* in the following and describes the top and the bottom deformation of the cell with the help of the simple Hertz model. Furthermore, Eq. 6.7 changes for negligible compressions $\eta_{g\gamma}$, i.e. in the limit of very stiff or very small cells or cell-like particles to

$$\begin{aligned}\eta &= \eta_{12} + \eta_{32} \\ &= \left[\frac{3F_c}{4E_2^*\sqrt{R_{12}}}\right]^{2/3}\cdot\frac{1}{\psi} \text{ with } \psi \;= \frac{R_{32}^{1/3}}{R_{12}^{1/3}+R_{32}^{1/3}},\end{aligned} \tag{6.10}$$

which in the following is called *simplified double contact model*. The *simplified double contact model* does not take into account the pre-deformation of the cell due to cell-substrate interactions, therefore, the initial contact between particle and substrate is described by a point. In the special cases of either $R_1 = R_3 = \pm\infty$ ($\psi = 1/2$; parallel plate compression) or $R_3 = \pm\infty$ (particle on a flat substrate) this simplified equation is already known in the literature [134, 135]. Nevertheless, in general, Eq. 6.10 is the simple Hertz model, but corrected by the factor $1/\psi$. In order to simplify the description: in the following, the *mixed double contact model*, the *simplified mixed double contact model* and the *double contact model* are classified under the term *pre-deformation models*. Furthermore, the pre-deformation models and the *simplified double contact model* (Eq. 6.10) are classified under the term *double contact models*.

6.3 Comparison of AFM Force-Indentation Curves (FICs) measured on pre-deformed and non-pre-deformed cell-like particles

In order to study the influence of a pre-deformation of the cell bottom side on the shape of Force-Indentation Curves (FICs), hereafter the four *double*

contact models are compared with the simple Hertz model. Exemplarily, Figure 6.2a shows FICs predicted by the different contact models for the case of parallel plate mechanics measurements on a soft cell-like particle with R_2 = 20 μm and a Young's modulus E_2 of 50 Pa.

In general, for a fixed Young's modulus E_2 the FICs of the pre-deformation models are situated between the curves of the simplified *double contact model* and the simple Hertz model. Thereby, the simple Hertz model shows always the lowest slope, whereas the *simplified double contact model* shows the steepest slope. *Vice versa*, analyzing a measured FDC curve with these five models, E_2 determined by the simple Hertz model is always the smallest, while E_2 determined by the *simplified double contact model* (Eq. 6.10) results in the highest value. The pre-deformation models give values in between these extremes.

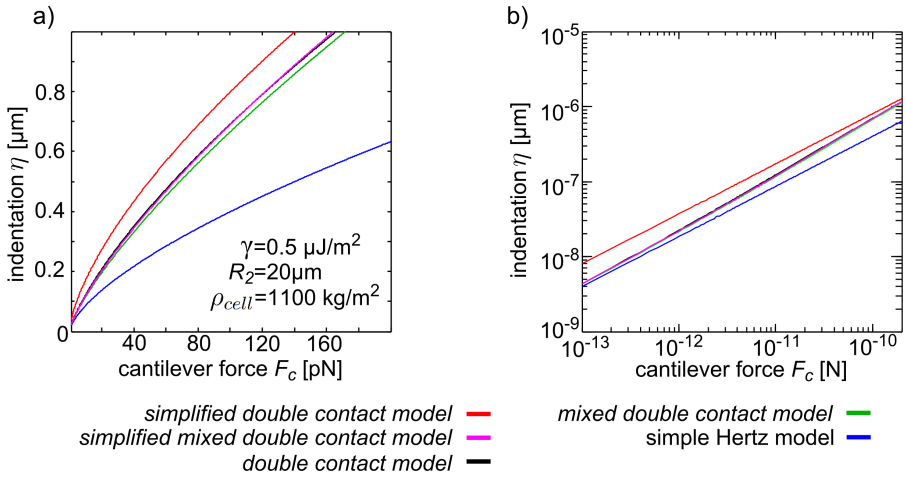

Figure 6.2: ***a)*** *Predicted Force-Indentation Curves (FICs) for the different contact models assuming parallel plate compression on a soft spherical particle with R_2 = 20 μm and a Young's modulus E_2 of 50 Pa. The FICs of mixed double contact model (Eq. 6.7), simplified mixed double contact model (Eq. 6.8) and double contact model (Eq. 6.9) (pre-deformation models) are always laying between the curves of the simple Hertz model and the simplified double contact model (Eq. 6.10), which do not take into account the particle pre-deformation.* ***b)*** *The same data as shown in* ***a)****, but on a logarithmic scale. Obviously, the pre-deformation models do not scale like the simple Hertz model, as the models show a transient behavior. For very small indentations the predicted FICs scale according to the simple Hertz model, whereas for larger indentations they scale like the simplified double contact model. For small adhesion (here: γ = 0.5 $\mu J/m^2$; see Eq. 6.18) pre-deformations induced by gravity may be important, whereas for larger adhesion attractive forces dominate the system and gravity might be neglected (not shown).*

Moreover, Figure 6.2b shows the data of Figure 6.2a, but on a logarithmic

scale. While the curves of the simple Hertz model and the *simplified double contact model* (Eq. 6.10) scale with the power of 2/3, the pre-deformation models are in between these two curves and do not scale with a constant exponent. Therefore, in the pre-deformation models $\eta(F_c)$ is not proportional to $F_c^{2/3}$. For very small indentations the particle compression happens mostly between AFM probe/indenter and spherical cell-like particle, therefore, these models scale like the simple Hertz model. For larger indentations both, the bottom and the top side of the cell-like particle, get deformed by the cantilever force F_c and, therefore, these models scale like Eq. 6.10. This transition behavior in sum leads to a slightly different shape of the predicted FICs. This means, that it is not possible to overlay the *double contact models* with the simple Hertz model by multiplying one of the curves with a constant scaling factor similar to $1/\psi$ in Eq. 6.10 (linear independence).

The AFM senses the acting force F_c due to the deflection d_c of the cantilever. This deflection, the spring constant of the cantilever k_c and the cantilever position z are related by the Eqs. 4.1 and 4.2. For nanoindentation experiments on approximately flat particles (such as gel drops with a flat bottom side on a flat rigid substrate), the bottom indentation η_{32} does not appear and, therefore, $\eta = \eta_{12}$. In this case, the upper indentation η_{12} can be calculated by solving only Eq. 4.1 and Eq. 4.2. Note, in the case of spherical cell-like particles, one of the four *double contact models* (Eqs. 6.7, 6.8, 6.9, 6.10) has to be considered additionally.

6.4 The influence of substrate and indenter shape on the error of Young's modulus estimation

Hereafter, the *simplified double contact model* is used. The radii of indenter R_1 and substrate R_3 are expressed as multiples of the cell radius R_2:

$$R_1 = \alpha R_2 \text{ and } R_3 = \beta R_2. \tag{6.11}$$

A concave curvature of the AFM probe/indenter or the substrate is expressed by a negative radius, and, therefore, by a negative value of α or β, whereas

positive values of α or β describe convex curvatures. As the simple Hertz model is not valid for the contact between an indenter with a concave radius smaller than the convex particle radius, the following restrictions appear: $\alpha, \beta \in \mathbb{R}$: $\alpha, \beta > 0$ for convex radii or $\alpha, \beta < -1$ in the case of concave radii [46]. Fitting the simple Hertz model to FICs measured on spherical particles may lead to wrong estimations of Young's modulus E_2, as the indentation of the substrate into the cell-like particle is not considered. In the following $E_s(\eta)$ designates the sample Young's modulus calculated with the help of the simple Hertz model, whereas $E_{sdc}(\eta)$ denotes the sample Young's modulus calculated with the *simplified double contact model* (Eq. 6.10). Hence, the relative error of Young's modulus E_2 using Eq. 6.2 instead of Eq. 6.10 is given by:

$$\Delta E = \frac{E_s(\eta) - E_{sdc}(\eta)}{E_{sdc}(\eta)} = \left(\frac{(\alpha\beta + \beta)^{1/3}}{(\alpha\beta + \beta)^{1/3} + (\alpha\beta + \alpha)^{1/3}} \right)^{3/2} - 1 \tag{6.12}$$

As the *simplified double contact model* (Eq. 6.10) is a multiple of the simple Hertz model, the relative error ΔE depends only on the parameters α and β but not on F_g^* or η. For this reason it is straightforward to study the influence of the indenter and substrate radii on the estimation of Young's modulus E_2.

Obviously, in the ideal case of insignificant deformations $\eta_{g\gamma}$ (no apparent weight force and adhesion), the absolute value of the particle radius R_2 is not the major factor for the quality of the estimation, but the ratios α and β between indenter/substrate radius and particle radius. The expression in the bracket on the right side of Eq. 6.12 is always greater than zero and smaller than one, showing that the simple Hertz model always leads to an underestimation of E_2, never to its overestimation.

Figure 6.3 shows the dependency of ΔE on α and β for parameter values between -10^6 and 10^6. The lines/areas in the plot indicated by the letters (a - f) correspond to different indenter-surface geometries as schematically depicted next to the error map. Figure 6.3 shows, that the application of the simple Hertz model to FICs measured on spherical cell-like particles might lead to significant errors if α is not much smaller than one. If $0 < \alpha \leq 0.01$, smaller errors (up to $\approx$ -25%) appear, in case β is not on the same scale or even smaller, which is a theoretical case, as the cell would have to be situated on a sharp tip-like substrate. Hence, a small cantilever tip according to $0 < \alpha \leq 0.01$ reduces

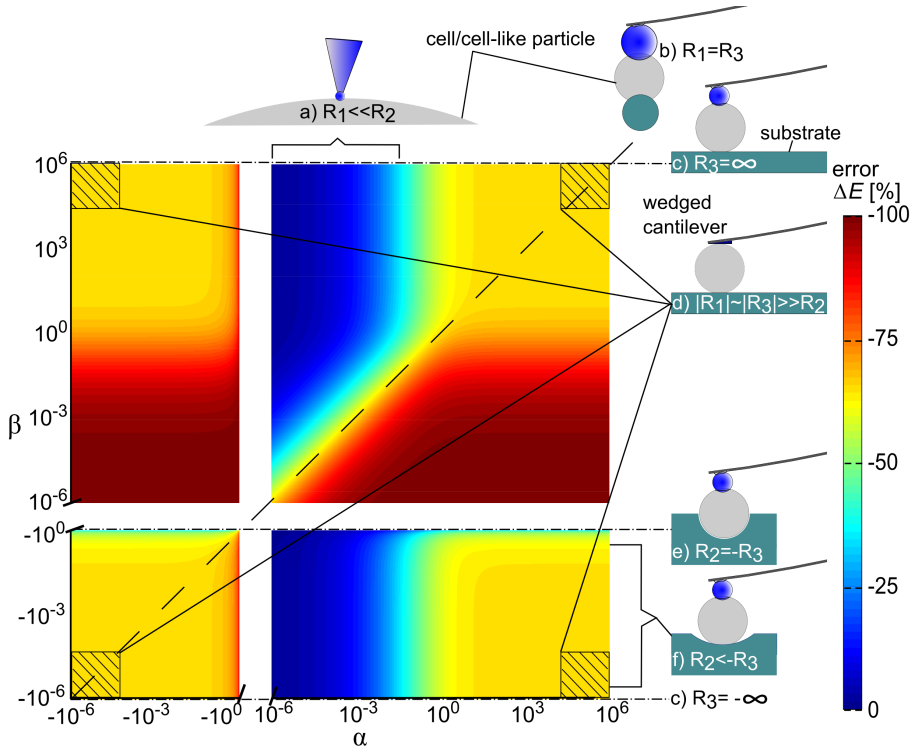

Figure 6.3: *The expected relative error ΔE in the determination of Young's modulus E_2 via simple Hertz model is shown, depending on the parameters α and β which give the ratio R_1/R_2 and R_3/R_2, respectively. The error is calculated using the simplified double contact model (Eq. 8). Various indenter-substrate setups are schematically shown:* ***a)*** *A general tendency towards small errors ΔE for convex $R_1 << R_2$ is observed if $R_1 << |R_3|$.* ***b)*** *If $R_1 = R_3$ the error is -64.6%.* ***c)*** *For $R_3 = \pm\infty$ the cell is situated on a flat substrate.* ***d)*** *For R_1 $R_3 >> R_2$ the cell is compressed between two parallel planes (parallel plate mechanics).* ***e)*** *In the case of $R_2 = -R_3$ the bottom side of the cell is enclosed by the substrate. In this case the simple Hertz model can be applied.* ***f)*** *If $R_2 < -R_3$ the cell rests in a well of the substrate.*

ΔE (Figure 6.3a); but a downscaling of α is always accompanied by a downscaling of η, because the simple Hertz model is only applicable for $\eta << R_1$ (and $\eta << R_2$). As in real experiments each measurement is superimposed by the thermal motion of the cantilever, a certain cantilever force is needed in order to have a sufficient signal to noise ratio. For example, for a super soft spherical cell-like particle (E_2 = 50 Pa, R_2 =5 μm), the simple Hertz model predicts a cantilever force of F_c = 1.1 pN for an indentation η_{12} of 200 nm, if a sharp nanoscopic tip (R_1 = 20 nm) is used. This small force is in the order of cantilever forces associated with the thermal motion of the cantilever [136] and hence, the signal to noise ratio of the measurement is low. For this reason, the downscaling of α is limited especially for very soft cell-like particles. This

limitation holds also if nanoscopic conical or pyramidal indenters are applied to very soft cell-like particles, as a large indentation η is needed to achieve a sufficient signal to noise ratio. This may lead to non-linear strains in the particle, resulting in an erroneous estimation of E_2 [137].

The use of one of the *double contact models* overcomes these limitations, as it allows even the application of AFM probes/indenters with infinite radius (wedged cantilever), which helps to increase the signal to noise ratio. Nevertheless, while a sharp tip could be used to extract E_2 with a high lateral resolution on the cell apex, the needed enlargement of the indenter will accompany a loss of lateral resolution.

For equal values of α and β (equal AFM probe/indenter and substrate radii; Figure 6.3b) it can be shown, that

$$\Delta E(\alpha = \beta) = \left(\frac{1}{2}\right)^{3/2} - 1 \approx -64.6\%. \tag{6.13}$$

In this case the deformations at top and bottom side of the particle are equal ($\eta_{12} = \eta_{32}$), independent of the acting cantilever force. A special case of this is given for parallel plate mechanics studies (Figure 6.3d). Nevertheless, the most common approach is given for $\beta = \pm\infty$. In this case, the cell is situated on a flat substrate (Figure 6.3c) and the error is given by

$$\Delta E(\beta = \pm\infty) = \lim_{\beta \to \pm\infty} \Delta E = \left(\frac{(\alpha+1)^{1/3}}{(\alpha+1)^{1/3} + \alpha^{1/3}}\right)^{3/2} - 1. \tag{6.14}$$

Here, ΔE strongly depends on α and minimizes for $\alpha \to 0$. For this reason, the indenter radius R_1 should be much smaller than the particle radius R_2 if the simple Hertz model is used for the analysis of the data. However, the minimization of indenter radius R_1 is limited by the aimed indentation depth that is needed to measure reliable FDCs with a sufficiently high signal to noise ratio, as mentioned before.

To protect the cell/cell-like particle from moving laterally, the cell can be placed in a hole of the substrate with the radius R_3 (Figure 6.3f). In this case ΔE decreases for $\beta \to -1$. In the case of an ideal spherical particle in a

half-spherical hole with the depth R_2 (Figure 6.3e), the error becomes minimal and the simple Hertz model can be applied:

$$\Delta E(\beta = -1) = \lim_{\beta \to -1} \Delta E = 0. \tag{6.15}$$

6.5 The influence of particle radius and mass density on the error of Young's modulus estimation

For a non-negligible pre-deformation $\eta_{g\gamma} = \eta_g$ caused by gravity (but not by adhesion), the error ΔE can be calculated by the use of Eq. 6.9. In this case, the relative error ΔE is given by Eq. 6.16:

$$\Delta E = \frac{E_s(\eta) - E_{dc}(\eta)}{E_{dc}(\eta)} = \frac{F_c}{\sqrt{\frac{\alpha R_2}{\alpha+1}}} \psi^{-3/2} - 1$$
$$\text{with } \psi = \left[\left(\frac{F_c}{\sqrt{\frac{\alpha R_2}{\alpha+1}}} \right)^{2/3} + \left(\frac{1}{\sqrt{\frac{\beta R_2}{\beta+1}}} \right)^{2/3} \cdot \left((F_c + F_g^*)^{2/3} - F_g^{*2/3} \right) \right]. \tag{6.16}$$

Here, E_{dc} denotes the value of Young's modulus determined with the *double contact model*. To solve Eq. 6.16, first the implicit Eq. 6.9 has to be solved numerically in order to find the value of F_c corresponding to a certain aimed indentation depth η. This was done by the use of the bisection method implemented in homemade MATLAB scripts [138].

In the literature, cell mass densities up to $\rho_{cell} = 1100$ kg/m^3 are reported [139, 140]. Figure 6.4 shows the expected error ΔE for the realistic case of a cell or cell-like particle in an aqueous solution with $\rho_{cell} = 1.05 \cdot \rho_{amb}$ for different values of cell size and Young's modulus E_2. For an increased cell radius R_2, the difference in cell Young's modulus calculated by the simple Hertz model and the *double contact model* decreases as the gravity-induced pre-deformation $\eta_g(F_g^*)$ increases. With increasing cell radius and for small indentations, the compression induced by F_c on the upper side of the cell is large, compared to the one induced on the cell bottom side. This is because the cell bottom side

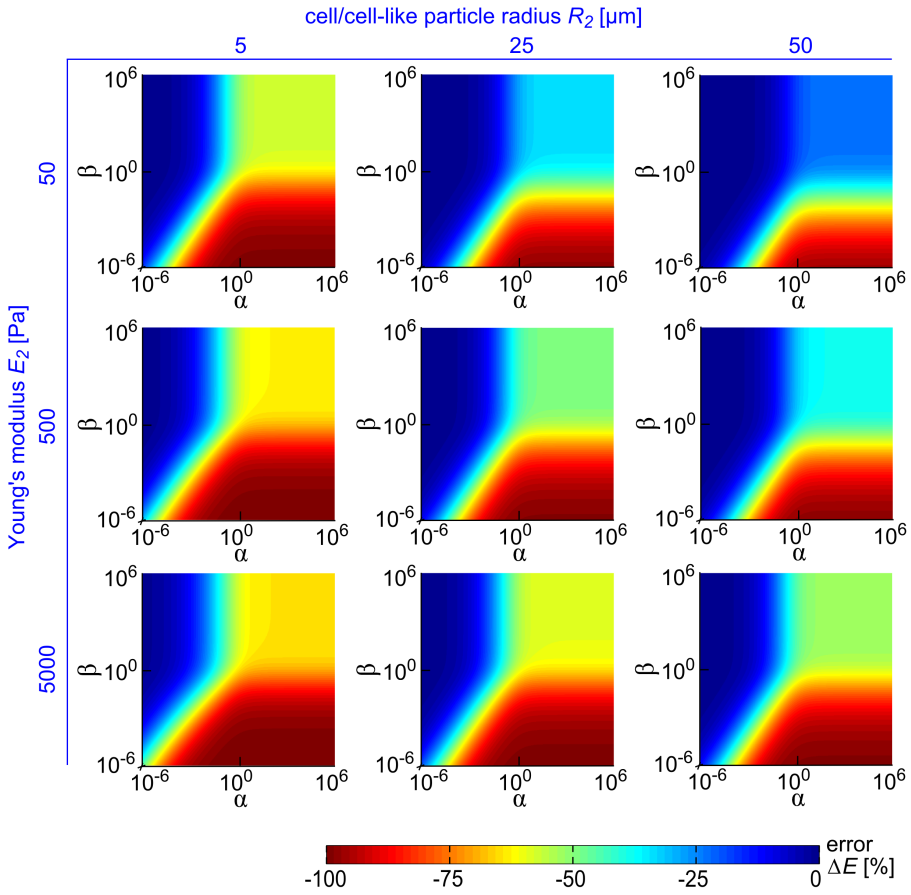

Figure 6.4: *The expected error ΔE in the estimation of Young's modulus E_2 (which is depending on the parameters α and β) is shown for positive values of α and β and for an indentation depth $\eta = 300$ nm. With increasing cell radius the error decreases, since initially the cell bottom side is already largely deformed compared with the aimed indentation depth. Therefore, under the load of the cantilever the bottom part of the cell will comply less than in the case of an ideal sphere. For an increasing Young's modulus E_2 the error increases, since the deformation due to F_g^* decreases and the initial cell shape comes closer to an ideal sphere.*

is already deformed and resists more to further deformations.

For example, assuming a soft spherical cell-like particle ($E_2 = 50$ Pa, radius $R_2 = 25$ μm and $\rho_{cell} = 1050$ kg/m^3) in water ($\rho_{amb} = 1000$ kg/m^3). In this case, the simple Hertz model predicts a cantilever force $F_c = 39.8$ pN needed for an indentation of 200 nm, if a wedged cantilever is used. The gravity force created by this particle in water is 32.1 pN. This means, the cantilever force is in the order of the gravity force and, therefore, gravity is not negligible.

For increasing values of Young's modulus E_2 the pre-deformation $\eta_g(F_g^*)$ decreases and, therefore, the initial cell shape before the indentation process comes closer to an ideal sphere. Hence, the error plot of Eq. 6.16 (Figure 6.4) for the case of $E_2 = 5$ kPa and $R_2 = 5$ μm resembles the error plot of Eq. 6.12 plotted in Figure 6.3.

6.6 AFM nanoindentation experiments on adherent cells and spherical cell-like particles

In some cases spherical cells/cell-like particles may show adhesion to the substrate, for example, in the case of particles linked to the substrate by specific interactions. In such cases the particle will not slide aside, if the cantilever does not precisely press on its apex. Therefore, the application of CPs is possible. An appropriate estimation for the surface energy γ might be obtained from the literature for a broad variety of materials [127]. In the case of comparatively large particles ($R_2 > 20$ μm) and small adhesion (see Figure 6.4) the *mixed double contact model* should be used for the data analysis, as both, gravity and adhesion, do significantly contribute to a pre-deformation of the cell bottom side. In contrast, if small cells/cell-like particles are investigated, gravity is not relevant (see Figure 6.4) and the *simplified mixed double contact model* can be used. More accurately: in order to decide which model should be used, the contact radii a_{sH} and a_{JKR} appearing on the cell bottom side according to the simple Hertz model and the JKR theory, may be compared:

$$a_{sH}^3 = \frac{3R_{32}F_g^*}{4E_2^*} = a_{JKR}^3 = \frac{9R_{32}^2\gamma\pi}{E_2^*}. \tag{6.17}$$

This leads to the estimate

$$\gamma = \Delta\rho g R_{32}^2/9. \tag{6.18}$$

Therefore, if γ is significant larger than $\Delta\rho g R_{32}^2/9$, gravity can be neglected in comparison to adhesion.

Please note, that if the model is applied to living spherical cells, some limitations appear. Cells are highly inhomogeneous objects. However, the majority

of cellular components (cytoskeleton filaments, organelles etc.) is cross-linked with each other. This creates a complex mechanical behavior of the whole cell, which was shown to behave linearly for small deformations. Therefore, theories for linear homogeneous elastic materials, such as the simple Hertz model or the JKR model can be applied.

Nevertheless, the cytoskeleton of cells is highly variable. After a certain experiment time, living adherent spherical cells might actively adapt their shape (cell bottom side) to the substrate morphology, causing a distinct contact area with the substrate, larger than predicted by the JKR model. In such cases, the use of the simple Hertz model for the analysis of FDCs measured on the cell might lead to a relatively good estimation of the cell Young's modulus E_2. Nevertheless, the use of substrate coatings is recommended. These can prevent such an adaption and facilitate nanoindentation experiments on cells in their native-like shape.

6.7 Comparison of the simple Hertz model and *mixed double contact model* using Polyethylene Glycol (PEG) microspheres

A crucial problem for some nanoindentation experiments on spherical cell-like particle is the weak adhesion between particle and substrate. If the AFM probe/indenter does not precisely press on the apex of the cell/cell-like particle, forces tangential to the cell surface appear and the cell tends either to slide or to roll under the load. Then the resulting FDCs are disturbed and a precise estimation of Young's modulus E_2 is not possible. It was shown, that wedged cantilevers can overcome this problem, since they inhibit the appearance of lateral forces [45]. To prove the applicability of Eq. 6.7 to real nanoindentation experiments on cells, soft (50 - 240 Pa) PEG microbeads ($\rho_{PEG} = 1.036 \cdot \rho_{H_2O}$) in Ultra Pure Water (UPW) were used as a model system. The measurements were carried out with the wedged cantilever developed in Chapter 4.2.2.

No adhesion effects between PEG microbeads and the glass substrate were observed, as the microbeads moved freely on the glass substrate. Therefore, the *double contact model* was applicable instead of the *mixed double contact*

model. The experiments showed a good agreement between the predictions of the *double contact model* and the measured data. Using Least Mean Squares (LMS) fits, Young's modulus E_2 has been determined for each microbead as the mean value of five measurements/fits. For each measurement the wedged cantilever was newly positioned over the microbead to reduce errors coming from an off-centered contact between the microbead and the microrectangle (of the wedged cantilever). The measurements on single beads showed a standard deviation of approximately 7% - 13% in Young's modulus E_2 for both models.

In Figure 6.5 typical fits to a measured force-indentation curve are shown. Note that the simple Hertz model does not match the data as well as the *double contact model*. Figure 6.6a shows values of Young's modulus E_2 which were

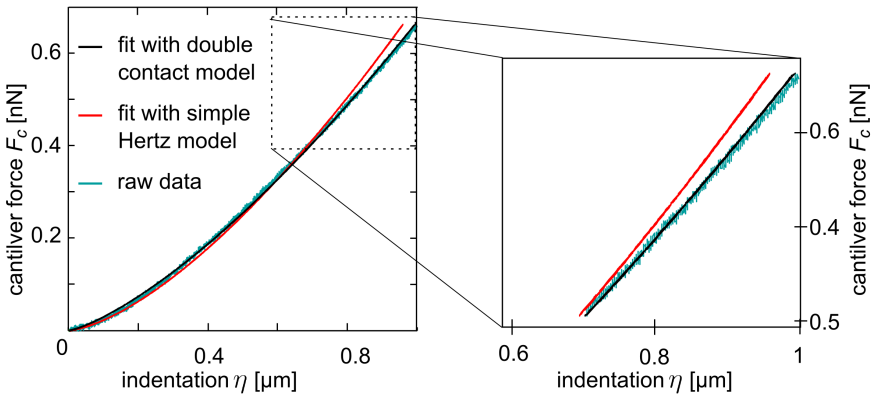

Figure 6.5: *Example of fitting curves for both models. The double contact model (black curve) describes the measured data better than the simple Hertz model (red curve).*

determined using either the simple Hertz model or the *double contact model*. While the simple Hertz model identified Young's moduli E_2 between 30 Pa and 90 Pa, the *double contact model* determined higher values between 60 Pa and 240 Pa. Please note that larger particles showed decreased elastic moduli. This is most likely due to a diffusion limitation of radicals cross-linking the PEG chains in case of larger particle diameters. In Figure 6.6b the green circles indicate ΔE for each microsphere. Obviously, the difference in Young's modulus E_2 between both models decreases for larger spheres, which is in good agreement with the predictions of Eq. 6.16. The blue triangles in Figure 6.6b show the relative difference in the determined LMS error, which is defined as $\Delta\epsilon^{(2)}_{LMS} = (\epsilon^{(2)}_{dc} - \epsilon^{(2)}_{sH})/\epsilon^{(2)}_{sH}$. Therefore, the LMS errors of the fits over the whole

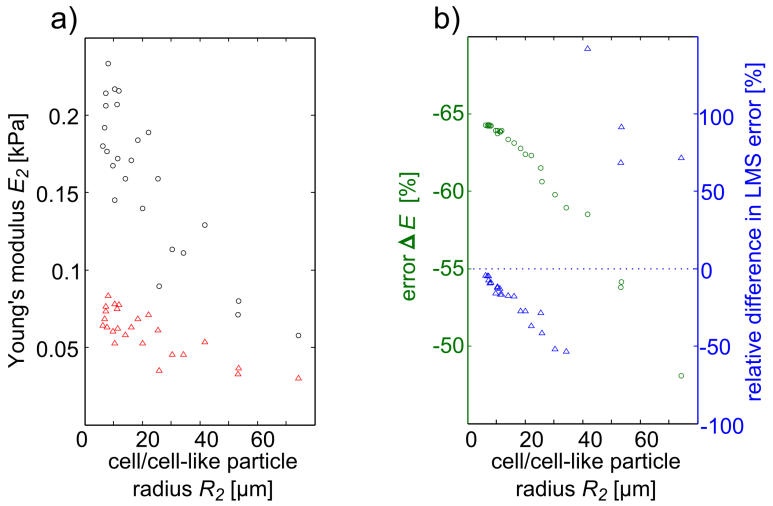

Figure 6.6: ***a)*** *The values of Young's modulus E_2 of the investigated microspheres for fitting the force-distance curves by either the simple Hertz model (red triangles) or the double contact model (black circles; Eq. 6.9).* ***b)*** *The green circles indicate the found difference in Young's modulus E_2 between both models. The blue triangles show the difference $\Delta\epsilon^{(2)}_{LMS}$ in the least mean squares (LMS) values of the fits.*

force-distance curve are compared (see Chapter 5.4) and "$\epsilon^{(2)}_{sH}$" describes the LMS error of the simple Hertz made fit, whereas "$\epsilon^{(2)}_{dc}$" denotes the LMS error of the fit calculated with the *double contact model* (Eq. 6.9). Obviously, for microbeads with radii up to ≈ 40 μm, all fits calculated with the *double contact model* show smaller LMS errors than those calculated with the simple Hertz model. Figure 6.6b also shows that $\Delta\epsilon^{(2)}_{LMS}$ decreases with increasing sphere radii, indicating that for larger particles, the pre-deformation becomes progressively important for the shape of the measured FICs. This is in good agreement with the predictions made by Eq. 6.16. In the limit of very large particles with radius $R_2 > 30$ μm, it was found that the LMS errors of the simple Hertz model-fits were twice as high as those of the fits calculated by the *double contact model*. Therefore, the FDCs of such large particles should be described neither by the simple Hertz model nor by the *simplified double contact model*, but by the *double contact model*. For spheres with radii larger then ≈ 40 μm, edge effects of the wedged cantilever appeared and disturbed the measurements. In these cases the fits showed less accuracy and a larger microrectangle would have been needed (on the end of the cantilever) to allow a proper measurement.

Chapter 7

Elasticity of cardiac fibroblasts in the context of Recent Onset Cardiomyopathy (ROCM)

In this chapter, the developed automated data analysis (Chapter 5) is used for the reliable analysis of AFM Force-Distance Curves (FDCs), measured on living human Cardiac Fibroblasts (CFBs). The study concerns the elasticity (elastic modulus E_2) of CFBs in the context of Recent Onset Cardiomyopathy (ROCM). Additionally, the precise determination of the contact point z_0 of FDCs facilitated by the developed data analysis is used to investigate the morphology of CFBs adhered to glass cover slips.
Morphological parameters such as the cell thickness h are correlated with the local cell elastic modulus E_2. Therefore, this chapter bases on the developments presented in Chapter 5.

7.1 Motivation and background - Basics about ROCM

Recent Onset Cardiomyopathy (ROCM) is a relevant cause of heart failure, leading to increased morbidity and mortality [141, 142]. ROCM is described as non-ischemic[1] and non-valvular[2] ventricular dysfunction with cardiac symptoms, appearing since less than six month in a patient [141]. A broad

[1] *Ischemia* describes the undersupply of tissue with blood.
[2] A valvular heart disease effects at least one of the four valves of the heart.

variety in the clinical course of the diseases is observed, ranging from end-stage heart failure to sufficient myocardial recovery. In some cases of ROCM a dilation of at least one heart ventricle appears, which is known as **Dilated Cardiomyopathy (DCM)**. Despite of the fact, that ROCM is not imperatively accompanied by a dilation of heart ventricles, the most predictive clinical parameter for cardiac recovery of patients with ROCM is the Left-Ventricular End-Diastolic Dimension (LVEDD) [141]. The LVEDD describes the diameter of the Left heart Ventricle (LV) during diastole[3] (Figure 7.1).

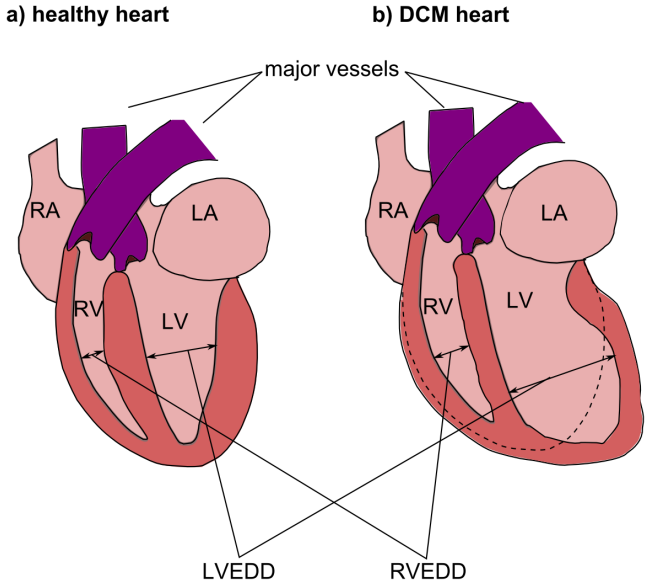

Figure 7.1: *Schematic on DCM. Patients suffering from DCM show at least one enlarged heart ventricle. Mostly the enlargement appears in the Left Ventricle (LV) but is also reported for the Right Ventricle (RV). The most common measures for this enlargement are the left ventricle end diastolic dimension (LVEDD) or the Right Ventricle End Diastolic dimension (RVEDD), describing the diameter of the heart chambers during they are filled with blood (diastole).*

DCM is the third most frequent type of heart failure (occurring in 1 of 2500 persons), and is the most frequent cause for a human heart transplantation [143]. The chamber dilations observed in DCM appear mostly in the left heart ventricle, leading to an increased LVEDD. Nevertheless, cases involving ventricular dysfunction and dilation in the Right Ventricle (RV) are known too [144]. Normally, the LVEDD is between 44 mm $\pm$ 4.2 mm (women) and 47 mm $\pm$ 4.2 mm (men) [145], while for people suffering from Dilated Cardiomyopathy (DCM) ventricle diameters up to 76 mm are reported [146]. Additionally,

[3]Diastole is the period in the cardiac cycle when the heart ventricle is filled with blood.

a loss of heart mass and a thinning of the ventricular walls can be part of the phenotype in DCM [147]. Aspects of the etiology of the chamber dilation are currently focus of numerous investigations. Especially the cardiac Extracellular Matrix (ECM) is believed to be a pathogenic key factor for the observed chamber dilation [148]. Dysbalances in the accumulation of collagens, dysbalances in ECM-regulating factors[4] and impaired cell-cell communication in the myocardium[5] have been reported. Please note that the most of the ECM-regulating proteins are created by Cardiac Fibroblasts (CFB)[149].

CFBs constitute the most frequent cell population in the heart muscle. Hence, **next to the production of ECM-regulating proteins, their elasticity could be of major importance for the development of ROCM. Changes in CFB elasticity could have significant influence on the macroscopic morphology and the biomechanics of the whole heart.** In fact, for the myocardium of patients suffering from DCM increased expressions of linkage, cytoskeletal and extracellular proteins have been found [150, 151]. This suggests a mechanical component of cardiomyopathies. Whereas activation, function and cell-cell communication of CFBs are incrementally investigated, the impact of cell elasticity on cardiac performance in human heart failures has not been investigated so far. Hence, **the contribution of CFBs to the development of ROCM as well as possible correlations between cell elasticity and parameters of cardiac performance are investigated in the following.**

7.2 Basics about Cardiac Fibroblasts (CFBs)

CFBs play a relevant role in inter cellular communication with cardiomyocytes, endothelial cells, smooth muscle cells and other CFBs. In addition to that, CFBs are involved in electrical activity, production of growth factors and cytokines [148, 152]. Furthermore, CFBs have been shown to act also as inflammatory cells by producing a variety of cytokines, such as Tumor Necrosis Factor (TNF)-alpha [149]. This variety of functions is believed to contribute to

[4] e.g. Matrix Metalloproteinases (MMPs)
[5] Myocardium: The cardiac/heart muscle

angiogenesis[6], myocardial hypertrophy[7], cell proliferation, apoptosis and cardiac inflammation. There is a growing number of publications showing that CFB dysfunction has an impact on the cardiac phenotype in patients. For example, primary CFBs from patients with heart failure with normal ejection fraction[8] produce more collagen after cytokine stimulation (with Transforming Growth Factor(TGF)-ß), which is associated with an accumulation of collagen in Endomyocardial Biopsies (EMB) of these patients [152]. All CFBs investigated in this study were derived from the Right (RV) and the Left (LV) heart Ventricle from patients suffering from ROCM using EMBs.

To study the elasticity of CFBs the setup was needed to regard the following three facts: *i)* As the nucleus of the investigated CFBs was found to be distinct smaller than the whole CFB volume, the elastic behavior of the CFBs is assumed to be determined mainly by the cytoplasm. *ii)* the investigated CFBs grew mostly separated from each other (on the used glass cover slips) and showed a large variety of cell size and shape. Some of the cells showed dimensions in the range of the maximum area scannable by the AFM 3D-scanner (100 μm). *iii)* The experiment time for each sample was limited to one hour, in order to make sure the proper state of the cells in the used BioCell (see Chapter 4.3.2). Hence, **measurement time was an important parameter for the setup**.

7.3 Control of developed measurement setup and data analysis

The ability of the used measurement system (Atomic Force Microscope (AFM), Colloidal Probe (CP) and Force-Distance Curve (FDC) data analysis) to detect differences in CFB elasticity was proofed by continuous FVMs (4 x 4 FDCs, 8 μm x 8 μm) on the CFBs in 525 μL culture medium (see Chapter 4.3.2). After 2 min without treatment 350 μL of a Paraformaldehyde (PFA) solution (10% PFA, 90% culture medium) were added, resulting in a 4% solution of culture medium and PFA. PFA was shown to cross-link proteins and cytoskeletal filaments and thereby to increase Young's modulus E_2 of cells [153].

[6]Angiogenesis: The newly creation of blood vessels from pre-existing vessels.
[7]Hypertrophy: The increase of tissues or organs due to an increased volume of their cells.
[8]Ejection fraction: The amount of blood pumped out of the heart during one cycle.

Here and for all the other investigations in this chapter, the simple Hertz model (Eq. 2.43) was used for the fitting of the data. The algorithm described in Chapter 5 was used for this FDC fitting. The sample radius R_2 was assumed to be infinite, as the fibroblasts showed a very flat morphology. Figure 7.2 shows a representative control measurement. For the 16 points on the cell surface E_2 is shown in dependency of the measurement time. Directly

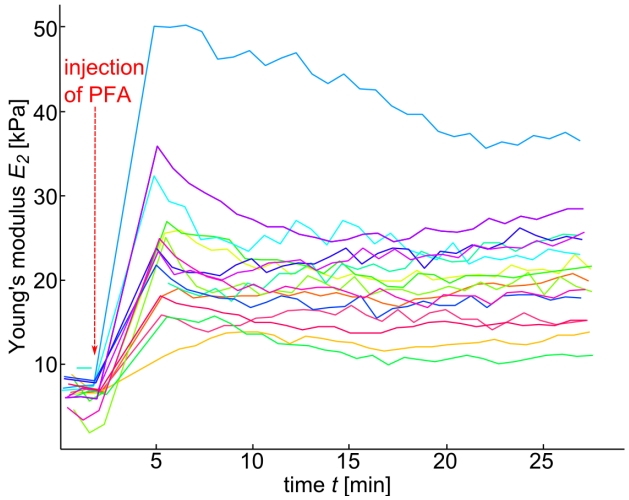

Figure 7.2: *Proof of the reliability of the applied measurement system. An example of a time dependent cell elasticity measurement based on continuous FVMs on a CFB is shown. Each line/color represents the curse of E_2 on a single point on the cell surface. Initially, all 16 points of the CFB showed an elastic modulus between 5 kPa and 10 kPa. After 2 min PFA was added to the buffer media, and subsequently Young's modulus E_2 increased. Approximately 4 min after PFA injection the maximum of the stiffening effect was observed, with elastic moduli between 16 kPa and 50 kPa.*

after the injection of the PFA the elastic modulus of the cell increased. The observed effect strength was very pronounced, as the untreated CFB showed elastic moduli between 5 kPa and 10 kPa, while approximately 4 min after PFA injection (time point of maximum effect strength) values of 16 kPa and 50 kPa were measured. Thereafter, the measured cell elasticity decreased slightly, what might be caused by disrupting cross links due to the continuous measurements. These control measurements proved the measurement system to be sensitive and reliable, as all 16 time dependent curves show the same behavior, peaking even at approximately the same time point.

7.4 Distribution of Young's modulus on single cell level

15 single living CFBs from 5 different patients were investigated by AFM Force-Volume Measurements (FVMs) with resolutions between 30 x 30 and 100 x 100 FDCs. Afterward, the measurements were compared with optical (bright field) images of the cell. Figure 7.3 gives a representative example for such a FVM. In the upper row an optical photograph (Figure 7.3a) of the

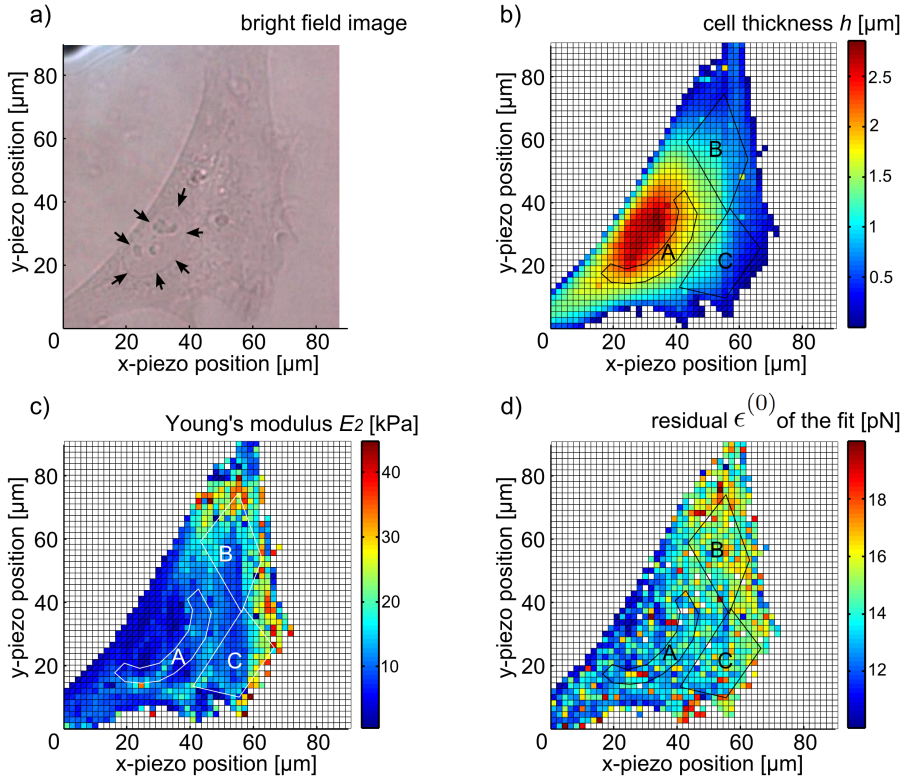

Figure 7.3: *Example for correlating optical and Atomic Force Microscopy (AFM) information.* ***a)*** *A Bright field image of the CFB is shown.* ***b)*** *The lateral distribution of the cell thickness h is shown. The thickest parts of the CFBs ($h > 2$ µm) were found in the vicinity of the nucleus. The thinner parts of the cells mostly extended into lamellipodia.* ***c)*** *lateral distribution of the local Young's modulus E_2 of the cell. Young's modulus E_2 (determined by the simple Hertz model) showed strong variations over the CFB; minimal values were always observed at and around the cell nucleus, while much higher values were found at the thinner cell parts. The Young's moduli measured in the vicinity of the nucleus (area A) were found to be the most representative for the elastic properties of the whole CFB (see text and Figure 7.4).* ***d)*** *The lateral distribution of the residuals $\epsilon^{(0)}$ of the FDCs with respect to the simple Hertz model (see Chapter 5.4).*

CFB is compared with the lateral distribution of its thickness (Figure 7.3b), as determined by the contact points z_0 of the FDCs of the FVM. Albeit, both methods derive their information with different approaches (optical and mechanical interaction), they lead to similar results with respect to the nucleus position and the cell shape.

The cell thickness over the nucleus was found to be between 2 μm and 5 μm, while the thinnest parts of the CFBs (lamellipodia in the vicinity of the cell boundary) showed thicknesses lower than 0.5 μm. This indicates that the CFB spread well on the surface, which is also visible in the optical micrograph. Furthermore, for each FDC of the FVMs the local elastic modulus E_2 of the cell was determined, according to the simple Hertz model (Eq. 2.43). The FDC fit-algorithm, which is described in Chapter 5 was used for that purpose. This also resulted in lateral distributions of E_2 and of the fitting residuals/error $\epsilon^{(0)}$. In Figure 7.3c the lateral distribution of E_2 is shown, while Figure 7.3d shows the distribution of the fitting residual $\epsilon^{(0)}$ over the cell surface.

As the fitting residual describes the similarity of the applied simple Hertz model and the measured data, can be interpreted as a measure for the reliability of the determined elastic modulus E_2. In general, the lowest errors (or residuals) were found at relatively thick parts of the cell ($h > 1.5$ μm), which were found nearby and directly over the nucleus. Thinner parts of the CFBs ($h < 1$ μm) showed significantly increased values of $\epsilon^{(0)}$ (red and yellow pixels in Figure 2d), which can be understood as a consequence of the substrate effect (compare Chapter 2).

At very thin parts (h<80 nm) of the CFB, the force profiles describe mainly the hard wall contact between colloidal probe (CP) and the supporting glass slide, superimposed by a slight contribution due to cell deformation. In these FDCs, the elastic modulus of the cell is not interpretable with the simple Hertz model, as the FDCs contain almost no elastic information about the CFB. Additionally, these FDCs are highly influenced by the substrate effect. The corresponding pixels are omitted in Figure 7.3 (white pixels) and rejected from further analysis (like those from the thicker cell parts, not satisfy the demanded fitting error limits).

FVMs as shown in Figure 7.3 contain much information about the elastic

properties of single CFBs. Nevertheless, as their measurement is time consuming ($\approx$ 1 hour/cell) the total amount of cells that can be measured within the available experiment time[9] is highly limited. Hence, it was investigated whether measuring Young's modulus E_2 at certain positions of a CFB might be representative for the whole CFB. To this end, distributions of E_2 measured across the complete surface of CFBs were compared with those measured on certain cell areas. Exemplary, Figure 7.4 shows the results of such a com-

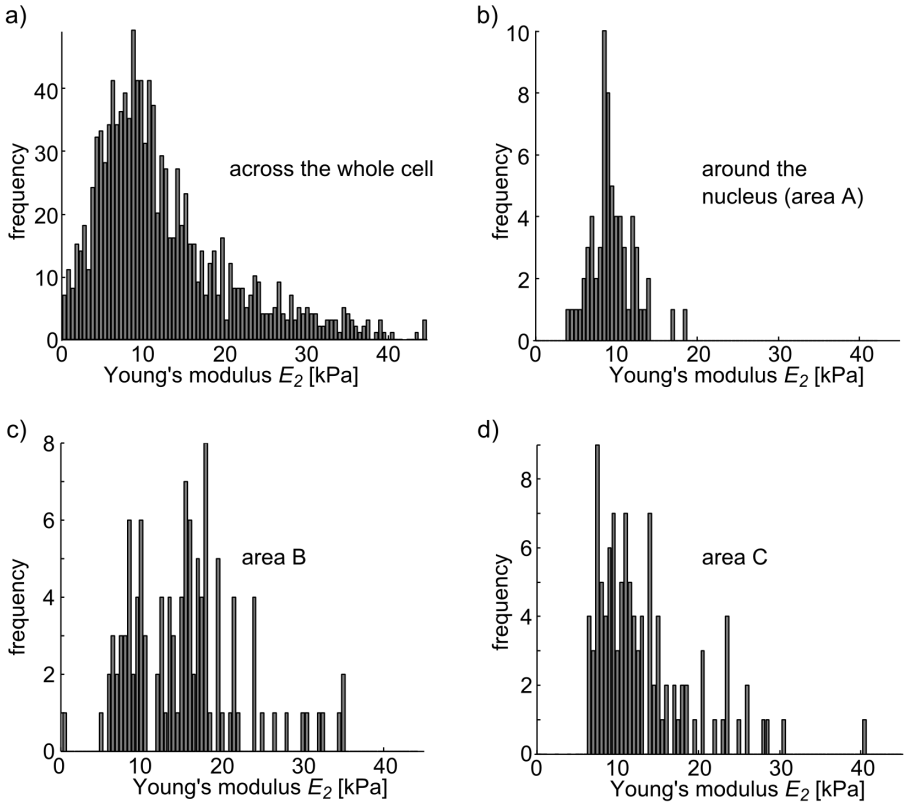

Figure 7.4: *Distribution of the local Young's modulus E_2 of the CFB shown in Figure 7.3 for:* ***a)*** *the whole cell surface;* ***b)*** *the region around the cell nucleus (in Figure 7.3 area A). Typically, the median $\langle E_2 \rangle$ of these distributions was very similar to those calculated over the whole cell, which means that the region around the nucleus approximately represents the elastic properties of the whole cell;* ***c*** *and* ***d)*** *The distributions of E_2 of two regions of low cell hight, which are indicated by the letters C and D in Figure 7.3. These distributions show an increased scattering of E_2 compared to the region around the nucleus.*

parison for the cell investigated in Figure 7.3. Therein, the distribution of E_2 over the whole cell is shown in Figure 7.4a, while Figure 7.4b shows the

[9]The measurement time was limited to one hour, in order to prevent the cells from being stressed.

one appearing if only the region in the vicinity[10] of the nucleus is investigated (area A in Figure 7.3). Furthermore, Figure 7.4c and Figure 7.4d show the distributions of E_2 for cell areas with low cell thickness h, indicated by area B and C in Figure 7.3. Comparing the four distributions, the best coincidence (with respect to the distribution measured on the whole cell) was found in the vicinity of the nucleus. This means, for all investigated CFBs, both distributions (the distribution around the nucleus and across the whole cell) showed a similar value of the median Young's modulus $\langle E_2 \rangle$. Additionally, E_2 exhibited the lowest scattering in the vicinity of the nucleus (standard deviation of E_2 in area A: 2754 Pa, in area B: 6858 Pa, in area C: 6152 Pa). **Hence, measuring force-distance curves in the vicinity of the nucleus, is a reliable measure for the CFB stiffness and can strongly decrease the number of measurements necessary to characterize a single CFB.**

7.5 Distribution of Young's modulus on cell population level

In order to characterize whole cell populations, for each patient and ventricle between 10 and 14 cells were investigated by measuring 6 FDCs on two different points in the vicinity of the nucleus. This resulted in data sets containing between 60 and 84 FDCs per patient and ventricle. The analysis of such data sets typically revealed in asymmetric distributions of the local elastic modulus E_2 with values ranging from approximately 200 Pa[11] to 20 kPa (Figure 7.5). Nevertheless, on some cells FDCs with values of $E_2 \approx 45$ kPa have been measured. A reason for such an enlarged rigidity could be given in thick cytoskeletal filaments situated directly under the cell membrane. Despite of such outliers, for the resulting distributions mostly

$$\langle E_2(\mathrm{LV}) \rangle < \langle E_2(\mathrm{RV}) \rangle \qquad \text{(on patient level)} \tag{7.1}$$

[10] A distance between 5 μm and 10 μm from the nucleus (in the projection) was estimated using an optical microscope.

[11] $E_2 = 200$ Pa is the bottom limit of the used fitting interval. Therefore, curves having exactly this Young's modulus might have a slightly smaller Young's modulus actually. Nevertheless, the error in the determination of E_2 must be very small, as otherwise the fits of these FDCs would show too high LMS errors, which would lead to the exclusion of the FDCs from the statistics.

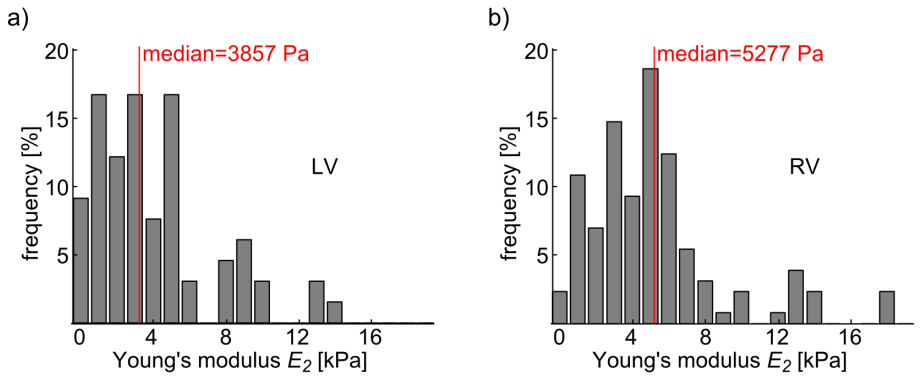

Figure 7.5: *Distribution of Young's modulus E_2 of human Cardiac Fibroblasts (CFBs) from one patient.* ***a)*** *CFBs extracted from the Left heart Ventricle (LV) typically showed a lower median elastic modulus $\langle E_2 \rangle$ than CFBs from the Right heart Ventricle (RV;* ***b)****.*

was observed. Therefore, the median elastic modulus of CFBs from the left heart ventricle was lower than for cells from the right ventricle. Nevertheless, on this single patient level the available amount of data was usually not large enough to show this trend with statistical significance.

7.6 Different elasticity of cells out of the Left (LV) and the Right (RV) heart Ventricle

In order to overcome the limited amount of data available on the patient level, data from different patients were combined. In sum 1038 FDCs measured on CFBs derived from the Left (LV; 7 patients) and from the Right (RV, 9 patients) heart Ventricle of all ROCM patients were combined. In average the CFB elasticity was found to be different between the ventricles (Figure 7.6). While CFBs derived from the LV showed a mean elastic modulus of $\langle E_2(\mathrm{LV}) \rangle^{mix} = 3374\,\mathrm{Pa} \pm 389\,\mathrm{Pa}$, the RV CFBs showed a mean elastic modulus of $\langle E_2(\mathrm{RV}) \rangle^{mix} = 4837\,\mathrm{Pa} \pm 690\,\mathrm{Pa}$. The superscripted "$mix$" indicates the use of a linear mixed-effects model (random intercept/slope model) for the analysis. This means, in the investigated ROCM patients, LV CFBs showed a significantly ($p = 0.011$) decreased Youngs's modulus compared to CBFs from RV (Figure 7.6). Therefore, for patients suffering from ROCM the relation between the Young's modulus of the CFBs in LV and RV can be described as:

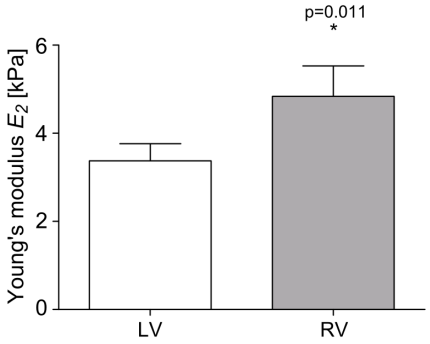

Figure 7.6: *Cell elastic modulus E_2 of human Cardiac Fibroblasts (CFBs). In average, Young's modulus $\langle E_2(RV)\rangle = 4837$ Pa $\pm$ 690 Pa was found to be significantly larger (43%) than the Young's modulus $\langle E_2(LV)\rangle = 3374$ Pa $\pm$ 389 Pa of cells from the LV.*

$$\langle E_2(\mathrm{LV})\rangle^{mix} < \langle E_2(\mathrm{RV})\rangle^{mix} \qquad \text{(over all patients).} \tag{7.2}$$

Please note, this difference is consistent with the (mostly not significant) observations on the patient level (Chapter 7.6).

7.7 Correlations between the ventricular end diastolic dimensions and cell Young's modulus

Further, the clinical relevance of the finding $\langle E_2(\mathrm{LV})\rangle^{mix} < \langle E_2(\mathrm{RV})\rangle^{mix}$ in patients suffering from ROCM was investigated. For this purpose, the Left Ventricular End Diastolic Dimension (LVEDD) and the Right Ventricular End Diastolic Dimension (RVEDD) were compared with the mean elastic modulus $\langle E_2\rangle^{mix}$ determined for each patient (Figure 7.7). The classic clinical parameters LVEDD and RVEDD were obtained by dimensional echocardiography (see Appendix A.1.1). For LV cells elastic moduli between 1811 Pa and 5967 Pa and LVEDDs between 48 mm and 72 mm were determined. For RV cells elastic moduli between 2442 Pa and 9520 Pa and RVEDDs between 19 mm and 46 mm were found. Therefore, $\langle E_2(\mathrm{LV})\rangle^{mix}$ scattered approximately by a factor 3.3, while $\langle E_2(\mathrm{RV})\rangle^{mix}$ varied approximately by a factor 3.9. Moreover, the mean Young's moduli $\langle E_2(\mathrm{LV})\rangle^{mix}$ and $\langle E_2(\mathrm{RV})\rangle^{mix}$ were compared with the LVEDD or the RVEDD, respectively. Interestingly, $\langle E_2(\mathrm{LV})\rangle^{mix}$ correlated

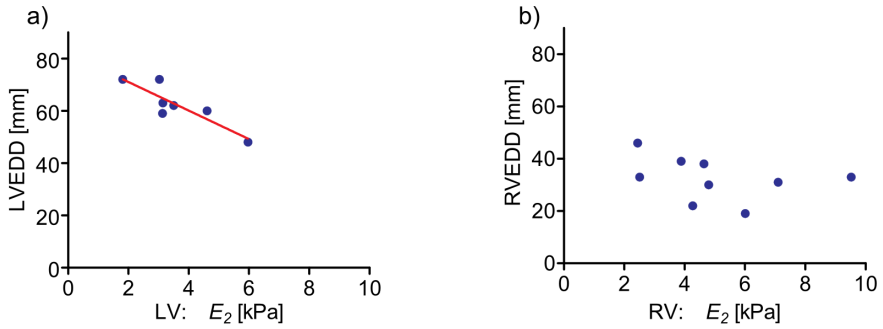

Figure 7.7: *Relationship between Young's modulus E_2 of CFBs and the Ventricular End-Diastolic Dimension for the Left (LVEDD) respectively the Right (RVEDD) ventricle.* ***a)*** *For the LV, a significant correlation between LVEDD and E_2 was found ($n = 7$, $p = 0.009$).* ***b)*** *Interestingly, even with a larger number of investigated patients, for the RV data no corresponding correlation between RVEDD and E_2 was found ($n = 9$, $p = 0.37$).*

negative with the LVEDD (Figure 7.7a; $n = 7$, $p = 0.009$), and the coherence

$$\text{LVEDD} = 81.934 \cdot [mm] - 0.005475 \cdot \langle E_2(\text{LV}) \rangle^{mix} \cdot [mm/Pa] \tag{7.3}$$

was found. This linear coherence is indicated by the red line in Figure 7.7a. In opposition to that, for the RV data no significant correlation (n=9, $p = 0.37$) with the ventricle dimension was observed (Figure 7.7), even though the number of investigated patients was larger in this case. Interestingly, a clear linear correlation between the mean Youngs's modulus $\langle E_2(\text{LV}) \rangle^{mix}$ of the CFBs in the LV and the mean Young's modulus $\langle E_2(\text{RV}) \rangle^{mix}$ of the CFBs in the RV was found. Figure 7.8 shows this significant correlation ($n = 10$, $p = 0.01$). As not for all patients CFBs from both ventricles were obtainable[12], the corresponding missing values were determined with the help of the linear mixed-effects model (blue triangles in Figure 7.8).

[12]For some patients difficulties in the culture of the cells appeared.

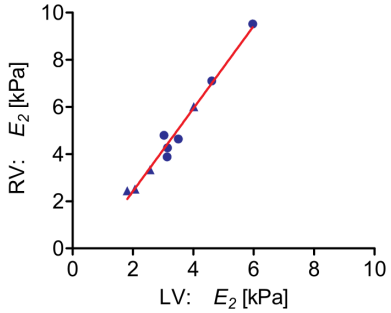

Figure 7.8: *The elastic moduli $\langle E_2(LV)\rangle^{mix}$ of the LV and $\langle E_2(RV)\rangle^{mix}$ of the RV were found to be linear correlated by Eq. 7.4. As not for all investigated patients CFBs from both ventricles were available, missing values (blue triangles) were determined using the linear mixed-effects model.*

Equation 7.4 gives the relation between $\langle E_2(\mathrm{RV})\rangle^{mix}$ and $\langle E_2(\mathrm{LV})\rangle^{mix}$:

$$\langle E_2(\mathrm{RV})\rangle^{mix} = -1079 \cdot [Pa] + 1.753 \cdot \langle E_2(\mathrm{LV})\rangle^{mix}. \tag{7.4}$$

7.8 Correlations between the ventricular fibrosis and ventricular dimension

In several types of cardiomyopathy cardiac fibrosis[13] has been observed as, for example, in viral myocarditis [155, 156]. Also in non-ischemic[14] cardiomyopathy, midwall myocardial fibrosis has been shown to be a major component of pathological remodeling of the heart ventricle [157]. Because there is a growing body of evidence suggesting that cardiac fibrosis is involved in LV dilation [158], the total collagen contents in LV and RV Endomyocardial Biopsies (EMBs; see Appendix A.1.4) were quantified. For the LV CFBs, fibrosis between 4% and 33% was found. For the samples coming from the RV fibrosis between 1% and 16% was observed. Interestingly, the extend of both right and left ventricular fibrosis did neither correlate with right or with left ventricular dilation, respectively (Figure 7.9). This suggests, that the observed heart ventricle dilations in the investigated patients might not be caused by fibrosis, but by changes in CFB elasticity.

[13] Fibrosis: The formation of redundant conjunctive (fibrous) tissue in organs or tissues [154]

[14] Ischemia: A lacking supply with O_2 in a tissue or organ.

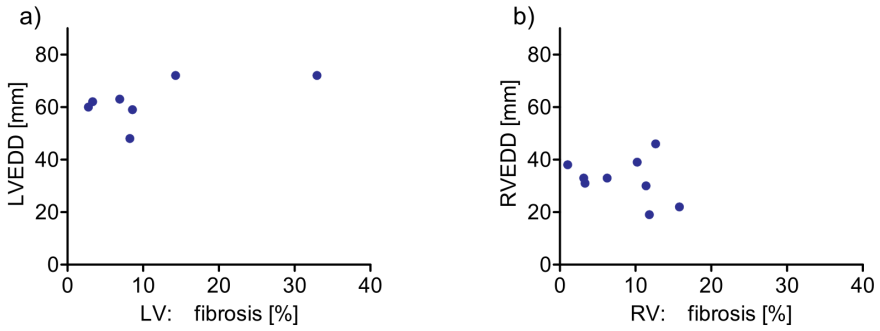

Figure 7.9: *Relationship between the Ventricular End-Diastolic Dimensions (LVEDD and RVEDD) of the patients hearts and fibrosis.* ***a)*** *No significant correlation between ventricular dimension and fibroses was observed for the left heart ventricle (LV; $n = 7$, $p = 0.15$).* ***b)*** *Also, no correlation between ventricular dimension and fibroses was found for the Right heart Ventricle (RV; $n = 9$, $p = 0.45$).*

7.9 Clinical interpretation of the data

To the best of the authors knowledge, this is the first study investigating quantitatively the elastic properties of single living primary human CFBs in the context of a cardiac disease. Despite of the large variations in Young's modulus E_2 observed for the cells derived from the same ventricle and patient, different elastic moduli of CFBs from LV and RV biopsies were found. Additionally, a statistically significant negative correlation between LVEDD and the mean elastic modulus $\langle E_2(\mathrm{LV})\rangle^{mix}$ of the patients CFBs was observed. The correlation is described by Eq. 7.3.

The data suggest a contribution of CFBs in the myocardium to pathological dilation of the LV. Currently, fibrosis and ventricular inflammation are focus of intense investigations, as they are thought to be major reasons for heart failures including LV dilation [159, 160, 161]. The findings discussed above prove the hypothesis (Chapter 7.1), that impaired cardiac performance might also be caused by changes in the structural (mechanical) characteristics of cardiac fibroblasts.

In contrast to the presented study concerning the microscopic mechanics of single cardiac cells, current research on cardiac diseases is mostly focused on the nanoscopic immunological parameters (e.g. gen expression levels) or macroscopic pathological parameters (e.g. Left Ventricle Ejection Fraction (LVEF)) of ROCM. The negative correlation between LVEDD and the mean elastic

modulus $\langle E_2(\mathrm{LV})\rangle^{mix}$ bridges between microscopic and macroscopic scale, and implies a new mechanism for LV dilation. As the correlation is pronounced, in future studies changes in CFB elasticity could be used as marker for DCM, as described in Chapter 1 for the case of non-cardiac diseases [162, 7, 8, 9].

7.10 Discussion of study limitations

This study includes several potential limitations. First, the study population size is relatively low, compared with other human studies investigating the impact of inflammation, fibrosis or cardiac performance in non-ischemic cardiomyopathy. However, despite of the small study group, the study succeeded to show a statistically significant correlation between CBF elasticity and left ventricular dilation in carefully characterized patients. Second, the investigated CFBs were cultured *in vitro*. Hence, the results cannot be ubiquitously transferred to an *in vivo* situation. Nevertheless, until now, no valid technique is available to analyze single CFB elasticity in cardiac tissue *in vivo*.

Chapter 8

Elasticity of neutrophil granulocytes in the context of Transfusion-Related Acute Lung Injury (TRALI)

In Chapter 7 the correlation between microscopic mechanical changes in cardiac fibroblasts and the shape/size of the macroscopic heart is investigated. Here the influence of nanoscopic antibodies on microscopic Polymorphonuclear Neutrophil (PMN) granulocytes is investigated in the context of Transfusion-Related Acute Lung Injury (TRALI). The results are then discussed and interpreted with respect to the macroscopic lung.

8.1 Motivation and background - Basics about TRALI

TRALI is a severe adverse effect of blood transfusion and appears mostly within six hours after the transfusion of a blood product, such as blood plasma[1] [163]. In 89% of all TRALI cases granulocyte or lymphocytotoxic antibodies were found in the used blood product [164]. The incidence of these antibody-mediated TRALI is reported to be $1:5000$ per transfused unit. A **subgroup of TRALI cases is induced by antibodies directed against Human**

[1] Blood plasma: The fluid part of blood, including clotting factors

Neutrophil Alloantigens[2] **(HNAs)** [165]. Different HNAs (e.g. HNA-3a or HNA-3b (in older literature designated by 5b or 5a [166])) are described in the literature. The HNA-3a was shown to be situated on the choline transporter-like protein 2 on the neutrophils surface. It is a glycoprotein[3] and its size is reported to be between 70 kDa and 95 kDa [167, 168]. Neutrophils in human beings can show the HNA-3a together with HNA-3b. In some cases only HNA-3a or HNA-3b are present on the neutrophil surface. In such a case cells are called homozygous.

In TRALI, antibodies against the HNA-3a and HNA-3b are transfused with blood products[4], causing an activation of the patients neutrophils. Severe cases of TRALI are frequently caused by antibodies directed against HNA-3a. The current understanding is that **HNA-3a antibodies bind to HNA-3a on the granulocyte surface, followed by neutrophil activation, production of Reactive Oxygen Species (ROS) and soluble mediators, such as Interferon (IFN), Interleukin-8 (IL-8) and enzymes.** Additionally, **neutrophil aggregation was observed as a consequence of neutrophil activation due to HNA-3a antibodies** [170].

Besides neutrophil aggregation, especially the reduction of neutrophil compliance (increase of cell elastic modulus E_2) could be critical for the development of an acute lung injury, as less compliant neutrophils may get stuck in the narrow microvasculature of the lung or lead to its occlusion due to an increased passage time [171]. Such a stiffening involving an increased neutrophil retention in narrow capillaries was already shown for neutrophils influenced by Formyl-Methionyl-Leucyl-Phenylalanine (FMLP) [172], a bacterial chemotactic peptide [173]. In the case of FMLP this (temporary) neutrophil stiffening was shown to be caused by F-actin polymerization, therefore, by changes in the Cytoskeleton (CSK). **In this chapter the question is addressed, if TRALI antibodies directed against the human neutrophil aloantigen HNA-3a on the neutrophil surface do induce changes in the**

[2]Alloantigen: An antigen which is not present in all human beings. Therefore, this antigen can create immune reactions when coming into the body of human beings not having this antigen.

[3]Glycoprotein: A macro molecule consisting of oligosaccharide chains covalently bound to polypeptides

[4]TRALI implicated blood products: blood plasma (50%), red blood cells (31%), platelets (17%), Cryoprecipitate-reduced plasma (2%) [169]

neutrophil elastic modulus E_2 (similar to FMLP). The existence of a TRALI-relevant antibody-induced neutrophil stiffening is still an unproved theory. In order to validate this theory, Atomic Force Microscopy (AFM) Force-Distance Measurements (FDMs) were carried out on neutrophils influenced by HNA-3a antibodies.

8.2 Basics about human neutrophils

Granulocytes are Polymorphonuclear leukocytes and are formed in the bone marrow. Neutrophils are a type of granulocytes, which are divided into three subgroups according to their behavior when treated with the Wright's stain: basophil granulocytes, eosinophil granulocytes and neutrophil granulocytes (or simply neutrophils). Neutrophils are part of the innate immune system. They are able to carry out phagocytosis and defend the host organism against different pathogens [174, 175]. Moreover, neutrophils are short-lived cells and the most abundant type of white blood cells (40% to 75%) [176]. In the blood stream human neutrophils show an approximately spherical shape and a diameter of 7 μm - 8 μm [35, 174, 177]. Nevertheless, during immune reactions neutrophils can actively change their morphology in order to transmigrate into endothelial tissues.

Activated[5] neutrophils can show an up-regulation of the adherence molecule CD11b on their surface or discharge Reactive Oxygen Species (ROS) which is called oxidative burst response [178]. Neutrophils are also present in pulmonary[6] blood streams. Hence, they have to pass through narrow pulmonary capillaries (diameter ≈ 5.5 μm) by undergoing pronounced morphological changes. This passage leads to retention and accumulation of neutrophils in the lung, which is described as being a mechanical process [179]. Neutrophils are highly sensitive to laborious/exogenous materials, e.g. glass. The contact with such materials mostly leads to their activation, spreading and adherence to the material. Neutrophils activated in this way are reported to show a changed elastic modulus [121].

For the here presented measurements, freshly derived neutrophils from 16

[5] Activation: the up-regulation of certain cellular processes
[6] pulmonary: regarding the lung

different donors were used. The donors were either HNA-3a homozygous or HNA-3b homozygous (for further information please see Appendix A.2.1). In order to keep neutrophils non-activated and in a spherical shape, while they are slightly adhered to the substrate, a new substrate coating was developed (see Chapter 4.3.3). Nevertheless, the extraction of neutrophils (from the blood of the donors) is a complex procedure and can stress the neutrophils. Hence, some of the neutrophils were already activated by this procedure. Such cells, showing a not spherical shape or cells which were not adhered to the substrate were excluded from the investigation.

8.3 Data analysis

In order to study the elastic properties of neutrophils, Force-Volume Measurements (FVMs; 7 μm x 7 μm, 12 x 12 FDCs) were measured on their top side. Such a single FVM took approximately three min, while the available experiment time was limited to one hour. Therefore, mostly 12 - 15 neutrophils were studied within one experiment (for a more detailed description please see Chapter 4.3). The Force-Distance Curves (FDCs) of the FVMs were analyzed by the algorithm described in Chapter 5. For this purpose, the simple Hertz model Eq. 2.43 was used with R_1 defining the radius of the AFM Colloidal Probe (CP) and R_2 defining the radius of the neutrophil surface. The latter was determined using bright field images from the cells.

After the FDC analysis, contact points z_0 and the cell elastic moduli E_2 were re-combined to force maps showing the lateral distribution of E_2 and of the (relative) cell thickness h. In the following these force maps are denoted as **force maps of first order**. Each pixel in such a force map corresponds to a FDC carried out on the neutrophil surface. Examples for such force maps (with respect to the relative cell height) can be seen in Figure 8.1a. The lateral step width between the FDCs of the FVM is 583 nm. The cell apex positions h^{max} in the force maps were determined using a moving average procedure in order to reduce influences of membrane protrusions and errors in the contact point determination. In this procedure a relative cell thickness $h(i,j)$ was assigned to each pixel of the force map, by the use of Eq. 8.1. This equation defines h as the median of the contact points of the pixel/FDC itself and its

four closest neighbored pixels/FDCs:

$$h(i,j) = \langle [z_0(i,j), z_0(i+1,j), z_0(i-1,j), z_0(i,j+1), z_0(i,j-1)] \rangle \tag{8.1}$$

Here i and j describe the line and the column of the map. In each FVM the FDC showing the maximum $max(h(i,j))$ was assumed to define the cell apex position. For the following analysis all FVMs (of cells with the same treatment) were summed up (and averaged) in a way that cell apex pixels overlapped (see Figure 8.1a). This resulted in new force maps, showing the averaged lateral distribution of z_0, such as schematized in Figure 8.1b. Moreover, the same average process but with respect to the local Young's modulus E_2 of the neutrophils results in force maps showing the averaged lateral distribution of E_2, such as shown in Figure 8.1c. In the following we denote this type of averaged force maps as **force maps of second order**.

As the apex of the cells was not always perfectly centered within the force maps of first order (12 x 12 pixels), averaged (second order) force maps showed larger pixel numbers (19 x 19 pixels). Additionally, important for the analysis of FVMs on spherical neutrophils was the fact, that not all FDCs resulted in reliable estimates of the local cell Young's modulus E_2. This is because FDCs measured on the steep flanks of neutrophils were significantly influenced by shear forces and disturbed by slipping off events of the AFM Colloidal Probe (CP) from the neutrophil surface.

Therefore, in a first step a reliable area was defined and only FDCs measured within this area (maximum 1.8 μm away from the cell apex) were used for the statistics. Assuming a cell radius $R_2 \approx 4$ μm within this area the lateral forces (due to steep cell flanks) do not exceed 10% of the normal forces applied by the AFM cantilever.

Please note, for the final statistics presented in the following, not a simple average (like schematized in Figure 8.1) but a linear mixed-effects model (described in Appendix A.3) was used to calculate averages of E_2. The respective mean values are denoted by angle brackets with superscripted "mix": $\langle E_2 \rangle^{mix}$ in the following. If no mixed model was used, the mean (or median) values are indicated just by angle brackets, such as $\langle E_2 \rangle$. The use of the mixed model

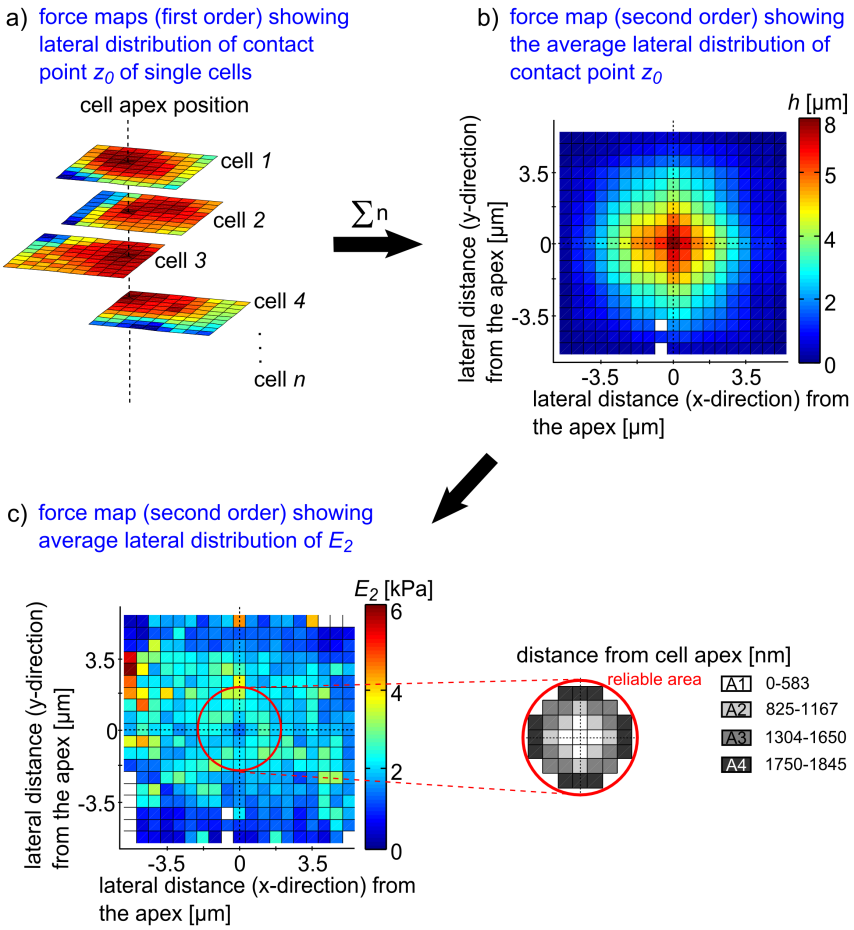

Figure 8.1: *Schematics on the applied data processing.* ***a)*** *n force maps (measurements of n neutrophils) were statistically summarized with respect to the cell apex.* ***b)*** *The force map of second order shows the averaged lateral distribution of the contact point z_0.* ***c)*** *The force map of second order shows the averaged lateral distribution of the local cell elastic modulus E_2. Only the FDCs measured in a maximum distance of 1845 nm from the cell apex were used for the statistics. The data in this reliable area were further divided into subareas A1 - A4.*

was needed in order to account for the fact, that not all force maps contribute with the same number of FDCs to the second order force map. Further more, a simple average of the (first order) force maps would lead to wrong estimations, as it was not possible to investigate the same amount of cells for all donors within the limited experiment time (one hour). For the use of the linear mixed-effects model the reliable area was divided into sub areas A1 - A4 with defined distances from the determined cell apex (cf. Figure 8.1). In a second step this trusted area was further reduced to a trusted ring (area A1 was excluded from the statistics), as described in the following Chapter 8.4.

8.4 Influence of the cell surface morphology on AFM nanoindentation experiments

The surface morphology of neutrophils varies largely. Some of them show a nearly smooth surface while others show a rough surface with pronounced membrane protrusions or recesses. Figure 8.2 exemplarily shows four Scanning Electron Microscopy (SEM) images of neutrophils with different surface roughness. While the neutrophils in Figures 8.2a/b show a relative smooth surface,

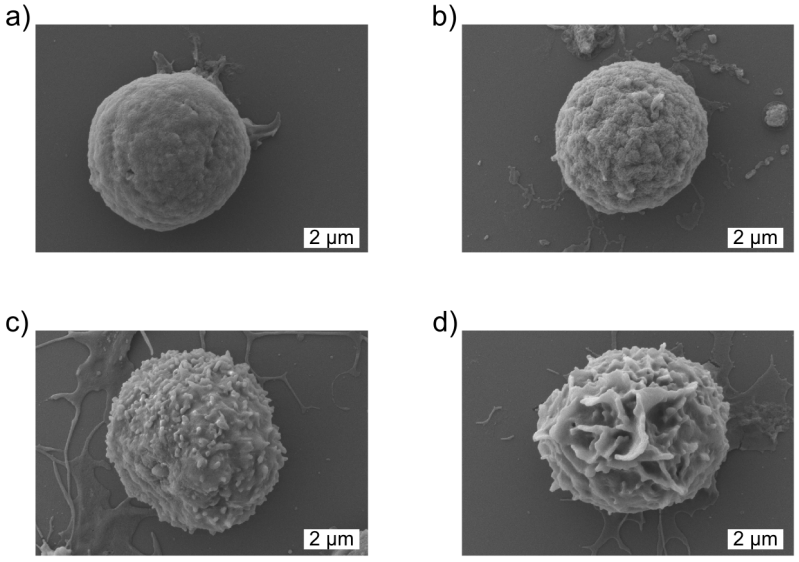

Figure 8.2: *Four Scanning Electron Microscopy (SEM) images of neutrophils on glass coated with Poly(2-hydroxyethyl methacrylate) (Poly-HEMA). The Neutrophils show an increasing surface roughness from* ***a)*** *to* ***d)****. While the neutrophils in* ***a)*** *and* ***b)*** *show surface roughnesses of* ≈ 50 *nm - 100 nm, the neutrophils in* ***c)*** *and* ***d)*** *show protrusions with lengths of* ≈ 200 *nm - 400 nm.*

the neutrophils in Figure 8.2c/d do show pronounced membrane protrusions. The neutrophil in Figure 8.2d shows protrusions with length up to ≈ 400 nm. These surface structures can influence the value of local cell elastic modulus E_2 sensed by the AFM system.

In general, FDCs measured on protrusions resulted in decreased values of E_2 identified by the applied data analysis. This is because the initial contact area between CP and protrusion is small compared to the cell radius R_2 determined *via* optical images of the cell. Therefore, the applied simple Hertz model underestimates E_2. Additionally, protrusions might kink under the load of the

CP, which would lead to an additional underestimation of E_2. Moreover, next to wrong estimates of E_2 the surface roughness of the neutrophils influences the accuracy of the cell apex determination *via* Eq. 8.1. Instead of the cell (body) apex membrane protrusions (near the cell apex) might be determined as highest point/cell apex.

In general, a membrane protrusion can be identified by comparing the contact points z_0 of neighbored FDCs. If for example the contact point of the investigated FDC is higher than all eight contact points of the eight adjacent FDCs (in the FVM), then the investigated FDC is a protrusion or at least a small evagination. *Vice versa*, if contact points of all eight neighbored FDCs are higher than the one of the investigated FDC, then a recess is identified. For example, for pure surface protrusions (all adjacent FDCs show a lower contact point) a difference in the contact point of 358 nm ± 294 nm was found, compared to the adjacent FDCs. For pure recesses (all adjacent FDCs show a higher contact point) this difference was found to be -327 nm ± 221 nm (for more details see Appendix A.2.2).

Therefore, there were FDCs clearly showing increased or decreased contact points compared to their adjacent FDCs in the measured FVMs. Please take notice, that these differences in the contact point position do not directly give the absolute length of surface protrusions, as the used CP had a diameter of 5 μm. Hence, the CP was not able to resolve narrow recesses on the cell surface. Nevertheless, this surface structures were found to have significant influence on the sensed Young's modulus E_2. Figure 8.3 shows a statistical analysis of the influence of surface structures on the results of nanoindentation experiments on neutrophils. The measurements were carried out in the control plasma P0, which did not contain any specific TRALI-relevant antibodies (see 4.3.3). In Figure 8.3a the local elastic modulus E_2 of FDCs normalized to the median

$$\begin{aligned} E_2^{surr}(i,j) = \langle [&E_2(i+1,j), E_2(i-1,j), E_2(i,j+1), \\ &E_2(i,j-1), E_2(i-1,j-1), E_2(i+1,j-1), \\ &E_2(i-1,j+1), E_2(i+1,j+1)] \rangle \end{aligned} \tag{8.2}$$

of the surrounding FDCs is shown as a function of the cell surface morphology. In Eq. 8.2 the line of the FVM is denoted by i, while j describes the column

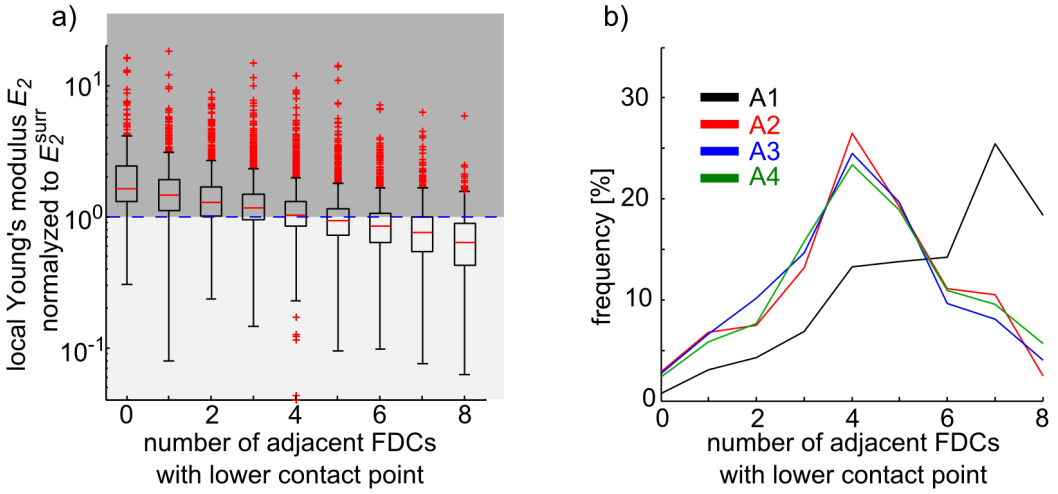

Figure 8.3: *Statistics on the correlation of membrane protrusions and the measured local elastic modulus E_2.* ***a)*** *The FDCs of 204 FVMs measured on neutrophils in the control plasma P0 were analyzed for the local elastic modulus E_2. Afterward, E_2 was normalized to the median E_2^{surr}. This normalized value is plotted in dependency of the number of adjacent pixels/FDCs with smaller contact point z_0. Obviously, with increasing number of adjacent FDCs with smaller contact point (compared to the investigated pixel) the measured value of E_2 decreases in comparison to the median E_2^{surr}. This means: when the AFM probe presses on a protrusion a lower value of E_2 is detected than when the AFM probe is pressing in a recess of the cell surface.* ***b)*** *For the areas A2 - A4 the frequency distributions show a balance between protrusions and recesses. In contrast, in the center area A1 the most pixels are part of surface protrusions (maximum at 7 surrounding FDCs with smaller contact point).*

of the FVM. More accurately: in Figure 8.3a the cell surface on and around the measurement point is characterized by the number of adjacent FDCs with contact points being lower than the one of the investigated FDC. Obviously, if the AFM probe is pressing on a protrusion (number of surrounding FDCs with lower contact point ≥ 6) the elastic modulus E_2 sensed by the system is lower than the median E_2^{surr} of the adjacent FDCs. *Vice versa*, when the probe is pressing in a recess (number of adjacent FDCs with lower contact point ≤ 2), E_2 sensed by the system is increased compared with E_2^{surr}. Furthermore, in Figure 8.3b the probability distribution of FDCs with a certain amount of surrounding FDCs having a lower contact point is shown for the subareas A1 - A4 around the cell apex (identified by Eq. 8.1). The distributions show, that for the areas A2, A3 and A4 an equilibrium is given, between protrusions and recesses. In opposition to that, the center/apex area A1 shows distinct more FDCs measured on a protrusion than FDCs measured on a recess. This proves the (statistical) influence of surface protrusions on the data derived in A1,

as the (first order) force maps were centered by the highest cell points. The described effects can also be seen in the center pixels of Figure 8.1b, which are highly influenced by protrusions and, therefore, show decreased values of E_2 compared to their surrounding pixels. Figure 8.4 shows the absolute strength of this effect (the logarithm of the mean Young's modulus $\langle E_2 \rangle^{mix}$) for FDCs measured in the areas A1 - A4 on the surface of neutrophils. The mean elastic

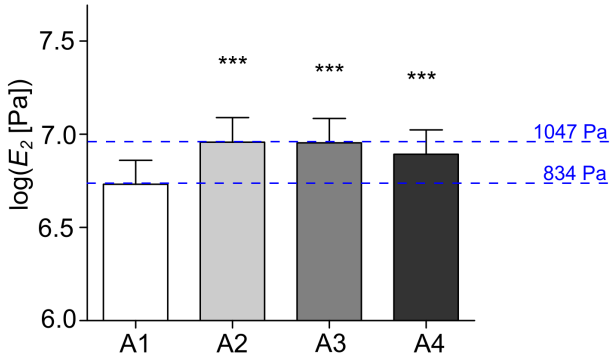

Figure 8.4: *As a consequence of the data processing, which centers the FVMs with respect to the cell apex, subarea A1 shows a significantly reduced mean elastic modulus* $\langle E_2 \rangle^{mix}$ *compared to the subareas A2 - A4.*

modulus $\langle E_2(A1) \rangle^{mix}$ in the center area of the reliable area was found to be decreased compared to $\langle E_2 \rangle^{mix}$ in the other sub areas (A2 - A4):

$$\langle E_2(A1) \rangle^{mix} < \langle E_2(A^*) \rangle^{mix} \text{ with } A^* = A2, A3 \text{ or } A3. \tag{8.3}$$

Hence, for the statistics of the following investigations only FDCs measured within a reliable ring (radius = 825 nm - 1845 nm) around the cell apex have been taken into account. Moreover, FDCs with Least Mean Squares (LMS) errors (with respect to the fit function) higher than described in Chapter 5.5.4 were also excluded from the analysis. Additionally, in the following the **elastic modulus $\boldsymbol{E_2(cell) = \langle E_2(A2, A3, A4) \rangle}$ of a single neutrophil is defined as the median of all local elastic moduli $\boldsymbol{E_2}$ measured in the areas A2, A3 and A4**.

8.5 Control of developed measurement setup and data analysis

8.5.1 Detectability of neutrophil elasticity changes

As control for the measurement system and the developed data analysis FVMs were carried out on neutrophils. These were incubated either in buffer (VLE-RPMI; see Chapter 4.3.3) or in a solution of buffer and Formyl-Methionyl-Leucyl-Phenylalanine (FMLP; see Chapter 4.3.3) which is a chemoatractant and is known to cause neutrophil stiffening [172], as already mentioned before. For the measurements neutrophils were settled on Poly-HEMA coated glass cover slips (cf. Chapter 4.3.3). The FMLP-influenced measurements were compared with measurements carried out on neutrophils incubated in buffer (control). In good accordance to the literature, the neutrophils incubated with the additional FMLP showed a 54.2% increased Young's modulus E_2 ($p = 0.013$) compared to the control group (Figure 8.5). Therefore, the

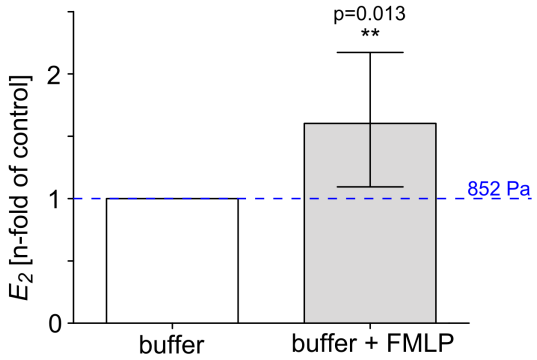

Figure 8.5: *Neutrophils incubated in buffer (VLE-RPMI) containing Formyl-Methionyl-Leucyl-Phenylalanine (FMLP) showed a significantly ($p = 0.013$) increased Young's modulus E_2 compared to neutrophils incubated in pure buffer media.*

applicability of the developed measurement system and data analysis (consisting of: colloidal probe, Poly-HEMA coated substrate (cf. Chapter 4.3.3) and data analysis consisting of FDC-fitting algorithm and reliable ring definition) for the detection of changes in neutrophil elasticity was shown. Furthermore, these control experiments were of importance for the experiments described in the following, as FMLP was used as routinely control for neutrophil stiffening. In the literature the FMLP-induced neutrophil stiffening is shown to disappear within $\approx$ 30 min at 37°C. Therefore, the fact that the FMLP-induced

neutrophil stiffening was detectable in the experiment time interval (30 min - 90 min after the beginning of the incubation) is of importance. It shows that the execution of the experiments at room temperature (T_r = 24°C) helps to slow down cellular processes, and thereby to increase the available measurement time.

8.5.2 Dependence of cell elasticity on cell size

Using optical microscopy, cells used for being probed were chosen randomly (from those cells not showing indications of cell activation). Nevertheless, as not all cells showed the same diameter, it was necessary to verify if there is a correlation between cell size and cell elastic modulus E_2. For this purpose the cell radius R_2 and the elastic modulus E_2 have been correlated. In Figure 8.6 the elastic modulus E_2 (bottom) of neutrophils is plotted as function of the cell radius R_2 (top). For neutrophils incubated in the control plasma P0 (n = 132 cells from N = 6 donors) and in the HNA-3a antibody containing plasmas P1, P2 and P3, gaussian cell size distributions were observed (only plotted for P1; n = 87 cells from N = 4 donors). The maximum positions R_2^{max} of the distributions were found to be very similar: R_2^{max} = 4.25 μm for P0 and R_2^{max} = 4.3 μm for the strongest plasma P1.

The widths of the distributions differ slightly, as for example the cell size distribution of the P0-incubated cells is slightly broader than the one of the P1-incubated neutrophils. Nevertheless, as the cell size distributions summarize cell radii of neutrophils from different donors, and as even the used cell number differs significantly between both distributions, this difference should not be over interpreted. Because of the very similar peak positions of the cell size distributions, the data support the assumption, that there is no cell size variation due to the incubation of the cells in different blood plasmas.

Furthermore, next to the similar peak positions of the cell size distributions the bottom part of Figure 8.6 shows that there is no significant correlation between cell size and elastic modulus E_2 of the cells. For all plasmas (P0, P1, P2, P3 and P4; data shown only for P0 and P1) and for all cell sizes the obtained values of E_2 scattered widely around the median $E_2(population)$ of the respective cell population. As the here investigated data were calculated from

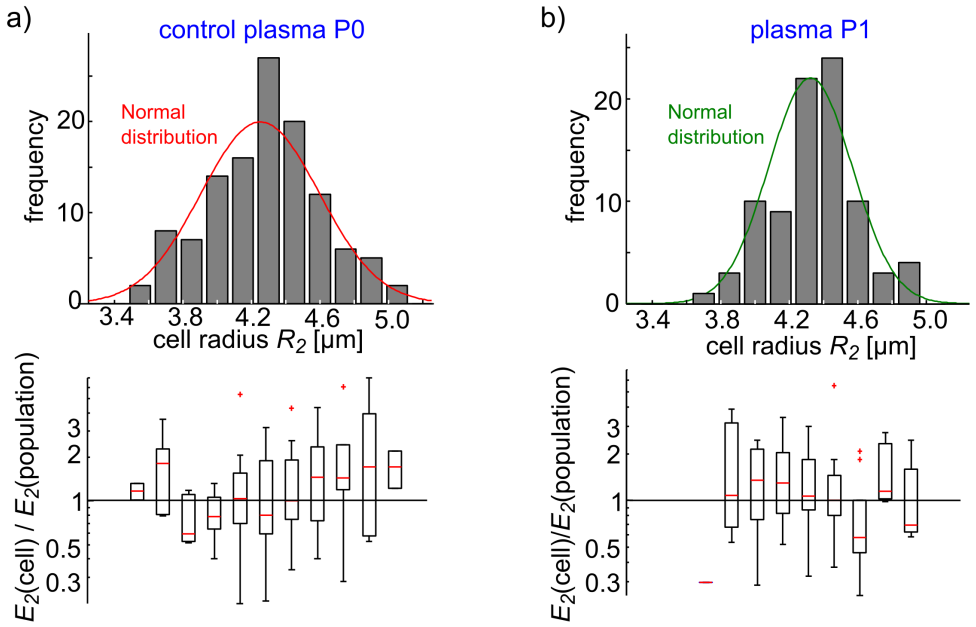

Figure 8.6: *Cell size and elastic modulus E_2* ***a) top:*** *The measured radii of neutrophils incubated in the control plasma P0 (see 4.3.3; $n = 132$ cells from $N = 6$ donors) situated in Poly-HEMA coated glass cover slips. The cell radius (determined by light microscopy images) corresponds to a normal distribution with a maximum at 4.25 µm.* ***a) bottom:*** *The determined elastic moduli E_2 of the cells are shown as function of the cell radius. No significant correlation was found between cell radius and E_2.* ***b) top:*** *The distribution of the radii of neutrophils situated on Poly-HEMA coated glass after incubation with the HNA-3a antibody containing plasma P1 ($n = 87$ cells from $N = 4$ donors). The distribution peaks approximately at the same radius $R_2 \approx 4.3$ µm like the distribution for the neutrophils incubated in control plasma P0. The width of the distribution is lower than for P0-incubated cells;* ***b) bottom:*** *The determined elastic moduli E_2 of the P1-incubated neutrophils are shown in dependency of the cell radii. No significant correlation between cell radius and E_2 was observed.*

the same cells used for the investigations discussed in the following Chapters, this shows that **no unwitting selection of cells with certain sizes or values of elastic modulus appeared in the experiments**.

8.5.3 Influence of the control plasma on the Young's modulus of neutrophils

In vivo neutrophils are situated in the blood stream. Therefore, a proper *in vitro* approximation for these environmental conditions is blood plasma, containing no cellular components but all antibodies, salts, clotting factors etc. For this reason, as control situation for all investigated HNA-3a antibody

containing blood plasmas (P1 - P3) the incubation of neutrophils in control plasma P0 was used, which is a pooled blood plasma (from 10 donors) and did not contain specific TRALI relevant antibodies. Figure 8.7 shows confocal microscopy images of neutrophils incubated in the plasmas P0, P1, P2 and P3. The DNA (nucleus) was stained with DRAQ5 (blue). Antibodies specifically binding to the surface of the cells were stained with Alexa Fluor 488 conjugated anti-human Fab'2 fragments (green). Obviously only for the plasmas P1, P2 and P3 specific antibody bindings appear. This shows, that the control

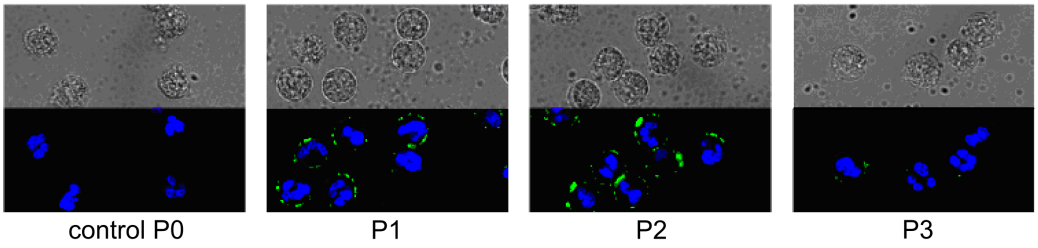

Figure 8.7: *Confocal microscopy images of neutrophils after incubation with the blood plasmas P0, P1, P2 and P3. The DNA of the neutrophils was stained with DRAQ5 (blue). Binding of HNA-3a antibodies was detected with Alexa Fluor 488 conjugated anti-human Fab'2 fragments (green). No binding antibodies were detected on the neutrophils incubated with the control plasma P0.*

plasma P0 does not contain antibodies specifically binding to the surface of neutrophils. Therefore, it can be seen as a good approximation for the natural environment of neutrophils *in vivo* of human beings not influenced by TRALI.

The mean elastic modulus $\langle E_2(P0)\rangle^{mix}$ of neutrophils incubated in P0 was found to be 123.2% higher than $\langle E_2(\text{buffer})\rangle^{mix}$ of cells incubated in buffer media (VLE-RPMI) (Figure 8.8). This is an interesting finding, as in the literature mostly the elasticity of neutrophils in buffer media is investigated. This finding implies that **experiments presented in the literature might underestimate the elastic modulus of neutrophils *in vivo***. The exact mechanism of this behavior remains still unclear, as no specifically binding antibodies were found on the surface of the P0-incubated neutrophils. Despite of the unknown molecular mechanism of this effect, the experiments support the use of blood plasma P0 as control situation, as it is very similar to the HNA-3a antibody containing plasmas P1, P2 and P3. This is also supported by the measurements shown in Chapter 8.6.3 (see Figure 8.11).

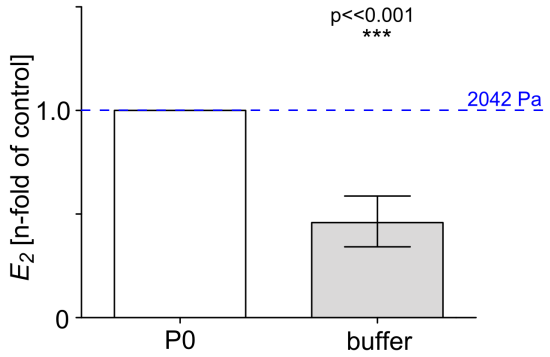

Figure 8.8: *Young's modulus $\langle E_2(P0)\rangle^{mix}$ of neutrophils incubated in the control plasma P0 was found to be increased (123.2%, $p << 0.001$) in comparison to $\langle E_2(buffer)\rangle^{mix}$ of neutrophils in buffer media (VLE-RPMI).*

8.6 Stiffening of neutrophils after contact with specific Human Neutrophil Alloantigen (HNA)-3a antibodies

8.6.1 Neutrophils in contact with HNA-3a antibodies

HNA-3a homozygous neutrophils adhered to Poly-HEMA coated glass cover slips (see Chapter 4.3.3), were incubated in three different HNA-3a antibody containing plasmas (P1 - P3) for half an hour. It was found that the cells showed an increased Young's modulus E_2 after the incubation compared to the control group which was incubated in the control plasma P0 (Figure 8.9).

The effect intensities were found to be dependent on the used blood plasmas (P1 - P3). While plasma P1 caused an increase of 40.1% in the averaged elastic modulus $\langle E_2\rangle^{mix}$, the effect strength of P2 was 34.2% and for the weakest plasma P3 an increase of 24.1% in $\langle E_2\rangle^{mix}$ was observed. This means, that not all blood plasmas (from different donors) containing HNA-3a antibodies lead to the same intensity of neutrophil stiffening. Parameters such as the antibody concentration in the plasma might influence the effect strength. Please note, that the intervals in Figure 8.9 are confidence intervals (not standard deviations), determining the precision of the estimate of $\langle E_2\rangle^{mix}$. As for all tested plasmas (P1, P2 and P3) the bottom border of these intervals was higher than 1.0, a statistically significant neutrophil stiffening effect is indicated. Nevertheless, as the confidence intervals are relatively large, the absolute effect strength

is not clearly defined. For example, in the case of P1 a repetition of the experiment is expected to show an averaged increase of neutrophil elastic modulus E_2 between 13% and 74%.

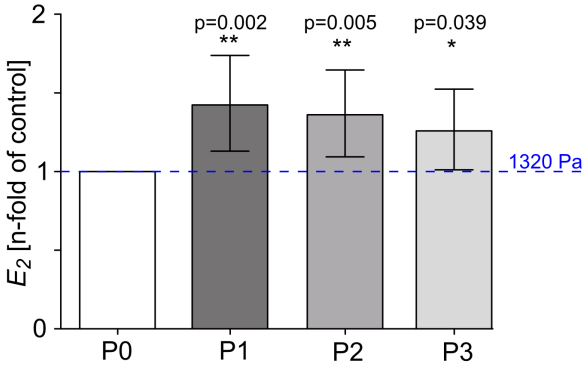

Figure 8.9: *Fold-changes in the elastic modulus of HNA-3a homozygous neutrophils after incubation with three different HNA-3a antibody containing plasmas (P1 - P3). Data were normalized to $\langle E_2(P0)\rangle^{mix}$ of the control cells which were incubated in plasma P0 containing no specific TRALI relevant antibodies. The* ***intervals are confidence intervals*** *of the experiments. After cell incubation in the plasmas the neutrophils showed in increased E_2 for all tested plasmas (P1, P2 and P3). Nevertheless, the effect strength was not the same for each plasma.*

8.6.2 Identification of HNA-3a antibodies as cause of the observed neutrophil stiffening

The used blood plasmas (P0, P1, P2 and P3) contain next to the HNA-3a antibodies a variety of other components, such as antibodies, salts and clotting factors. In order to clarify the contribution of the specific HNA-3a antibodies to the observed cell stiffening, experiments similar to those described in Chapter 8.6 were carried out for HNA-3b homozygous neutrophils, using the strongest plasma P1. HNA-3b homozygous cells do not have the HNA-3a, but only HNA-3b. Therefore, no specific binding of HNA-3a specific antibodies to the neutrophils appears. Figure 8.10 shows the results of these experiments. In contrast to the equivalent experiments of Chapter 8.6.1 plasma P1 did not increase the elastic modulus of HNA-3b homozygous neutrophils. However, HNA-3b homozygous neutrophils incubated with FMLP increased their elastic modulus, as already observed for the HNA-3a homozygous cells (see Chapter 8.5.1). This shows, that the **specific binding of the HNA-3a antibodies to the HNA-3a is needed to induce neutrophil stiffening. Moreover,**

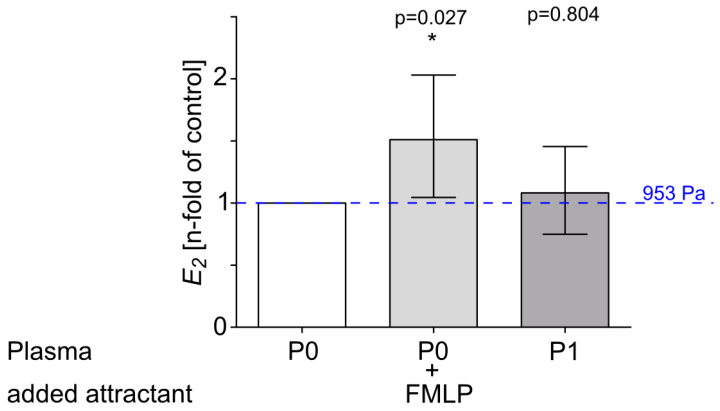

Figure 8.10: *Fold-changes in cell elastic moduli of HNA-3b homozygous neutrophils incubated either in plasma P0 or in a solution of P0 and FMLP or in plasma P1. For the FMLP treated neutrophils a cell stiffening was observed, while the HNA-3a antibody containing plasma P1 did not cause a cell stiffening.*

the data indicate that FMLP-induced and HNA-3a-induced neutrophil stiffening may be caused by independent biochemical pathways. Please note, as a side finding of these measurements, it was proved that HNA-3a homozygous neutrophils do not have a different elastic modulus than HNA-3b homozygous neutrophils (see Appendix A.3).

8.6.3 The role of actin for the HNA-3a antibody-induced neutrophil stiffening

For fast changes in neutrophil elastic modulus E_2 induced by chemoatractants, such as FMLP (see Figure 8.5), actin polymerization was reported to be the major cause [180, 181, 172]. In order to clarify if actin is involved in the observed HNA-3a mediated cell stiffening effect (Chapter 8.6) too, additional experiments were carried out. In these experiments neutrophils were incubated either in a solution of P0 and Cytochalasin D (CD) or in a solution of P0, FMLP and CD or in a solution of P1 and CD before the AFM FVMs. CD is a cell-permeable inhibitor of actin polymerization and was shown to disrupt F-actin microfilaments [182, 183]. Therefore, the actin of the cell consists mostly of G-actin [184] and actin oligomers after the application of CD, and cell elastic modulus is reported to decrease by this process [19]. If the observed HNA-3a antibody-induced neutrophil stiffening is not caused by an F-actin polymerization, then the incubation of neutrophils in P1 should lead to a cell stiffening, even if F-actin polymerization is suppressed.

Figure 8.11 shows the results of these measurements. According to the literature, CD was decreasing the elastic modulus of neutrophils (Figure 8.11a). Therefore, in order to resolve HNA-3a mediated changes in E_2 under the influence of CD, CD has to be added also to the plasma P0 of the control cells (Figure 8.11b). In Figure 8.11b the results concerning the influence of HNA-3a

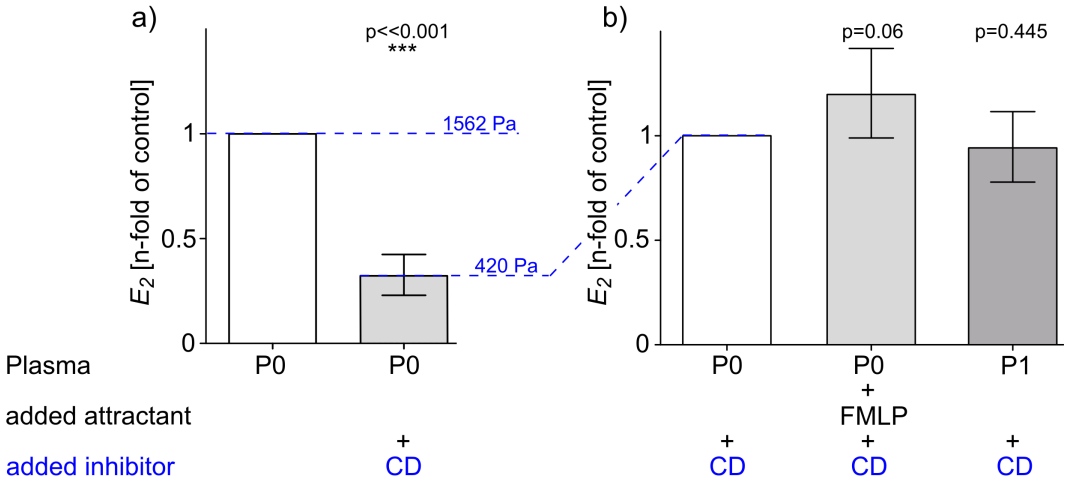

Figure 8.11: ***a)*** *Fold-changes in the elastic modulus of neutrophils incubated in the control plasma P0 decreased due to the addition of CD to the plasma.* ***b)*** *Fold-changes in the elastic moduli of HNA-3a homozygous neutrophils after incubation in: i) a solution of control plasma P0 and CD (left) or ii) in a solution of control plasma P0 and FMLP and CD (middle; used as control measurement) or iii) in a solution of plasma P1 and CD. Note, the right bar of graph* ***a)*** *was here used as control. Due to the addition of CD, neither the FMLP nor plasma P1 initialized a significant cell stiffening. This indicates the involvement of actin in the observed HNA-3a-induced neutrophil stiffening process (see Figure 8.9).*

antibodies on the neutrophil elastic modulus under suppressed F-actin polymerization (by CD) are shown.

Obviously, under the influence of CD, neither FMLP nor plasma P1 did significantly increase the elastic modulus of the neutrophils. For FMLP this effect is already known in the literature [19]. For plasma P1 this result is interpretable as indication for the involvement of F-actin in the HNA-3a mediated stiffening effect. Nevertheless, Fluorescence Activated Cell Sorting (FACS) analysis showed that the amount of F-actin in HNA-3a homozygous neutrophils does not significantly increase after cell activation by the HNA-3a antibodies (see Appendix A.1).

One possibility to interpret this is the assumption that HNA-3a activated neutrophils show an increased cross-linking of actin filaments but not an increased F-actin content, as they do after FMLP stimulation. As CD depolymerizes F-actin, such a cross-linking of small G-actin monomers and actin oligomers would not significantly increase the elastic modulus of neutrophils.

8.6.4 Kinetics of cell elasticity during the measurement process

Neutrophil stiffening induced by FMLP shows pronounced kinetics. Within a few seconds, this F-actin content based process [172] leads to a significantly increased F-actin concentration in neutrophils. For the investigated neutrophils a maximum F-actin concentration was observed after $\approx$ 1 min (see Appendix A.1). Therefore, measuring the elastic modulus E_2 of neutrophils in a time frame between 30 min and 90 min after the beginning of the incubation will resolve only a weak rest of the FMLP mediated cell stiffening effect. Hereafter the question is addressed, if for the HNA-3a-induced neutrophil stiffening such pronounced kinetics exists, too. The study is limited to data measured within the experiment time of 60 min.

In the following the averaged elastic modulus $E_2(population)$ of a cell population is defined as the median of the single cell elastic moduli $E_2(cell)$ of the n cells of the population:

$$E_2(population) = \langle [E_2(cell_1), E_2(cell_2), ..., E_2(cell_n)] \rangle. \tag{8.4}$$

In order to investigate the kinetics of the HNA-3a-induced neutrophil stiffening, the elastic modulus $E_2(cell)$ of neutrophils incubated in HNA-3a containing plasma (P1, P2 or P3) was normalized to the elastic modulus $E_2(population)$ of their cell population. Afterward, the data were correlated with the respective measurement time point. Figure 8.12 shows the results of this investigation including 211 neutrophils. The red line in Figure 8.12 indicates the cell population median after normalization, which is always one.

Furthermore, the black line indicates a moving average curve. Each point

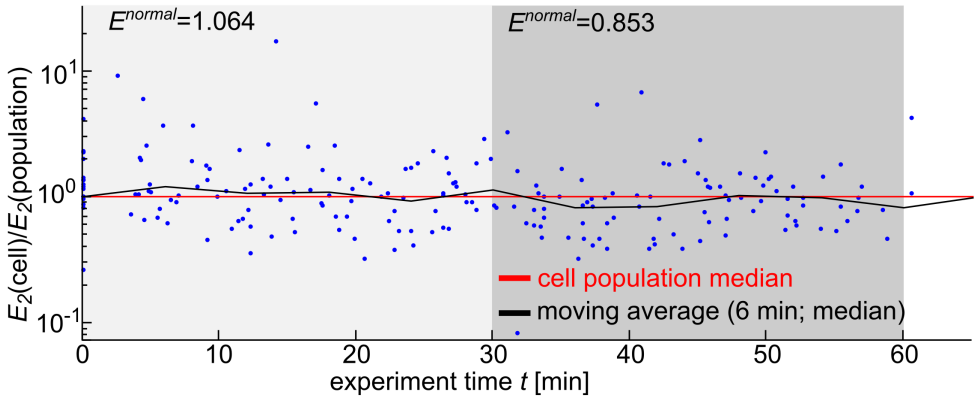

Figure 8.12: *Kinetics of the elastic modulus $E_2(cell)$ of 211 HNA-3a homozygous neutrophils incubated in HNA-3a antibody containing plasmas (P1 - P3). Each blue dot shows $E_2(cell)$ of a single cell normalized to the median $E_2(population)$ of the corresponding cell population. The black line shows the corresponding average (median) values E^{normal} in 6 min intervals. A weak dependency of E_2 on the measurement time was observed.*

of the curve represents the median E^{normal} of a six minutes interval, which is defined by

$$\begin{aligned} E^{normal} = \langle [&E_2(cell_1)/E_2(population(cell_1)), \\ &E_2(cell_2)/E_2(population(cell_2)), ..., \\ &E_2(cell_n)/E_2(population(cell_n)),] \rangle \\ &\text{with } n = \text{number of cells measured in the time interval.} \end{aligned} \tag{8.5}$$

Obviously, there is a weak dependency of the cell elastic modulus E_2 on the experiment time, as the moving average curve of the fist 30 min is located mostly over the cell population median line, while for the period between 30 min and 60 min the curve runs mostly under this line. Hence, the elastic modulus of the cells decreased slowly during the measurement time.

An additional proof for this thesis can be found *via* the partition of the data into two time intervals: 0 min - 30 min and $>$ 30 min - 60 min (see Figure 8.12). While $E^{normal} = 1.064$ for the first interval, in the second interval $E^{normal} = 0.853$ was found. As in the control group (P0-incubated neutrophils; see Appendix A.2) no corresponding trend was observed, this finding can be interpreted as proof for slow ($\propto$ 1 hour) kinetics in the decay of the HNA-3a-induced stiffening effect. Please note, as all measurements have been carried

out at room temperature (24°C; see also Chapter 4.3.3) **the kinetics of the observed stiffening effect under physiologic conditions (37°C) could be faster**. According to Figure 8.12 the effect size could be underestimated by the used experimental setup, as also data from the second half of the experiment time interval are included in the statistics. Moreover, as no temporary increase of E^{normal} was observed during the experiment time, the HNA-3a antibody mediated stiffening process must have been occurred while the 30 min lasting incubation before the measurement period.

8.7 Correlation of HNA-3a antibody-induced cell stiffening with clinical observations

After the identification of HNA-3a antibodies as being the specific key factor for neutrophil stiffening in TRALI, the correlation of this stiffening with other TRALI relevant processes was of interest. For example, in clinical studies it was observed that after activation by HNA-3a antibodies neutrophils start to form aggregates. The test used for the investigation of this phenomenon is called Granulocyte Agglutination Test (GAT). In a GAT, neutrophils are incubated in dilutions of the HNA-3a antibody containing plasmas P1, P2 and P3. For this purpose these plasmas are diluted with the control plasma P0. Therefore, the antibody concentration of the plasmas P1, P2 and P3 is varied. GAT showed P1 to cause neutrophil aggregation up to a plasma dilution of 1 : 124. For P2 neutrophil aggregation was observed up to a dilution of 1 : 64, while in the weakest plasma P3 neutrophils aggregated only up to a dilution of 1 : 8. Interestingly, this order of aggregation effect intensities coincides with the order of the intensities of the observed neutrophil stiffening effects (with respect to the used plasmas). This correlation is shown in Figure 8.13. This may indicate the that HNA-3a antibody concentration in the plasma has a direct influence on the intensity of the observed neutrophil stiffening effect. Please note, as only three plasmas were measured this is not a significant trend.

Next to this observation, additional (preliminary) data correlating the HNA-3a antibody-induced cell stiffening with clinical observations are presented in the Appendix (A.2.2).

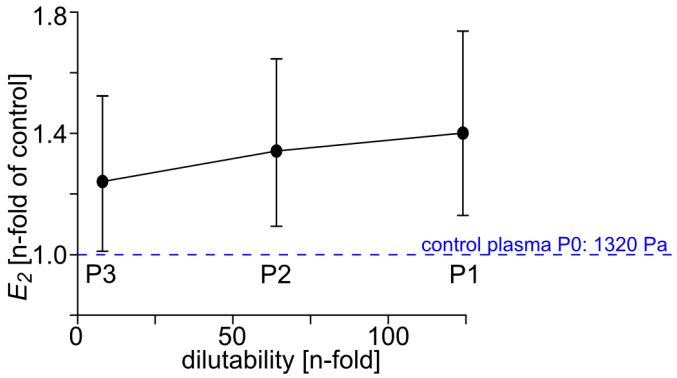

Figure 8.13: *Effect intensity of the HNA-3a mediated stiffening effect over the maximum dilution of the plasma which still leads to a neutrophil aggregation. For the three investigated plasmas the following was observed: The higher the plasma is dilutable the more pronounced was the observed stiffening effect.*

8.8 Clinical interpretation of the data

In order to keep neutrophils in a spherical adhered non-actived state during AFM FVMs, a new substrate coating protocol was developed (see Chapter 4.3.3). FVMs on neutrophils showed that neutrophil surface protrusions can lead to significantly reduced values of the measured local cell elastic modulus E_2. A measurement setup including an appropriate data analysis was developed in order to reduce the influence of surface protrusions on the measurements. Using this setup, FVMs were carried out on neutrophils incubated in different blood plasmas. A **neutrophil stiffening was observed for HNA-3a homozygous neutrophils incubated in blood plasmas containing specific HNA-3a antibodies.**

The effect strength appeared to be dependent on the used blood plasma, or more precisely on the antibody concentration of the plasma (not significant). The observed cell stiffening effect was relatively pronounced, as the median cell elastic modulus $\langle E_2 \rangle^{mix}$ of neutrophils activated by specific HNA-3a antibodies was found to be up to 40.1% higher than in the control group. Nevertheless, the confidence intervals of the data are large, therefore the real effect size is expected to be between 13% and 74%. Including the fact that there are kinetics in the HNA-3a-induced neutrophil stiffening, the real effect size might be even higher. Nevertheless, due to the large range of the expected effect sizes, it is not possible to definitively answer the question regarding the clinical impact

of the observed neutrophil stiffening on the development of TRALI. Nevertheless, it can be assumed, that the observed cell stiffening effect is increasing the transition time of neutrophils *in vivo* passing through narrow microscopic capillaries in the human lung. **Therefore, the observed neutrophil stiffening might be a potentially new pathological mechanism of TRALI.**

In addition to that, the results suggest that **FMLP-induced and HNA-3a-induced neutrophil stiffening may be caused by independent biochemical pathways (see Figures 8.10 and A.6) and mechanisms (see Appendix A.1)**. While FMLP causes neutrophil stiffening *via* an increased F-actin content (actin polymerization), the HNA-3a-induced neutrophil stiffening might be caused by an altered F-actin cross-linking.

8.9 Discussion of study limitations

In this study neutrophils from 16 different donors (13 HNA-3a homozygous and 3 HNA-3b homozygous) have been investigated by 1429 FVMs ($\approx 2.05 \cdot 10^5$ FCDs). Out of this, 41590 FDCs were used for the statistics presented here, as the rest was not part of the reliable ring defined in Chapter 8.4. The HNA-3a mediated neutrophil stiffening was shown for three different blood plasmas containing HNA-3a antibodies. For all statistical analysis at least triplets (three independent measurement days with each 10 - 16 neutrophils from different donors) were measured. The existence of an HNA-3a mediated neutrophil stiffening was even proved by 5 - 7 independent measurements for each plasma. Highly significant trends were found, nevertheless, as the study population (16 donors) is relatively small the here presented results should be reproduced in large scale studies. This might help to decrease confidence intervals and allow a clear estimation of the clinical impact of the observed HNA-3a mediated neutrophil stiffening.

Chapter 9

The impact of the Apelin Receptor (APLNR) on biomechanical and morphological properties of Human Umbilical Vein Endothelial Cells (HUVECs)

In the Chapters 7 and 8 the AFM was mainly used to investigate the correlation between changes in the microscopic cell elasticity and macroscopic observations in organs (heart or lung). In this chapter the AFM (and the data analysis developed in Chapter 5) is used to investigate the dependency of the cell elastic modulus E_2 of microscopic endothelial cells on the function of a nanoscopic surface receptor (APLNR).

9.1 Motivation and background - Basics about endothelial cells and their responses to shear stress

The endothelium is created by a monolayer of Endothelial Cells (ECs) which cover the inner walls of vessels. In the human vessels endothelial cells cover an area of $\approx$ 350 m^2 [185]. In sum there are between $1 \cdot 10^{13}$ and $6 \cdot 10^{13}$ endothelial cells in the human body with a total mass of approximately 1 kg.

The endothelium creates a permeable barrier allowing elements of the blood stream (e.g. proteins or hormones) to diffuse into the body [186]. Endothelial cells influence the vascular tone[1], platelet adherence and blood flow. Moreover, *via* controlled interactions with leukocytes, monocytes and lymphocytes, immune and inflammatory processes are influenced by the endothelium [187].

In order to do so, endothelial cells are able to sense hormonal and hemodynamic[2] stimuli and to react on these stimuli by the secretion of several (chemical) mediators [188]. Especially hemodynamic forces, e.g. shear forces created by the blood stream, have attracted scientific interest in the last years. Ion channels [189], tyrosine kinase receptors [190], adhesion proteins (e.g. integrins; [191]), glycocalyx [192], primary cilia[3] [193] and **G-Protein-Coupled Receptors** (**GPCRs**; [194]) have been identified as key biomolecular components transducing these biomechanical forces into biochemical intracellular signals. These signals lead to cell adaptation to shear forces. This adaptation is a complex process involving alterations in cell shape, subcellular distribution of structural proteins and cellular function [195, 196]. For example: cytoskeletal remodeling, due to formation of F-actin stress fibers [197], coalignment of microtubules and intermediate filaments with the shear vector [198], and reorganization of adhesion complexes [199] have been reported. However, **the exact mechanisms of endothelium-mediated mechanotransduction remain poorly understood**.

Guanosine Nucleotide-Binding Proteins (G-proteins) have a key role in signal transmitting from the extracellular to the intracellular space. Moreover, G-proteins are GTPases, which means that they transmit signals by the hydrolyzation of Guanosine Triphosphate (GTP). The activation of G-proteins was already described to be important for initial cell-responses after shear flow exposure [200]. **Shear stress-induced signal transduction was reported for direct G-protein activation, but also for GPCR induction.** GPCRs are also called Seven-Transmembrane (7TM) receptors, as they consist of seven α-helical protein structures, which cross the cell membrane. Figure 9.1 shows a schematic of a GPCR. By the activation of a GPCR (e.g. by the binding of

[1] vascular tone: actively created tension of a vessel wall
[2] hemodynamic: "*due to the kinetics of the blood*"
[3] cilia: long and slender protuberances from cell bodies

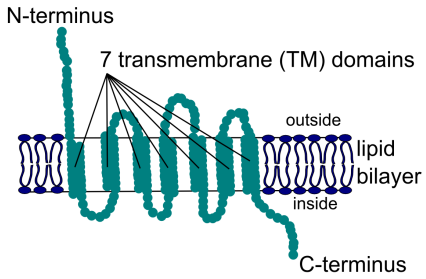

Figure 9.1: *Schematic of a G-Protein-Coupled Receptor (GPCR) with its seven transmembrane domains.*

a ligand to the receptor), the GPCR undergoes a conformation change. Afterward, the changed GPCR can activate an associated G-protein. This activation process is described to appear *via* the exchange of a bound Guanosine Diphosphate (GDP) for a Guanosine Triphosphate (GTP) on an associated G-protein.

Hence, **GPCRs use associated G-proteins for their signal transduction processes.** A prominent example is the Bradykinin B2 Receptor (BK2R), a GPCR which is involved in the fluid flow-dependent processes of mechanotransduction [201]. Recently another shear-regulated GPCR was described: the endothelial Apelin Receptor (APLNR/APJ receptor) in Human Umbilical Vein Endothelial Cells (HUVECs) [202]. The APLNR is a dual receptor. First, it is the receptor for the specific ligand apelin and second, it works as a direct mechanosensor for mechanical stimuli. Experiments on cardiomyocytes (from mice) with APLNR knockout showed the APLNR to be "*a receptor for mechanical stretch*", independent of specific ligands [203]. Based on these observations in cardiomyocytes, **is can be assumed that APLNRs might also be part of the complex adaptation mechanism in ECs, facilitating their mechanosensitivity. Therefore, in the following the relevance of the GPC APLNR on the endothelial elasticity (Young's modulus E_2), spreading and shape is investigated.**

9.2 Expression and Distribution of APLNR in the vascular endothelium

In order to investigate the influence of physiologic laminar Endothelial Shear Stress (ESS) on the expression and distribution of Apelin Receptor (APLNR)

in confluent endothelial cell monolayers, HUVEC monolayers were exposed to laminar ESS of 150 mN/m^2. In these experiments the APLNRs were tagged by Green Fluorescent Protein (GFP). The nuclei were stained in blue (NucBlue; see Chapter 4). The top part of Figure 9.2 shows time resolved representative distributions of APLNR expression (green) in HUVECs under laminar ESS. With increasing experiment time the HUVECs adopted to the shear stress and changed their APLNR expression: Initially APLNRs were observed all over the cell membranes and in the perinuclear regions, like described by Kleinz et al. [204]. With increasing time of flow exposure the GFP signal in that central perinuclear regions increased. Moreover, also in the junctional sur-

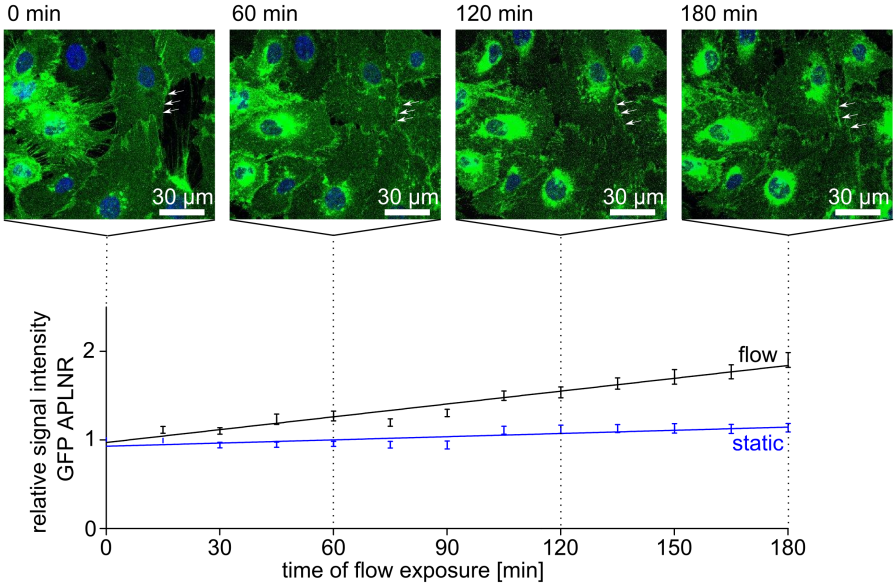

Figure 9.2: *Top: time resolved representative distributions of the endothelial Apelin Receptor (APLNR) stained with Green Fluorescence Protein (GFP; green) on the surface of Wild Type (WT) HUVECs under shear stress. The nuclei were stained with NucBlue (blue). After three hours of shear stress exposure especially in the perinuclear regions and near the junctional surfaces (white arrows) HUVECs showed increased expression of APLNR. Bottom: absolute GFP signal intensity (near junctional surfaces) over time. While for WT HUVECs under static conditions (fluorescence images not shown) no significant increase of the GFP signal was observed, for WT HUVECs exposed to shear stress the GFP signal intensity increased by 67% within three hours.*

faces[4] APLNRs were detectable initially. After flow exposure, the cells spread and the cellular interactions became closer (white arrows in Figure 9.2). In

[4]junctional surface: inter cellular surface providing contact between neighbored cells or between cell and Extra Cellular Matrix (ECM)

these regions of cellular junctions an increase in GFP signal was detected, too. The bottom part of Figure 9.2 shows time resolved the respective GFP signal intensity for defined perinuclear regions either exposed (black; "*flow*") or not exposed (blue; "*static*") to shear stress. After three hours of shear stress an increase of 67% in GFP expression was detected, compared to the control group (static), which did not show significant changes in the GFP signal. This means, that the investigated HUVECs actively adapted their APLNR density to the appearing shear stress.

9.3 AFM Force-Distance Measurements (FDMs) on HUVECs

9.3.1 Data analysis

In order to characterize the local elastic modulus E_2 of HUVECs Atomic Force Microscopy (AFM) Force-Volume Measurements (FVMs; 20 x 20 Force-Distance Curves (FDCs), 100 μm x 100 μm) were carried out on HUVECs adhered to glass cover slips. The FDCs of the FVMs were analyzed with the algorithm described in Chapter 5. In contrast to the former chapters, here two different contact models were applied in order to fit the data: the simple Hertz model (Eq. 2.43) and the thin layer model of Dimitriadis et al. (Eq. 2.49).

Due to the flat shape of the HUVECs the cell radius R_2 was assumed to be infinite, as already done for the human cardiac fibroblasts (Chapter 7). As for the application of the thin layer model the cell thickness h was needed to be determined, only FVMs showing at least one FDC measured on the bare glass substrate were used for the analysis. Hence, fully confluent monolayers of HUVECs were not preferable for the experiments. Nevertheless, most HUVEC monolayer regions showed at least small sub areas not covered by the cells. The absolute local cell thickness $h(i,j)$ determined by the FDC in line i and column j of a FVM was calculated *via*

$$h(i,j) = z_0(i,j) - min(z_0). \tag{9.1}$$

This is the difference between the locally found contact point $z_0(i,j)$ and the minimum contact point $min(z_0)$ of the whole FVM. Local maximums $h^{\max}$ of

the cell thickness h, which mostly corresponded to cell apexes, were identified by the following condition (pseudocode):

$$\begin{aligned} h(i,j) = h^{\max}(i,j) \text{ if } h(i,j) = max([h(i,j), h(i-1,j), \\ h(i+1,j), h(i,j-1), h(i,j+1), h(i-1,j-1), \\ h(i+1,j+1), h(i-1,j+1), h(i+1,j-1)]). \end{aligned} \quad (9.2)$$

Please take note, that this is a slightly different approach than applied for the measurements on single neutrophils (Chapter 8.3) where only one cell apex was needed to be identified per FVM. In contrast to those measurements, the here used step width between two neighbored FDCs in a FVM is much larger (5 μm compared to 583 nm in the case of neutrophils). Therefore, the mean difference of adjacent contact points z_0 measured near the cell apex was higher, and by this cell surface roughness did not play an important role. The cell apex position was determined (only) with an accuracy of 5 μm. Nevertheless, as the cells showed typical diameters of more than 30 μm this resolution was sufficient.

Figure 9.3 shows exemplarily the analysis of such a FVM. In Figure 9.3a a representative FVM is shown. On the left side of Figure 9.3a a bright field image of the investigated HUVECs on a glass substrate is shown, while in the middle and on the right the lateral distributions of the contact point z_0 (determined by the two contact models) are plotted. FDCs measured on cell apexes (black circles in Figure 9.3a) and their four closest neighbored FDCs (black crosses in Figure 9.3a) were determined by a homemade MATLAB algorithm based on Eq. 9.2. These FDCs were used for the statistics of cell apex elasticity measurements. Nevertheless, some of these FDCs could not be correlated with cells visible in the bright field image. Hence, in a second step these FDCs were excluded manually from the selected FDCs (white filled circles/white crosses in Figure 9.3a) in order to increase the reliability of the investigations.

The simple Hertz model and the thin layer model of Dimitriadis et al. determined very similar cell surface profiles (lateral distribution of z_0) with cell thicknesses h of more than 4 μm in perinuclear regions. Nevertheless, for very thin sample regions, the fits calculated according to the thin layer model

tended to show slightly higher values of z_0 than those calculated with the simple Hertz model.

Larger differences were found in the lateral distribution of the local Young's modulus E_2 (Figure 9.3b) and in the absolute values of E_2. In general, the absolute values of E_2 determined with the simple Hertz model were higher than E_2 determined with the thin layer model. Furthermore, E_2 determined by the simple Hertz model showed a clear correlation with the cell thickness h (Figure 9.3a). This effect was distinctly reduced for the thin layer model.

Nevertheless, the fits of both models showed increased Least Mean Squares (LMS) fitting errors $\epsilon^{(2)}$ (contact area of the FDC; see also Chapter 5), if very thin cell areas were probed (Figure 9.3c). *Vice versa*, near the cell apexes both models showed decreased standard deviations of the determined local cell elastic modulus E_2, while $\epsilon^{(2)}$ showed local minima. This probably results from the fact, that for thin cell regions the assumption to probe a homogeneous material gets more violated. In these thin cell areas small local differences in cytoskeletal properties (e.g. F-actin density) can have an increased influence on the measurement.

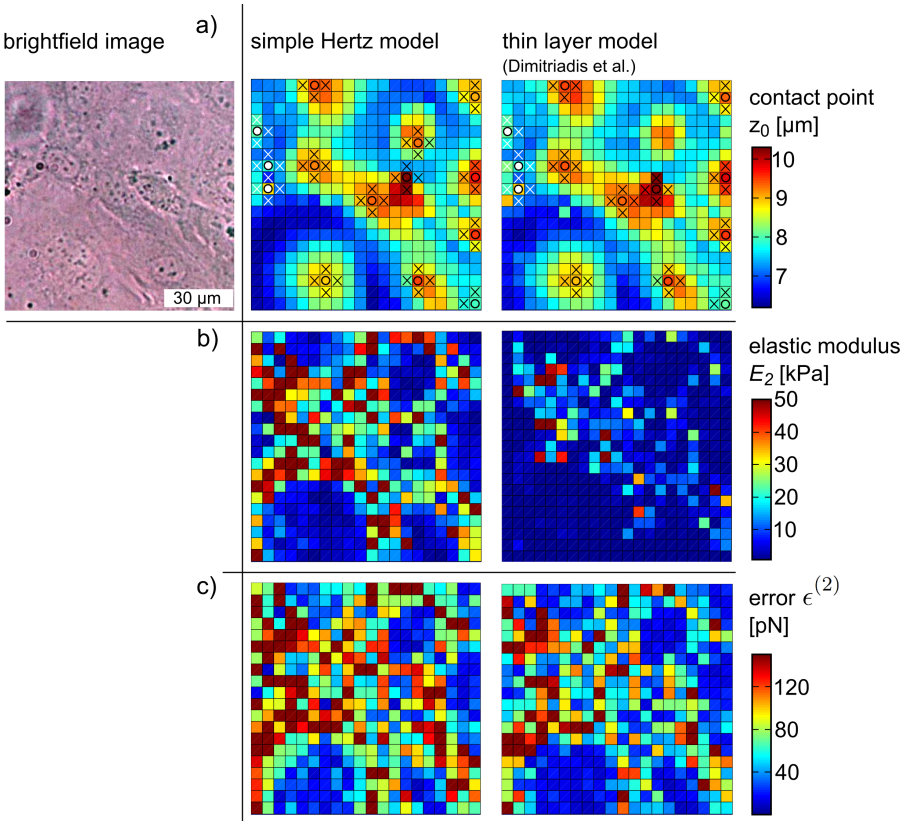

Figure 9.3: *A representative Force-volume Measurement (FVM) on HUVECs.* ***a)*** *left: Bright field image of the cells adhered to the glass substrate; middle: The lateral distribution of the contact point z_0 for fitting the data with the simple Hertz model is shown. Points of maximum cell thickness (black circles/black crosses) were determined with homemade numerical routines. Afterward, some of them were excluded manually (white filled circles/white crosses), as according to the bright field image they did not correspond to cell apexes; right: The lateral distribution of the contact point z_0 for fitting the data with the thin layer model according to Dimitriadis et al. is shown. The application of the fitting algorithm described in Chapter 5 to both contact models led to very similar surface morphology reconstructions of the cells. Nevertheless, for very thin sample regions, the fits calculated with the thin layer model tended to show slightly higher values of z_0.* ***b)*** *Lateral distributions of the local elastic modulus E_2 for both contact models. FVMs analyzed with the thin layer model showed significantly smaller variations of E_2 than the ones analyzed with the simple Hertz model.* ***c)*** *The lateral distributions of the Least Mean Squares (LMS) fitting error $\epsilon^{(2)}$ (contact area of the FDC) are shown. The LMS errors of the fits increased for both models in case FDMs were carried out on very thin cell parts or even pure glass. Nevertheless, in average $\epsilon^{(2)}$ was smaller for the fits with the thin layer model.*

9.3.2 The impact of the APLNR on Endothelial Cell (EC) elasticity

In order to investigate the role of the APLNR in the cell mechanics and the mechanotransduction of HUVECs, AFM FVMs were carried out (as described above) on HUVECs either kept under static conditions or stressed by physiologic shear flow (ESS of 150 mN/m^2 for three hours) before the measurements. Moreover, the respective experiments were also carried out for APLNR-Knock Down (KD) HUVECs. For further information on the KD process please see Chapter 4.3.4. As described in Chapter 9.3.1 the FVM analysis allowed the determination of the local cell thickness h and the distinction of thin (0.5 μm $< h <$ 1 μm) as well as thick cell parts (in the proximity of the cell apex). These both regions were in focus of the experiments described hereafter.

Figure 9.4 shows the results of the FVMs carried out on the relatively thick apex regions ($h \approx 4$ μm) of Wild Type (WT) HUVECs and APLNR-KD HUVECs. A data analysis with the thin layer model of Dimitriadis et al. (Fig-

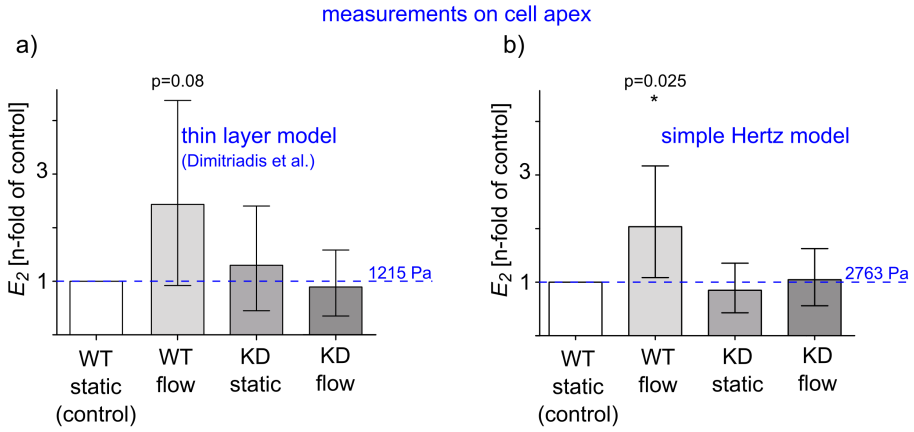

Figure 9.4: *Local Young's modulus $\langle E_2 \rangle^{mix}$ of HUVECs (normalized to control) measured on the cell apex pixels. Mean values with standard errors of the mean are shown.* ***a)*** *Data analyzed with the thin layer model of Dimitriadis et al. A pronounced, but not significant trend ($p = 0.08$) to increased $\langle E_2 \rangle^{mix}$ for WT HUVECs after shear stress exposure was observed. For the APLNR-KD HUVECs no change of $\langle E_2 \rangle^{mix}$ was observed.* ***b)*** *Data analyzed with the simple Hertz model. The Young's modulus $\langle E_2 \rangle^{mix}$ of WT HUVECs was found to be significantly increased after shear stress. Like in* ***a)*** *$\langle E_2 \rangle^{mix}$ did not change for shear stressed APLNR-KD HUVECs.*

ure 9.4a) revealed a stiffening of WT HUVECs induced by the shear flow. More exactly, the mean elastic modulus $\langle E_2 \rangle^{mix}$ of the WT HUVECs was increased

by 100.7% after three hours of shear flow exposure. The superscribed "mix" in $\langle E_2 \rangle^{mix}$ indicates here and in the following the use of a linear mixed-effects model for this calculation, which is described in the appendix (see A.3).

This finding fits with the observations of Sato et al. [15]. Nevertheless, the observed cell stiffening effect is not statistically significant ($p = 0.08$). Therefore, the observed trend was confirmed by a data analysis with the simple Hertz model ($p = 0.025$; Figure 9.4b). Here smaller standard errors of $\langle E_2 \rangle^{mix}$ appeared, compared to the analysis with the thin layer model. Interestingly, the same experiments carried out for APLNR-KD HUVECs (Figure 9.4a/b) did not show such a trend, neither for a data fitting with the simple Hertz model nor for a fitting with the thin layer model.

Nevertheless, the great amount of the HUVEC cell body shows much lower thicknesses h than the cell apex, as typically the cell thickness in the peripheral regions of HUVECs is between 500 nm and 1000 nm. For this reason, also the thin parts of the cells were investigated. For such thin samples the simple Hertz model is not applicable, as shown for the FVM presented in Figure 9.3. Hence, only the thin layer model of Dimitriadis et al. was used for the data analysis. The results of these investigations are shown in Figure 9.5. The ana-

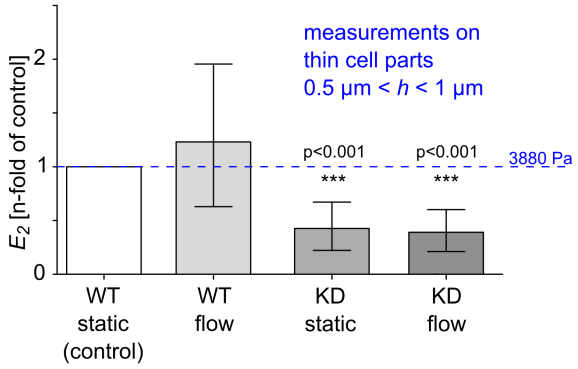

Figure 9.5: *Averaged Young's modulus $\langle E_2 \rangle^{mix}$ of HUVECs (normalized to control) for thin cell parts (0.5 µm < h < 1 µm). Mean values with standard errors of the mean are shown. Neither for WT nor for APLNR-KD HUVECs significant changes of $\langle E_2 \rangle^{mix}$ caused by the shear stress were observed. Interestingly, for this thin cell areas $\langle E_2 \rangle^{mix}$ of APLNR-KD cells was significantly reduced (60%, $p < 0.001$) compared to WT HUVECs.*

lysis revealed no significant cell stiffening in WT and APLNR-KD HUVECs after flow exposure. Nonetheless, Young's modulus E_2 of APLNR-KD cells

was found to be significantly reduced ($p < 0.001$) by approximately 60% in comparison to the WT (control) cells.

Moreover, interesting differences between WT and KD-HUVECs appeared by the comparison of the local elastic modulus E_2 of their thin and thick areas. The data of this investigation are shown in Figure 9.6. For example, comparing the thin areas ($0.5\ \mu\text{m} < h < 1\ \mu\text{m}$) with the thick (cell apex) areas of non-sheared WT HUVECs, the thin areas were found to show 2.15 times higher values of E_2 than the thick cell regions. An opposite trend was observed for non-sheared APLNR-KD HUVECs, which showed 1.31 times higher values of Young's modulus E_2 in the cell apex regions compared to their thin areas. Interestingly, after shear stress exposure for both cell types (WT and APLNR-KD cells) these differences were not found.

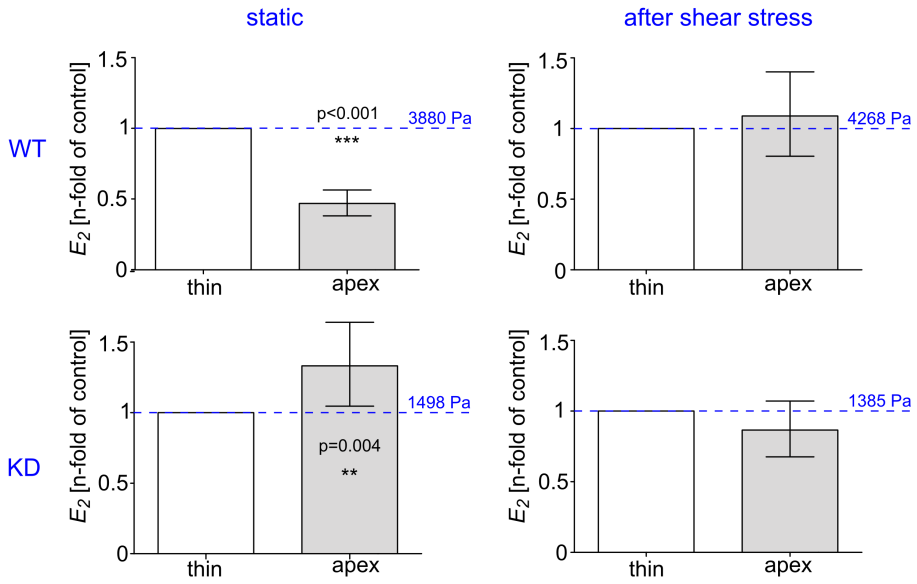

Figure 9.6: *Comparison of the cell elasticity in thick ("apex") and thin cell areas ("thin") using the thin layer model of Dimitriadis et al. (Eq. 2.47). Mean values with standard errors of the mean are shown. While for non-sheared Wild Type (WT) HUVECs the thin cell regions showed significantly increased values of Young's modulus $\langle E_2 \rangle^{mix}$ compared to their cell apex regions, for APLNR-Knock Down (KD) HUVECs the opposite was observed. After shear exposure both cell types (WT and KD cells) did not show significant differences between thin and thick cell parts.*

9.4 The influence of the APLNR on the cytoskeleton structure in Endothelial Cells (ECs)

There are more than 600 shear-stress regulated genes in ECs [205] which influence the entire function and morphology of ECs [195]. One influence of these genes was observed in altered ECs elastic properties [206, 18]. The elastic modulus E_2 of HUVECs is mainly determined by the subcellular density distribution, thickness, cross linking and structure of cytoskeletal filaments (see also Chapter 3) [207].

In order to elucidate the observed differences in HUVEC elasticity (Chapter 9.3.2), Confocal Laser Scanning Microscopy (CLSM) live cell imaging based investigations of the Cytoskeleton (CSK) were carried out. These investigations allowed the time resolved observation of F-actin as well as Tubulin and Intermediate Filaments in HUVECs. In Figure 9.7 representative 3D projections of the F-actin distribution in WT HUVECs are shown for different durations of physiological ESS (max 180 min).

A pronounced CSK remodeling was observed for all cell regions. Before onset of ESS ("*0 min*" in Figure 9.7), cells were randomly orientated and randomly oriented F-actin was concentrated in the cell periphery, forming band like structures. Over the nucleus only thin F-actin filaments were observed. With increasing duration of the Endothelial Shear Stress (ESS), the cell morphology aligned according to the flow direction (white arrow). Moreover, the HUVECs showed thicker aligned F-actin bundles and in the vicinity of the junctional surfaces (indicated by yellow arrows in Figure 9.7) a dense F-actin microfilament network was created by the cells. These microfilament frameworks partially covered the nuclei, a trend which has already been described by Galbraith et al. [198].

In contrast such a behavior was not found for APLNR-KD HUVECs with silenced APLNRs (Figure 9.8). For these cells almost no additional stress-fiber building after onset of physiologic laminar ESS was observed, and the cells showed no morphological alignment with the shear vector. Their F-actin fibers did not become thicker, remained mostly concentrated in peripheral bands and did not cover the central perinuclear part of the HUVECs. Moreover, some of

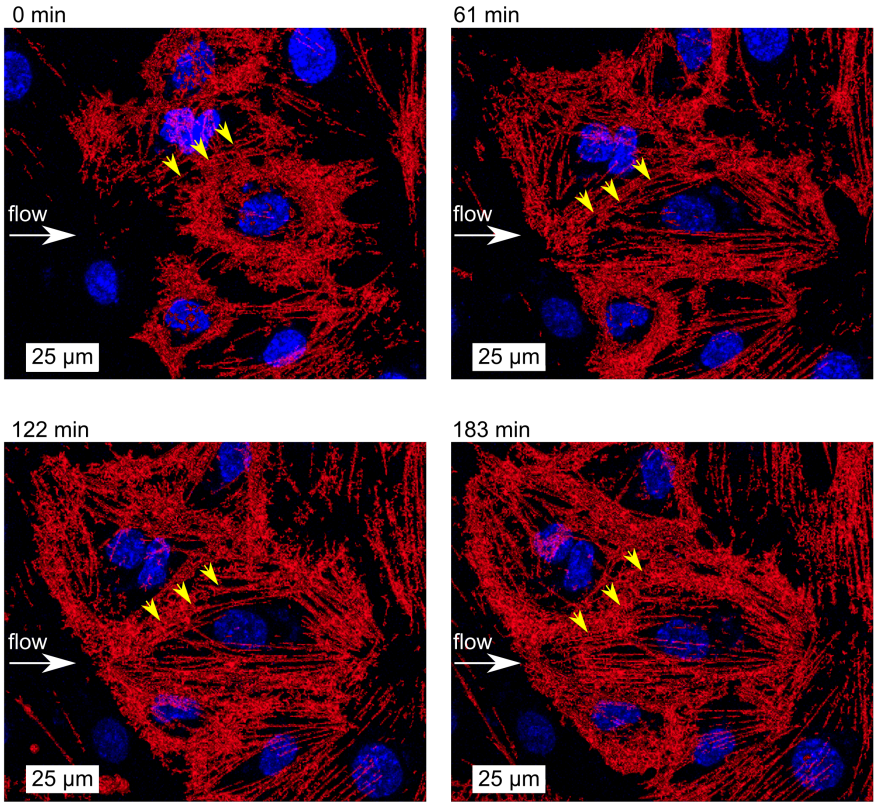

Figure 9.7: *Confocal Laser Scanning Microscopy (CLSM) images of the time dependent F-actin distribution in Wild Type (WT) HUVECs under flow. Red Fluorescent Protein (RFP; red) was used for staining the F-actin. Nuclei were stained in blue (NucBlue). As response to the shear stress of the flow, after three hours of flow the amount of F-actin is significantly increased and thick parallel F-actin bundles were formed by the cells. The yellow arrows indicate junctional surfaces. In the vicinity of these surfaces a strong increase of the F-actin density was observed after shear exposure.*

the cells contracted suddenly after onset of flow or lost their close attachment to neighboring cells in the monolayer (yellow arrows in Figure 9.8).

Please note, no reportable changes in Intermediate Filament (IF)- or Tubulin-structure were found for WT and APLNR-KD HUVECs (data not shown).

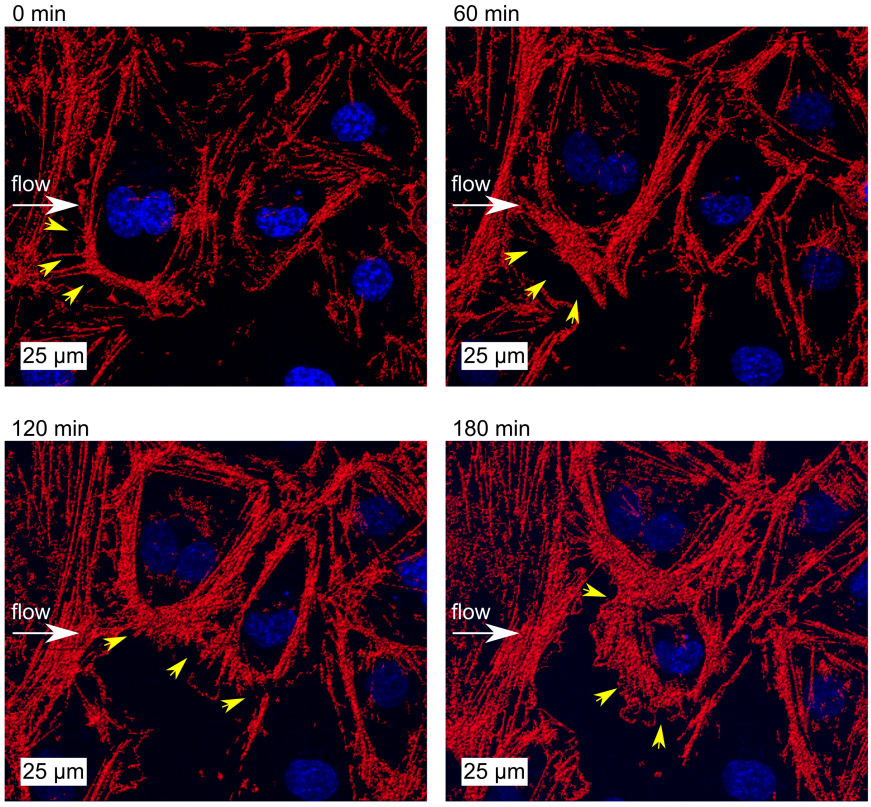

Figure 9.8: *Confocal Laser Scanning Microscopy (CLSM) images on the time dependent F-actin distribution in APLNR-KD HUVECs under flow. Red Fluorescent Protein (RFP; red) was used for staining the F-actin. Nuclei were stained in blue (NucBlue). No clear response to the shear stress of the flow was observed after three hours of flow, neither in the F-actin content nor in filament structure and direction.*

9.5 Discussion of the observations

The mechanical adaptation mechanisms of Endothelial Cell (EC) monolayers to various levels of shear stress has already been studied extensively using different techniques, such as flexible microposts or AFM [195, 208]. However, as these adaptation mechanisms are complex, there are still open questions and their description is still incomplete. The apelinergic system consisting of the APLNR and its specific ligand Apelin is described to have relevance for the regulation of fluid homeostasis[5] and is also expressed in significant levels in HUVECs [209, 210, 204]. It was shown that the apelinergic system in human ECs is ESS-regulated [202]. Here an *in vitro* perfusion model was used to investigate the impact of the endothelial G-protein coupled APLNR on the function and morphology of ECs under shear stress.

[5]fluid homeostasis: (dynamic) balance of body fluids

The APLNRs were shown to be located also in the junctional surfaces of HUVECs, which is an interesting finding, as this membrane compartment was shown to undergo the highest tension during flow-exposure. Additionally, a lot of mechanotransduction-related structures are located there [211]. **A linear relation between APLNR expression and duration of laminar ESS (Figure 9.2) was found**.

Contrary to other published shear stress investigations in which HUVECs were used as a model for arterial flow conditions, here **physiologic ESS** of 150 mN/m^2 was used for the AFM studies [212, 213]. Please note, that by the use of physiologic shear stress this study mimicked the flow conditions in the human body. Therefore, also by the reproduction of some results (e.g. shear-induced changes in WT elastic modulus or CSK structure) already published in the literature, new knowledge applicable for human biology was created.

In contrast to publications in the literature, here AFM FDCs have been analyzed with a thin layer model (of Dimitriatis et al.) and with the simple Hertz model. The use of the thin layer model reduced errors in the (absolute) estimation of E_2 originating from small cell thicknesses h. Interestingly, the observed standard errors of the mean $\langle E_2 \rangle^{mix}$ were larger for the thin layer model than for the simple Hertz model. Even if the observed shear-induced stiffening effect on WT HUVECs was not statistically significant for the thin layer model analysis, **the observed effect size was nearly the same as observed with the simple Hertz model**. By this, the application of the thin layer model supports the results already reported in the literature, and shows that the shear-induced cell stiffening effect is not caused by changes in cell thickness h. In other words, **the shear-induced cell stiffening is real, and not a measurement artifact caused by substrate effects.**

For the very thin cell parts ($h < 1$ μm) only a small cell stiffening (not statistically significant) was found. This is in good accordance with the data of Ohashi et al., who showed a significant cell stiffening especially for central cell compartments [18]. Ohashi et al. observed the stiffening after six hours of flow-exposure, while for the physiologic shear stress investigated here already after three hours cell stiffening was observed. For APLNR-KD HUVECs no

general trend of cell stiffening after flow onset was observed. Moreover, the mean elastic modulus $\langle E_2 \rangle^{mix}$ of the thin regions of APLNR-KD HUVECs was reduced compared to WT HUVECs for sheared and non-sheared cells. Therefore, **the function of APLNR seams to significantly contribute to the biomechanics of ECs and to the biomechanical adaptation mechanism of ECs to shear stress**.

The AFM-based cell elasticity results were furthermore correlated with detailed Confocal Laser Scanning Microscopy (CLSM) studies on the kinetics of the CSK and the APLNRs. While for tubulin and intermediate filaments no significant changes were observed due to the shear stress, AFM data and confocal data matched very well for F-actin. In WT HUVECs the creation of a dense F-actin network in the vicinity of the nucleus was observed as reaction to the shear stress. As the nucleus (which is known to act as mechanosensor in ECs [92]) is a prominent structure of the cell which undergoes great tension, the creation of this dense F-actin network might be interpretable as a stabilizing scaffold for the nucleus.

In general, the cell morphology and the F-actin fibers of the whole cells reoriented in shear direction. Moreover, a trend to the creation of thick F-actin bundles was observed in WT HUVECs. These CLSM data fit very well to previous publications [214]. In contrast, for the thinner WT HUVEC areas no significant increase in F-actin density was observed but a re-structuring of F-actin filaments was also detectable. For APLNR-KD HUVECs no significant changes neither in F-actin density nor in filament distribution were observed. Accordingly, **APLNR-KD endothelial cells are not able to accomplish a convenient F-actin fiber network as adaptation to current flow conditions**. That seems to be a suitable explanation for the reduced elasticity of sheared APLNR-KD cells.

9.6 Discussion of study limitations

The investigations and statistics described in this chapter have been carried out carefully, using 52 FVMs (20 x 20 FDCs, 100 μm x 100 μm). Each FVM included FDCs measured on approximately 5 - 15 cells. Even after the exclusion of some FDCs due to erroneous curve fitting (see Chapter 5) for each inves-

tigation sufficiently large data sets remained (32 - 50 cells; 282 - 446 FDCs). Nevertheless, a larger cell population might have been needed to show statistically significant the shear-induced WT HUVEC stiffening with the thin layer model of Dimitriadis et al. Furthermore, the tested HUVECs were settled on glass substrate, in order to allow cell adhesion and prevent them from being washed off of the substrate by the applied shear flow. This might have led to changes in the absolute cell elastic modulus E_2 [121]. Nevertheless, in this study only relative changes were reported, which might minimize the influence of this effect on the reported results.

Chapter 10

Conclusions and Outlook

10.1 Conclusions of the thesis

The Atomic Force Microscope (AFM) has become an important tool for probing the mechanical properties of cells and microparticles by force-indentation experiments. In this thesis optimized AFM approaches for these experiments are developed and applied to three types of living human cells in order to answer biologically relevant questions about their mechanics. These microscopic investigations are then interpreted with respect to nanoscopic and macroscopic biologic parameters, such as the function of cell surface receptors or the size of human heart ventricles. This thesis comprises two physical/technical chapters and three medical/biological chapters. The physical/technical chapters discuss the measurement process itself, aiming for its improvement with respect to a proper data analysis and contact model (for spherical cells). The medical/biological chapters investigate the elasticity of cells by the use of optimized AFM approaches, with respect to the used data analysis.

10.1.1 Physical/technical developments

First, a fast and reliable algorithm is developed, enabling the analysis of AFM Force-Distance Curves (FDCs) in a fully automated fashion. The algorithm is tested extensively via the analysis of large data sets, which were created in order to answer the medical/biological questions addressed in this thesis. The algorithm is implemented in MATLAB and is used to extract the two main parameters of this work from FDCs: the contact point z_0 of FDCs and the local Young's modulus E_2 of cells. Moreover, the algorithm strongly reduces

uncertainties in the determination of these parameters appearing when FDCs are analyzed manually or semi-automatically. Furthermore, the algorithm facilitates the fast analysis of large amounts of FDCs, as they may appear in clinical studies. An automatic estimation of the quality of the Young's modulus-determination is possible by the use of strict rules with regard to the Least Mean Squares (LMS) residuals appearing between obtained fit function and measured FDC. These residuals are determined for different parts of the FDCs.

Second, the proper measurement and analysis of FDCs, in the case of spherical weakly bound cells or cell-like particles, is addressed. Such measurements are under discussion in the literature, as spherical cells tend to roll or slide under the load of the AFM cantilever. To improve these measurements, flat wedged cantilevers are developed. Well defined smooth cantilever surfaces are needed for experiments. Using a new Electron Beam Lithography (EBL) approach, the production of cantilevers with such high quality wedges is enabled. Moreover, not only the measurement process itself, but also the contact models used for the analysis of FDCs, measured on soft spherical cells, are still under discussion. A novel *mixed double contact model* is derived. In contrast to single contact models (e.g. the simple Hertz model), which consider only one deformation site on the cell (the cell top), the new model considers two sites of deformation: the cell top, which is deformed by the AFM probe and the cell bottom part, which is deformed by cell-substrate interactions. The *mixed double contact model* describes the top part of the cell *via* the simple Hertz model, while its bottom part is described by the Johnson-Kendall-Roberts (JKR) theory. If FDCs (measured on spherical cells) are analyzed by the simple Hertz model, Young's modulus E_2 of the cell is underestimated. The occurring error is estimated. The *mixed double contact model* reduces this error, which is proofed by measurements on soft Polyethylene Glycol (PEG) microspheres.

10.1.2 Medical/biological investigations

In the first medical/biological part the local Young's modulus E_2 of living human Cardiac Fibroblasts (CFBs) is investigated in the context of Recent Onset Cardiomyopathy (ROCM), a severe heart disease. ROCM can involve the enlargement/dilation of human heart ventricles. For this purpose AFM Force Volume Measurements (FVMs) and single FDCs are measured on the

surface of CFBs. Measurements in the vicinity of the nucleus are shown to be representative for measurements carried out over the whole cell surface. Additionally, Young's modulus E_2 of CFBs derived from the Left heart Ventricle (LV) is found to be significantly lower than E_2 of CFBs out of the Right heart Ventricle (RV). Next to this, a strong negative correlation between the macroscopic diameter of the left heart ventricle and Young's modulus E_2 of the microscopic CFBs from this ventricle is shown. This implies a potentially new mechanism for macroscopic LV dilation observed in ROCM patients.

The second medical/biological part investigates the local Young's modulus E_2 of human neutrophil granulocytes (neutrophils) in the context of Transfusion Related Acute Lung Injury (TRALI), a severe effect of blood transfusion. Using AFM FVMs, for neutrophils having the Human Neutrophil Alloantigen-3a (HNA-3a) on their surface, a cell stiffening after the binding of specific antibodies to HNA-3a is observed. As numerous publications show a correlation between cell activation state and cell elasticity, the measurements are carried out on spherical non-activated neutrophils. This is achieved by a newly developed substrate coating procedure, preventing neutrophils from getting activated by cell-substrate interactions. The procedure allows to coat glass cover slips with Poly(2-hydroxyethyl methacrylate) (Poly-HEMA) spots of homogeneous lateral density. The observed antibody-induced cell stiffening might be an important aspect in the development of TRALI. By the application of the biochemical inhibitor Cytochalasin D (CD) the F-actin network in neutrophils is shown to be involved in this cell stiffening.

The third medical/biological part focuses on the Young's modulus E_2 of Human Umbilical Vein Endothelial Cells (HUVECs), stressed by physiologic shear forces. Young's modulus E_2 is determined in dependency of the function of the endothelial Apelin Receptor (APLNR). The investigations are carried out by AFM FVMs. The data analysis in the first physical/technical chapter is used to determine E_2 with two different contact models: the simple Hertz model and a thin layer model published by Dimitriadis et al.[41] The results of both models are compared and discussed for different areas on the cell surface. With both models a striking influence of the APLNR on Young's modulus E_2 of HUVECs and on their ability to adapt to shear forces is found. Cells with working APLNRs show an increased Young's modulus E_2 after shear exposure.

Using confocal microscopy, shear stress-induced changes in E_2 are correlated with rearrangements in the F-actin structure of the HUVEC Cytoskeleton (CSK). APLNR-deficient HUVECs are shown to be unable to rearrange their cytoskeleton properly when they are sheared.

10.2 Outlook

Cell elasticity has been shown to be an important marker for the state of cells, for example in the case of cancer. In order to establish routinely clinical screenings of the elasticity of (spherical) cells, the newly developed wedged cantilever could be used. Large amounts of soft human spherical cells, such as neutrophil granulocytes, could be probed fast and reliably. The cells could be situated on non-adhesive and non-cell-activating substrates, while they are probed in an automated fashion. For this purpose an AFM could be equipped with an optical image analyzing software, steering the AFM cantilever to the cells, in order to probe them. The here developed algorithm for the analysis of AFM FDCs (Chapter 5) could be used to analyze the appearing large amounts of FDCs with the novel *mixed double contact model*.
In this thesis biophysical basics were investigated and new medical/biological insights were obtained. These biophysical observations give rise to address new questions concerning their biochemical reasons. For example, for the CFBs investigated in the context of ROCM, the biochemical causality of the decreased Young's modulus of CFBs from the diseased/dilated left ventricle has to be investigated in further studies. In the case of TRALI, for neutrophil granulocytes, the biochemical signaling cascade inducing the cell stiffening after activation of HNA-3a, still needs to be investigated. The same is true for the observed shear stress-induced cell stiffening in HUVECs. Here the biochemical signaling cascade induced by the APLNR has to be studied in future investigations.

Bibliography

[1] R. Hooke, *Micrographia*, Royal Society, London, 1665.

[2] G. Mendel, *Proceedings of the Natural History Society of Brünn* , 3 (1865).

[3] F. Baltzer, *Science* **144**, 809 (1964).

[4] W. S. Sutton, *Biological Bulletin* **4**, 24 (1902).

[5] J. D. Watson and F. H. C. Crick, *Nature* **171**, 737 (1953).

[6] C. elegans Sequencing Consortium, *Science* **282**, 2012 (1998).

[7] S. C. Kozma and G. Thomas, *Bioessays* **24**, 65 (2002).

[8] S. Y. Ko, I. H. Lin, T. M. Shieh, H. A. Ko, H. I. Chen, T. C. Chi, S. S. Chang, and Y. C. Hsu, *Cell Biochemistry and Biophysics* **66**, 537 (2013).

[9] S. K. Powers, M. P. Wiggs, J. A. Duarte, A. M. Zergeroglu, and H. A. Demirel, *American Journal of Physiology-Endocrinology and Metabolism* **303**, E31 (2012).

[10] D. Di Carlo, *Jala* **17**, 32 (2012).

[11] M. J. Mela, *Biophysical Journal* **7**, 95 (1967).

[12] M. Plodinec, M. Loparic, C. A. Monnier, E. C. Obermann, R. Zanetti-Dallenbach, P. Oertle, J. T. Hyotyla, U. Aebi, M. Bentires-Alj, R. Y. H. Lim, and C. A. Schoenenberger, *Nature Nanotechnology* **7**, 757 (2012).

[13] E. C. Faria, N. Ma, E. Gazi, P. Gardner, M. Brown, N. W. Clarke, and R. D. Snooka, *Analyst* **133**, 1498 (2008).

[14] M. M. Brandao, A. Fontes, M. L. Barjas-Castro, L. C. Barbosa, F. F. Costa, C. L. Cesar, and S. T. O. Saad, *European Journal of Haematology* **70**, 207 (2003).

[15] M. Sato, K. Nagayama, N. Kataoka, M. Sasaki, and K. Hane, *Journal of Biomechanics* **33**, 127 (2000).

[16] A. M. Collinsworth, S. Zhang, W. E. Kraus, and G. A. Truskey, *American Journal of Physiology-Cell Physiology* **283**, C1219 (2002).

[17] N. Walter, T. Busch, T. Seufferlein, and J. P. Spatz, *Biointerphases* **6**, 79 (2011).

[18] T. Ohashi, Y. Ishii, Y. Ishikawa, T. Matsumoto, and M. Sato, *Bio-Medical Materials and Engineering* **12**, 319 (2002).

[19] C. Rotsch and M. Radmacher, *Biophysical Journal* **78**, 520 (2000).

[20] J. Solon, I. Levental, K. Sengupta, P. C. Georges, and P. A. Janmey, *Biophysical Journal* **93**, 4453 (2007).

[21] T. G. Kuznetsova, M. N. Starodubtseva, N. I. Yegorenkov, S. A. Chizhik, and R. I. Zhdanov, *Micron* **38**, 824 (2007).

[22] I. Dulinska, M. Targosz, W. Strojny, M. Lekka, P. Czuba, W. Balwierz, and M. Szymonski, *Journal of Biochemical and Biophysical Methods* **66**, 1 (2006).

[23] M. Lekka, D. Gil, K. Pogoda, J. Dulinska-Litewka, R. Jach, J. Gostek, O. Klymenko, S. Prauzner-Bechcicki, Z. Stachura, J. Wiltowska-Zuber, K. Okon, and P. Laidler, *Archives of Biochemistry and Biophysics* **518**, 151 (2012).

[24] R. M. Bauersachs and H. J. Meiselman, *Clinical Hemorheology* **6**, 459 (1986).

[25] P. S. Sit, A. A. Spector, A. J. C. Lue, A. S. Popel, and W. E. Brownell, *Biophysical Journal* **72**, 2812 (1997).

[26] M. Puig-de Morales, M. Grabulosa, J. Alcaraz, J. Mullol, G. N. Maksym, J. J. Fredberg, and D. Navajas, *Journal of Applied Physiology* **91**, 1152 (2001).

[27] P. A. Valberg and J. P. Butler, *Biophysical Journal* **52**, 537 (1987).

[28] S. H. Cartmell, A. Keramane, G. R. Kirkham, S. B. Verschueren, J. L. Magnay, A. J. El Haj, and J. Dobson, *Fifth International Conference on Fine Particle Magnetism* **17**, 77 (2005).

[29] J. Sleep, D. Wilson, R. Simmons, and W. Gratzer, *Biophysical Journal* **77**, 3085 (1999).

[30] K. Q. Wang, J. P. Cheng, S. H. Cheng, and D. Sun, *Applied Physics Letters* **103** (2013).

[31] J. A. Hildebrand and D. Rugar, *Journal of Microscopy-Oxford* **134**, 245 (1984).

[32] R. Dalal and S. C. Kuo, *Molecular Biology of the Cell* **10**, 30a (1999).

[33] H. J. Butt, B. Cappella, and M. Kappl, *Surface Science Reports* **59**, 1 (2005).

[34] D. C. Lin, E. K. Dimitriadis, and F. Horkay, *Journal of Biomechanical Engineering-Transactions of the Asme* **129**, 430 (2007).

[35] R. M. Hochmuth, *Journal of Biomechanics* **33**, 15 (2000).

[36] R. Benitez, S. Moreno-flores, V. J. Bolos, and J. L. Toca-Herrera, *Microscopy Research and Technique* **76**, 870 (2013).

[37] U. G. Hofmann, C. Rotsch, W. J. Parak, and M. Radmacher, *Journal of Structural Biology* **119**, 84 (1997).

[38] I. M. Tolic-Norrelykke and N. Wang, *Journal of Biomechanics* **38**, 1405 (2005).

[39] Y. Ni and M. Y. M. Chiang, *Soft Matter* **3**, 1285 (2007).

[40] H. Hertz, *Journal für die reine und angewandte Mathematik* **92**, 156 (1881).

[41] E. K. Dimitriadis, F. Horkay, J. Maresca, B. Kachar, and R. S. Chadwick, *Biophysical Journal* **82**, 2798 (2002).

[42] F. Rico, P. Roca-Cusachs, N. Gavara, R. Farre, M. Rotger, and D. Navajas, *Physical Review E* **72** (2005).

[43] L. Sirghi, J. Ponti, F. Broggi, and F. Rossi, *European Biophysics Journal with Biophysics Letters* **37**, 935 (2008).

[44] M. J. Rosenbluth, W. A. Lam, and D. A. Fletcher, *Biophysical Journal* **90**, 2994 (2006).

[45] M. P. Stewart, A. W. Hodel, A. Spielhofer, C. J. Cattin, D. J. Muller, and J. Helenius, *Methods* **60**, 186 (2013).

[46] L. Landau and E. Lifshitz, *Lehrbuch der theoretischen Physik - VII Elastizitätstheorie*, Verlag Harri Deutsch, Frankfurt am Main, 7 edition, 2010.

[47] A. Spencer, *Continuum mechanics*, Dover Publications, Mineola (N.Y.), 2004.

[48] P. Ciarlet, *Mathematical Elasticity*, volume 1, Elsevier Science Publishers B.V., Amsterdam, The Netherlands, 1988.

[49] W. Becker and D. Gross, *Mechanik elastischer K´orper und Strukturen*, volume 1, Springer-Verlag, Berlin, Heidelberg, New York, 2002.

[50] L. Segerlind, *Applied finite element analysis*, John Wiley & Sons, Inc., New York, N.Y., 1984.

[51] M. Silhavy, *The Mechanics and Thermodynamics of Continuous Media*, volume 14, Springer-Verlag, Heidelberg, Germany, 1997.

[52] W. Slaughter, *The linearized theory of elasticity*, Bikhäuser, Boston, 2002.

[53] V. H. Carneiro, J. Meireles, and H. Puga, *Materials Science-Poland* **31**, 561 (2013).

[54] J. M. J. den Toonder, J. A. W. van Dommelen, and F. P. T. Baaijens, *Modelling and Simulation in Materials Science and Engineering* **7**, 909 (1999).

[55] K. L. Johnson, K. Kendall, and A. D. Roberts, *Proc. R. Soc. Lond. A* **324** (1971).

[56] M. T. Kim, *Thin Solid Films* **283**, 12 (1996).

[57] J. Domke and M. Radmacher, *Langmuir* **14**, 3320 (1998).

[58] F. Q. Yang, *Mechanics of Materials* **30**, 275 (1998).

[59] R. S. Chadwick, *Siam Journal on Applied Mathematics* **62**, 1520 (2002).

[60] G. X. Cao and N. Chandra, *Physical Review E* **81** (2010).

[61] J. D. Humphrey, *Cardiovascular Solid Mechanics: Cells, Tissues and Organs*, Springer-Verlag, New York, 2002.

[62] D. Boal, *Mechanics of the Cell*, Cambridge University Press, 2 edition, 2012.

[63] J. Kas, H. Strey, J. X. Tang, D. Finger, R. Ezzell, E. Sackmann, and P. A. Janmey, *Biophysical Journal* **70**, 609 (1996).

[64] T. Heimburg, *Thermal Biophysics of Membranes*, WILEY-VCH, Weinheim, Germany, 2007.

[65] D. Marsh, *European Biophysics Journal with Biophysics Letters* **39**, 513 (2010).

[66] S. J. Singer and G. L. Nicolson, *Science* **175**, 720 (1972).

[67] G. Muller, *Febs Letters* **531**, 81 (2002).

[68] S. Takahashi and P. M. Pryciak, *Current Biology* **18**, 1184 (2008).

[69] Y. Hayashi, D. T. Asuzu, S. J. Gibbons, K. H. Aarsvold, M. R. Bardsley, G. A. Lomberk, A. J. Mathison, M. L. Kendrick, K. R. Shen, T. Taguchi, A. Gupta, B. P. Rubin, J. A. Fletcher, G. Farrugia, R. A. Urrutia, and T. Ordog, *Plos One* **8** (2013).

[70] J. S. Clegg, *American Journal of Physiology* **246**, R133 (1984).

[71] K. Luby-Phelps, *International Review of Cytology - a Survey of Cell Biology, Vol 192* **192**, 189 (2000).

[72] W. R. Trickey, F. P. T. Baaijens, T. A. Laursen, L. G. Alexopoulos, and F. Guilak, *Journal of Biomechanics* **39**, 78 (2006).

[73] O. Lieleg, M. M. A. E. Claessens, and A. R. Bausch, *Soft Matter* **6**, 218 (2010).

[74] M. Mofrad and R. Kamm, *Cytoskeletal Mechanics*, Cambridge University Press, 2011.

[75] F. Huber, J. Schnauss, S. Ronicke, P. Rauch, K. Muller, C. Futterer, and J. Kas, *Advances in Physics* **62**, 1 (2013).

[76] Y. C. Lin, G. H. Koenderink, F. C. MacKintosh, and D. A. Weitz, *Soft Matter* **7**, 902 (2011).

[77] A. Vandecandelaere, S. R. Martin, M. J. Schilstra, and P. M. Bayley, *Biochemistry* **33**, 2792 (1994).

[78] F. Gittes, B. Mickey, J. Nettleton, and J. Howard, *Journal of Cell Biology* **120**, 923 (1993).

[79] W. Q. Yu and P. W. Baas, *Journal of Neuroscience* **14**, 2818 (1994).

[80] M. K. Gardner, M. Zanic, C. Gell, V. Bormuth, and J. Howard, *Cell* **147**, 1092 (2011).

[81] C. Storm, J. J. Pastore, F. C. MacKintosh, T. C. Lubensky, and P. A. Janmey, *Nature* **435**, 191 (2005).

[82] V. Pelletier, N. Gal, P. Fournier, and M. L. Kilfoil, *Physical Review Letters* **102** (2009).

[83] N. Wang and D. Stamenovic, *American Journal of Physiology-Cell Physiology* **279**, C188 (2000).

[84] Y. C. Lin, N. Y. Yao, C. P. Broedersz, H. Herrmann, F. C. MacKintosh, and D. A. Weitz, *Physical Review Letters* **104** (2010).

[85] P. A. Janmey, *Living Cell in Four Dimensions* **226**, 304 (1991).

[86] E. Fuchs and D. W. Cleveland, *Science* **279**, 514 (1998).

[87] T. D. Pollard, *Annual Review of Biophysics and Biomolecular Structure* **36**, 451 (2007).

[88] S. Tojkander, G. Gateva, and P. Lappalainen, *Journal of Cell Science* **125**, 1855 (2012).

[89] M. L. Gardel, J. H. Shin, F. C. MacKintosh, L. Mahadevan, P. Matsudaira, and D. A. Weitz, *Science* **304**, 1301 (2004).

[90] H. J. Price, A. H. Sparrow, and A. F. Nauman, *Experientia* **29**, 1028 (1973).

[91] I. G. Minkevich and L. I. Patrushev, *Russian Journal of Bioorganic Chemistry* **33**, 439 (2007).

[92] E. Tkachenko, E. Gutierrez, S. K. Saikin, P. Fogelstrand, C. Kim, A. Groisman, and M. H. Ginsberg, *Biol Open* **2**, 1007 (2013).

[93] F. Guilak, J. R. Tedrow, and R. Burgkart, *Biochemical and Biophysical Research Communications* **269**, 781 (2000).

[94] N. Caille, O. Thoumine, Y. Tardy, and J. J. Meister, *Journal of Biomechanics* **35**, 177 (2002).

[95] W. D. Merryman, P. D. Bieniek, F. Guilak, and M. S. Sacks, *Journal of Biomechanical Engineering-Transactions of the Asme* **131** (2009).

[96] S. Kumar, I. Z. Maxwell, A. Heisterkamp, T. R. Polte, T. P. Lele, M. Salanga, E. Mazur, and D. E. Ingber, *Biophysical Journal* **90**, 3762 (2006).

[97] B. A. Smith, B. Tolloczko, J. G. Martin, and P. Grutter, *Biophysical Journal* **88**, 2994 (2005).

[98] R. E. Mahaffy, J. Kas, and C. K. Shih, *Biophysical Journal* **78**, 379a (2000).

[99] D. Ambrosi and P. Ciarletta, *International Journal of Non-Linear Mechanics* **56**, 56 (2013).

[100] H. Haga, S. Sasaki, K. Kawabata, E. Ito, T. Ushiki, and T. Sambongi, *Ultramicroscopy* **82**, 253 (2000).

[101] X. L. Shi, L. Qin, X. J. Zhang, K. M. He, C. Y. Xiong, J. Fang, X. H. Fang, and Y. Y. Zhang, *Physical Chemistry Chemical Physics* **13**, 7540 (2011).

[102] S. Vichare, M. M. Inamdar, and S. Sen, *Soft Matter* **8**, 10464 (2012).

[103] W. Kern and J. Vossen, *Thin film processes*, volume 1, Academic Press, New York, 1978.

[104] W. Kern, *Handbook of Semiconductor Cleaning Technology*, Noyes Publications, Park Ridge, 1993.

[105] J. P. Cleveland, S. Manne, D. Bocek, and P. K. Hansma, *Review of Scientific Instruments* **64**, 403 (1993).

[106] H. J. Butt and M. Jaschke, *Nanotechnology* **6**, 1 (1995).

[107] P. M. Morse and H. Freshbach, *Methods of Theoretical Physics*, McGraw-Hill, New York, 1953.

[108] J. E. Sader, J. W. M. Chon, and P. Mulvaney, *Review of Scientific Instruments* **70**, 3967 (1999).

[109] S. Block, *On Surface Forces and morphology of linear polyelectrolytes physisorbed onto oppositely charged surfaces*, PhD thesis, 2010.

[110] J. E. Sader, *Journal of Applied Physics* **84**, 64 (1998).

[111] D. Johnson, N. Hilal, and W. Bowen, *Basic Principles of Atomic Force Microscopy*, Elsevier, 2009.

[112] D. Pussak, M. Behra, S. Schmidt, and L. Hartmann, *Soft Matter* **8**, 1664 (2012).

[113] D. Pussak, D. Ponader, S. Mosca, S. V. Ruiz, L. Hartmann, and S. Schmidt, *Angewandte Chemie-International Edition* **52**, 6084 (2013).

[114] L. Hartmann, K. Watanabe, L. L. Zheng, C. Y. Kim, S. E. Beck, P. Huie, J. Noolandi, J. R. Cochran, C. N. Ta, and C. W. Frank, *Journal of Biomedical Materials Research Part B-Applied Biomaterials* **98B**, 8 (2011).

[115] J. Bux and J. Chapman, *Transfusion* **37**, 977 (1997).

[116] E. A. Jaffe, R. L. Nachman, C. G. Becker, and C. R. Minick, *Journal of Clinical Investigation* **52**, 2745 (1973).

[117] J. Riedl, A. H. Crevenna, K. Kessenbrock, J. H. Yu, D. Neukirchen, M. Bista, F. Bradke, D. Jenne, T. A. Holak, Z. Werb, M. Sixt, and R. Wedlich-Soldner, *Nature Methods* **5**, 605 (2008).

[118] Y. M. Efremov, E. V. Dzyubenko, D. V. Bagrov, G. V. Maksimov, S. I. Shram, and K. V. Shaitan, *Acta Naturae* **3**, 93 (2011).

[119] C. Rotsch, F. Braet, E. Wisse, and M. Radmacher, *Cell Biology International* **21**, 685 (1997).

[120] J. L. Hutter, J. Chen, W. K. Wan, S. Uniyal, M. Leabu, and B. M. C. Chan, *Journal of Microscopy-Oxford* **219**, 61 (2005).

[121] P. Roca-Cusachs, I. Almendros, R. Sunyer, N. Gavara, R. Farre, and D. Navajas, *Biophysical Journal* **91**, 3508 (2006).

[122] C. Schulze, K. Muller, J. A. Kas, and J. C. Gerdelmann, *Cell Motility and the Cytoskeleton* **66**, 193 (2009).

[123] C. B. Lombello, S. M. Malmonge, and M. L. F. Wada, *Journal of Materials Science-Materials in Medicine* **11**, 541 (2000).

[124] P. A. Klein, J. H. Xiang, and A. K. Kimura, *Clinical & Experimental Metastasis* **2**, 287 (1984).

[125] G. P. Raeber, M. P. Lutolf, and J. A. Hubbell, *Biophysical Journal* **89**, 1374 (2005).

[126] M. Kalin and M. Polajnar, *Applied Surface Science* **293**, 97 (2014).

[127] Y. L. Chen, C. A. Helm, and J. N. Israelachvili, *Journal of Physical Chemistry* **95**, 10736 (1991).

[128] D. F. Gerson and J. Akit, *Biochim Biophys Acta* **602**, 281 (1980).

[129] L. F. Dumee, S. Gray, M. Duke, K. Sears, J. Schutz, and N. Finn, *Desalination* **323**, 22 (2013).

[130] M. Kalin and M. Polajnar, *Tribology International* **66**, 225 (2013).

[131] V. Lulevich, T. Zink, H. Y. Chen, F. T. Liu, and G. Y. Liu, *Langmuir* **22**, 8151 (2006).

[132] A. Khan, J. Philip, and P. Hess, *Journal of Applied Physics* **95**, 1667 (2004).

[133] D. Pesen and J. H. Hoh, *Biophysical Journal* **88**, 670 (2005).

[134] K. Hidaka, L. Moine, G. Collin, D. Labarre, J. L. Grossiord, N. Huang, K. Osuga, S. Wada, and A. Laurent, *Journal of the Mechanical Behavior of Biomedical Materials* **4**, 2161 (2011).

[135] M. E. Dokukin, N. V. Guz, and I. Sokolov, *Biophysical Journal* **104**, 2123 (2013).

[136] D. P. E. Smith, *Review of Scientific Instruments* **66**, 3191 (1995).

[137] A. R. Harris and G. T. Charras, *Nanotechnology* **22** (2011).

[138] G. R. Wood, *Mathematical Programming* **55**, 319 (1992).

[139] W. H. Grover, A. K. Bryan, M. Diez-Silva, S. Suresh, J. M. Higgins, and S. R. Manalis, *Proceedings of the National Academy of Sciences of the United States of America* **108**, 10992 (2011).

[140] T. P. Burg, M. Godin, S. M. Knudsen, W. Shen, G. Carlson, J. S. Foster, K. Babcock, and S. R. Manalis, *Nature* **446**, 1066 (2007).

[141] D. M. McNamara, R. C. Starling, L. T. Cooper, J. P. Boehmer, P. J. Mather, K. M. Janosko, r. Gorcsan, J., K. E. Kip, and G. W. Dec, *Journal of the American College of Cardiology* **58**, 1112 (2011).

[142] J. Stypmann, K. Glaser, W. Roth, D. J. Tobin, I. Petermann, R. Matthias, G. Monnig, W. Haverkamp, G. Breithardt, W. Schmahl, C. Peters, and T. Reinheckel, *Proceedings of the National Academy of Sciences of the United States of America* **99**, 6234 (2002).

[143] D. J. Marchant, J. H. Boyd, D. C. Lin, D. J. Granville, F. S. Garmaroudi, and B. M. McManus, *Circ Res* **110**, 126 (2012).

[144] B. J. Maron, J. A. Towbin, G. Thiene, C. Antzelevitch, D. Corrado, D. Arnett, A. J. Moss, C. E. Seidman, and J. B. Young, *Circulation* **113**, 1807 (2006).

[145] A. Sadeghpour, M. Shahrabi, H. Bakhshandeh, and N. Naderi, *Arch Cardiovasc Imaging* **1**, 72 (2013).

[146] F. Tarasoutchi, M. Grinberg, G. S. Spina, R. O. Sampaio, L. Cardoso, E. G. Rossi, P. Pomerantzeff, F. Laurindo, P. L. da Luz, and J. A. Ramires, *Journal of the American College of Cardiology* **41**, 1316 (2003).

[147] P. A. Harvey and L. A. Leinwand, *Journal of Cell Biology* **194**, 355 (2011).

[148] D. Fan, A. Takawale, J. Lee, and Z. Kassiri, *Fibrogenesis Tissue Repair* **5**, 15 (2012).

[149] E. M. Zeisberg and R. Kalluri, *Circ Res* **107**, 1304 (2010).

[150] A. Heling, R. Zimmermann, S. Kostin, Y. Maeno, S. Hein, B. Devaux, E. Bauer, W. P. Klovekorn, M. Schlepper, W. Schaper, and J. Schaper, *Circ Res* **86**, 846 (2000).

[151] H. Tsutsui, K. Ishihara, and G. t. Cooper, *Science* **260**, 682 (1993).

[152] D. Westermann, D. Lindner, M. Kasner, C. Zietsch, K. Savvatis, F. Escher, J. von Schlippenbach, C. Skurk, P. Steendijk, A. Riad, W. Poller, H. P. Schultheiss, and C. Tschope, *Circulation-Heart Failure* **4**, 44 (2011).

[153] C. Klockenbusch and J. Kast, *Journal of Biomedicine and Biotechnology* (2010).

[154] G. Toprak, H. Yuksel, O. Demirpence, Y. Islamoglu, O. Evliyaoglu, and N. Mete, *European Review for Medical and Pharmacological Sciences* **17**, 2302 (2013).

[155] A. Riad, D. Westermann, F. Escher, P. M. Becher, K. Savvatis, O. Lettau, M. M. Heimesaat, S. Bereswill, H. D. Volk, H. P. Schultheiss, and C. Tschope, *American Journal of Physiology-Heart and Circulatory Physiology* **298**, H2024 (2010).

[156] A. Riad, D. Westermann, C. Zietsch, K. Savvatis, P. M. Becher, S. Bereswill, M. M. Heimesaat, O. Lettau, D. Lassner, A. Dorner, W. Poller, M. Busch, S. B. Felix, H. P. Schultheiss, and C. Tschope, *Journal of Immunology* **186**, 2561 (2011).

[157] S. Lehrke, D. Lossnitzer, M. Schob, H. Steen, C. Merten, H. Kemmling, R. Pribe, P. Ehlermann, C. Zugck, G. Korosoglou, E. Giannitsis, and H. A. Katus, *Heart* **97**, 727 (2011).

[158] M. T. Elnakish, M. D. H. Hassona, M. A. Alhaj, L. Moldovan, P. M. L. Janssen, M. Khan, and H. H. Hassanain, *Plos One* **7** (2012).

[159] A. Yilmaz, I. Kindermann, M. Kindermann, F. Mahfoud, C. Ukena, A. Athanasiadis, S. Hill, H. Mahrholdt, M. Voehringer, M. Schieber, K. Klingel, R. Kandolf, M. Bohm, and U. Sechtem, *Circulation* **122**, 900 (2010).

[160] I. Kindermann, *Circulation* **118**, E493 (2008).

[161] B. Lubiszewska, E. Gosiewska, P. Hoffman, A. Teresinska, J. Rozanski, W. Piotrowski, W. Rydlewska-Sadowska, K. Kubicka, and W. Ruzyllo, *Journal of the American College of Cardiology* **36**, 1365 (2000).

[162] S. S. An, B. Fabry, X. Trepat, N. Wang, and J. J. Fredberg, *Am J Respir Cell Mol Biol* **35**, 55 (2006).

[163] J. Cruz, E. Skipworth, D. Blue, D. Waxman, L. McCarthy, and D. Smith, *Journal of Clinical Apheresis* **23**, 96 (2008).

[164] M. A. Popovsky and S. B. Moore, *Transfusion* **24**, 433 (1984).

[165] J. Bux, *Vox Sanguinis* **94**, 277 (2008).

[166] B. R. Curtis, N. J. Cox, M. J. Sullivan, A. Konkashbaev, K. Bowens, K. Hansen, and R. H. Aster, *Blood* **115**, 2073 (2010).

[167] M. de Haas, E. Muniz-Diaz, L. G. Alonso, K. van der Kolk, M. Kos, L. Buddelmeijer, L. Porcelijn, and A. E. G. K. von dem Borne, *Transfusion* **40**, 222 (2000).

[168] A. Greinacher, J. Wesche, E. Hammer, B. Furll, U. Volker, A. Reil, and J. Bux, *Nature Medicine* **16**, 45 (2010).

[169] L. Holness, M. A. Knippen, L. Simmons, and P. A. Lachenbruch, *Transfusion Medicine Reviews* **18**, 184 (2004).

[170] A. Davoren, B. R. Curtis, I. A. Shulman, A. F. Mohrbacher, J. Bux, B. J. Kwiatkowska, J. G. McFarland, and R. H. Aster, *Transfusion* **43**, 641 (2003).

[171] G. S. Worthen, B. Schwab, E. L. Elson, and G. P. Downey, *Science* **245**, 183 (1989).

[172] M. Bathe, A. Shirai, C. M. Doerschuk, and R. D. Kamm, *Biophysical Journal* **83**, 1917 (2002).

[173] M. L. Nystrom, M. A. Barradas, and D. P. Mikhailidis, *Platelets* **4**, 156 (1993).

[174] V. Witko-Sarsat, P. Rieu, B. Descamps-Latscha, P. Lesavre, and L. Halbwachs-Mecarelli, *Laboratory Investigation* **80**, 617 (2000).

[175] D. C. Dale, L. Boxer, and W. C. Liles, *Blood* **112**, 935 (2008).

[176] J. Wang and H. Arase, *Ann N Y Acad Sci* (2014).

[177] J. Bux, *Vox Sanguinis* **100**, 122 (2011).

[178] N. B. Sorensen, H. L. Nielsen, K. Varming, and H. Nielsen, *Gut Pathogens* **5** (2013).

[179] G. P. Downey, D. E. Doherty, B. Schwab, E. L. Elson, P. M. Henson, and G. S. Worthen, *Journal of Applied Physiology* **69**, 1767 (1990).

[180] A. Arcaro and M. P. Wymann, *Biochemical Journal* **296**, 297 (1993).

[181] G. Cicchetti, P. G. Allen, and M. Glogauer, *Critical Reviews in Oral Biology & Medicine* **13**, 220 (2002).

[182] J. F. Casella, M. D. Flanagan, and S. Lin, *Nature* **293**, 302 (1981).

[183] J. A. May, H. Ratan, J. R. Glenn, W. Losche, and P. Spangenberg, *Thromb Haemost* , P2706 (1997).

[184] T. Oda, M. Iwasa, T. Aihara, Y. Maeda, and A. Narita, *Nature* **457**, 441 (2009).

[185] A. R. Pries, T. W. Secomb, and P. Gaehtgens, *Pflugers Archiv-European Journal of Physiology* **440**, 653 (2000).

[186] C. M. Kolka and R. N. Bergman, *Physiology* **27**, 237 (2012).

[187] B. E. Sumpio, J. T. Riley, and A. Dardik, *International Journal of Biochemistry & Cell Biology* **34**, 1508 (2002).

[188] P. M. Vanhoutte, *Hypertension* **13**, 658 (1989).

[189] J. P. Cooke, E. Rossitch, N. A. Andon, J. Loscalzo, and V. J. Dzau, *Journal of Clinical Investigation* **88**, 1663 (1991).

[190] A. Shay-Salit, M. Shushy, E. Wolfovitz, H. Yahav, F. Breviario, E. Dejana, and N. Resnick, *Proceedings of the National Academy of Sciences of the United States of America* **99**, 9462 (2002).

[191] J. Y. Shyy and S. Chien, *Circ Res* **91**, 769 (2002).

[192] G. Siegel, M. Malmsten, D. Klussendorf, A. Walter, F. Schnalke, and A. Kauschmann, *Journal of the Autonomic Nervous System* **57**, 207 (1996).

[193] B. P. Hierck, K. Van der Heiden, F. E. Alkemade, S. V. de Pas, J. V. Van Thienen, B. C. W. Groenendijk, W. H. Bax, A. Van der Laarse, M. C. DeRuiter, A. J. G. Horrevoets, and R. E. Poelmann, *Developmental Dynamics* **237**, 725 (2008).

[194] S. Gudi, J. P. Nolan, and J. A. Frangos, *Proceedings of the National Academy of Sciences of the United States of America* **95**, 2515 (1998).

[195] P. F. Davies, *Physiol Rev* **75**, 519 (1995).

[196] A. M. Malek and S. Izumo, *Journal of Cell Science* **109**, 713 (1996).

[197] B. P. Helmke and P. F. Davies, *Annals of Biomedical Engineering* **30**, 284 (2002).

[198] C. G. Galbraith, R. Skalak, and S. Chien, *Cell Motility and the Cytoskeleton* **40**, 317 (1998).

[199] S. McCue, S. Noria, and B. L. Langille, *Trends in Cardiovascular Medicine* **14**, 143 (2004).

[200] S. R. P. Gudi, C. B. Clark, and J. A. Frangos, *Circ Res* **79**, 834 (1996).

[201] M. Chachisvilis, Y. L. Zhang, and J. A. Frangos, *Proceedings of the National Academy of Sciences of the United States of America* **103**, 15463 (2006).

[202] A. Strohbach, M. C. Busch, S. B. Felix, and R. Busch, *European Heart Journal* **32**, 521 (2011).

[203] M. C. Scimia, C. Hurtado, S. Ray, S. Metzler, K. Wei, J. M. Wang, C. E. Woods, N. H. Purcell, D. Catalucci, T. Akasaka, O. F. Bueno, G. P. Vlasuk, P. Kaliman, R. Bodmer, L. H. Smith, E. Ashley, M. Mercola, J. H. Brown, and P. Ruiz-Lozano, *Nature* **488**, 394 (2012).

[204] M. J. Kleinz, J. N. Skepper, and A. P. Davenport, *Regulatory Peptides* **126**, 233 (2005).

[205] N. Ohura, K. Yamamoto, S. Ichioka, T. Sokabe, H. Nakatsuka, A. Baba, M. Shibata, T. Nakatsuka, K. Harii, Y. Wada, T. Kohro, T. Kodama, and J. Ando, *Journal of Atherosclerosis and Thrombosis* **10**, 304 (2003).

[206] K. A. Barbee, P. F. Davies, and R. Lal, *Circ Res* **74**, 163 (1994).

[207] M. Sato, K. Suzuki, Y. Ueki, and T. Ohashi, *Acta Biomaterialia* **3**, 311 (2007).

[208] R. H. W. Lam, Y. B. Sun, W. Q. Chen, and J. P. Fu, *Lab on a Chip* **12**, 1865 (2012).

[209] R. Ladeiras-Lopes, J. Ferreira-Martins, and A. F. Leite-Moreira, *Arquivos Brasileiros De Cardiologia* **90**, 374 (2008).

[210] Y. S. J. Li, J. H. Haga, and S. Chien, *Journal of Biomechanics* **38**, 1949 (2005).

[211] Y. C. Fung and S. Q. Liu, *Journal of Biomechanical Engineering-Transactions of the Asme* **115**, 1 (1993).

[212] A. Kamiya, R. Bukhari, and T. Togawa, *Bulletin of Mathematical Biology* **46**, 127 (1984).

[213] Y. S. Chatzizisis, A. U. Coskun, M. Jonas, E. R. Edelman, C. L. Feldman, and P. H. Stone, *Journal of the American College of Cardiology* **49**, 2379 (2007).

[214] A. R. Wechezak, R. F. Viggers, and L. R. Sauvage, *Laboratory Investigation* **53**, 639 (1985).

[215] A. Riad, H. M. Z. Schwabedissen, K. Weitmann, L. R. Herda, M. Dorr, K. Empen, A. Kieback, A. Hummel, M. Reinthaler, M. Grube, K. Klingel, M. Nauck, R. Kandolf, W. Hoffmann, H. K. Kroemer, and S. B. Felix, *Journal of Biological Chemistry* **287**, 27236 (2012).

[216] L. R. Herda, C. Trimpert, U. Nauke, M. Landsberger, A. Hummel, D. Beug, A. Kieback, M. Dorr, K. Empen, F. Knebel, R. Ewert, A. Angelow, W. Hoffmann, S. B. Felix, and A. Staudt, *Am Heart J* **159**, 809 (2010).

[217] M. D. Cheitlin, J. S. Alpert, W. F. Armstrong, G. P. Aurigemma, G. A. Beller, F. Z. Bierman, T. W. Davidson, J. L. Davis, P. S. Douglas, L. D. Gillam, R. P. Lewis, A. S. Pearlman, J. T. Philbrick, P. M. Shah, R. G. Williams, J. L. Ritchie, K. A. Eagle, T. J. Gardner, A. Garson, R. J. Gibbons, R. A. ORourke, and T. J. Ryan, *Circulation* **95**, 1686 (1997).

[218] J. Fox and S. Weisberg, *The car package available from CRAN contains the data for the book and extensive additional functionality for R.*, 2 edition, 2011.

Appendix A

A.1 Human Cardiac Fibroblasts (CFBs)

Please note, echocardiography and endomyocardial biopsies (as described in the following) were carried out by Priv.-Doz. Dr. med. Alexander Riad (University Medicine of the Ernst-Moritz-Arndt-University, Greifswald, Germany). The cell culture until 24 hours before the AFM measurements was carried out by Dr. Jeannine Witte (University Medicine of the Ernst-Moritz-Arndt-University, Greifswald, Germany).

A.1.1 Echocardiography

Echocardiography was performed as described previously [215, 216]. The Left Ventricle (LV) and Right Ventricle (RV) performance was analyzed by quantification of the LV End-Diastolic Dimension (LVEDD) and LV Ejection Fraction (LVEF; biplane manner to Simpson's methodology), RV End-diastolic Dimension (RVEDD), systolic Pulmonary Arterial Pressure (PAP), and Tricuspid Annular Plane Systolic Excursion (TAPSE). All measurements were performed by 2-dimensional echocardiography according to the guidelines from the American College of Cardiology and the American Heart Association [217].

A.1.2 Endomyocardial Biopsies

Endomyocardial Biopsies (EMBs) from the RV septum were performed as previously described [215]. Briefly, right jugular vein access was used to introduce a guiding sheath (7F, St. Jude Medical, St. Saint Paul, MN, USA). Biopsy specimens were taken using a disposable, dedicated cardiac biotome (7F 50 cm, Ref 502-402B, Cordis, The Netherlands) under biplane fluoroscopic

control (40° LAO and 90° LAO), which helps guiding the tip of the catheter to the septum. LV biopsies were performed according to a modified previously published protocol [215]. Right femoral artery access was used to introduce a guiding sheath (9F, Cordis, The Netherlands). Under fluoroscopic control (30° RAO), the guiding catheter (9F, MP A1, St. Jude Medical, St. Saint Paul, MN, USA) was positioned in the LV. Biopsy specimens were taken from the LV using a disposable, dedicated cardiac biotome (7F, 104 cm, Ref 502-400B, Cordis, The Netherlands). The procedure was performed under heparinization with 5.000 IE UFH.

A.1.3 Cell culture

Human heart derived fibroblasts have been cultured and proliferated by the following protocol.

After the biopsy of tissue from the Left (LV) and the Right (RV) heart Ventricle, the tissue was divided and seeded in 6-well culture plates(83.1839, Sarstedt, Nümbrecht, Germany) filled with 3 mL of culture medium (79 % of iscove basalmedium, 10% fetal calf serum, 10% human serum, 1% pen-strep; FG-0465, 10270-106, C05-020 and P11-010, Biochrom, Berlin, Germany) respectively and incubated at 37°C. After one week, the medium was exchanged for the first time. Afterward, the medium was exchanged every 4 days. When the fibroblasts have been grown confluently on the biopsy surface, the first passage was carried out. For this purpose the medium was removed and the fibroblasts were washed twice with PBS (+/+ (Ca2+/Mg2+) L1815 PBS-/- L1825, Biochrom, Berlin, Germany) containing no calcium and magnesium. Thereafter, 3 μL trypsin (L11-004, Biochrom, Berlin, Germany) were added in each well and the fibroblasts were stored for 3 min at 37°C in the incubator. After this incubation, wells were filled with the culture medium. Subsequently, the medium of wells containing cells from the same heart ventricle was pooled and centrifuged for 10 min at 300 g. Thereafter, the culture medium was replaced by fresh culture medium. For further proliferation respectively 5 mL of this medium were filled in cell culture flasks (50 cm^3; Greiner bio-one, Frickenhausen, Germany) and the culture medium was changed every 4 days until the next passage.

A.1.4 Histology

The total collagen content of the Endomyocardial Biopsies (EMBs) was analyzed in Masson's trichrome-stained slides using the interactive program "*Quantuepatho*" as described previously [160]. The percentage of stained area to total area was calculated to quantify cardiac fibrosis.

A.2 Neutrophil granulocytes

Please note, neutrophil purification and Flow Cytometry (FC) (as described in the following) were carried out by Dipl.-Biologist Tom Berthold (University Medicine of the Ernst-Moritz-Arndt-University, Greifswald, Germany).

A.2.1 Neutrophil purification

Unless otherwise stated, only neutrophils from HNA-3a homozygous donors were used for the experiments. Neutrophils were isolated from Ethylene-Diamine-Tetra-Acetic Acid (EDTA)-anticoagulated whole blood of healthy, HNA-3a homozygous donors by dextran sedimentation and subsequent gradient centrifugation of the leukocyte-rich supernatant (Biocoll; 1.077 g/mL, Biochrom AG). Remaining Red Blood Cells (RBCs) were lysed in ice cold (4°C) ammonium chloride buffer for 5 min. Neutrophils were washed twice with Phosphate-buffered Saline (PBS without $Ca2+$ and $Mg2+$, Biochrom AG) followed by centrifugation with $140g$ for 5 min at room temperature T_r and resuspension in VLE-RPMI 1640 media (Gibco-Invitrogen, Cat. No. 27016-021). Cell concentration was adjusted to $5 \cdot 10^7$ cells/mL and suspensions were stored at 4°C until treatment.

A.2.2 Additional results

Sensed height differences of surface protrusions

In Chapter 8.4 the influence of surface protrusions and recesses on AFM Force-Distance Measurements (FDMs) is investigated. The following Table A.1 gives the height differences sensed by the colloidal probe (diameter = 5 μm). The sensed height differences depend strongly on the number of adjacent FDCs which show a lower contact point z_0 than the investigated FDC.

adjacent FDCs with lower z_0	z_0(FDC) − $\langle z_0$(adjacent FDCs)$\rangle$ [nm]	standard deviation [nm]
8	358	294
7	244	181
6	156	112
5	97	80
4	-5	61
3	-102	90
2	-169	145
1	-280	220
0	-327	221

Table A.1: *Difference in determined contact points z_0 and the median contact point $\langle z_0$(adjacent FDCs)$\rangle$ of the closest neighbored FDCs.*

Time dependent F-actin content and elasticity of neutrophils

In Chapter 8.6.4 the kinetics of the absolute F-actin content in HNA-3a homocygous neutrophils after their activation by HNA-3a antibodies is discussed. Flow Cytometry (FC) was used to investigate this F-actin content. For this purpose, $1 \cdot 10^6$ neutrophils (in 50 μL VLE-RPMI; see Chapter 4.3.3) were treated with 50 μL of plasma P1 or control plasma P0. Treatments were stopped by fixation with 3.7% Paraformaldehyde (PFA; Sigma-Aldrich, Taufkirchen, Germany) after 0; 0.25; 0.5; 0.75; 1; 2; 4; 6; 8; 10; 30 and 60 min. A similar reaction kinetics using 1 μM FMLP served as control. After washing with PBS, cells were permeabilized with 0.5% saponin (Sigma-Aldrich, Taufkirchen, Germany) for 30 min at room temperature T_r. After washing with PBS (with 0.1% saponin), permeabilized cells were stained with phalloidine-ATTO488 (Atto-Tec, Siegen, Germany;) for 30 min at T_r in the presence of 0.1% saponin. Neutrophils were washed twice and F-actin content was analyzed by flow cytometry on a Beckman Coulter FC500 system (Brea, CA, USA). Figure A.1 shows FC data concerning the F-actin content of neutrophils. While Formyl-Methionyl-Leucyl-Phenylalanine (FMLP) caused a fast and pronounced increase (followed by a decrease) of the F-actin content, for the HNA-3a antibody containing plasma P1 no significant changes were observed.

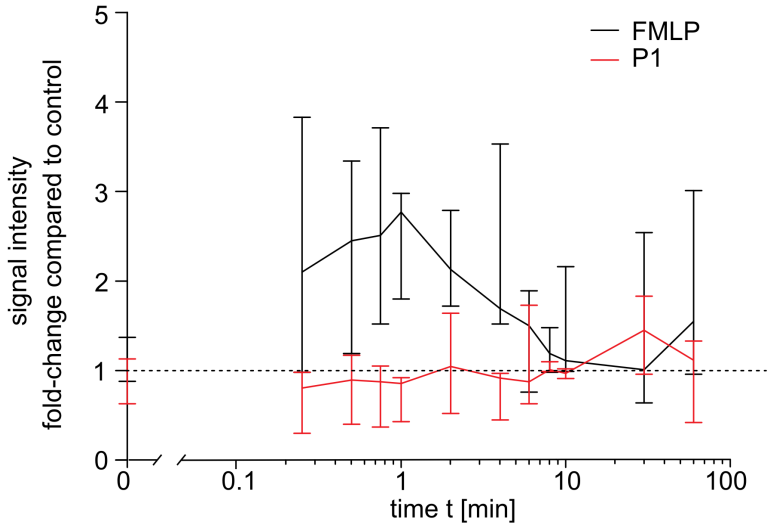

Figure A.1: *Flow Cytometry (FC) investigation on the F-actin content of HNA-3a homocygous neutrophils after contact with Formyl-Methionyl-Leucyl-Phenylalanine (FMLP) or HNA-3a antibodies.*

Nevertheless, in Chapter 8.6.4 slow kinetics in the cell elastic modulus E_2 of HNA-3a activated neutrophils were observed. Figure A.2 shows the kinetics of elastic modulus E_2 of 193 HNA-3a homocygous neutrophils after their incubation in the control plasma P0. Plasma P0 does not contain specific antibodies for the neutrophils. No time dependency of the cell elastic modulus E_2 was

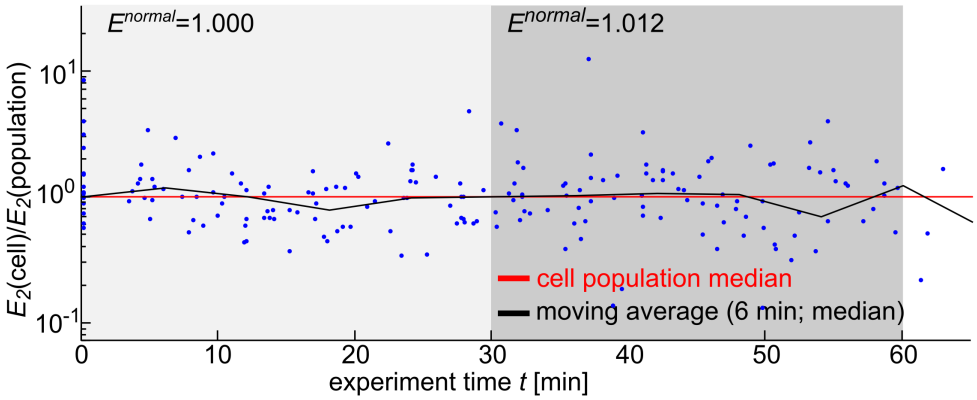

Figure A.2: *Kinetics of the elastic modulus E_2 of HNA-3a homozygous neutrophils incubated in the control plasma P0. Each blue dot shows the median E_2 of a single cell normalized to the median E_2 of the corresponding cell population. The black line shows the corresponding average (median) values E^{normal} (see Chapter 8.6.4) in 6 min intervals.*

observed, in contrast to neutrophils incubated with plasma P1 (see Chapter 8.6.4).

Comparison of the Young's modulus of HNA-3a and HNA-3b homozygous cells

Hereafter the cell Young's modulus E_2 of HNA-3a homocygous and HNA-3b homocygous neutrophils is compared. The measurements were carried out using AFM nanoindentation experiments, as described in Chapter 8. During the measurements the cells were adhered to Poly-HEMA coated glass cover slips in the control plasma P0. Figure A.3 shows, that there was no statistically significant difference observed.

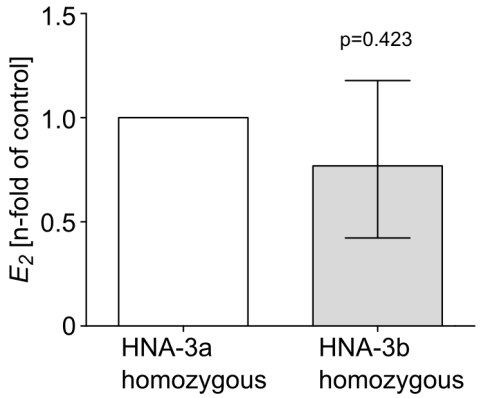

Figure A.3: *There was no statistically significant difference found, between the elastic modulus $\langle E_2 \rangle^{mix}$ of HNA-3a homozygous and $\langle E_2 \rangle^{mix}$ of HNA-3b homozygous neutrophils.*

Comparison of the Young's modulus of neutrophils incubated in control plasma P0 and FMLP

In Figure A.4 the elastic modulus $\langle E_2 \rangle^{mix}$ of HNA-3a homocygous neutrophils in the control plasma P0 is compared with the elastic modulus of neutrophils incubated in a solution of buffer and FMLP. Interestingly, no significant differences were observed in the elastic modulus $\langle E_2 \rangle^{mix}$ of both groups. This indicates, that the control plasma P0 has an impact on the cell elastic modulus, which is in the same scale as the impact of FMLP.

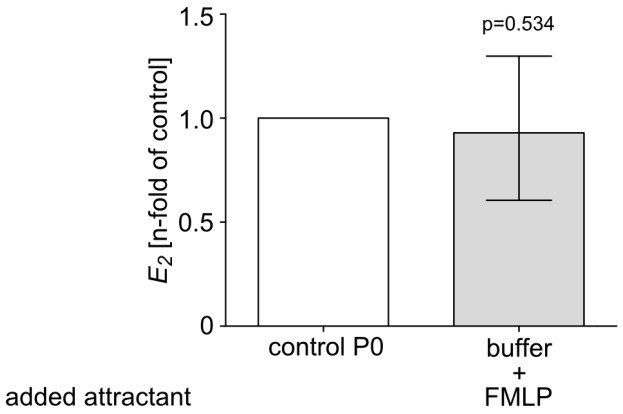

Figure A.4: *Neutrophils incubated in the control plasma P0 and neutrophils incubated in a solution of buffer and FMLP did not show a statistically different elastic modulus $\langle E_2 \rangle^{mix}$. Therefore, the increase of $\langle E_2 \rangle^{mix}$ caused by the control plasma P0 is approximately of the same intensity like the one caused by FMLP.*

Further correlations of the HNA-3a antibody induced cell stiffening with clinical observations

Unpublished clinical studies showed that HNA-3a antibody induced neutrophil aggregation can be inhibited by the trypsin-like serine protease inhibitor (TLCK), by the chymotrypsin-like serine protease inhibitor (TPCK) and by the NADPH[1] oxidase inhibitor (VAS). Next to the inhibition of neutrophil aggregation, neutrophil Reactive Oxigen Species (ROS) production (after HNA-3a activation) was shown to be inhibited by VAS and Diphenyleneiodonium chloride (DPI). Moreover, TLCK, TPCK, VAS and DPI were shown to inhibit the activation of the CD11b receptor. In order to investigate if (HNA-3a-induced) neutrophil stiffening is also prevented by these inhibitors, additional AFM cell elasticity measurements were carried out. First the influence of DPI, TLCK, TPCK and VAS on neutrophils incubated in the control plasma P0 was tested. Figure A.5 shows the results of these experiments. The elastic modulus $\langle E_2 \rangle^{mix}$ is shown, normalized to the elastic modulus of the control group which was incubated with plasma P0, containing no TRALI relevant specific antibodies. For DPI and VAS a neutrophil stiffening of 69.5% and 266.6% was observed. Furthermore, for TLCK no significant change in neutrophil elastic modulus was found, while TPCK induced a reduction of Young's modulus E_2 by 67%. This means: despite of TLCK all tested inhibitors (solved in Dimethyl Sulfoxide (DMSO)) induced variations in the cell elasticity. Therefore, in order

[1]NADPH: nicotinamide adenine dinucleotide phosphate

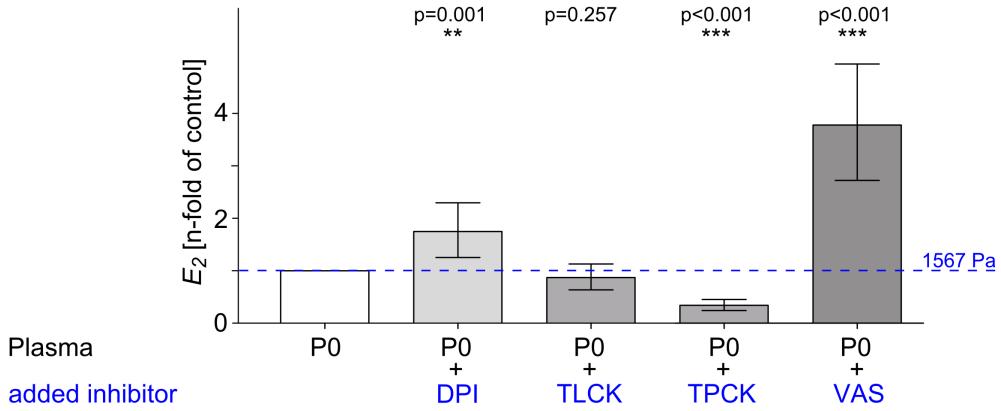

Figure A.5: *The influence of clinical relevant inhibitors on the Young's modulus E_2 of HNA-3a homozygous neutrophils. Neutrophils were incubated with the control plasma P0 or in solutions of the control plasma P0 and an inhibitor. The following inhibitors have been tested: DPI, TLCK, TPCK and VAS. For all inhibitors, except TLCK a significant change of the cell elasticity was observed.*

to test if the inhibitors have influence on the HNA-3a mediated stiffening the respective inhibitors were needed to be added also to the control plasma P0. Hence, FDMs were carried out for neutrophils incubated either in a solution of P0 and inhibitor or in a solution of P0 and FMLP and inhibitor or in a solution of P1 and inhibitor.

In Figure A.6 the results of these investigations are shown. Elastic modulus $\langle E_2 \rangle^{mix}$ is shown, normalized to the elastic modulus of the control cells. Under the additional influence of the inhibitors DPI, TPCK and VAS no change in cell elasticity was detected for FMLP and for P1. Nevertheless, as the observed confidence intervals are large in this case no definite interpretation on the influence of these inhibitors on the HNA-3a antibody induced neutrophils stiffening can be found by these measurements. Intriguingly, for the TLCK inhibitor, which did not change E_2 of the neutrophils by its own, a significantly increased E_2 was observed for P1 incubated cells, while FMLP did not induce a cell stiffening. This can be interpreted as further hint for different cellular mechanisms involved in the FMLP- and HNA-3a-induced neutrophil stiffening.

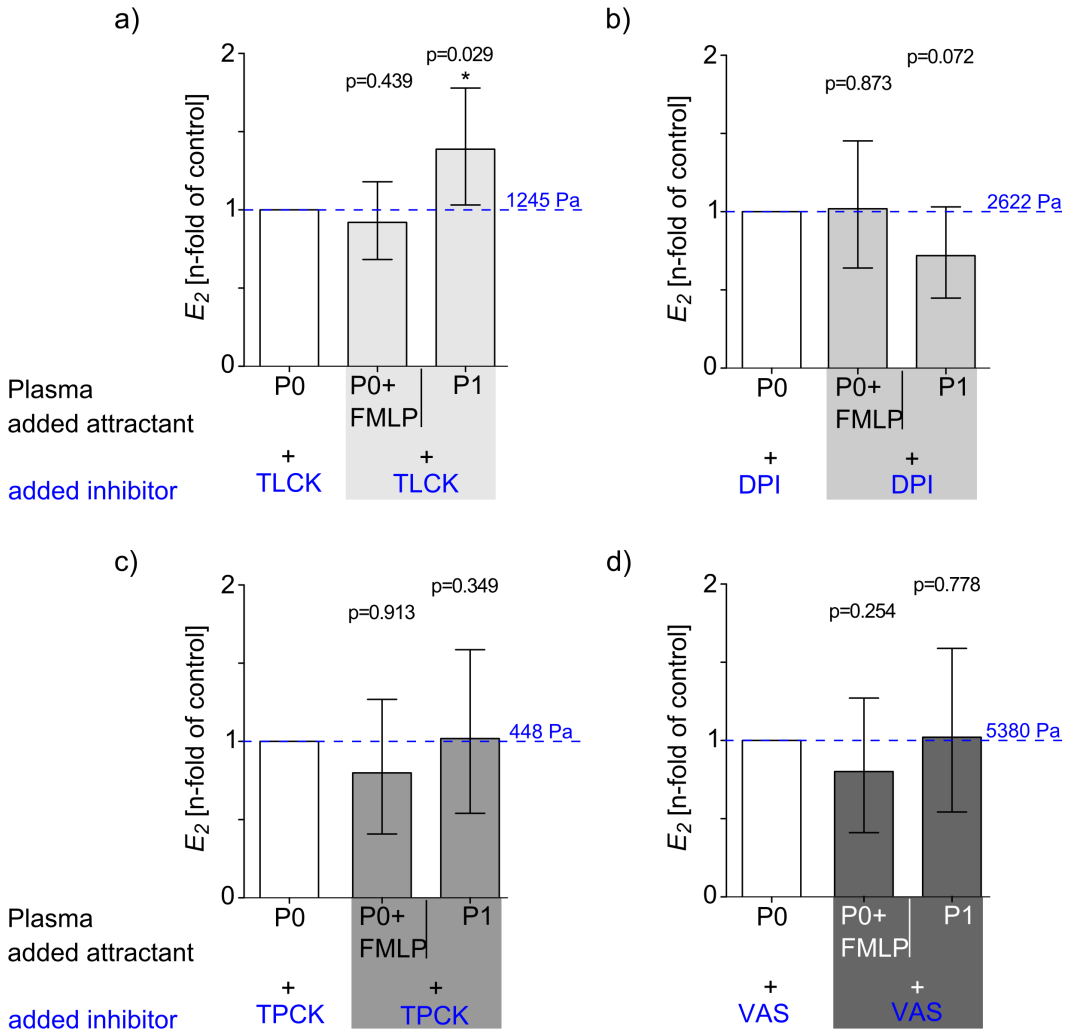

Figure A.6: *The influence of HNA-3a antibodies on the elastic modulus of HNA-3a homozygous neutrophils in the presence of diverse inhibitors. Neutrophils were incubated in a solution of the control plasma P0 and an inhibitor or in a solution of P0 and FMLP or in plasma P1. The following inhibitors have been tested:* ***a)*** *TLCK,* ***b)*** *DPI,* ***c)*** *TPCK and* ***d)*** *VAS. Probably due to the strong influence of the inhibitors (see Figure A.5) the elastic modulus E_2 showed a pronounced scattering. Only for TLCK which was shown to have no significant influence on E_2 the HNA-3a antibody induced stiffening remained, while TLCK inhibited completely the cell stiffening due to FMLP.*

A.3 Statistical Analysis

Please note, the (secondary) data analysis with linear mixed-effects models (as described in the following) was carried out by Dr. Stefan Groß (DZHK, Greifswald, Germany).

A.3.1 Human Cardiac Fibroblasts (CFBs)

Differences in Young's modulus E_2 between LV- and RV-derived CFBs were analyzed by a linear mixed-effects model (random intercept/slope model) which includes patient-ID, fibroblast-ID, and measurement-ID as random factors. Young's modulus data were log-transformed. Normality of residuals was ensured by visually checking Q-Q and density plots. Homogeneity of variances was ensured by visually checking residuals vs. fitted plots. P-values were obtained by Wald tests. Correlations between LVEDD/RVEDD and E_2, and LVEDD/RVEDD and fibrosis, were analyzed by univariate linear regression models. Normality of the response variable was ensured by the use of a Shapiro-Wilk test. P-values were obtained on the basis of F-values. The relationships between LV and RV cell stiffness and LV and RV performance were analyzed by using Pearson's correlation tests. All statistical analysis have been performed using R (version 2.15.0, R Development Core Team 2012) with the "*lme4*" package and the "*car*" package [218]. The significance level was set to 0.05.

A.3.2 Neutrophil granulocytes

Young's modulus E_2 data were analyzed using a linear mixed-effects model with donor-ID and cell-ID as random factors and treatment (4 rings in the reliable zone of the force-volume measurements) as fixed factor. Values of E_2 were log-transformed to ensure normality of model residuals and homoscedasticity. Additionally the data were visually checked by Q-Q plots, kernel density plots and residuals-vs-fitted plots. All calculations were done using R (v2.15.3; R Development Core Team, 2013) and the R-packages "*car*" [218] and "*lme4*". The Data are presented as fold-change (geometric mean ratio) against the reference level by exponentiating the beta-coefficients with 95% confidence intervals. The significance level was set to 0.05. For statistical analysis, SPSS Statistics 21 (IBM, Armonk, USA) and Graph Pad Prism 5 (GraphPad Software, La Jolla, CA, USA) were used. Statistical differences between different neutrophil treatments were analyzed using a non-parametric Mann-Whitney U test.

A.3.3 Human Umbilical Vein Endothelial Cells (HUVECs)

AFM data were analyzed using a linear mixed-effects model with donor-ID and cell-ID as random factors and treatment (4 levels) as fixed factor. Values of Young's modulus E_2 were log-transformed to ensure normality of model residuals and homoscedasticity. Additionally the data were visually checked by Q-Q-plots, kernel density plots and residuals-vs-fitted plots. All calculations were carried out using R (v2.15.3) and the R-packages "*car*" [218] and "*lme4*". Data are presented as fold-change (geometric mean ratio) against the reference level by exponentiating the beta-coefficients with 95% confidence intervals. The significance level was set to 0.05.

Selbstständigkeitserklärung

Hiermit erkläre ich, dass diese Arbeit bisher von mir weder an der Mathematisch-Naturwissenschaftlichen Fakultät der Ernst-Moritz-Arndt-Universität Greifswald noch einer anderen wissenschaftlichen Einrichtung zum Zwecke der Promotion eingereicht wurde. Ferner erkläre ich, dass ich diese Arbeit selbständig verfasst und keine anderen als die darin angegebenen Hilfsmittel und Hilfen benutzt und keine Textabschnitte eines Dritten ohne Kennzeichnung übernommen habe.

Unterschrift des Promovenden

Lebenslauf und Veröffentlichungen

Lebenslauf

Persönliche Daten

Name	Michael Glaubitz
Anschrift	Makarenkostraße 20a
	17491 Greifswald
Geburtsdatum	18/07/1984

Schulische Ausbildung

08/1995 - 06/2001	1. Mittelschule, Riesa
27/06/2001	Abschluss: Realschulabschluss
08/2001 - 07/2004	Berufliches Schulzentrum für Technik, Riesa
02/07/2004	Abschluss: Allgemeine Hochschulreife

Studium

10/2004 - 03/2010	Ernst-Moritz-Arndt-Universität, Greifswald
	Diplomstudium Physik (Spezialfach: Plasmaphysik)
26/03/2010	Abschluss: Diplom-Physiker
10/2010 - 08/2014	Zentrum für Innovationskompetenz (ZIK HIKE), Greifswald
	Promotion im Bereich Biophysik

Veröffentlichungen

Artikel

- Otte, M., Laqua, H. P., Chlechowitz, E., Drewelow, P., **Glaubitz, M.**, Marsen, S., Muller, E., Podoba, Y., Schacht, J., Stange, T., Steffen, F., Wagner, F., Wolf, R., Zhang, D., "Overview of Experimental Results from the WEGA Stellarator", Contributions to Plasma Physics, 2010. 50(8): p. 780-784.

- Otte, M., Laqua, H. P., Chlechowitz, **Glaubitz, M.**, Marsen, S., Podoba, Y., Stange, T., Zhang, D., "Electron Bernstein Waves at the WEGA Stellarator- Heating and Emission", Plasma Fusion Res., 2010. 5, S2011.

- Zhang, D., **Glaubitz, M.**, Laqua, H. P., Marsen, S.,Otte, M., Stange, T., "Determination of electron thermal diffusivity at the WEGA stellarator", Nuclear Fusion, 2012. 52(4)

- **Glaubitz, M.**, Block, S., Witte, J., Empen, K., Groß, S., Schlicht, RC et al., "Stiffness of Left Ventricular Cardiac Fibroblasts Is Associated With Ventricular Dilation in Patients With Recent-Onset Nonischemic and Nonvalvular Cardiomyopathy", CIRCULATION JOURNAL. 2014, Vol. 78 No. 7 1693-1700

- **Glaubitz, M.**, Medvedev, N., Pussak, D., Hartmann, L., Schmidt, S., Helm, C.A., Delcea M., "A novel contact model for AFM indentation experiments on soft spherical cell-like particles", Soft Matter, 2014, 10 (35), 6732 - 6741

Poster

- **Glaubitz, M.**, Block, S., Witte, J., Gottschalk, K.E., Felix, B.F., Riad, A., Helm, C.A., "Different elasticity of left-ventricular and right-ventricular fibroblasts of DCM-patients", DPG Frühjahrstagung, Regensburg 2012.

- **Glaubitz, M.**, Block, S., Witte, J., Gottschalk, K.E., Felix, B.F., Riad, A., Helm, C.A., Delcea, M., "Different elasticity of left-ventricular and right-ventricular fibroblasts of DCM-patients", Nanoscale, Bristol 2012.

- **Glaubitz, M.**, Berthold, T., Helm, C.A., Delcea, M., Greinacher, A. et al., "Increased Stiffness of Neutrophils after Activation by Transfusion Related Acute Lung Injury-Relavant Antibodies", DPG Frühjahrstagung, Regensburg 2013.

- **Glaubitz, M.**, Medvedev, N., Pussak, D., Hartmann, L., Schmidt, S., Helm, C.A., Delcea, M., "A novel contact model for AFM indentation experiments on soft spherical cell-like particles", NMC, Madrid 2014.

Vorträge

- **Glaubitz, M.**, Block, S., Witte, J., Gottschalk, K.E., Felix, B.F., Riad, A., Helm, C.A., Delcea, M., "Different elasticity of left-ventricular and right-ventricular fibroblasts of DCM-patients", MPI Summer School, Lecce 2012.

Danksagung

An dieser Stelle möchte ich mich ganz herzlich bei jenen bedanken, welche mir Stütze und Orientierung beim Schreiben dieser Arbeit und für meine berufliche Entwicklung waren. Zu allererst gilt dieser Dank Prof. Christiane A. Helm und Dr. Mihaela Delcea, die sich immer wieder viel Zeit nahmen, um mit mir über Projekte, Daten, Veröffentlichungen und die eine oder andere verrückte Idee zu sprechen.

Zudem danke ich den Initiatoren des ZIK HIKE: Prof. Stephan Felix, Prof. Andreas Greinacher, Prof. Werner Weitschies und Prof. Christiane A. Helm dafür, dass ich die Möglichkeit bekam am ZIK HIKE zu arbeiten. Ich möchte auch allen Mitarbeitern des ZIK HIKE für die vielen guten Diskussionen danken, die es einem Plasmaphysiker erst ermöglichten, statt an Kernfusion an Zellkerne zu denken. Mein besonderer Dank gilt dabei Dr. Hans-Peter Müller, Dr. Raghavendra Palankar, Dr. Mykola Medvedev und Sven Brandt.

Im Rahmen dieser Arbeit kamen zahlreiche kleine und große Kooperationen zum Tragen. Ich danke daher Dr. Stephan Gross vom DZHK in Greifswald, den Abteilungen Transfusionsmedizin und Kardiologie des Universitätsklinikums Greifswald, der Arbeitsgruppe der von Prof. Christiane A. Helm, Dr. Laura Hartmann und Dr. Daniel Pussak vom Max-Planck-Institut für Kolloid- und Grenzflächenforschung in Potsdam und Dr. Stephan Schmidt von der Universität Leipzig. Insbesondere danke ich an dieser Stelle Tom Berthold und Malte Pennewitz. Vor allem die Zell-Projekte wären ohne ihren engagierten Einsatz wohl weit weniger erfolgreich gewesen.

Eine wichtige Stütze waren mir auch zahlreiche Personen aus dem nichtphysikalischen Bereich. Hier sei meine Familie erwähnt, allen voran meine Frau Ines, meine Mutter Annette und ihr Mann Burkhard, sowie mein Großvater

Wolfgang. Diese haben mir in guten und in schlechten Labortagen stets ermutigend zur Seite gestanden. Mein größter und letzter Dank gilt jedoch $A\&\Omega$.